On-chip THz Systems

Christopher David Wood B.Sc, M.Sc

Submitted in accordance with the requirements for the degree of Doctor of Philosophy

The University of Leeds

School of Electronic and Electrical Engineering

October 2006

The candidate confirms that the work submitted is his own and that appropriate credit has been given where reference has been made to the work of others.

This thesis is dedicated to my parents. I couldn't have wished for better.

I would also like to dedicate this to my friends back home in Burnley, with special mention to Lee Gaughan who died too soon... wish you were here Gordy.

Abstract

A variety of novel on-chip terahertz systems have been developed with the aim of advancing current on-chip spectroscopic techniques. A novel methodology for the fabrication and positioning of isolated regions of photoconductive LT-GaAs thin film has been developed, allowing generation and detection of THz signals in-plane with a microstrip transmission line device. Devices with bandwidths in excess of 1.2 THz have been demonstrated.

The introduction of novel, THz frequency passive resonator elements, in the form of quarter-wave band stop filters, into a transmission line device allowed measurements of the properties of overlaid dielectric films by monitoring of the resonant shift. Cascading multiple resonators along a single interconnect allowed simultaneous measurements to be performed at isolated frequencies at discrete locations on a single device. The first full characterisation of the resonant shift as a function of load thickness for a THz filter is performed, with measurements obtained in excellent agreement with subsequent free space studies, whilst requiring a 10^5 reduction in sample volume.

Design modifications provided ultrahigh spectroscopic resolution in the terahertz range of < 2 GHz, allowing the measurement of overlaid films of DNA in single and double stranded form down to quantities of 0.211 femtomoles, almost double the sensitivity, in terms of average relative resonant shift per base pair, when compared to literature values. The active region of the devices designed for this work is $\sim$ 123 times less than existing topologies and therefore represents an increase in resonant shift per unit active area of two orders of magnitude.

Contents

Acknowledgements

Firstly I would like to thank my supervisors, Dr. John Cunningham, Professor Ian Hunter and Professor Giles Davies for their guidance and input throughout my project. Thank you also to EPSRC and Research Councils UK Basic Technology for funding the project.

My appreciation extends to several colleagues, who have provided invaluable assistance with my work. Thanks to Dr. Mark Stringer for being a funny and knowledgeable guy, to Dr. Prashanth Upadhiya who knows everything and doesn't mind going out of his way to help you, and to Dr. Andrew Hartley and Dr. Ben Johnson for their advice in the cleanroom.

On a more personal level, I would like to thank my parents for being there and for believing in me for all these years, and my two brothers for not making fun of me too much. A big thank you to Dr. Paul Tosch for his friendship, advice, barbecues and enthusiasm and also for raising my blood caffeine levels so very, very high. Thanks also to my friends and colleagues Dr. Graham Rangel-Sharp and Dr. Hiang Teik Tan for their help consuming beer and coffee in unprecedented amounts. A special thank you to Emika for being my little brown rock and for making me smile when I needed to.

List of Figures

List of Tables

List of Principal Symbols

C	Transmission line shunt capacitance (F)
c_0	Free space light velocity ($2.988 \times 10^8\ ms^{-1}$)
d	Substrate thickness (μm)
E	Electric field (Vm^{-1})
f_0	Fundamental resonant frequency (Hz)
f_c	Cut-off frequency for a transmission line (Hz)
f_{max}	Maximum frequency for a Fast Fourier Transform (Hz)
f_{ref}	Reference frequency of band stop response (Hz)
f_{shift}	Absolute frequency of shifted band stop response (Hz)
G	Transmission line shunt conductance (S)
I	Current (A)
j	$\sqrt{-1}$
k	Wave vector (m^{-1})
L	Transmission line series inductance (H)
l_{bp}	Bond pad length (μm)
l_p	Probe arm length (μm)
m	Total mass of DNA (g)
M_r	Mass of single DNA plasmid (g)
n	Moles of DNA (mol)
R	Transmission line series resistance (Ω)
$r_{shift/bp}$	Relative resonant shift per base pair DNA
$\tan\delta$	Loss tangent of a dielectric

V	Voltage (V)
W	Transmission line width (μm)
Z_0	Characteristic impedance (Ω)
Z_{in}	Input impedance to a transmission line section (Ω)
Z_l	Transmission line load impedance (Ω)
Å	Avogadro's number (6.022×10^{23})
α	Attenuation constant (dB)
α_c	Conductor losses (dB)
α_d	Dielectric losses (dB)
β	Phase constant (m^{-1})
Γ	Reflection coefficient
γ	Complex propagation constant
Δx	Time delay (ps)
δ_s	Skin depth (m)
ϵ_0	Free space permittivity (8.854×10^{-12} Fm^{-1})
ϵ_{eff}	Effective permittivity for microstrip
ϵ_r	Relative permittivity
$\mathcal{F}_{[Vin]}$	Fourier transform of input pulse
$\mathcal{F}_{[Vout]}$	Fourier transform of output pulse
θ	Electrical length (°)
λ_0	Free space wavelength (m)
λ_{eff}	Effective wavelength in microstrip (m)
μ_0	Permeability of free space ($4\pi \times 10^{-7}$ Hm^{-1})
σ	Electrical conductivity (S)
υ_{ph}	Phase velocity in microstrip (ms^{-1})

Chapter 1

Introduction

On-chip spectroscopic analysis is rapidly becoming a viable alternative to complementary free space technologies. Whilst offering fundamental advantages for general spectroscopy - such as reduction in sample volume and increased interaction length between sample and probing signal - on-chip approaches also offer more subtle benefits when considering certain specific technological applications. This emerging technology has potential uses in biomolecular sensing, environmental monitoring, and in the analysis of condensed matter systems. The technology is readily adaptable for forming biological hybrids with chemically functionalised surfaces, use with carbon nanotubes for sensing, and operation at cryogenic temperatures.

An increasingly wide range of applications are presently being investigated using THz spectroscopy, including molecular fingerprinting for drug assay [1], medical imaging [2] and genetic analysis [3]. THz frequencies represent a non-ionising, non-destructive form of radiation, making them an attractive tool for medical and biological applications. It has been demonstrated that many light chemicals and molecules exhibit intramolecular resonances whose frequencies lie within the THz region, allowing molecular fingerprinting to be performed in this band. Until quite recently (within the last fifteen years or so), the sources of generation available were limited to large, expensive and more importantly, incoherent THz sources. The area of THz detection has also been relatively undeveloped [4] when compared

to that of more commonly used radiation such as infra-red, x-rays and radio waves. As technology has progressed however, terahertz generation and detection has become much more tractable, and the range of THz techniques used has become very diverse, ranging from semiconductor antenna generation to optical parametric oscillation. Several areas of THz technology, including generation and detection in free space and on-chip systems, and existing on-chip THz techniques will be discussed in this chapter.

1.1 Free Space Terahertz Generation

1.1.1 Nonlinear Optics

When lasers became available in the early 1960's [5], monochromatic optical powers available for experimentation increased tremendously. The high electric fields offered by such devices allowed scientists to quickly utilise the fact that linear optics is only the low-power limit to the realm of non-linear optics. At high laser intensities, certain optical media were found to generate higher harmonics of the incident wavelength, attributed to nonlinear polarisation within the material [6]. The use of non-linear crystals leads to several similar, but distinct, methods of THz generation and detection. All of the following techniques utilise a high second order susceptibility within the non-linear crystal to generate an output frequency within the THz region.

Introduction to Nonlinear Optics - Second Harmonic Generation

Whilst optical second harmonic generation is itself not suitable for THz generation, it does provide a basis for the understanding of further nonlinear effects. A suitable material for the production of optical harmonics must have several intrinsic properties; it must have a nonlinear dielectric coefficient and it must be transparent not only to the incident optical frequency, but to all the required

harmonic outputs [7]. The basis for most nonlinear optical theory stems from a Taylor expansion of a materials polarisation, P, in powers of the incident electric field, E. The scalar form of this is

$$P = \epsilon_0(\chi^{(1)}E + \chi^{(2)}E^2 + \chi^{(3)}E^3 + ...), \tag{1.1}$$

where $\epsilon_0 \approx 8.85$ x 10^{-12} Fm^{-1} is the permittivity of free space, $\chi^{(1)}$ is the linear susceptibility, related to the refractive index by $n^2 = 1 + \chi^{(1)}$, and $\chi^{(n)}$ represent the n^{th} order susceptibilities. The relative intensities of the higher order terms decrease rapidly as n increases, requiring that very high powered lasers, focussed into the crystal, are used for harmonic generation.

A high conversion efficiency from the lower frequency pump beam (longer wavelength) to the high frequency output beam (shorter wavelength) requires that the two are kept in phase. Since the speed of light in a material generally varies with wavelength due to dispersion of the index of refraction, this is not always the case. Phase matching can be achieved however, by utilising a property called *birefringence* in some nonlinear media. In birefringent crystals, the refractive index depends not only on wavelength, but also on the polarisation direction of the incident field with respect to the crystal. In uniaxial crystals, one cartesian axis (called the *c-axis*) has a different refractive index to the other two equivalent axes. E-fields with polarisation parallel to this axis are said to be ordinary rays and experience the ordinary refractive index n_0, whereas the orthogonal counterparts are said to be extra-ordinary and experience the corresponding extra-ordinary refractive index, n_e. A particular crystal orientation can be found where the fundamental and second harmonic light see the same index of refraction and so remain in phase as they propagate.

In other nonlinear materials periodic poling is introduced during the crystal fabrication, which is used to keep the waves approximately in phase [8]. This is achieved by inverting the polarity of adjacent crystal domains [9] in ferroelectric

materials using one of a variety of techniques, such as electric fields applied via lithographically defined electrodes [10], with periods spaced in multiples of the desired operational wavelength. This technique, called quasi-phase matching, is commonly used for lithium niobate and lithium tantalate, and greatly expands the options for efficient frequency doubling at various wavelengths and temperatures, often presenting much higher nonlinear output powers than found with birefringent crystals. Even under such conditions, the second order output signal inherently is of much lower power than the original, so a high power incident optical beam must be used in order to generate a detectable signal at the higher frequency.

Optical Parametric Generation

Another form of THz generation using nonlinear crystals is called Optical Parametric Oscillation (OPO). Contrary to SHG, OPO relies on a material's nonlinear response under the influence of a pump laser beam, to convert photons from *shorter* to *longer* wavelengths. As seen in Figure 1.1, which shows a colinear optical parametric oscillator (OPO), the incident high energy pump beam of wavelength λ_p generates two lower energy *signal* and *idler* beams, whose wavelengths λ_s and λ_i must satisfy the condition:

$$\frac{1}{\lambda_p} = \frac{1}{\lambda_s} + \frac{1}{\lambda_i}, \tag{1.2}$$

and correspondingly the wave vectors

$$k_p = k_s + k_i \tag{1.3}$$

to satisfy conservation of energy. The exact wavelengths of the signal and idler are determined by the angle which the incident pump wave makes with the crystal

axis. As for second harmonic generation, efficient generation of the signal and idler waves only occurs under phase matched conditions.

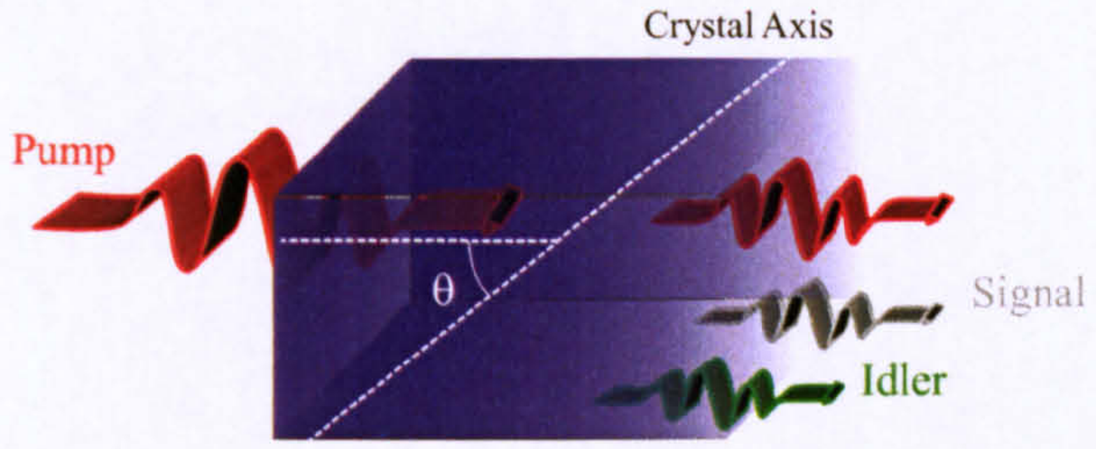

Figure 1.1: Generation of a signal and idler beam in a nonlinear crystal, where θ shows the angle between the pump beam and the crystal axis.

As the crystal is rotated, the the refractive index experienced by the signal and idler waves changes, and only selected frequencies are phase matched at any one angle. This leads to tunability of the output wavelengths by variation of the crystal angle with respect to the pump beam. Continuously tunable, compact sources which operate at room temperature have been demonstrated with frequency tunability from 1.02 - 3.5 THz and 100 GHz spectral resolution [11] in non-colinear systems.

OPO systems also have the advantage of being able to situate the nonlinear crystal in a cavity which is resonant at either the signal or idler frequency (singly resonant) or both (doubly resonant), which acts as a gain region to increase the output power of one, or both, of the waves. Doubly resonant cavities have an advantage in that the pump laser threshold power is lower than for singly resonant structures, but it also becomes increasingly complicated to align to achieve both phase matching *and* double resonance.

Difference Frequency Mixing

Difference frequency mixing, also referred to as optical rectification, involves the use of two near infrared (NIR) lasers of slightly differing frequencies, incident on

a birefringent crystal (Figure 1.2). The total electric field, E, present at a depth x into the crystal at any particular time is given by the sum of the fields of the two pump beams:

$$E(x,t) = E_1 \sin(k_1 x - \omega_1 t) + E_2 \sin(k_2 x - \omega_2 t),$$

with radial frequencies ω_1 and ω_2, and wave vectors k_1 and k_2 representing the two pump waves. If we consider the instantaneous power at a position $x = 0$,

$$\begin{aligned} P &\propto [E(x,t)]^2_{x=0} \\ &= (E_1 \sin(\omega_1 t) + E_2 \sin(\omega_2 t))^2 \\ &= E_1^2 \sin^2(\omega_1 t) + E_2^2 \sin^2(\omega_2 t) + \\ &\quad E_1 E_2 \cos(\omega_1 + \omega_2)t + E_1 E_2 \cos(\omega_1 - \omega_2)t, \end{aligned}$$

we see that there are components at each pump frequency, as well as mixed components at frequencies $\omega_1 + \omega_2$ and $\omega_1 - \omega_2$, the latter of these constituting the THz signal. By varying the frequencies of the pump lasers we can tune the difference frequency over a very broad range, for example 0.3 - 4.9 THz in GaSe [12]. The unwanted signals may then be filtered out to produce a pure THz signal.

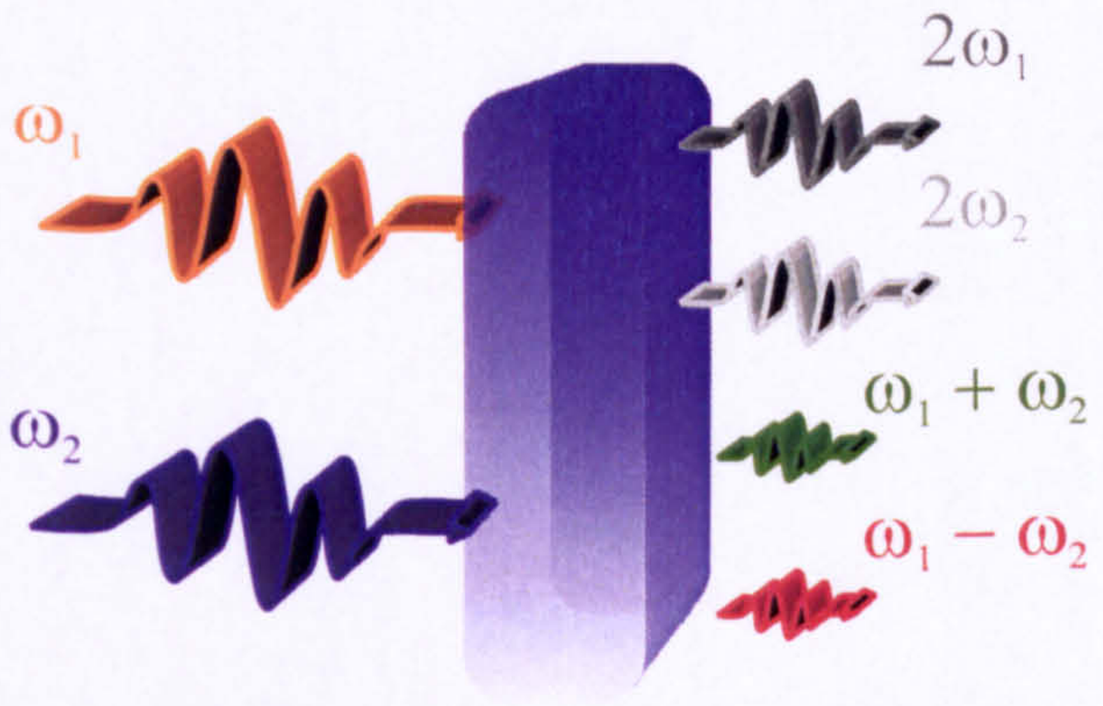

Figure 1.2: Simple schematic of Difference Frequency Mixing in a nonlinear crystal.

1.1.2 Quantum Cascade Lasers

Semiconductor quantum-effect devices, including both vertically grown quantum-well structures and laterally confined mesoscopic devices, are man-made quantum mechanical systems in which the sub-band energy levels can be selected by altering the dimensions of the device (e.g. well depth, barrier width, barrier height etc.). Such mulitlayered semiconductor devices form the basis for quantum cascade lasers (QCLs). Figure 1.3 demonstrates the basic operation of a quantum cascade lasing system, which is based upon intersubband transitions, as opposed to the interband transitions exploited in classical semiconductor lasers. Typically, the frequency corresponding to the intersubband transitions is in the millimeter-wave range ($\Delta E \sim 1$ - 4 meV) for the lateral quantum-effect devices [13], and THz up to infrared for the vertical quantum wells [14]. The QCL consists of sequential repeated sections, or periods, each comprised of a carrier injector region and an active (light emitting) region. Under an applied electric field, carriers may tunnel through the injector region into the required energy level in the active region (labelled 2 in Figure 1.3). The lifetime and tunneling probability may be engineered to achieve population inversion in this energy state, from which carriers then decay to the lower level releasing energy in the form of a photon. Decayed carriers tunnel into the next injection region and can therefore lase again in the second repeat period. A single electron may therefore generate as many photons as there are periods within the structure.

Whilst most quantum cascade lasers operate in the low temperature regions, their radiation may be used to measure systems at room temperature. Recent spectroscopic analysis of semiconductors has been performed by detecting cyclotron resonance within a material under a magnetic field [16] at room temperature, although the QCL itself remained cryogenically cooled. Power outputs for QCL's are reaching several tens of milliwatts [17] [18] - although at this stage in time only at lower temperatures ($\approx$ 80K), which prevents their uses outside a cryostat. These devices represent a potential transformation in Terahertz technology in the

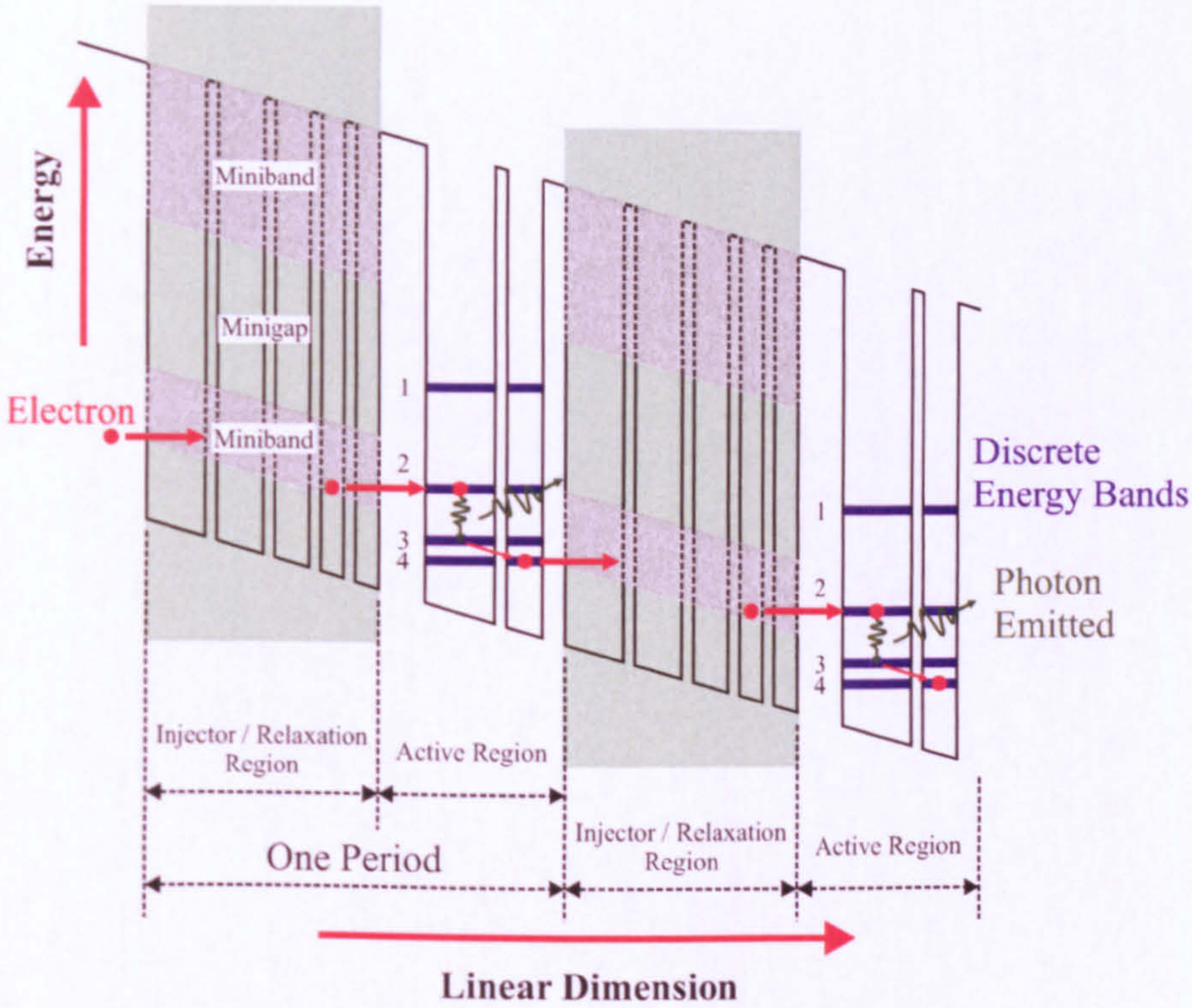

Figure 1.3: The lasing process in a Quantum Cascade Laser adapted from [15].

advent of their commercial viability [15], though as they are not yet directly integrable into a room temperature, on-chip environment, their use is not applicable for this study. Another major disadvantage is the bandwidth of emission characteristic to QCL's. Due to the nature of the intersubband transitions, the lasing action produces only either monochromatic emission, or multimode emission over a narrow bandwidth and not the broadband signals required in spectroscopic studies.

1.1.3 Photoconductive Antenna

The most common method of generating broadband THz signals is in the use of pulsed-laser excited, photoconductive semiconductors coupled to antenna structures. The basis behind the operation of photoconductive antenna lies with the coherent optical generation of ultra-short (< 1 ps) lifetime carriers within a semiconductor, and their subsequent acceleration under an applied electric field. The

antenna itself consists of a metal electrode structure fabricated on the surface of the photoconductive semiconductor material. Focussing a pulsed laser with energy greater than the semiconductor band gap onto the surface, excites carriers from the valence to the conduction energy band (carrier generation) providing free carriers which are accelerated by an applied electric field between biased electrodes. This leads to a transient photocurrent, $I(t)$, flowing between the electrodes. This current rises very rapidly immediately on carrier injection (i.e. at the time the laser pulse strikes the semiconductor surface) and decays according to the carrier recombination lifetime of the semiconductor. The electric field radiated from the structure is proportional to the time derivative of the photocurrent [19, 20]:

$$E_{THz} \propto \frac{\partial I(t)}{\partial t}, \tag{1.4}$$

and has frequency components which reflect the lifetime of the generated pulse [21]. With laser pulses of $\approx 10 fs$ and subsequent sub-ps excited pulses, generation of field frequencies up to 35 THz [22] have been achieved. The overall principle is shown diagrammatically in Figure 1.4, which also demonstrates that THz radiation is generated in both the forward (transmitted) and backward (reflected) direction, with respect to the incident laser pulse.

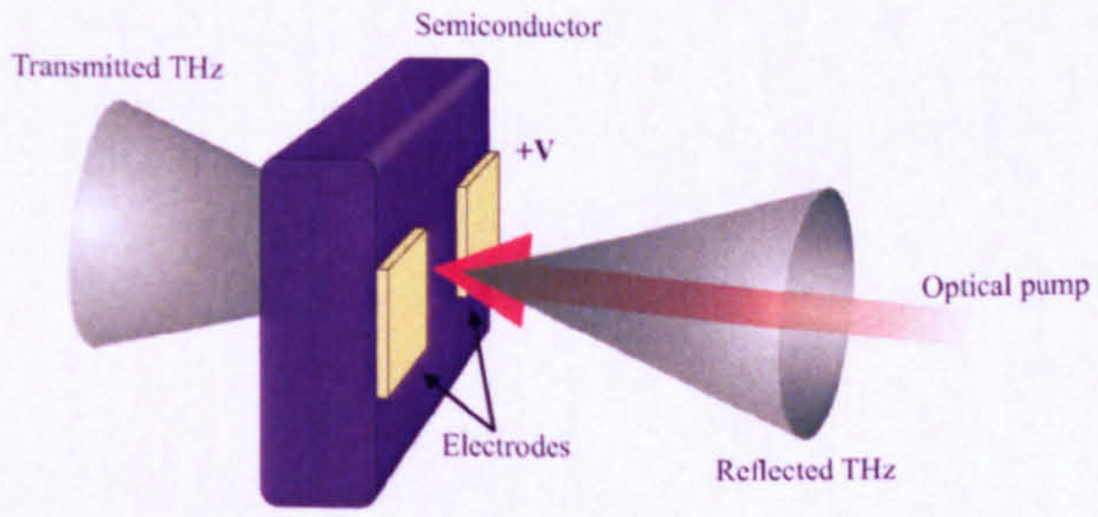

Figure 1.4: Diagram of a photoconductive antenna illuminated by a pulsed laser beam and generating transmitted and reflected THz signals.

Use of either directed signal has both advantages and disadvantages, with the forward generated wave typically being of higher THz power, but being limited in

frequency resolution by reflections within the semiconductor, whilst the reflected beam has a typically broader spectral bandwidth [22], albeit at lower powers.

Three dimensional Monte-Carlo simulations have been performed [23], [24], which consider the effects controlling the pulse widths generated in photoconductive switches such as those used in free space antenna. The excitation laser pulse constitutes one of the main variables in the generated pulse width, since this controls the time over which carriers are generated within the photoconductive material, and hence controls the rise time of the emitted signal. Increasing the optical pulse width above 40 fs is suggested to introduce a screening field which counters the applied bias across the gap (due to the increased carrier generation time) and leads to a decrease in generated THz power. A second important variable is the carrier lifetime of the excited electron-hole pairs generated in the switch, which control the pulse decay time when laser illumination is terminated. Carriers excited directly into the Γ valley of the conduction band have the shortest lifetime, whilst those excited into neighbouring L side-valleys have a higher effective mass, with a corresponding lower mobility and therefore longer lifetime. It is expected that high energy photons (i.e. shorter wavelength) will therefore cause THz signal broadening due to an increased number of carriers excited into L valleys. The final contribution to the generated THz pulse width arises from the finite laser spot size, which introduces a minimum excitation region and hence a time broadening of $\Delta t = \frac{l}{v_{ph}}$, where l is the excitation spot diameter, and v_{ph} the phase velocity, although this effect is only important when coupling the radiation into waveguide structures, as discussed in Chapter 4.

1.2 Free Space THz Detection

Conventional THz detection relies on liquid helium cooled bolometers, which measure the THz radiation intensity [25]. Such devices are limited in sensitivity by background radiation and provide no phase information and so it is preferred to perform direct, coherent measurement of the THz electric field in the time

domain (as opposed to simply its average intensity), which allows evaluation of the refractive index and absorption coefficient of a material. The most common approaches to this involve detection either by antenna structures similar to those in Section 1.1.3, or by electro-optic sampling in a non-linear material.

1.2.1 Detection Using Photoconductive Antenna

A photoconductive antenna such as that described in Section 1.1.3 may also be used for detection of THz radiation. A probing laser beam generates carriers within the antenna structure in the same mechanism as for THz generation. In this case however, the electric field is not produced by a standing voltage across the electrodes, but by the time dependent field of the THz pulse itself. Current therefore only flows when *both* the laser induced photocarriers *and* the THz electric field are present, and is proportional to the THz electric field. By altering the time delay of the probe laser beam, different parts of the THz pulse may be measured, which allows construction of a time-resolved map of the THz electric field. Moderate pulse broadening occurs due to the carrier lifetime within the semiconductor, as for photoconductive generation, so for sensitive detectors it is necessary to choose semiconductors with both high mobility and short carrier lifetime. Suitable materials include Low Temperature-GaAs (LT-GaAs) and radiation damaged silicon-on-sapphire (SOS) [26].

A more recent development in antenna material consists of MBE grown ErAs quantum dots, or nanoislands [27] $\sim$ 1.2 monolayers high, embedded into a GaAs semiconductor matrix. The ErAs - GaAs layers form a superlattice structure of period, L, (Figure 1.5) which provides an advantage over LT-GaAs as variation of the period size allows direct control over the lifetime of excited carriers. Adjustment ErAs content and of the growth temperatures also provides control over the carrier trapping density of the superlattice, as well as its dark resistance. By fabricating antenna structures on the superlattice similar to those previously discussed and using them to detect broadband THz signals, Prasankumar *et al.*

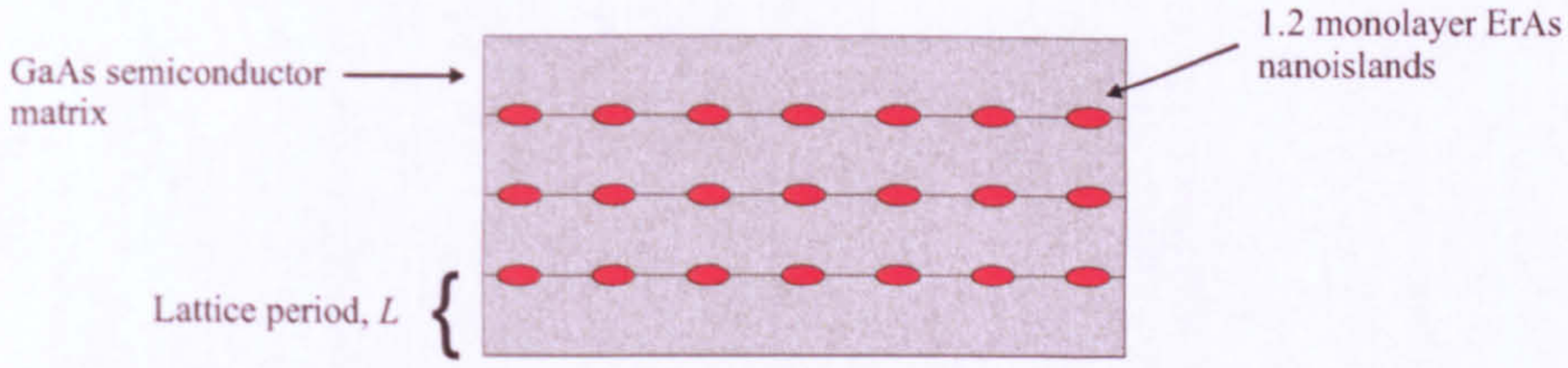

Figure 1.5: Structure of an ErAs - nanoisland / GaAs semiconductor superlattice used in antenna structures for free space THz detection, taken from [27].

report performances comparable to or better than those exhibited in LT-GaAs systems, with conclusive results demonstrating an increase in carrier capture times as a function of period thickness from 0.839 ps for $L = 25$ nm, to 1.62 ps for $L = 50$ nm.

1.2.2 Electro-optic Detection

Electro-optic detection of THz radiation utilses the Pockels effect [28] which is the production of birefringence in an optical material, induced by a constant or varying electric field. This results in a change in the refractive index of the optical crystal (such as ZnTe) which is proportional to the incident THz electric field. Such a change in the refractive index is measured by monitoring a change in polarisation of an optical beam propagating through the crystal at the instant a THz beam strikes. The optical signal polarisation is altered by the induced birefringence [29], and is then passed through a quarter wave plate to produce an elliptical polarisation, followed by propagation through a Wollaston prism to separate the orthogonal components (Figure 1.6). The relative intensity of each component is then measured on a pair of balanced photodiodes, the output current of which is linearly proportional to the THz electric field. The technique is mainly limited by non-equal phase velocities of the optical pulse and THz signal within the crystal, which introduces a coherence length, l_c, for which the signals remain in phase. For crystals thicker than l_c, interference occurs between the optical and THz signals and reduces system bandwidth. However, for crystal thicknesses

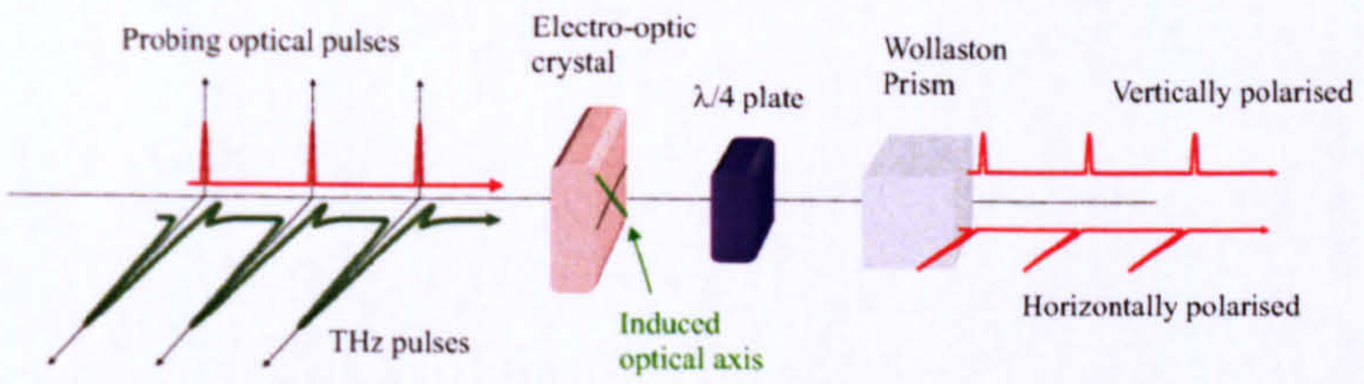

Figure 1.6: Electro-optic detection of THz pulses using the Pockels Effect.

$\ll l_c$, bandwidths in excess of 100 THz have been successfully obtained [30].

1.3 THz Waveguiding Techniques

The main limitation of free space THz spectroscopy is the strong absorption of THz radiation by water. If long distances are to be traversed by a signal in a humid environment, use of THz frequencies begins to become unfeasible. Even for short distances, water absorption lines and dispersion are seen in broadband THz signals which can interfere with spectroscopy, and limit system bandwidth. Free space studies often use N_2 purged systems in which to generate, propagate and detect THz waves, thus isolating the THz radiation from water absorption. In cases where this is impractical however, such as medical imaging of live subjects, or for compact, portable systems, other low-absorption techniques must be investigated. Neither conventional microwave waveguides nor optical fibres can be considered useful as THz waveguides due to high conductor and dielectric losses. When we also consider that broadband, pulsed THz signals are utilised for spectroscopic applications we are further constrained by the requirement for low-dispersion guided transmission. This requires that more novel techniques must be considered for free space guided THz waves.

1.3.1 Metal Wires

In a traditional coaxial transmission line, signals propagate down a central conductor and coupling of the electric field occurs to an outer, usually grounded

conductor, separated by a dielectric medium. This mode of propagation is known as transverse electromagnetic (TEM) - see Chapter 2 for a fuller treatment of TEM propagation. For THz waveguides this method is unsuitable due to finite conductor losses which increase with frequency. First proposed in the 1960's, King *et al.* suggested the removal of the outer conducting layer and propagation of a broadband THz signal along a simple wire [31, 32]. The metal wire waveguide was revisited by Wang *et al.* in 2004 [33], presented in the configuration shown in Figure 1.7.

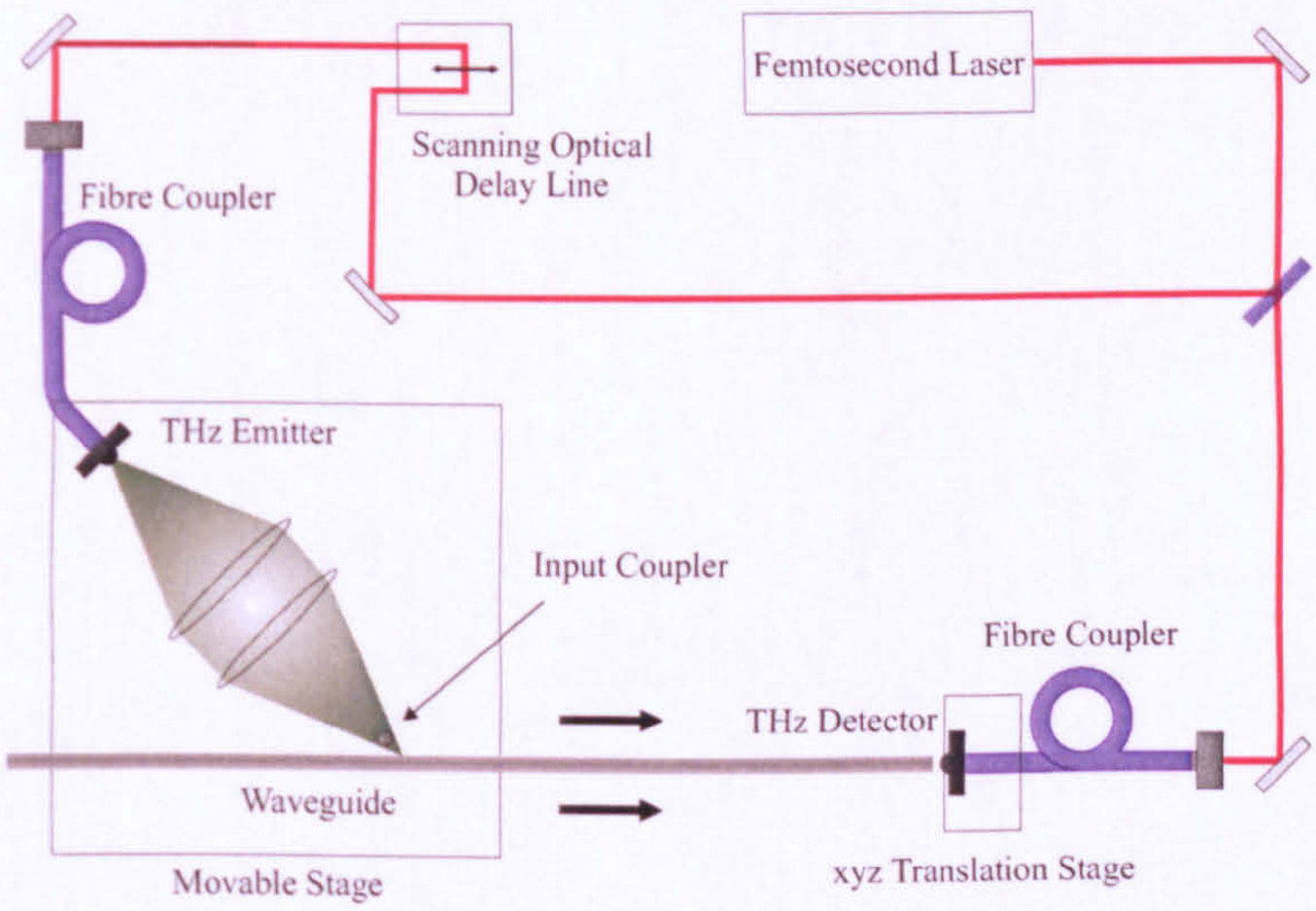

Figure 1.7: Optical setup of ultrafast photo-stimulated THz radiation coupled into a stainless steel wire transmission line, taken from [34].

An ultrafast NIR laser is fibre coupled onto a semiconductor based antenna and the transmitted THz radiation (as discussed in Section 1.1.3) is collimated, and then focussed onto a stainless steel wire. At the focal point of the THz beam is a so-called input coupler consisting of a second stainless steel wire arranged perpendicularly to the waveguide (out of plain of the diagram). The free space THz wave scatters off the input coupler in many modes, some of which match the guided mode of the wire and can therefore propagate along the wire. Recent advances in coupling technology included generation of THz radiation *directly* onto the end of the wire via an affixed photoconductive semiconductor antenna. The electric field around the wire was measured to be radial, suggesting that

the dominant supported mode of the wire is TEM, as for coaxial lines. The structure demonstrates an average attenuation coefficient up to 1 THz of less than 0.03 cm^{-1}, the lowest of any THz waveguide yet reported. The structure has also been demonstrated to be largely dispersion free for distances up to 24 cm from the coupling site. Detection of such guided wave radiation is simple, since the guided mode propagates directly into free space and can be measured using methods discussed in Section 1.2. An interesting feature of THz propagation from the end of the wire and extending several centimetres into free space, is that it maintains its radial electric field. This has led to several attempts to couple the radiation *back* into a second wire after reflection from a surface, in the design of a THz endoscope in both linear and right angled forms.

Though such a device demonstrates state-of-the-art transmission properties for THz waveguides, the main limitation lies in the very large coupling losses between the free space THz signal and the guided signal. More effective matching will be required to make this promising technology more viable for use in THz experimentation.

1.3.2 Photonic Crystal Fibres

Another method for single mode propagation of pulsed THz signals involves the use of photonic crystal fibres (PCFs), consisting of a central waveguiding core surrounded by a spatially periodic lattice. The core is formed by introducing a defect or discontinuity into the photonic crystal to create a region with locallised optical properties differing from those of the cladding lattice. The dominant supported mode of such a structure is determined by the refractive index of the core with respect to the cladding. A higher index core entails light propagation by total internal reflection, whereas low index cores guide the wave by the photonic bandgap effect [35]. Conventional PCFs are fabricated for optical frequencies from silica, but silica losses and dispersion are prohibitively high for THz propagation. Recent developments using high density polyethylene (HDPE) tubes and filaments

have provided much more promising results. Perhaps the first example of a PCF for guiding THz consisted of high density tubes stacked in a two dimensional triangular array (Figure 1.8a) with a single, solid HDPE rod in the centre to generate the optical discontinuity [36]. THz is focussed into the waveguide using a parabolic mirror and collected at the opposite end in the same fashion, before being focussed onto an antenna for detection. This photonic crystal fibre has been demonstrated to guide THz radiation from 0.1 - 3.0 THz. Although this method out performs conventional metal waveguides, the losses are still relatively high at 0.5 cm^{-1} above 0.6 THz, meaning only small sections could be used before losses became too great for signal resolution. This loss would likely improve with more stringent fabrication techniques.

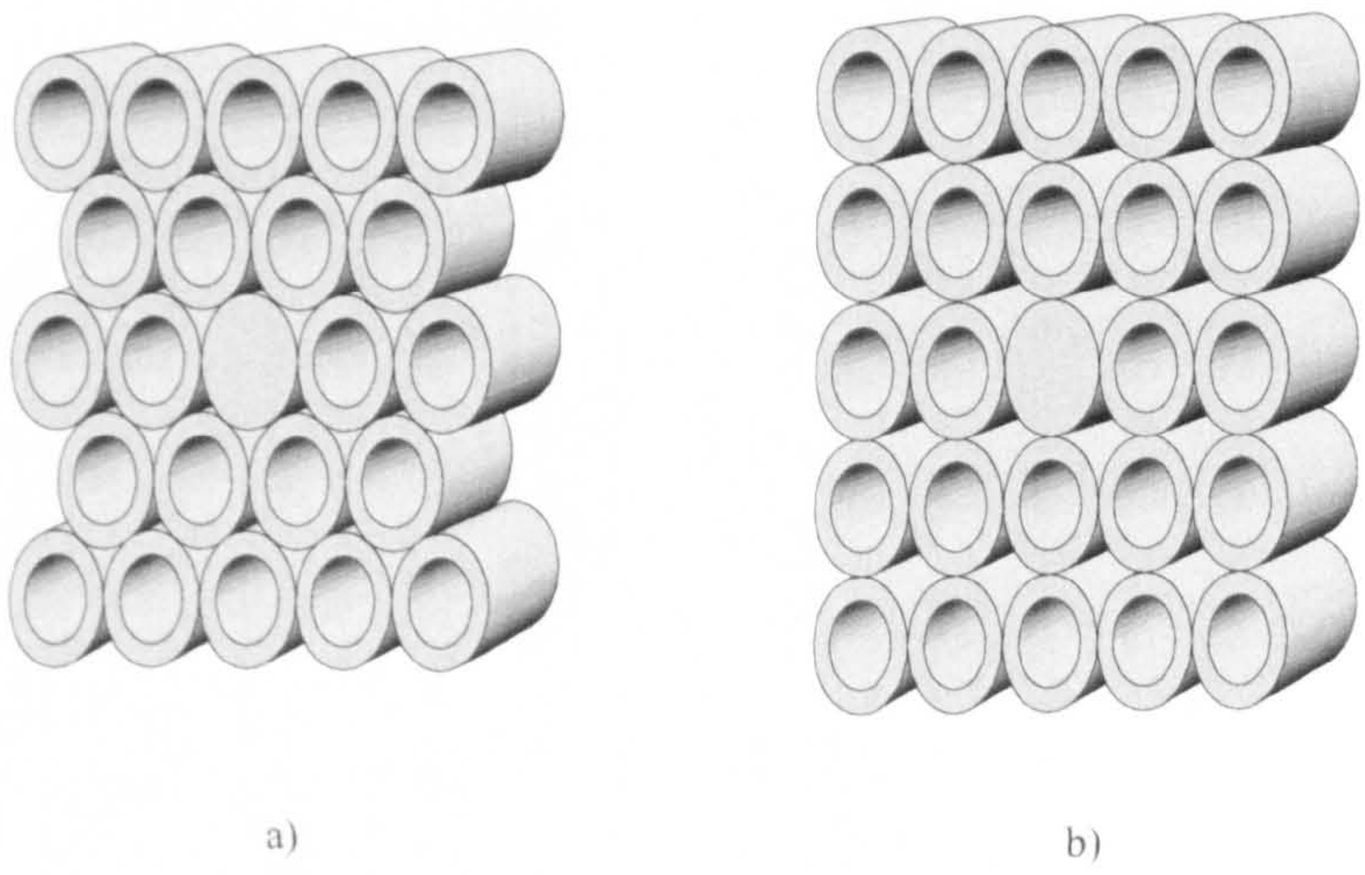

Figure 1.8: Diagrams of the two dimensional a) triangular array [36] and b) rectangular array [37] of high density polyethylene tubes surrounding a solid core.

A slight variation to this technique involves rearranging the structure from a triangular to a square lattice whilst retaining the use of polyethylene (Figure 1.8b). Whilst both this and the previous structure demonstrate near zero dispersion above $\approx$ 0.3 THz, this slight modification demonstrates an attenuation of $\approx$ 0.2 cm^{-1} [37], and will most likely be improved in the future.

1.4 On-Chip THz Generation and Detection

Whilst free space generation of THz radiation is rather more developed in comparison to on-chip techniques, there are several reasons why it is advantageous to contain all THz radiation within a planar device. Primarily, absorption by water present in the atmosphere is avoided since electric fields are mostly contained within a dielectric, negating the need for purged atmospheres or free space waveguides. For cryogenic studies of semiconductor systems, it is of benefit to contain all THz signals within the cryostat to avoid dispersion at the access windows and to remove problematic reflections from these same interfaces. Although only one specific area of on-chip THz generation has been a target of much development, it is now becoming a much more interesting prospect as THz technology advances.

1.4.1 Optical Switches

Generation of on-chip THz signals is dominated by the use of photoconductive materials operating as switches, which are activated by incident laser light. The first example of this method involved the use of two lasers of differing wavelengths which acted as the 'on' and 'off' pulses to control the switch. The experiment consisted of a microstrip transmission line mounted on a high resistivity (10^4 Ωcm) silicon substrate with a ground plane beneath. A break in the transmission line marks the position of the optical switch (Figure 1.9). The silicon substrate itself assumes the role of the photoconductive switch rather than an independent structure.

The laser used was an Nd:glass laser with operating wavelength of 1.06 μm, which was beam split with one part passing through frequency doubling KDP (as discussed in Section 1.1.1) crystal to obtain a second pulse of 0.53 μm wavelength. The 0.53 μm pulse illuminates the switch region, creating a thin layer of charge carriers at the surface of the high resistivity Si and allowing current to flow between input and output, in a similar fashion to carrier generation in antenna

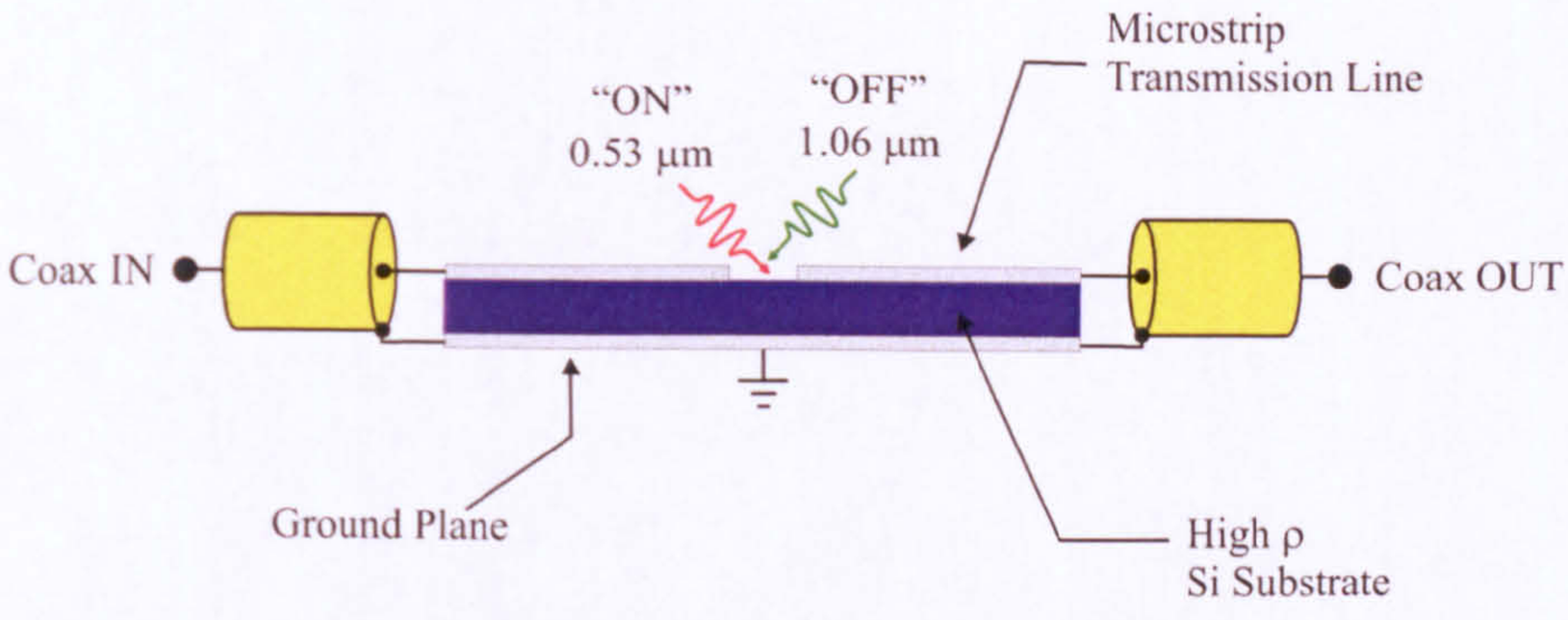

Figure 1.9: Taken from [38], this figure shows the arrangement used by Auston *et al.* to generate nanosecond voltage pulses in a transmission line structure. The 'Coax In' and 'Coax Out' labels represent coaxial connector feed lines, biased at 20V with respect to each other.

structures. The 1.06 μm pulse is passed through a time delay before itself illuminating the switch a short time later. Due to the longer absorption depth of the second pulse within the silicon, a high conductivity region is generated which spans the gap between microstrip and ground plane, short circuiting the input of the transmission line and preventing further conduction across the structure. In this fashion, ultrashort voltage pulses are generated in and propagate down the transmission line. A time-resolved image of the pulse is found by measuring the structure in an optical pump-probe setup. This method involves splitting a single laser beam into two parts, one of which is diverted around an optical delay line. By altering the time delay it is possible to use the second pulse to scan the signal generated by the first at sequential positions along the waveform (Figure 1.10).

The fall time shown in Figure 1.10 was found to be $\approx$ 15 psec in comparison to a rise time of $\approx$ 10 psec. The time difference was attributed to velocity dispersion of the signal within the microstrip. Carrier lifetime does not contribute to the pulse shape as it does for free space antenna generation of THz, since the device is actively switched off by an external source and carriers are not left to decay naturally. Carrier recombination time is however, an important consideration for other types of optical switch [39]. This method is not appropriate for on-chip THz studies since the pulsewidths generated suggest that transients of only a few tens of GHz and below are generated.

(1) 0.53 μm (0 ps) (3) 0.53 μm (τ ps)
(2) 1.06 μm (15 ps) (4) 1.06 μm (τ + 15 ps)

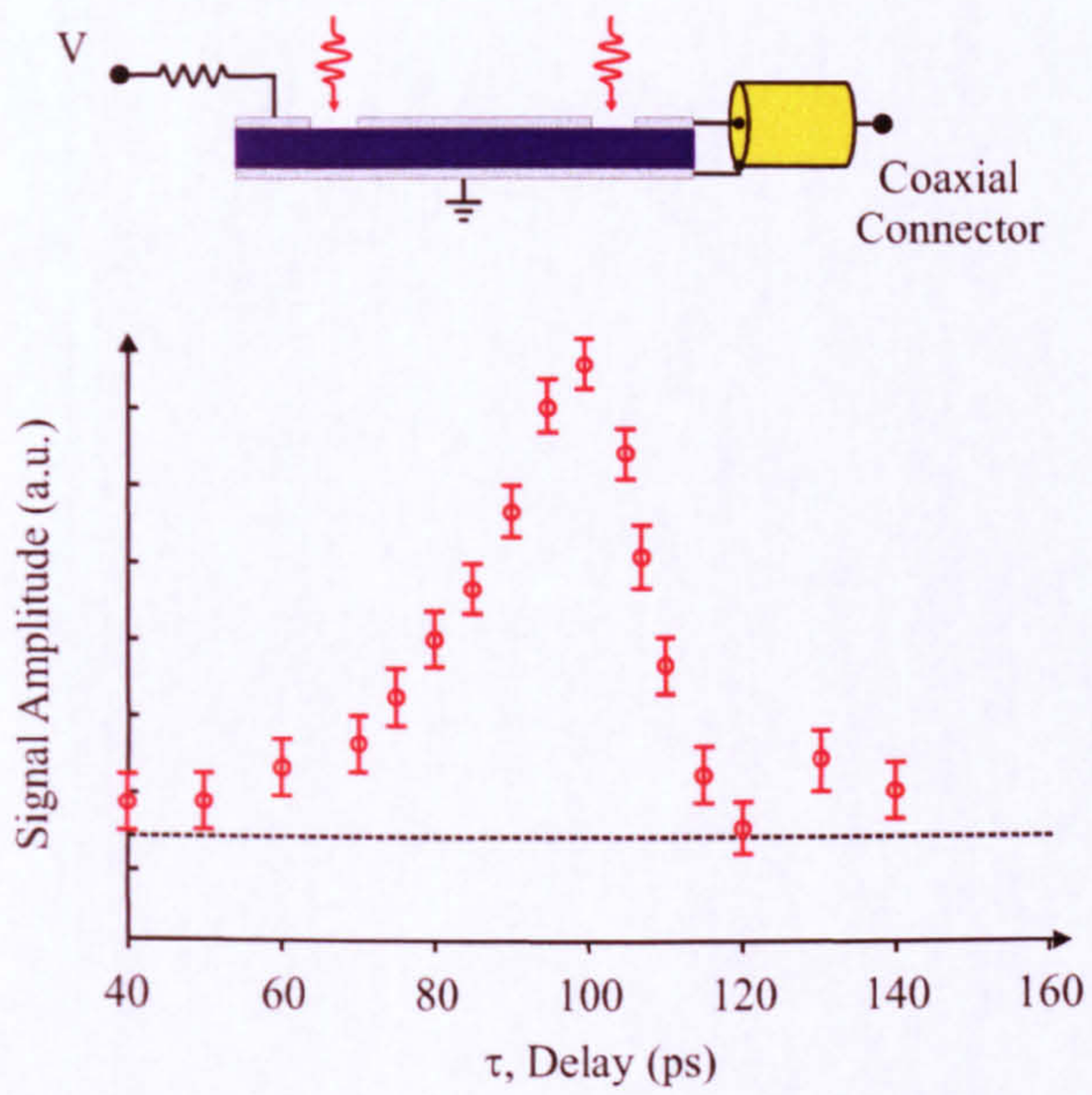

Figure 1.10: The two switch setup used to produce a time resolved scan of the generated pulse by Auston *et el.*

An advancement to this technique, which reduced the generated pulse widths to as low as 3.6 ps, operated by introduction of a switch consisting of an optically active material placed in the transmission line gap, rather than using the substrate as a switch. Pulse widths generated in this device are controlled by the incident laser pulse width and the carrier lifetime within the photoconductive material, as was seen for photoconductive antenna. A typical early example of picosecond pulse generation involved use of the photoconductive material forming a thin film layer between an insulating substrate and the microstrip electrodes [40], as seen in Figure 1.11a. The main limitation to this arrangement was that any guided THz components would experience the high dielectric permittivity of the thin film along the entire transmission line length, which would introduce high losses to the system. A better alternative would be to isolate the thin film to small regions at the excitation and detection points, as seen in Figure 1.11b. A technique for fabrication of isolated switch regions has been developed for this study and is presented in Chapter 3.

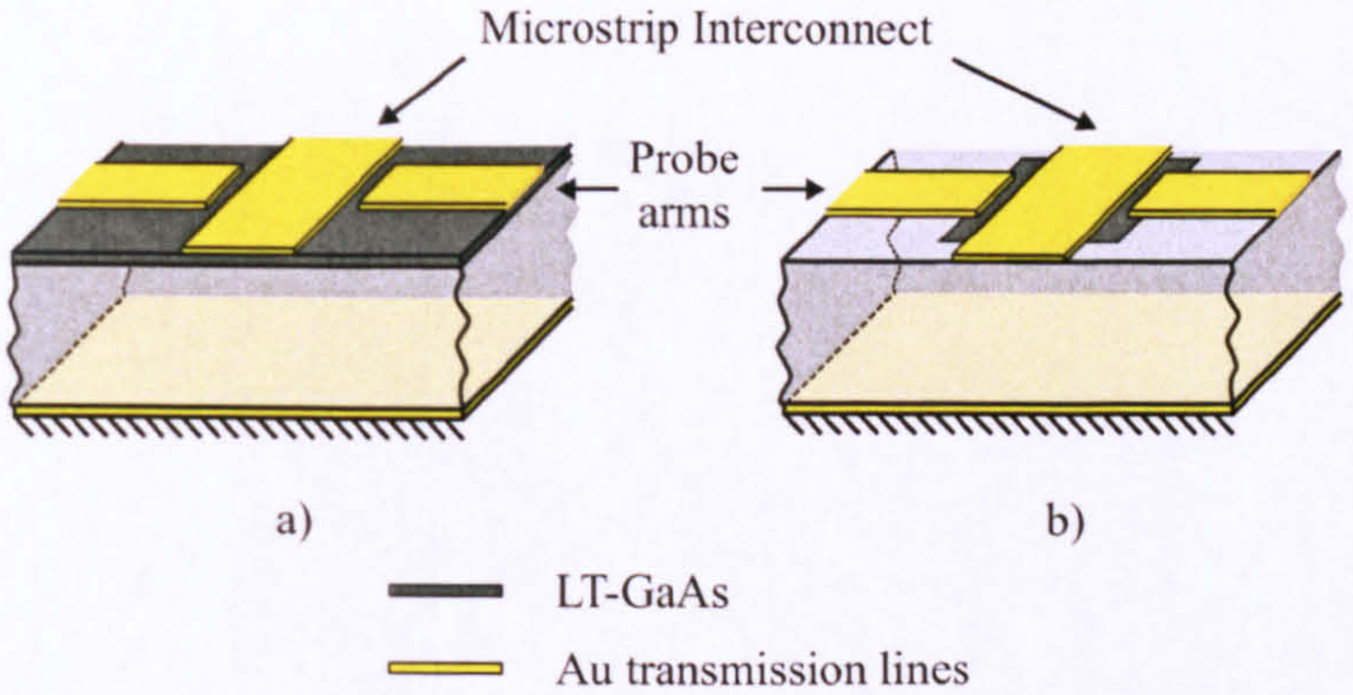

Figure 1.11: Schematic showing a photoconductive layer forming switch regions between probe arms and transmission line a) covering the entire substrate beneath the metallisation and b) in an isolated region beneath the lines.

A picosecond optical laser pulse is focussed on the active region of the photoconductor, which consists of a small gap in the top microstrip electrode, similar to the technique discussed previously involving high resistivity silicon. Rather than requiring a separate laser pulse of longer wavelength to disable the switch, simply terminating illumination allows the carriers within the material to recombine, returning the switch resistivity to it's high dark value. Two important factors arise from this: firstly, the carrier recombination lifetime of the material must be as short as possible to prevent a broadening of the generated pulse, and secondly the dark resistivity of the switch material (i.e. that when the switch is *not* illuminated by the laser) must be high to minimise dark current and so improve the signal to noise ratio (SNR) of the device. Several different geometries for the pulse generation and time resolved sampling have been investigated [41]. Figure 1.12a shows the first topology which involves both the generating and sampling switches being placed in series along the transmission line. The impedance matched attenuator situated between the two switches was present to reduce reflections within the structure. The second layout, Figure 1.12b, has the sampling region in parallel to the main transmission line, which has the effect of increasing the signal to noise ratio and decreasing the response time of the circuit due to removal of the attenuator.

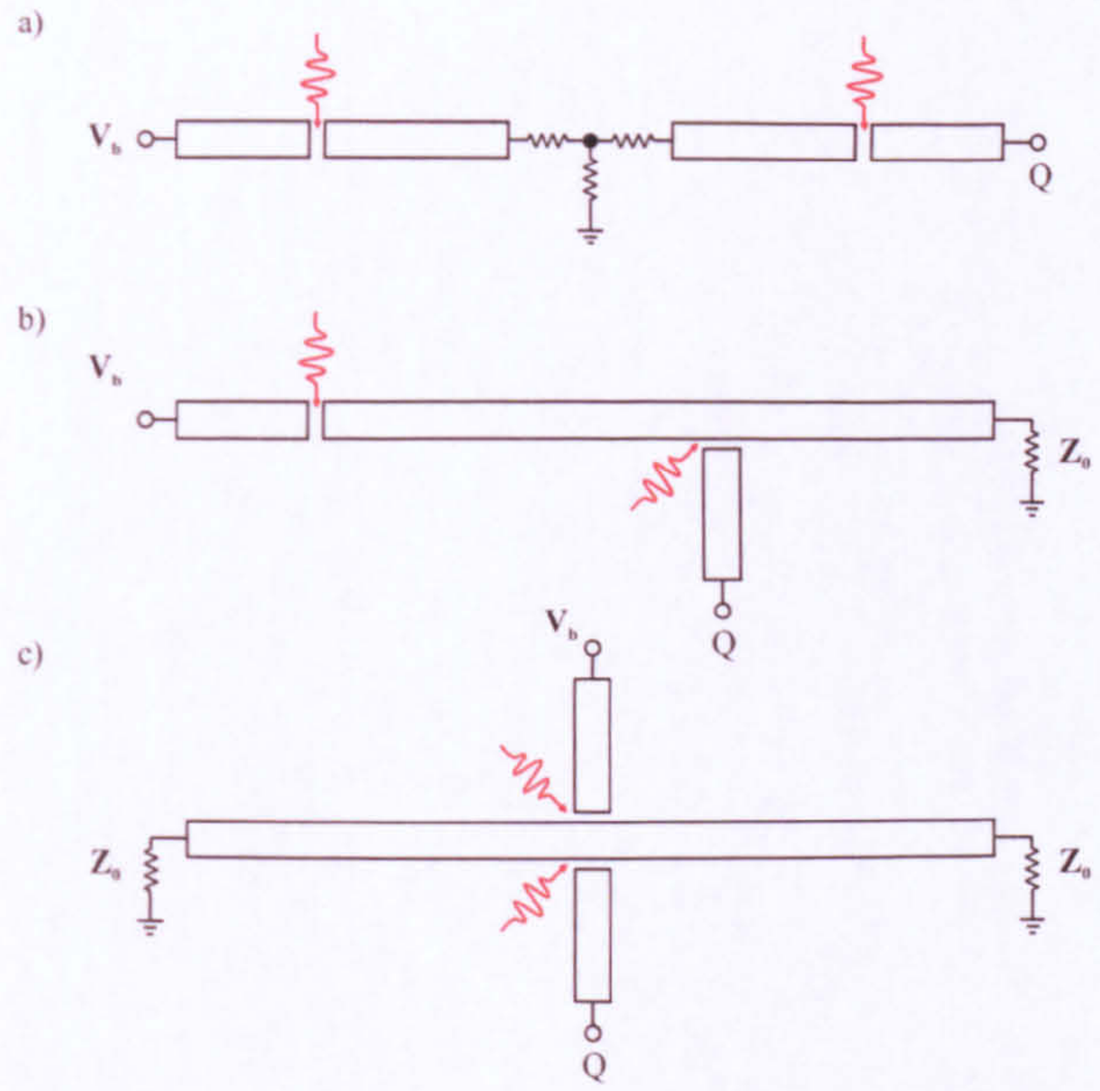

Figure 1.12: The three switch - probe geometries analysed by Auston *at. al* in [41], probed at point Q, with applied bias voltages V_b, terminating impedances Z_0.

The third geometry in Figure 1.12c allows analysis of the terahertz pulse before it has propagated down the transmission line. Measurement of the input pulse is necessary for comparison with an output measurement (see Chapter 2), to determine the transmission characteristics of such a device, and to analyse changes in such characteristics when performing spectroscopic measurements.

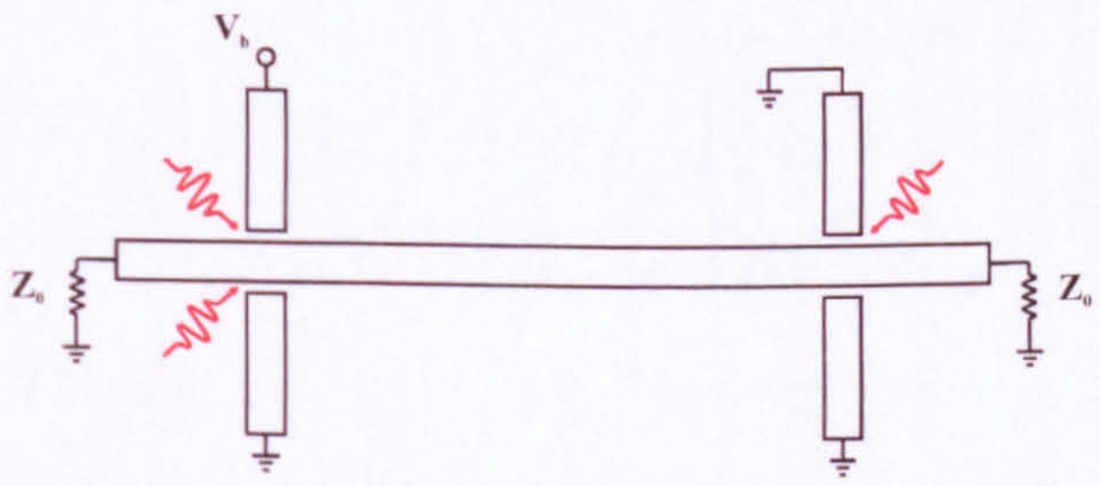

Figure 1.13: Adaptation of Figure 1.12c with two effective switch areas on a single transmission line

If two such arrangements are used on the transmission line, separated by a defined distance over which a signal would propagate (as seen in Figure 1.13), then the pulse could be monitored both before and after propagation along this distance providing information on signal dispersion and attenuation, and on the dielectric

properties of the materials used for the microstrip substrate.

1.4.2 Low-Temperature GaAs Processing Techniques

In order to minimise the relaxation time of carriers within the photoconductive switch, the switch material used must be considered carefully. The current standard is provided by Low-Temperature grown GaAs, or LT-GaAs, which has been shown to have sub-picosecond carrier lifetimes [42]. LT-GaAs is epitaxially grown at $\approx 250°C$ as opposed to standard GaAs growth temperatures of $\approx 600°C$ [43]. Since this method of fabrication makes the material quite expensive, it is impractical to have a thin film beneath all of the circuit topology. More importantly however, is that due to the high permittivity of LT-GaAs, the presence of this extra dielectric layer would increase attenuation in the line and reduce the observed transmitted signal. To avoid this, I have developed a method of fabricating smaller, localised semiconductor regions (as seen in Figure 1.11b, Section 1.4.1) specifically for this work. The film is grown onto a release layer of AlAs on a normal GaAs substrate. In [44], the film is shown with a supporting structure consisting of an AlGaAs - GaAs - AlGaAs multilayer, which enables ease of handling of the film. The thin film is released from the substrate by selective etching of the AlAs release layer in HF acid [45] (see Figure 1.14), and then the film may be transferred to the substrate on which the microstrip is to be formed.

Black wax is applied to the structure prior to this etch for two reasons. Firstly the wax applies tension to the edges of the film when the selective etching of the AlAs release layer is in progress. This has the effect of lifting the film edges slightly, therefore allowing the byproduct of the etch (H_2 gas) to escape the etched channel without fracturing the thin film. Secondly, the film may then be manipulated via the wax which avoids application of pressure directly to the very fragile film.

Once the film has been transferred, application of slight pressure bonds the film to the substrate via Van der Walls forces [46]. Transferral of the film whilst still

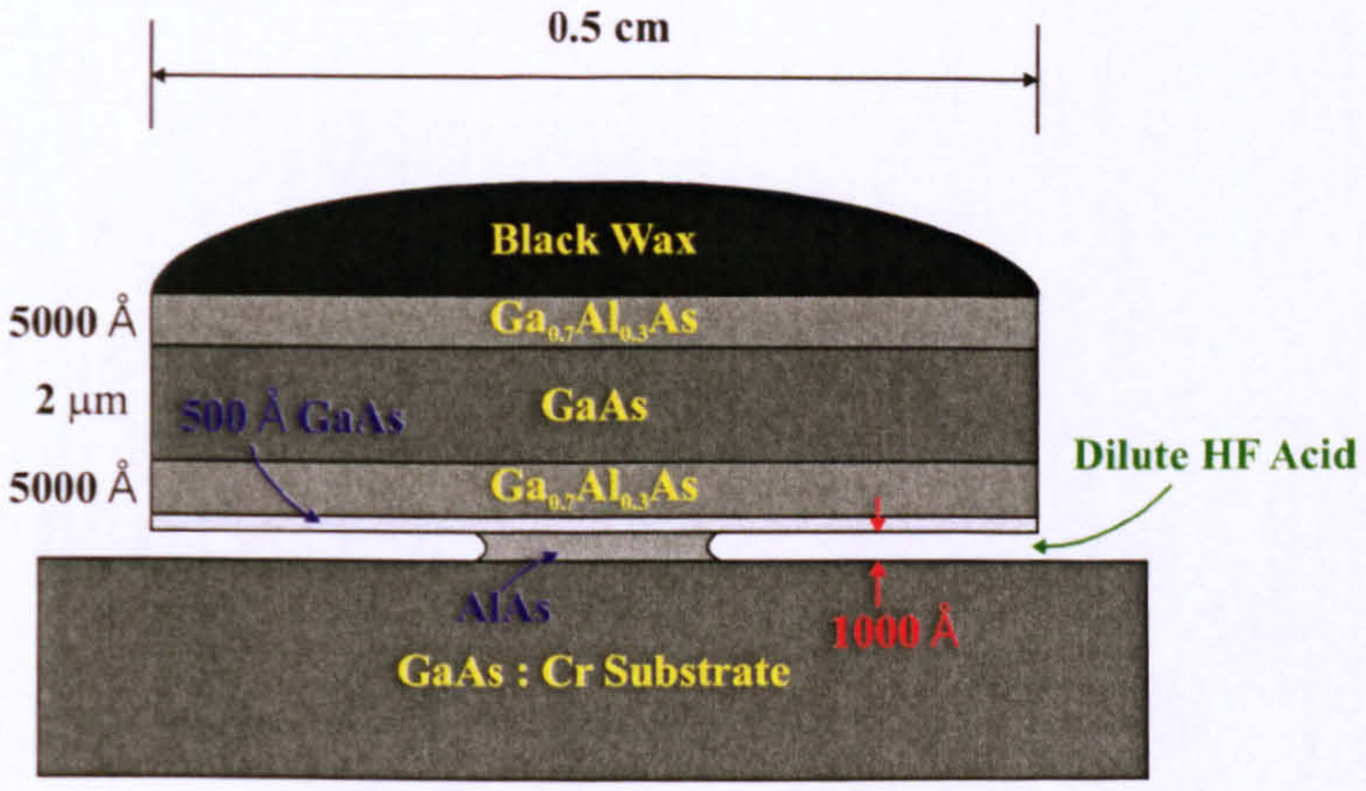

Figure 1.14: Showing the selective etching of AlAs to remove a LT-GaAs thin film from its growth substrate, taken from [45].

wet aids in the bonding process by expelling air and water from the interface via capillary action. The microstrip structure may then be evaporated onto the chip with the LT-GaAs switch in the appropriate position. Proof that an electrical signal generated in such a switch can enter a microstrip transmission line was given by Yi-Yan *et al.* [47].

1.4.3 On-chip Technological Applications

Existing technologies have shown on-chip studies to be useful in genetic diagnostics [48] and spectroscopic analysis of overlaid films [49], but potential uses extend to a much broader range of applications. Some existing technology will be discussed here.

1.4.4 Genetic Sequencing

On-chip devices offer the potential for measuring a change in dielectric properties of an overlaid material caused by a chemical reaction, such as a binding event between two molecules. Indeed, in any system where binding alters the far infrared dielectric properties of an overlaid biomolecular system, this device could

potentially be used. A good example of this potential is provided in measuring binding events between two DNA molecules, to perform such tasks as genetic sequencing.

Genetic sequencing has been traditionally performed using a microarray, or gene-chip, which consists of a large array of discrete cells, each of which has been functionalised with a single stranded DNA probe molecule. In order to understand the operation of a gene chip, it is necessary to briefly discuss the physical nature of DNA. DNA exists as a double stranded (hybridised) molecule, each strand consisting of a combination of the four bases Adenine (A), Cytosine (C), Guanine (G) and Thymine (T) (see Figure 1.15a).

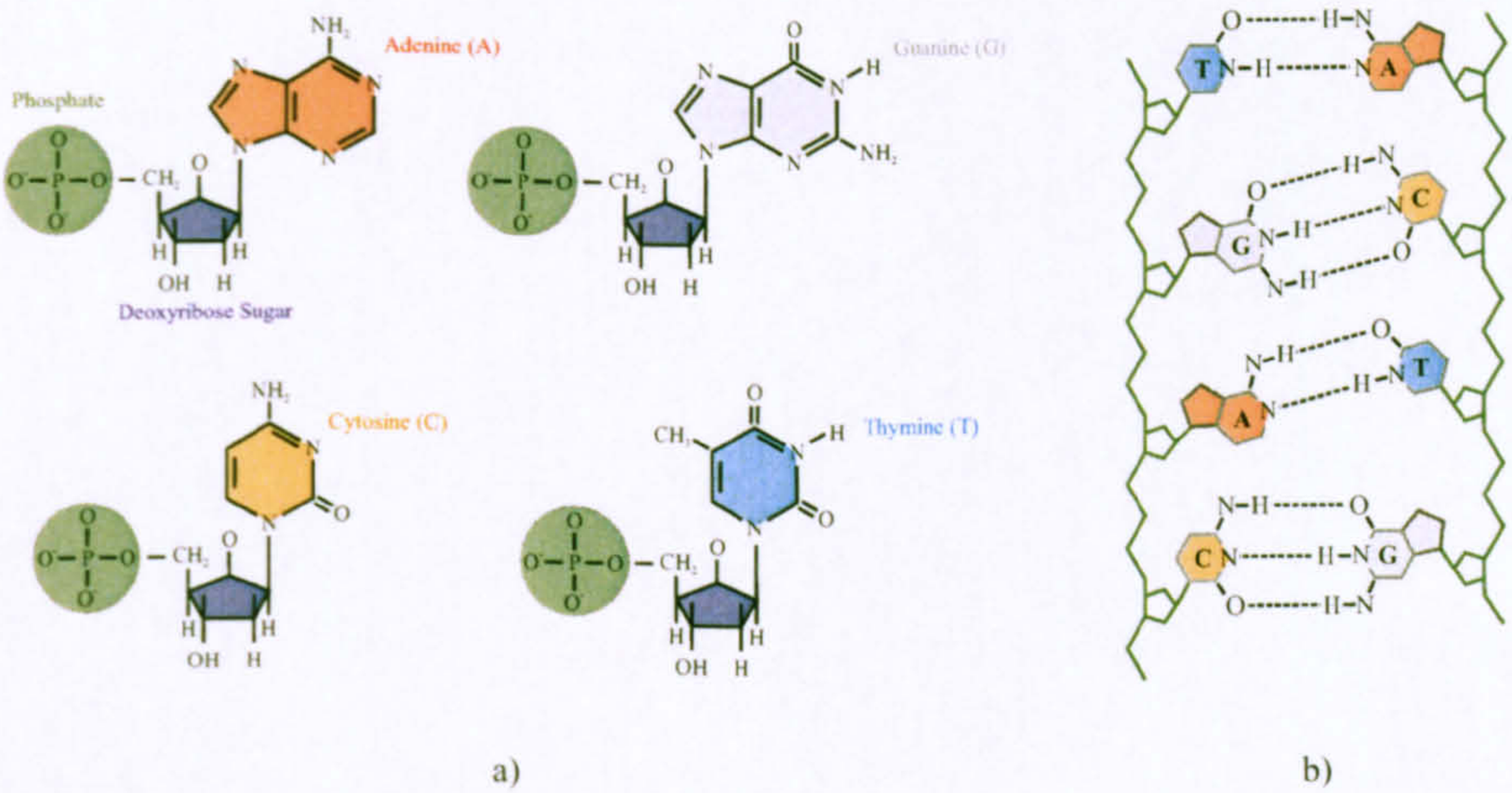

Figure 1.15: Chemical diagrams of a) the four bases and sugar-phosphate molecules which constitute DNA and b) hydrogen bonding between complementary basis to form a DNA double helix.

The bases in each strand are connected together via a deoxyribose sugar and a phosphate group, these two molecules forming what is referred to as the DNA backbone. The bases form a ladder-like structure up the centre of the helix, bound together by hydrogen bonds. Due to the spatial location, orientation and number of hydrogen bond sites on each base, stable bonds will form only between A and T, or between G and C [50] as seen in Figure 1.15b. This makes binding between two long single stranded DNA molecules containing a complex array of bases very highly specific. Each strand will only bond to another strand

containing complementary bases [51]. The extremely high binding specificity is very useful when trying to determine either the sequence of an unknown strand of DNA, or the quantity of a known sequence present in a sample. The unknown DNA strand is separated into two single strands (denatured), one of which is used for testing. This single strand is then broken into smaller sections using enzymes which cleave the DNA backbone, and the different sections are separated by capillary gel electrophoresis (CGE). Each distinct sample is then labelled by chemically attaching a fluorescent molecule to the end of the DNA strands, and this hybrid is referred to as the target molecule. Targets are introduced into the gene chip containing a large number of probe molecules and where they meet a complimentary strand, binding will occur and fluorescence will be seen in that cell. This allows the sequence of each target to be obtained and hence the full sequence of the unknown DNA molecule. Whilst such technology is well established [52], there are certain aspects which it would be profitable to alter. The fluorescent labeling step is expensive and time consuming, and the very presence of these fluorescent markers can alter the conformation of the DNA strand and interfere with binding [34]. This causes high variation in data quality between tests [53] and, coupled with the long times involved in processing, lead to the desire for new techniques.

Recently, THz analysis of DNA has experienced some interest since it was calculated [54, 55] and then shown experimentally, that the far infra-red dielectric functions of the constituents of DNA are dominated by vibrational modes associated with intermolecular motion between individual molecules held together by hydrogen bonds [56], i.e the base pairs. Recent efforts have been directed into discovering how the THz dielectric function changes between hybridised and unhybridised DNA samples, since it is possible that the interaction of a THz pulse with a hybridised DNA molecule would be correspondingly greater due to the presence of these vibrational modes.

Earlier tests for DNA hybridisation states involved free-space terahertz Time Domain Spectroscopy (TDS) [57] of samples of oligonucleotide (i.e. synthetic DNA

strands of a few tens of bases) with their complementary strands. Measurements of the time resolved transmission through large samples of the oligonucleotides, demonstrated a dependence of the complex refractive index on the hybridization state of the DNA molecules (Figure 1.16). By monitoring THz transients, determination of the binding state of oligonucleotides is possible by the change in refractive index, and a genetic sequence may be obtained by monitoring their binding to a known single-stranded probe polynucleotide, as for gene chips. This method was successful without the need for fluorescent labelling of the target molecules but, despite the potential of this technique, the free space approach requires the use of DNA volumes many orders of magnitude greater than in gene chips, which counteracts the advantage gained from removal of the labelling step.

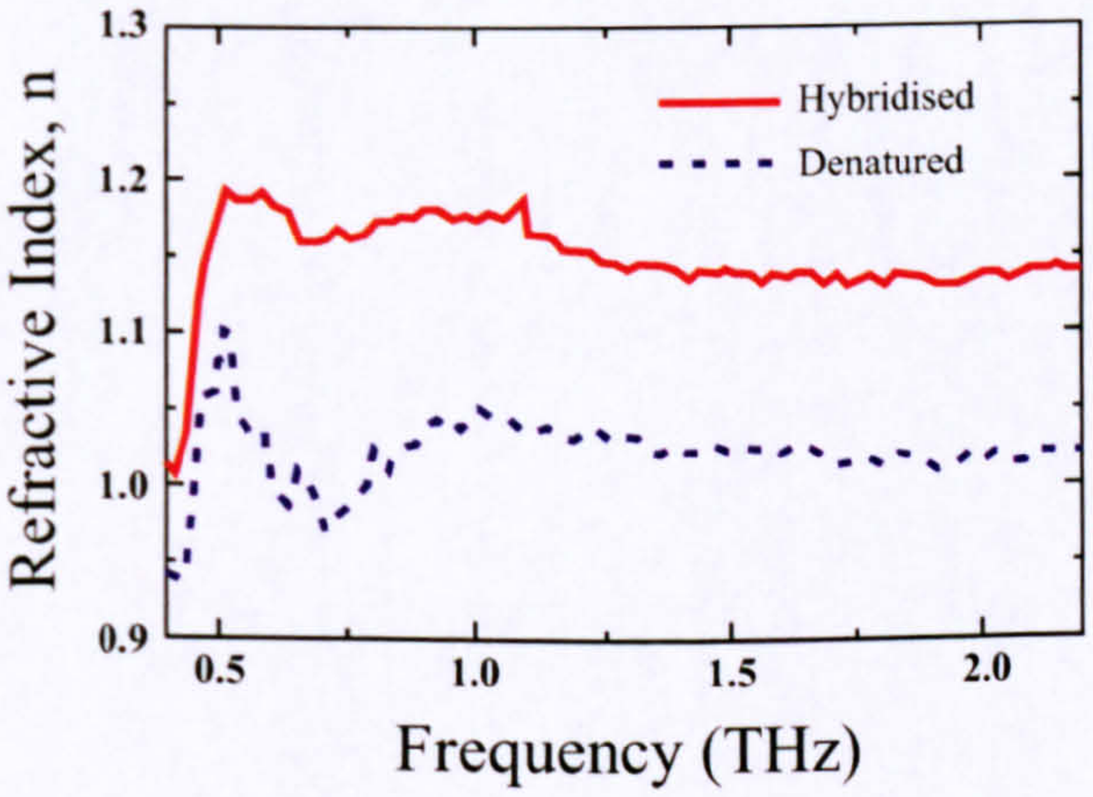

Figure 1.16: Comparison of the complex refractive indices for hybridised and denatured DNA samples determined from THz TDS, taken from [57].

On-chip THz techniques offer the same label-free advantage as a free space THz approach, but with the added benefit of femtomolar sample volumes comparable to gene chip technology being required for measurements. Some interest has therefore been diverted from the free space method to an on-chip approach. The first of these involved a 600 GHz edge coupled, bandpass microstrip filter fabricated on a BCB dielectric [58]. The coupled sections in the filter are a quarter wavelength long at the centre frequency of operation of the filter and produce a resonant response at this frequency (for a fuller treatment of microstrip filter operation, refer to Chapter 2). The device, shown in Figure 1.17, is connected in

series to an LT-GaAs optical switch similar to those in Section 1.4.1, for generation of a THz pulse using a pulsed NIR laser source.

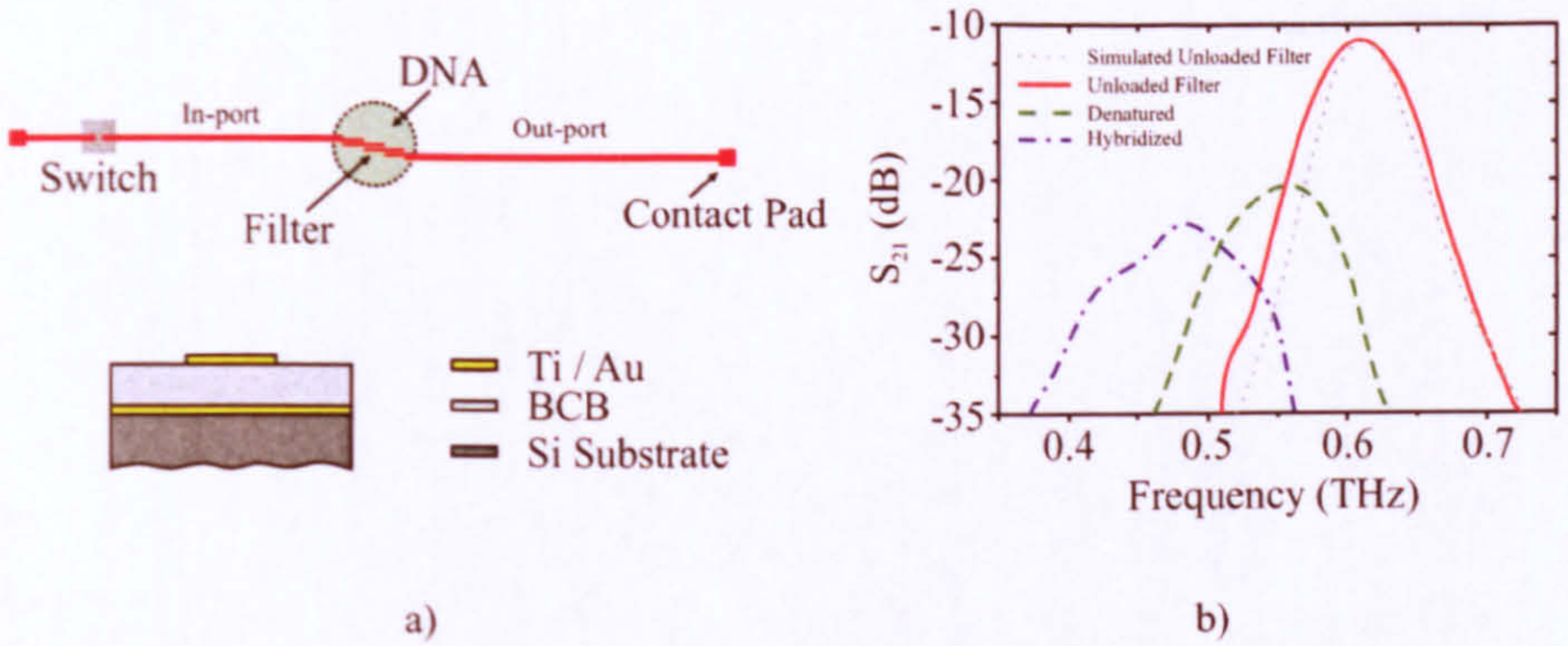

Figure 1.17: Showing a) the microstrip topology used, and b) the bandpass response for the unloaded filter, with hybridised and denatured DNA deposited as a dielectric load onto the filter, taken from [58].

The amplitude of the resonant frequency shift observed in this device under DNA loading far exceeds simulations of overlaid materials using the refractive indices measured in the free space arrangement in Figure 1.16, and the exact nature of this shift is as yet not fully understood. It is possible that unsimulatable characteristics, such as the resonances predicted in [54] and [55], are responsible for the unexpected response. As yet, no repeat measurements of an identical device have been performed under conditions of DNA loading to verify this data.

Although the technique presented by Nagel *et al.* seems to offer reasonable results, efforts are still being made to increase the sensitivity, accuracy and reproducibility of the tests. A later development involved the use of the ring resonator (discussed in Chapter 2) shown in Figure 1.18. The surface of the filter has been functionalised with probe DNA molecules [59] (Figure 1.19) in parody of the gene chip. To bond the DNA to the gold, the DNA is chemically modified with a thiol group $(-(CH_2)_6 - SH)$ [60]. The sulphur readily forms a highly stable bond to gold surfaces, effectively and securely tethering the DNA to the filter.

If the target DNA is complementary to this probe sample, a binding event will occur and the response of the resonator alters. The authors claim a sevenfold

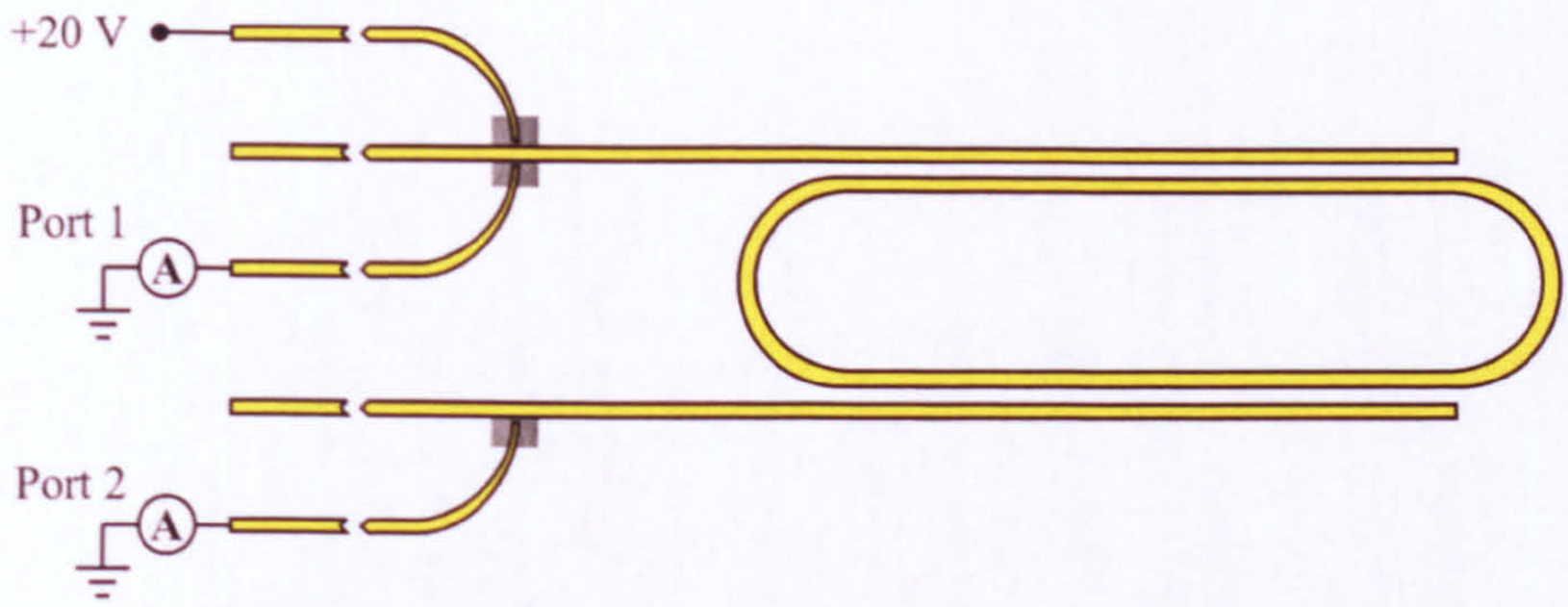

Figure 1.18: Ring resonator topology used by Nagel *et al* [59], with Port 1 used to measure input signals, and Port 2 for output signals.

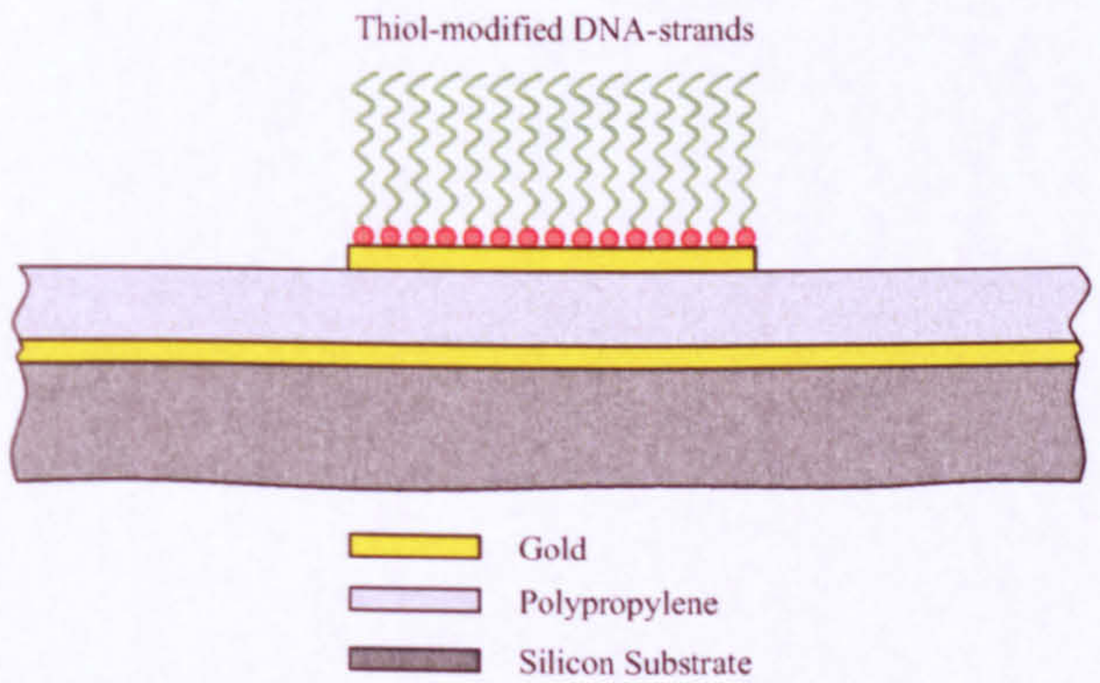

Figure 1.19: Graphical representation of a metal surface functionalised with sulphur modified DNA, from [59].

increase in sensitivity when compared to the previous band pass filter approach, due to the reduced amount of material required for testing (less than 40 fmol).

Although only on-chip techniques for DNA analysis have been addressed here, measurement of the dielectric properties of almost any overlaid material is also possible, making on-chip techniques a competitive alternative to complimentary free space spectroscopy.

1.4.5 Analysis of Condensed Matter Systems

Broadband, pulsed THz techniques have potential application in sensing a wide range of condensed matter systems, such as two dimensional electron gases (2-

DEGs), including observation of cyclotron resonance, magnetoplasmon resonance [61] and ballistic electron transport [62]. For free space time-resolved measurements, the THz radiation passes through a thin structure containing the 2-DEG layer, and analysis of a single property, such as transmission or reflection, allows spectroscopic information to be retrieved. On-chip approaches propagate the radiation parallel to the structure, thereby actively incorporating the 2-DEG into the dielectric of the on-chip waveguide. This allows interactions with the 2-DEG layer to affect loss and dispersion within the waveguide and spectroscopic information to be extracted. An important result of this is that the propagation length between sample and probing signal is increased significantly from analogous free space techniques, since the radiation passes along the entire structure rather than through the short axis of the test sample, potentially increasing probe sensitivity. Such studies must also be performed at cryogenic temperatures which, for free space studies, introduces the extra difficulty of focussing THz radiation through optical access windows. This reduces reproducibility across experiments due to the inherently difficult task of focussing onto the exact same sample region for each measurement. Lithographically defined on-chip designs in which THz is generated in the plane of the test sample, would circumvent both difficulties in focussing and targeting of the THz radiation.

Earlier examples of on-chip studies involved the use of superconducting microstrip such as $YBa_2Cu_3O_{7-\delta}$ (YBCO) [63]. High quality YBCO superconductors can only be fabricated on lattice matched substrates, which initially hindered their use owing to the extremely high permittivities of suitable materials ($\epsilon_r \approx 1000$ for $SrTiO_3$). Advances in material technology soon solved this with the introduction of much lower permittivity lattice matched materials such as $LaAlO_3$. THz pulses of $\approx$ 1 THz bandwidth were generated in a gold, coplanar waveguide containing radiation damaged silicon photoconductive switches, which were excited with 100 fs NIR laser pulses. The generated pulses had full width half maximums (FWHM) of $\approx$ 750 fs duration and 500 mV amplitude. The coplanar waveguide was coupled to the superconducting transmission lines in a flip chip geometry, with silver

forming an ohmic contact between the two guiding structures (Figure 1.20). The THz pulse then propagated across this interface and into the superconducting transmission lines. Input and output pulse measurements are made by electro-optic sampling in reflection mode at two $LiTaO_3$ crystals embedded beneath the superconducting line, separated by 3 mm.

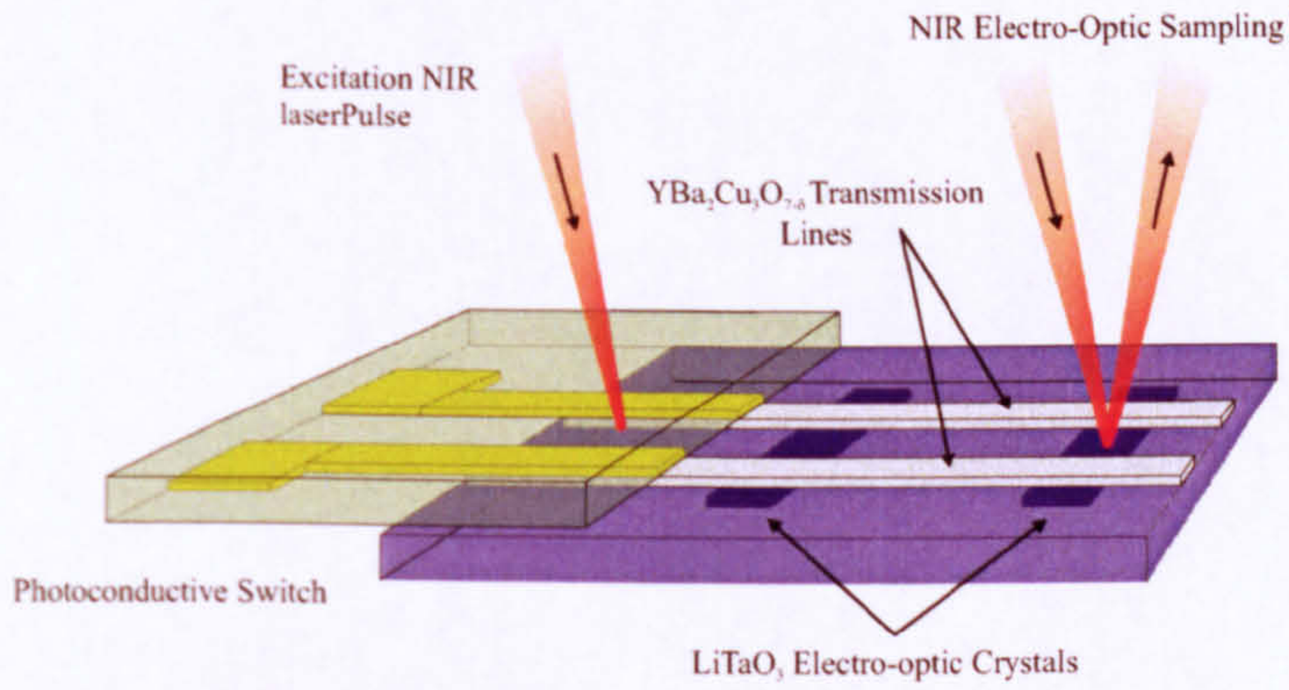

Figure 1.20: Flip-chip arrangement used by [63] to launch, propagate and detect THz pulses on superconducting YBCO transmission lines at cryogenic temperatures.

The main limitation with this geometry lies with the generation of the initial pulse in a separate waveguiding entity. The coupling losses introduced at the interface between gold and superconductor reduce the pulse amplitude by 50 % and broaden the pulse significantly to 1.4 ps. After propagation along a 3 mm length of superconductor with almost zero conductor losses, the pulse has further broadened to 2.6 ps, almost double the initial value in the line. This dispersion is likely caused by the still high permittivity of the supporting growth structure for the superconducting lines and further limits the potential of this technology.

A variation on this technique involved the use of gold coplanar waveguides [62, 64] in place of superconducting transmission lines. Photoconductive switches, fabricated from LT-GaAs, were integrated into the waveguides which dramatically reduces the coupling losses experienced in the design involving superconductors, although the bandwidth exhibited in these structures was reduced to ~ 200 GHz. The coplanar structure was fabricated on a multilayer substrate of 2 μm LT-GaAs on 200 μm sapphire, which was subsequently bonded to a silicon support.

The NIR lasers used to excite the optical switches were fibre-optically coupled through the back of the silicon. In order to measure the condensed matter system, the 2-DEG structure was attached to the end of the waveguide in a flip-chip geometry similar to the previous method, and gaps filled with epoxy. The 2-DEG became capacitively coupled to the electric field within the waveguiding structure and could thus affect transmission loss and dispersion, allowing time domain information on the electron system to be measured.

The reported measurements for ballistic transport time were twice as long as the expected time of flight and the extra dispersion is, as yet, unexplained. However, using the 2-DEG as a superstrate for part [64] or all [62] of the waveguide will increase the effective permittivity experienced by the guided mode. The use of unspecified epoxy material of unknown THz characteristics to bond between the two structures may also have affected these results. Part of the work presented in this thesis will address improvements on the on-chip cryogenic generation, propagation and detection of THz radiation including increase in bandwidth and reduction in dispersion with the aim of further advancing time resolved picosecond studies of condensed matter systems.

Chapter 2

Microstrip Theory and Filter Design

2.1 Introduction

The aim of this chapter is to provide an overview of basic microstrip theory with the intention of developing an understanding of terahertz (THz) on-chip system design. Several intrinsic properties of on-chip signal propagation will be discussed, along with their applications to the systems used in this project. A review of several common forms of transmission line which may be suitable for use as THz interconnects will be given, alongside choices of dielectric materials required for low-loss operation. The chapter will also consider the design of resonant filter structures and their introduction into microstrip interconnects. Comparisons between different propagating systems are drawn which justify the final choice selected for use in this work.

2.2 Transmission Line Theory

When considering the differences between standard lumped component electronics and transmission line theory, the electrical length scale of the circuitry involved is fundamental. As we move up in frequency, away from lumped elements and toward transmission lines, the length of the circuit becomes comparable to the wavelength of the propagating signal and can no longer be assumed to be zero

[65]. Since the amplitude of the propagating wave is now varying along the length of the circuit, the voltage and current amplitudes and phases are also varying, necessitating consideration of the system as a distributed network. A distributed network is an intermediate between low frequency lumped components and free space electromagnetic field theory, and knowledge of both is necessary for complete understanding of transmission line behaviour.

2.2.1 Lumped-element Transmission lines

Classical microwave transmission lines which support transverse electromagnetic (TEM) propagation, must always contain a minimum of two conducting surfaces; a ground plane and signal plane. These conductors are separated by a dielectric medium in which the majority of the electric field lines are confined. The two conductors may be represented schematically by the two wire line in Figure 2.1a, a small segment (Δx) of which may be considered at a particular time, t, using the equivalent lumped element circuit shown in Figure 2.1b, with corresponding series impedance $Z\Delta x$ and shunt acceptance, $Y\Delta x$.

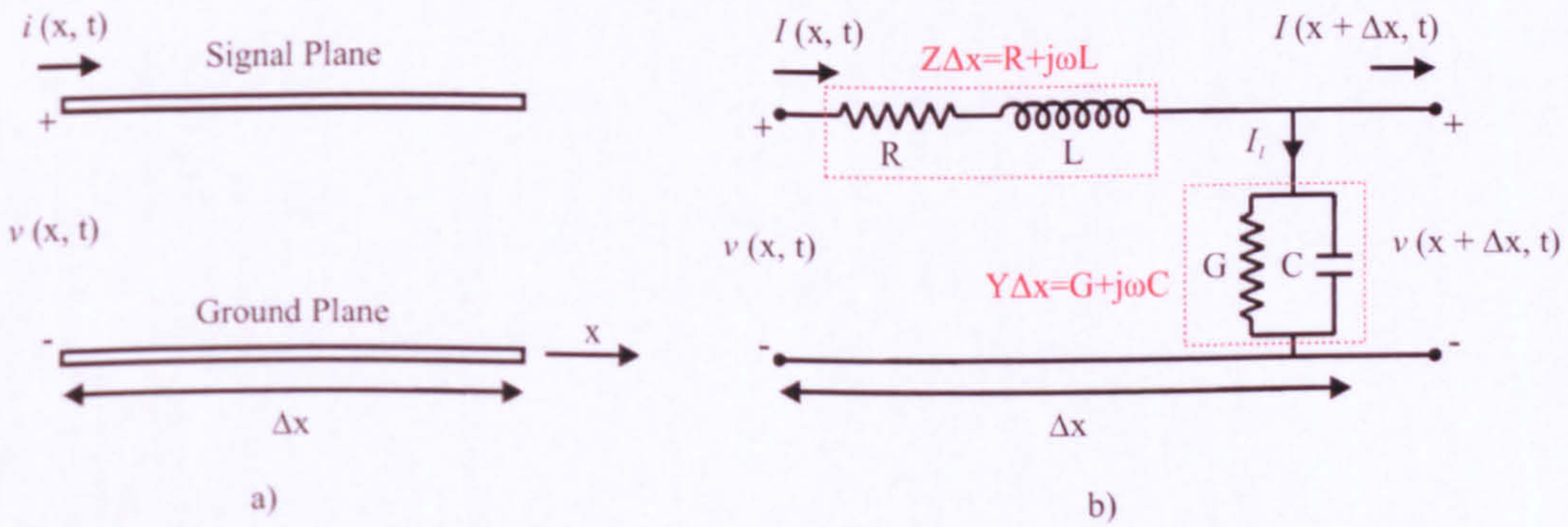

Figure 2.1: Schematics including voltage and current definitions for a) a two-wire line representation and b) a lumped element model, for a segment Δx of transmission line.

The loss in such a transmission line is represented by the series resistance arising from the finite conductivity of each metal layer, and the shunt conductance between the lines caused by a non-zero conduction in the dielectric, labeled R and G respectively. An inductance value, L, arises from the self-inductance of the

transmission line caused by a propagating electrical signal, and the capacitance, C, is caused by the close proximity of the two parallel conducting surfaces. Application of Kirchoff's laws to the circuit in Figure 2.1b whilst taking the limit as $\Delta x \rightarrow 0$ [66] for a voltage, V, and current, I, at a position x along the line yields:

$$\frac{dV(x)}{dx} = -(R + j\omega L)I(x), \tag{2.1}$$

$$\frac{dI(x)}{dx} = -(G + j\omega C)V(x). \tag{2.2}$$

Differentiating these equations allows us to solve them simultaneously to produce the following one dimensional wave equations for voltage and current at a position x on the line:

$$\frac{d^2V(x)}{dx^2} - \gamma^2 V(x) = 0, \tag{2.3}$$

$$\frac{d^2I(x)}{dx^2} - \gamma^2 I(x) = 0, \tag{2.4}$$

where the substitution

$$\gamma = \alpha + j\beta = \sqrt{(R + j\omega L)(G + j\omega C)}, \tag{2.5}$$

is the frequency dependent complex propagation constant. The real part of γ represents the losses in a transmission line and is known as the attenuation constant, often expressed in decibels per unit length. The imaginary part, β, is known as the phase constant and represents wave propagation in the line. Travelling wave solutions to (2.3) and (2.4) result in

$$V(x) = V_0^+ e^{-\gamma x} + V_0^- e^{\gamma x}, \tag{2.6}$$

and

$$I(x) = I_0^+ e^{-\gamma x} + I_0^- e^{\gamma x}, \tag{2.7}$$

where the negative and positive exponential terms represent voltage or current propagation in the $+x$ or $-x$ directions respectively. By applying (2.2) to (2.7), we determine the voltage in the line as

$$V(x) = \frac{\gamma}{G + j\omega C}\,[I_0^+ e^{-\gamma x} - I_0^- e^{\gamma x}], \tag{2.8}$$

where the characteristic impedance of a transmission line is given as:

$$Z_0 = \frac{\gamma}{G + j\omega C} = \sqrt{\frac{R + j\omega L}{G + j\omega C}}\ . \tag{2.9}$$

By substituting Z_0 into (2.8) and replacing the V(x) and I(x) terms with those in (2.6) and (2.7), examination of the coefficients for the negative and positive travelling waves reveals

$$\frac{V_0^+}{I_0^+} = Z_0 = \frac{-V_0^-}{I_0^-}, \tag{2.10}$$

which defines Z_0 as the ratio of voltage to current amplitudes in the line in the absence of reflections (i.e. an infinite or perfectly matched line). This result is useful when considering reflections at transmission line terminations (Section 2.2.3). Careful selection of materials when designing a transmission line system allows specific characteristic impedances to be chosen. Converting the voltage in (2.6) into the time domain and reintroducing the complex representation of the propagation constant γ, from (2.5) allows expression of the voltage waveform as

$$v(x,t) = |V_0^+|cos(\omega t - \beta x)e^{-\alpha x} + |V_0^-|cos(\omega t + \beta x)e^{\alpha x}. \tag{2.11}$$

This equation yields several important properties of wave propagation along a transmission line when we consider the definition of a wavelength, λ_r, in the line. Measured as the distance between two successive maxima, minima or any other equivalent points on a wave, we can use (2.11) to show that

$$[\omega t - \beta x] - [\omega t - \beta(x + \lambda_r)] = 2\pi,$$

so

$$\lambda_r = \frac{2\pi}{\beta}. \tag{2.12}$$

If we consider sitting at a peak of the voltage waveform in (2.11) as it propagates in time, we intuit that the rate of change of angle, $\theta = (\omega t - \beta x)$, with respect to time is zero. Therefore we have

$$\frac{\partial \theta}{\partial t} = 0$$

and therefore,

$$\frac{\partial(\omega t - \beta x)}{\partial t} = 0$$

$$\omega - \beta \frac{\partial x}{\partial t} = 0$$

$$\frac{\partial x}{\partial t} = \frac{\omega}{\beta} = v_p, \tag{2.13}$$

where the phase velocity, v_p is defined as the velocity at which a particular phase angle, θ, (e.g. a maxima) of the travelling wave propagates along the transmission line. This information is critical when calculating the expected time domain positions of reflected signals in a pulsed, on-chip system as seen in Chapter 4. We also see that the phase constant, β, is frequency dependent, which essen-

tially means that different frequencies propagate with different velocities along a transmission line, leading to an effect known as dispersion. This is observed as pulse broadening of a multi-frequency signal as its propagation distance along a transmission line increases.

2.2.2 Losses in Transmission Lines

Whilst the lumped element approach discussed in the previous section introduces the rather intuitive resistive losses associated with transmission line signal propagation, a more in depth treatment of the dielectric losses is necessary to fully understand signal attenuation. The attenuation constant α, first described in (2.5), may actually be separated into two main contributions; the conductor losses (α_c) arising from the series resistance R of the metallisation, and substrate losses (α_d) generated by losses within the dielectric, where the total attenuation constant $\alpha = \alpha_c + \alpha_d$. Signal propagation within a dielectric material is described by the materials' permittivity, given by

$$\epsilon' = \epsilon_r \epsilon_0, \tag{2.14}$$

where ϵ_r is the relative permittivity of the dielectric medium, and ϵ_0 the permittivity of an electromagnetic signal propagating in free space. This equation is valid when considering a lossless dielectric, but for all real materials the permittivity experienced by a signal must be represented as a value containing an imaginary component corresponding to the associated dielectric loss:

$$\epsilon = \epsilon' - j\epsilon'', \tag{2.15}$$

where ϵ'' represents heat losses within the dielectric due to dipole damping in the presence of an oscillating electric field. Manipulation of Maxwell's equations [66] allows us to show that the conductivity loss in the dielectric, σ_{dc}, and frequency

dependent dipole damping, $\omega\epsilon''$, are indistinguishable and may be considered as a total effective dielectric conductivity, allowing us to define the loss tangent of a dielectric as

$$tan\delta = \frac{\omega\epsilon'' + \sigma_{dc}}{\omega\epsilon'}. \tag{2.16}$$

Microwave materials are commonly characterised by referring to their relative permittivity, ϵ_r, and loss tangent at a particular frequency. These properties become more useful when considering specific transmission line geometries to be discussed later in the chapter.

2.2.3 Terminated Transmission Lines

An important property of transmission lines is their ability to propagate signals in either direction simultaneously, as seen in (2.6) and (2.7). This means that a signal propagating in a particular direction along a line may reflect when it reaches the line termination. When considering using on-chip waveguiding technology for measuring overlaid material properties, the presence of reflections which may interfere with the time domain signal is an important consideration and so their origin must be fully understood.

Consider the section of transmission line of characteristic impedance Z_0 in Figure 2.2, which is terminated by a load impedance Z_L. Assuming a propagating voltage wave of the form $V(x) = V_0^+ e^{\gamma x}$ and corresponding current $I(x) = I_0^+ e^{\gamma x}$, generated at a position $x < 0$, the characteristic impedance Z_0 is given by the ratio of V(x) to I(x), as for (2.10). However, if the terminating impedance $Z_L \neq Z_0$, then the ratio of V_L to I_L, the voltage and current at the load, cannot equal Z_0. Hence, a reflected wave is excited with specific voltage and current amplitudes such that the superposition of the positive and negative waves satisfy this characteristic impedance condition.

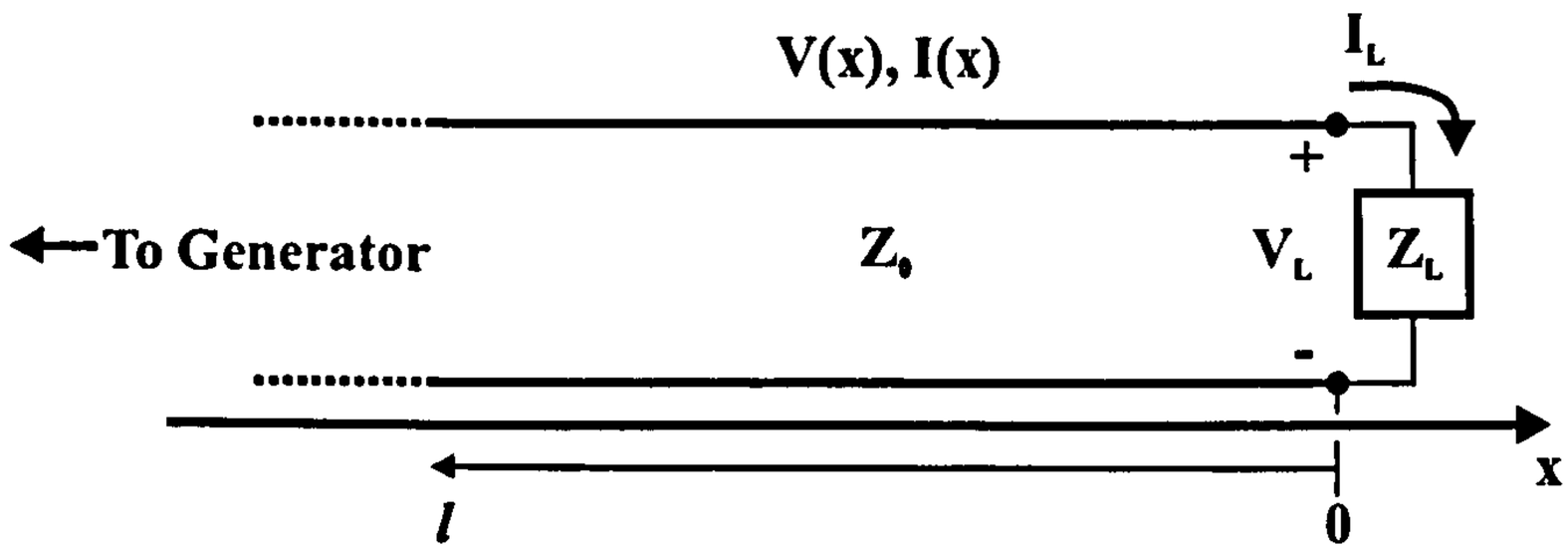

Figure 2.2: A transmission line of impedance Z_0, terminated by an arbitrary impedance Z_L, carrying a voltage signal $V(x) = V_0^+ e^{\gamma x}$ and corresponding current $I(x) = I_0^+ e^{\gamma x}$.

Using Ohm's law, the voltage and current at the load are related by the load impedance, so using (2.7) and (2.8) at $x = 0$ we must have

$$Z_L = \frac{V(0)}{I(0)} = \frac{I_0^+ - I_0^-}{I_0^+ + I_0^-} Z_0. \tag{2.17}$$

Solving for $-I_0^-$ and normalising to the incident current wave, I_0^+, generates a term known as the reflection coefficient:

$$\Gamma = \frac{-I_0^-}{I_0^+} = \frac{Z_L - Z_0}{Z_L + Z_0} \qquad (\equiv \frac{V_0^-}{V_0^+}), \tag{2.18}$$

which allows us to rewrite (2.7) and (2.8) as

$$V(x) = Z_0 I_0^+ [e^{-\gamma x} + \Gamma e^{\gamma x}], \tag{2.19}$$

and

$$I(x) = I_0^+ [e^{-\gamma x} - \Gamma e^{\gamma x}]. \tag{2.20}$$

So, in essence, we have a superposition of voltages and currents on the lines, consisting of the incident and reflected waves, in the ratio Γ. For the special

circumstance where $Z_L = Z_0$, $\Gamma = 0$ and there is no reflected signal; such a load is said to be *matched* to the transmission line impedance.

Since the voltage and current amplitudes are varying with position along the line, it is intuitive that the input impedance looking into a section of line will also be oscillatory with position. If we therefore consider the input impedance Z_{in}, looking into this transmission line at an arbitrary distance $x = -l$ from the load, we see that

$$Z_{in} = \frac{V(-l)}{I(-l)} = \frac{I_0^+[e^{\gamma l} + \Gamma e^{-\gamma l}]}{I_0^+[e^{\gamma l} - \Gamma e^{-\gamma l}]} Z_0. \tag{2.21}$$

This becomes more useful when we substitute (2.18) for the reflection coefficient in (2.21):

$$Z_{in} = Z_0 \frac{(Z_L + Z_0)e^{\gamma l} + (Z_L - Z_0)e^{-\gamma l}}{(Z_L + Z_0)e^{\gamma l} - (Z_L - Z_0)e^{-\gamma l}},$$

which, using the trigonometric identities $e^{\theta} = \cosh\theta + \sinh\theta$ and $\tanh\theta = \sinh\theta/\cosh\theta$ yields

$$Z_{in} = Z_0 \frac{Z_L + Z_0 \tanh\gamma l}{Z_0 + Z_L \tanh\gamma l}. \tag{2.22}$$

This equation is simpler to analyise in the lossless case where $\alpha = 0$ and $\gamma = j\beta$ where, using the identity $\tanh(j\theta) = j\tan\theta$, we have:

$$Z_{in} = Z_0 \frac{Z_L + jZ_0 \tan\beta l}{Z_0 + jZ_L \tan\beta l}. \tag{2.23}$$

This is a very important result when considering the input impedance of a transmission line segment with an arbitrary load impedance. Some special cases with specific load impedances will now be discussed.

Special Cases

A variety of terminated transmission lines result in very useful properties, some of which which will be discussed here. Let us first consider the transmission line in Figure 2.2 with an impedance $Z_L = 0$, i.e. a short circuit. We can see from (2.18) that for a short circuit load, $\Gamma = -1$, which implies that the reflected voltage wave, V_0^-, is 180° out of phase with the incident voltage signal [67]. This is necessary to satisfy the condition that the total voltage at a short circuit termination cannot be non-zero, and in physical terms means that a voltage pulse incident on a short circuit termination will be opposite in sign, but equal in magnitude when reflected. From (2.23) we see that the short circuit termination gives an input impedance of

$$Z_{in} = jZ_0 \tan \beta l, \tag{2.24}$$

so at a position $l = 0$, $Z_{in} = Z_0$, and yet if we move a distance $\lambda/4$ from the load we now have an input impedance equal to infinity, which corresponds to an open circuit.

Similarly, with a terminating impedance of $Z_L = \infty$ (open circuit), the reflection coefficient $\Gamma = 1$, implying that the reflected signal is in the same phase as the incident wave, and the input impedance becomes $Z_{in} = -jZ_0 \cot \beta l$ [67]. Analogously to the previous case, moving a distance $\lambda/4$ from the load converts the open circuit impedance to a short circuit. This may be extended to any quarter wavelength transmission line, or more generally to a length $l = (n+1)\lambda/4$ for $n = 0, 2, 4...$, terminated in an arbitrary load Z_L, where (2.23) gives the input impedance as

$$Z_{in} = \frac{Z_0^2}{Z_L}. \tag{2.25}$$

This has important connotations when considering transmission lines containing

multiple frequency signals, since (2.25) will then be valid for a frequency f_0 at which the transmission line is $\lambda/4$, as well as frequencies $3f_0$, $5f_0$, etc., and becomes increasingly important when considering resonant circuits (see Section 2.3). Such lines are referred to as *quarter wave transformers* since they transform the load impedance in an inverse manner depending on the characteristic line impedance.

2.2.4 Transmission Line Geometries

The particular geometry of transmission line chosen for on-chip propagation has obvious relevance to fundamental transmission properties such as loss and dispersion, as well as more basic considerations such as ease of fabrication and measurement. This section will discuss several different on-chip geometries and define the underlying reasons behind the final choice of propagating topology. Ideally, the four geometries discussed would all support pure transverse electromagnetic signals (TEM). However, there exists a small longitudinal electric field component at the surface of each conductor due to the finite loss within that conductor [68], which means the dominant mode is now *quasi*-TEM. This longitudinal component accounts for conductor losses in the transmission line and is incorporated into the attenuation constant, α, in (2.5). Figure 2.3 shows schematic comparisons of four types of planar transmission line geometries; slotline, stripline, coplanar waveguide and microstrip.

Slotline

The geometry of a planar slotline, as shown in Figure 2.3a, consists of a narrow gap, or 'slot', in a conducting plane on one side of a dielectric block [71] in which a potential difference exists between the slot edges. For a slotline to be useful as a transmission line, the permittivity of the supporting dielectric must be very high such that the supported slot wavelength is small compared to the free

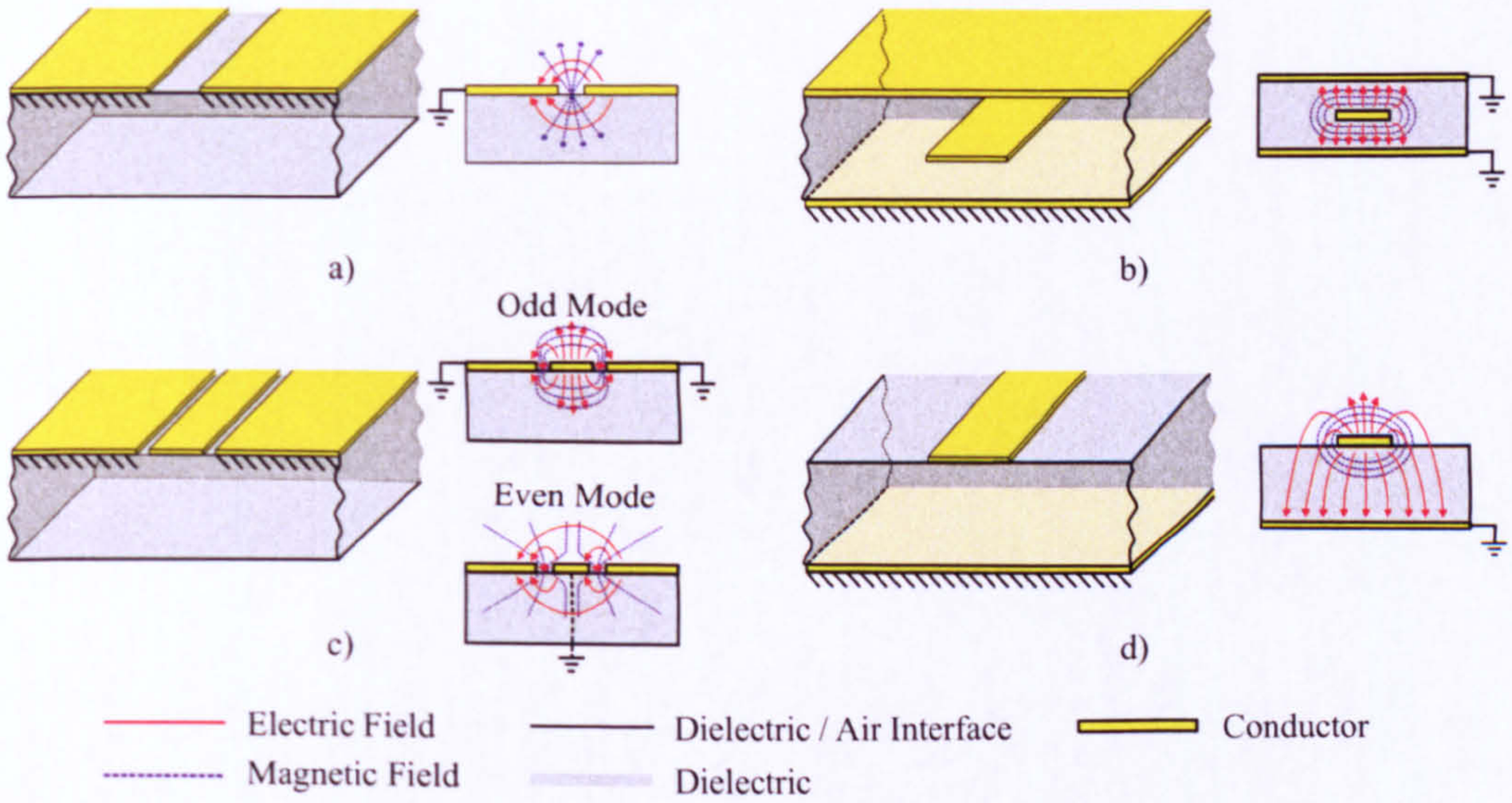

Figure 2.3: Diagrams showing the physical geometry and simplified E-M field distributions around a) slotline [69], b) stripline, c) coplanar waveguide (in both even and odd-modes) [70] and d) microstrip transmission line [66].

space wavelength, resulting in close confinement of the fields to the slot. Whilst ease of fabrication is a major advantage in this type of waveguide, the main disadvantage lies in a non-TEM mode supported by the structure alongside the required quasi-TEM mode [69]. This mode leads to strongly frequency dependent characteristic impedance and phase velocity when compared to the other devices shown in Figure 2.3, which would lead to significant dispersion when considering a broadband pulsed measurement. This property prevents slotline designs being a useful topology for use as a broadband THz probe of overlaid material.

Stripline

A stripline geometry consists of a thin conducting strip sandwiched in a dielectric block and centered between two comparatively large conducting ground planes. Since this device has two conductors, the dominant mode supported is again quasi-TEM as discussed above, although higher order TE or TM modes may also propagate. From a fabrication perspective, the centre conductor must often be etched on one side of a dual layer dielectric and then covered with another

grounded layer of the same dielectric. Due to the problems fabricating or obtaining pre-clad dielectrics sufficiently thin to support THz frequencies, this method would be impractical. Instead, a dielectric preparation for the lower portion, followed by evaporation of the stripline and subsequent preparation of the upper dielectric portion would be a preferred method. However, an intrinsic criteria for developing an on-chip spectroscopic system is accessibility of a spectroscopic sample to the measurement region which, in the case of stripline, would be precluded by the presence of the upper dielectric region and ground plane. Development of a removable upper region would be non-trivial, again due to the thinness (as discussed in Section 2.2.5) and inherent fragility of the materials being used. This topology was therefore deemed inappropriate for the present work.

Coplanar Waveguide

A conventional coplanar waveguide (CPW) is a structure in which all the conducting media are equiplanar [72], as seen in Figure 2.3c. Ideally, the dielectric beneath the conductors should be of infinite thickness, but in practice it only need be sufficiently thick to prevent field leakage. CPW designs offer several advantages over other transmission lines when incorporating active devices, or passive components such as filters, as the planar layout negates the need for via holes or wraparounds for ground connections. Further advantages arise when considering the ease with which the characteristic impedance of such a line may be altered without changing the overall dimensions of the device, since this is controlled by the ratio of the centre conductor width to the total separation between ground planes, and may be varied significantly [73].

The main disadvantage of the coplanar technology is its ability to support two different quasi-TEM modes as opposed to the single mode evident in other guiding technologies, although efforts have been made to utilise this property to some advantage [74]. The modes are referred to as *even mode* and *odd mode*, according to the symmetry of the electric field on either side of the central conductor. As

seen in Figure 2.3c, the average dimension of the transverse electric field lines for even mode signals is greater than that of the odd mode, since this dimension is controlled by the separation of the two outer conductors. This increased width makes the even mode more dispersive and attenuating than the odd mode and less useful for signal propagation at high frequencies. Since the two modes have different propagation characteristics, asymmetries or discontinuities in the circuit may lead to mixing of the modes which would increase loss and introduce signal distortion [74]. Such changes would likely mask any spectroscopic information generated during measurement of a sample, or change it so radically as to render it unusable. Another disadvantage of CPWs is their potential for signal radiation as frequencies approach the sub-mm range [75] due to higher order leaky surface waves being excited at such frequencies, which increases signal loss. It was therefore decided that such a propagation medium, although potentially very useful, would be unsuitable for use in broadband THz spectroscopic analysis.

Microstrip Transmission Line

The fourth and final waveguiding system, depicted in Figure 2.3d, is the microstrip transmission line. Microstrip is one of the most popular types of planar transmission line for microwave circuits, since it may be fabricated photolithographically and is easily integrated with other passive and active devices. Although the previous device types offer similar advantages, microstrip can also be scaled directly for operation at THz frequencies without excitation of unwanted higher order modes. As seen in Figure 2.3d, the electric field lines of a microstrip section are mostly concentrated in the dielectric between the two conductors, with some fraction in the air above the substrate. For this reason, the microstrip cannot support a pure TEM mode since the phase velocity within the dielectric would be less than that in air by a factor of $(\epsilon_r)^{-1/2}$. Microstrip transmission lines actually support a hybrid of TE and TM propagation modes which requires significantly more advanced analysis than a standard TEM mode. However, for substrate thicknesses $d \ll \lambda$ (Figure 2.4a) the dominant mode may be assumed to be quasi-TEM [66].

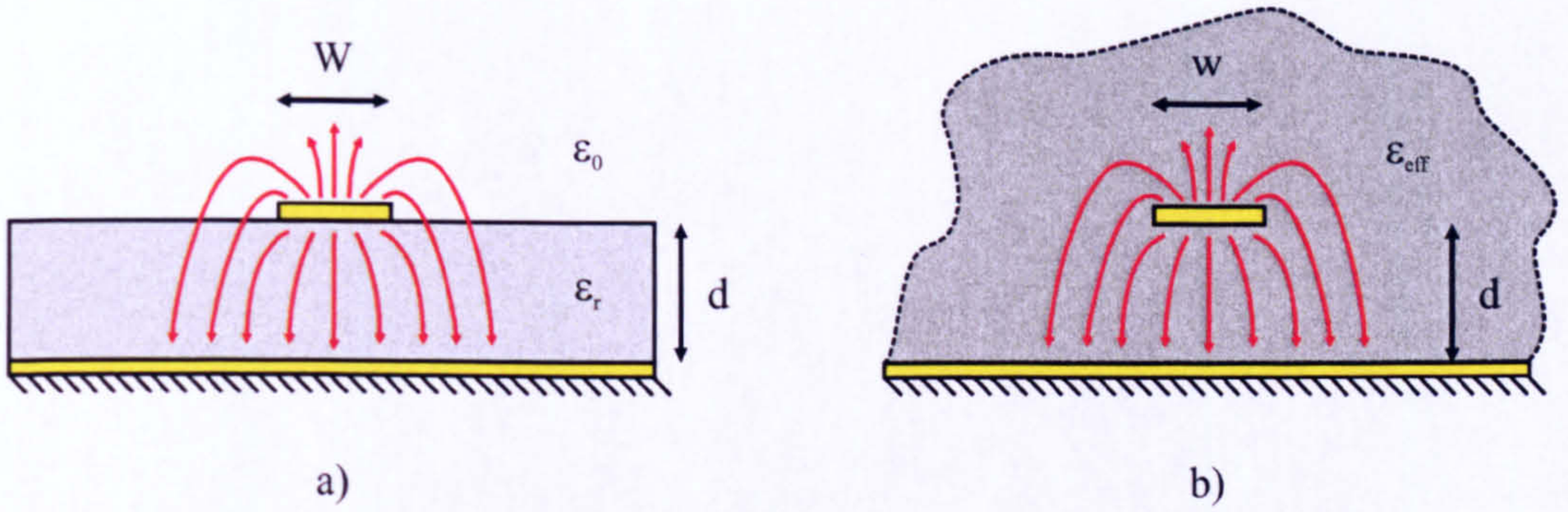

Figure 2.4: Microstrip transmission line showing a) line geometry and electric field and b) the equivalent geometry of a quasi-TEM line where the dielectric slab of thickness d, permittivity ϵ_r and the air above the microstrip of permittivity ϵ_0 have been replaced with a continuous, homogeneous medium of effective permittivity ϵ_{eff}.

Since the electric field exists in two separate media, the field does not only experience the permittivity of the dielectric, in contrast to stripline for example, but also the free space permittivity, ϵ_0, of the air above. If we interpret the two separate regions of permittivity as a single, homogeneous region as seen in Figure 2.4b, we now have a material of overall *effective* permittivity, ϵ_{eff}, surrounding the microstrip and extending to infinity, in which we must calculate the characteristic properties of the transmission line. This effective dielectric constant for a transmission line of width W above a dielectric of thickness d and permittivity ϵ_r is given by:

$$\epsilon_{eff} = \frac{\epsilon_r - 1}{2} + \frac{\epsilon_r - 1}{2\sqrt{1 + \frac{12d}{W}}}. \tag{2.26}$$

Future calculations of the phase velocity (2.13) and phase constant (2.12) for microstrip lines will therefore be performed using ϵ_{eff} instead of ϵ_r. The characteristic impedance of the line in Figure 2.4a is given by

$$Z_0 = \frac{120\pi}{\sqrt{\epsilon_{eff}}[\frac{W}{d} + 1.393 + 0.667ln(\frac{W}{d} + 1.444)]} \qquad [ohms], \tag{2.27}$$

for a geometry where $W/d > 1$. The effective permittivity becomes particularly

useful when considering the total losses experienced by a signal propagating in a microstrip system. The total dielectric losses, α_d, formed by a combination of dielectric conductivity and damping of dipole oscillations (Section 2.2.2) are given by [76]

$$\alpha_d = 27.3\frac{\epsilon_r(\epsilon_{eff}-1)tan\,\delta}{(\epsilon_r-1)\sqrt{\epsilon_{eff}}\lambda_0} \qquad [dB/mm], \tag{2.28}$$

using the loss tangent as described in (2.16) and with λ_0 in mm. The attenuation due to conductor losses is given by

$$\alpha_c = \frac{8.686\sqrt{\frac{\pi f \mu_0}{\sigma}}}{1000.Z_0.W} \qquad [dB/mm], \tag{2.29}$$

taking $\mu_0 = 4\pi$ x 10^{-7} Hm^{-1} as the permeability of free space, f as the frequency of operation and σ as the conductivity of the metal used. The total transmission line attentuation constant is then given by $\alpha = \alpha_c + \alpha_d$ (Section 2.2.2). For carefully chosen dielectrics with low permittivities, conductor losses often dominate substrate losses. When defining the thickness of the transmission line itself, it is important to consider a quantity known as *skin depth.* Skin depth is defined as the distance from the surface of a conductor at which point the electric field has decayed by a factor of e^{-1}, or 36.8% [66] and is given by

$$\delta_s = \sqrt{\frac{1}{\pi f \mu_0 \sigma}}, \tag{2.30}$$

taking σ as the metal conductivity in Sm^{-1}. It has been proposed [77], calculated theoretically [78] and proven empirically [79] that there is an optimum value for conductor thickness of ≈ 3 times the skin depth at a particular frequency, at which a minimum in the conductor resistivity is encountered [80]. Thicker metallisation does not significantly alter the line attenuation, but reducing the thickness below this optimum begins to greatly increase resistance and therefore

loss in a transmission line. Traditionally, microstrip transmission lines and filter devices are characterised by their S parameters. If we consider the simple two conductor transmission line in Figure 2.1a as a two-port network, with the input as port one and the output as port two, the S_{21} parameter, measured in decibels (dB), is a logarithmic ratio of the input and output pulse measurements, where 0 dB represents perfect, lossless transmission and negative values represent the losses discussed here.

2.2.5 Selection of Dielectric Material

In order to minimised ϵ_{eff} in (2.26) and α_d in (2.28), a dielectric medium of low ϵ_r across a broad range of frequencies should be chosen. The chosen material must also demonstrate good adhesion to a selection of metals and substrates and exhibit planarity for varying thicknesses [81]. Very few dielectric materials have been fully characterised at THz frequencies, with the exception of Benzocyclobutene (BCB) and polypropylene. Devices using polypropylene as a dielectric material have demonstrated a relative permittivity, ϵ_r, of 2.41 at 400 GHz, which would be ideal for the purposes of this project [48]. However, the self-adhesive polypropylene suitable for this technique has a total thickness of 67 μm which would mean, in order to satisfy the criteria that $W/d > 1$ in (2.27) a microstrip transmission line width of greater than 67 μm is required. Whilst on first impression this may seem feasible, if we now consider the effect of transverse resonance, which occurs when the width of a line exceeds $\approx \lambda/4$ [82], 67 μm corresponds to a line wavelength $\lambda_{eff} = \lambda_0/\sqrt{\epsilon_{eff}}$ of 0.194 mm, or a frequency of 1.1 THz (calculated for the ratio $W/d = 1$). In effect we would be limiting the system bandwidth of such a device to below 1 THz and indeed, in [48], measurements were only taken up to 800 GHz (Figure 2.5). Closed form equations exist for ratios of $W/d \leq 1$ [66], but reducing the line width would increase the characteristic impedance in (2.27) and potentially introduce greater conductor loss.

A useful method of determining the maximum operational frequency of a mi-

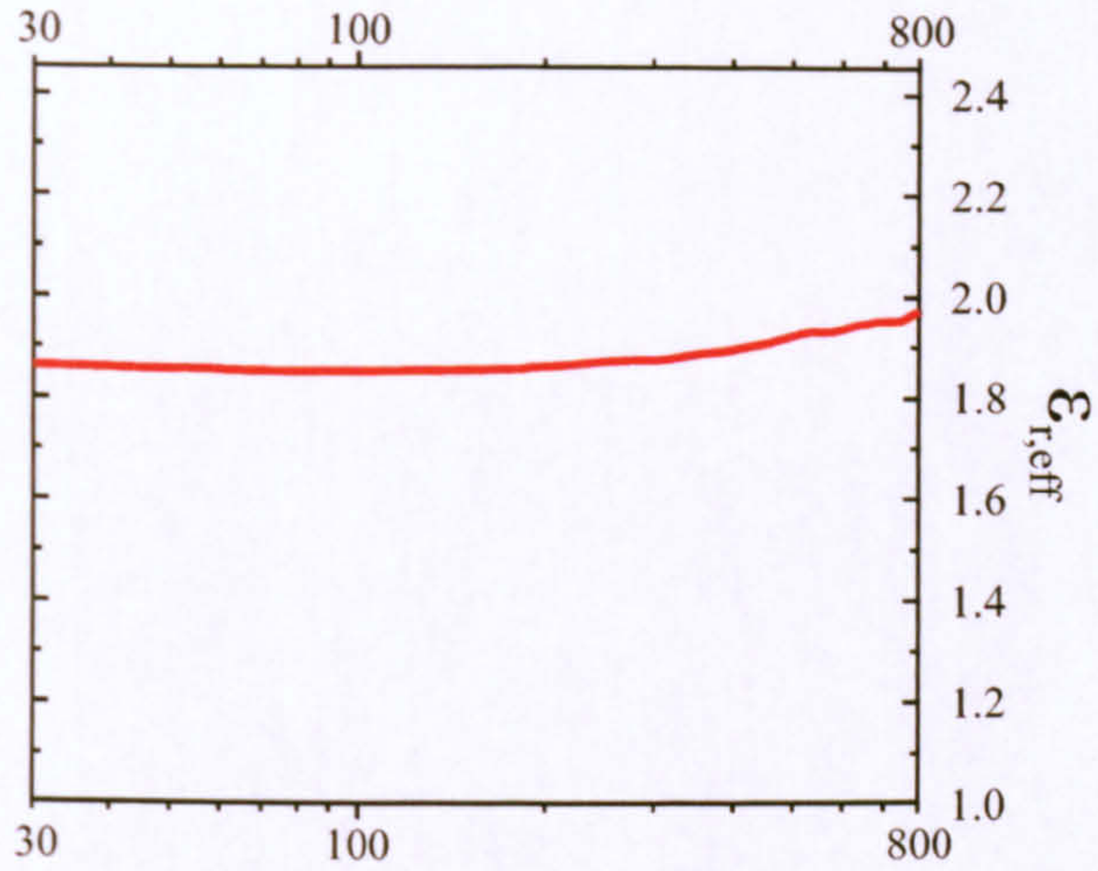

Figure 2.5: Measured effective permittivity $\epsilon(f)$ of polypropylene between 30 and 800GHz, adapted from [48].

crostrip line of the form in Figure 2.4a, is to calculate the upper cut-off frequency of the dominant quasi-TEM mode in a microstrip line, although significant dispersion and attenuation is likely to occur for any length of transmission line at frequencies below this. The cut-off frequency [83] is given by:

$$f_c = \frac{c_0 Z_0}{2\eta_0 d}, \tag{2.31}$$

where $\eta_0 = 377\,\Omega$ is the characteristic impedance of free space and $c_0 = 2.998$ x $10^8\, ms^{-1}$ is the free space light velocity. The geometry discussed above would have $Z_0 = 91\,\Omega$, which yields a cut-off frequency of $f_c \approx 550$ GHz, clearly too low for broadband THz spectroscopic measurements.

BCB however, has a published ϵ_r of 2.65 [84] at 20 GHz and a measured ϵ_r of 2.57 at 400 GHz [48] and is therefore only a slightly more lossy dielectric than polypropylene. A major advantage of BCB however, is that it may be applied to a ground plane via spin-coating, allowing formation of layers down to 6 μm thickness. This allows us to satisfy $W/d > 1$ whilst still producing a low impedance transmission line. For example, a 16.2 μm wide transmission

line formed on $6\mu m$ BCB dielectric would produce $Z_0 = 50\,\Omega$. Using (2.31) we find an upper cut-off frequency of $f_c \approx 3$ THz. The wavelength of a 3 THz signal in BCB is of the order of 60 μm, which is far greater than the dielectric thickness, allowing treatment of the dominant microstrip mode as quasi-TEM, as discussed in Section 2.2.4. BCB is therefore highly suited to THz frequency on-chip measurements and was chosen as the medium for use in the present work.

2.3 Microstrip Filter Design

It was suggested in Section 1.4.1 that a simple microstrip interconnect would not be a useful spectroscopic tool for measuring unknown materials, since the response of a transmission line does contain any specific features which may be used as a point of reference to be monitored for discrepancies under dielectric loading, nor does it contain a sensitive region over which material could be overlaid. The introduction of resonant passive filters into an interconnect produces just such reference points in the form of band-pass or band-stop regions in the transmission response, which are highly sensitive to changes in the local dielectric environment. Several types of filter used in other work have been discussed in Section 1.4.3, but slightly more detail will be used here to justify the final choice of filter geometry. For all of the filters discussed in this section, the lengths involved are subject to modification due to the presence of edge fields. These correspond to electric field lines protruding from either end of the coupled sections which increase the *effective* length of each section. Modification of these lengths, usually performed in an electromagnetic simulation package afer calculation of initial values, is necessary to produce resonance at the exact desired frequency.

2.3.1 Band-pass Filters

Band-pass filters, as the name suggests, allow a specific frequency range (or pass-band) to propagate through a device, whilst blocking all others (Figure 2.6). This

is achieved by introducing sections of microstrip which are resonant at a specific frequency and which couple this frequency across a boundary or discontinuity, such as a gap in the transmission line.

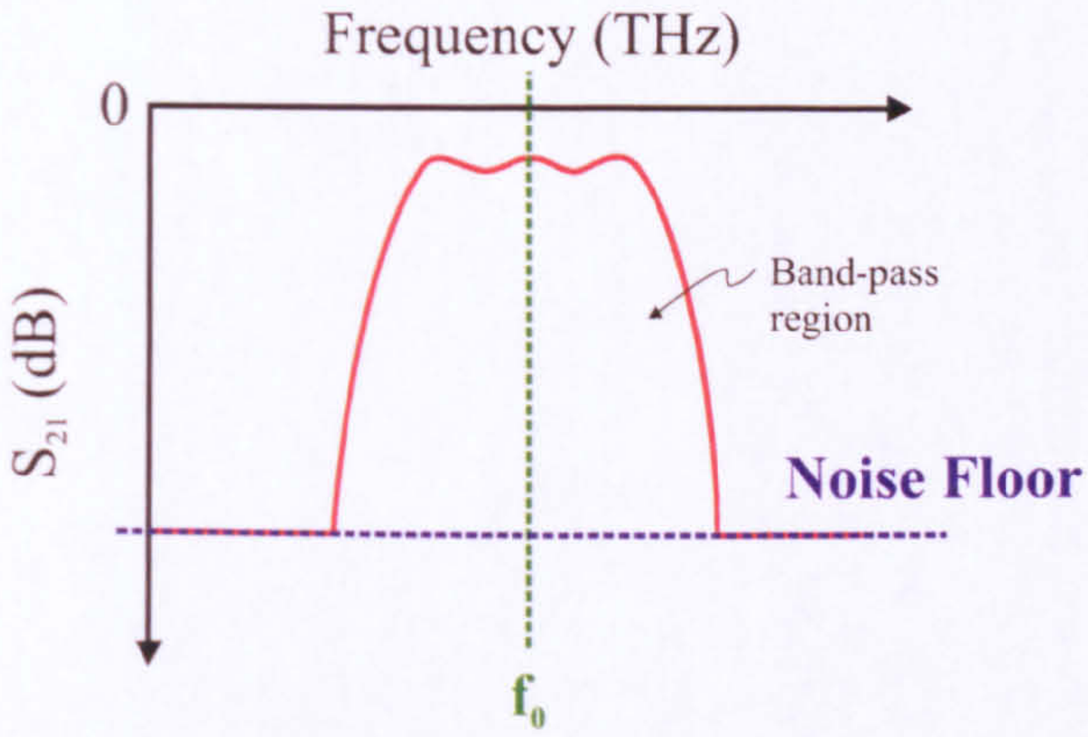

Figure 2.6: Demonstration of the expected transmission response (S_{21}) in decibels of an arbitrary band-pass filter, with f_0 as the chosen resonant frequency.

Frequencies which are not coupled are reflected back from the discontinuity and are not seen at the device output. Band-pass filter designs include, amongst others: series coupled stubs, edge coupled band pass filters and ring resonators, all of which will now be briefly described. All references to wavelength in this section are of the effective wavelength, λ_{eff}, i.e. the wavelength *within* the transmission line as opposed to the freespace wavelength, λ_0.

Series Coupled Stubs

The series coupled stub, in its most basic form, consists of a length $w = \lambda_{eff}/2$ segment capacitively coupled between two microstrip transmission lines, as shown in Figure 2.7. The reason a half-wavelength stub is used becomes clear when we consider the voltage waveform within the resonant section. In precisely the same manner as for the open circuited termination described in Section 2.2.3, a voltage signal propagating within this section will reflect from the open circuited ends with zero phase inversion, and a reflection coeffiecient $\Gamma = 1$. This will occur at both ends of the stub and a standing wave will be formed. For frequencies

at which $w \neq \lambda_{eff}/2$, the reflections will interfere destructively and such frequencies cannot therefore, be supported in the coupled section. As the frequency approaches the value at which $w = \lambda_{eff}/2$ however, the two open circuit ends will correspond to adjacent antinodes within the voltage waveform and the structure will therefore resonate at this frequency. If the separations s_1 and s_2 between the resonant section and the transmission lines are sufficiently small, and therefore the capacitances sufficiently large, this frequency will be coupled across the gaps and may propagate to the device output.

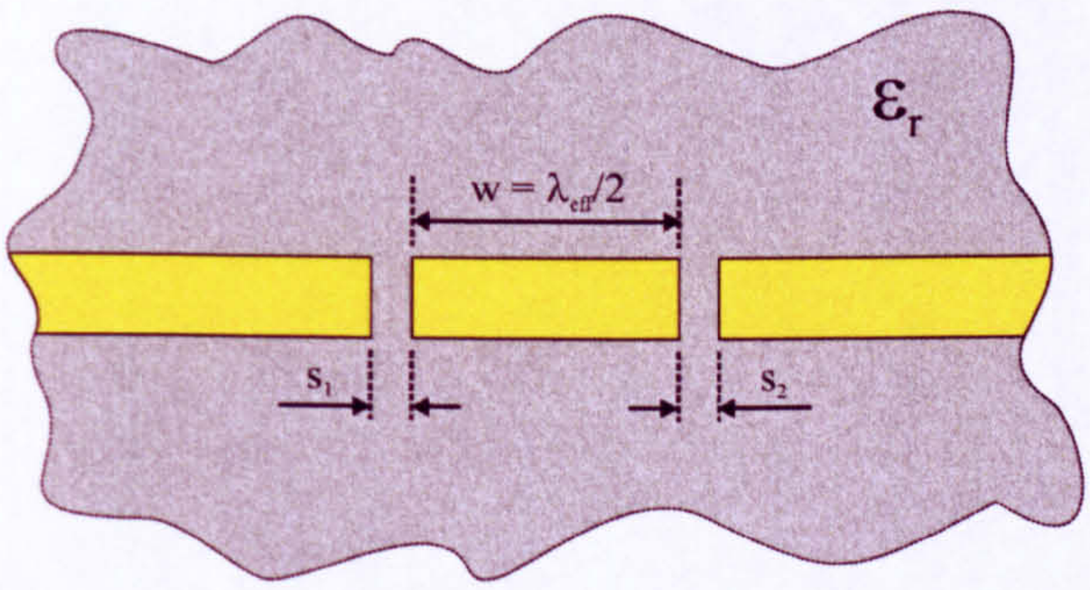

Figure 2.7: Sketch of a series coupled resonator capcitively coupled to two microstrip transmission lines across a gap widths s_1 and s_2, fabricated on a dielectric of permittivity ϵ_r.

In a similar fashion to the quarter wavelength terminations in Section 2.2.3, the coupled stub will re-resonate at frequencies whose wavelength satisfy the critera of supporting antinodes at either end of the stub. This corresponds to wavelengths of $n\,\lambda_{eff}/2$ for $n = 1, 2, 3....$

Ring Resonators

The first form of parallel coupled filter to be discussed in this chapter consists of the ring resonator. As seen in Figure 2.8, the ring resonator consists of a ring a single wavelength in circumference which is coupled by a segment of length l_1 to the input microstrip line. The output is simlarly coupled to, in this case, the opposite side of the ring by a segment of length l_3. Again, the capacitive gaps determine the strength of coupling between the ring and the supply lines, and

since the coupling length has been increased from the previous scenario - where only the line width provided the coupling region - to a much longer section, we would nominally expect stronger coupling in this design.

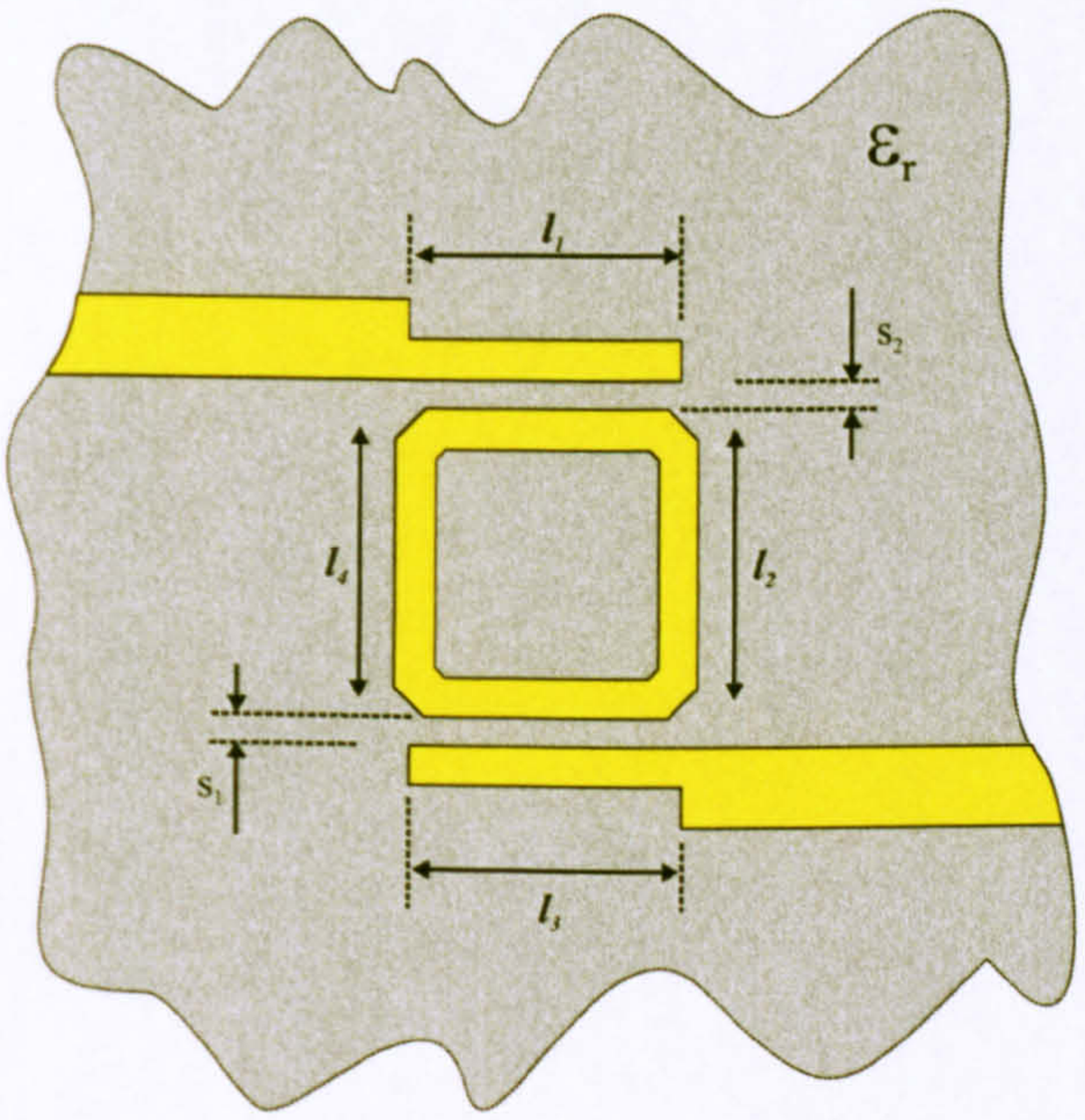

Figure 2.8: Sketch of a parallel coupled ring resonator capacitively coupled to input and output microstrip feedlines across gap widths, s_1 and s_2, fabricated on a dielectric of permittivity ϵ_r.

Since the resonating section is a closed loop, the standing waveform within the resonator must be continuous, requiring that the total circumference of the ring constitutes a single wavelength at resonance. When this criteria is satisfied, the coupling lengths l_1 and l_3, and the capacitive gaps s_1 and s_2 may be varied to accomplish the desired filter response. It is also evident from Figure 2.8 that the input and output transmission line widths narrow slightly around the coupled regions. This is due to the capicitance from the ring section slightly altering the characteristic impedance of the feed lines. To avoid reflections from such a discontinuity, the width is altered to maintain a constant impedance.

Edge Coupled Filters

The final band-pass filter to be discussed is the edge-coupled resonator. This consists of a series of $\lambda/2$ stubs, similar to the series coupled filter, but cascaded across the gap between the input and output feed lines as shown in Figure 2.9. The lengths l_1 and l_2 are approximately $\lambda_{eff}/4$ in length, and l_3 is $\lambda_{eff}/2$ long. Each resonator is coupled to the previous and succeeding sections by a quarter wavelength long capacitive gap. In the geometry shown in Figure 2.9, the filter consists of three resonant sections, but in principle this may be any integer value depending on the exact type of filter required (e.g. maximally flat, equal ripple...). The beauty of the designs discussed so far is that they exhibit rotational symmetry about their centres, requiring that only half of the coupled segments and gaps require mathematical treatment. Similar to the ring resonator scenario, the end sections of the feed lines on the edge coupled device must be altered in width to maintain constant line impedance, which has been altered by the presence of coupled sections.

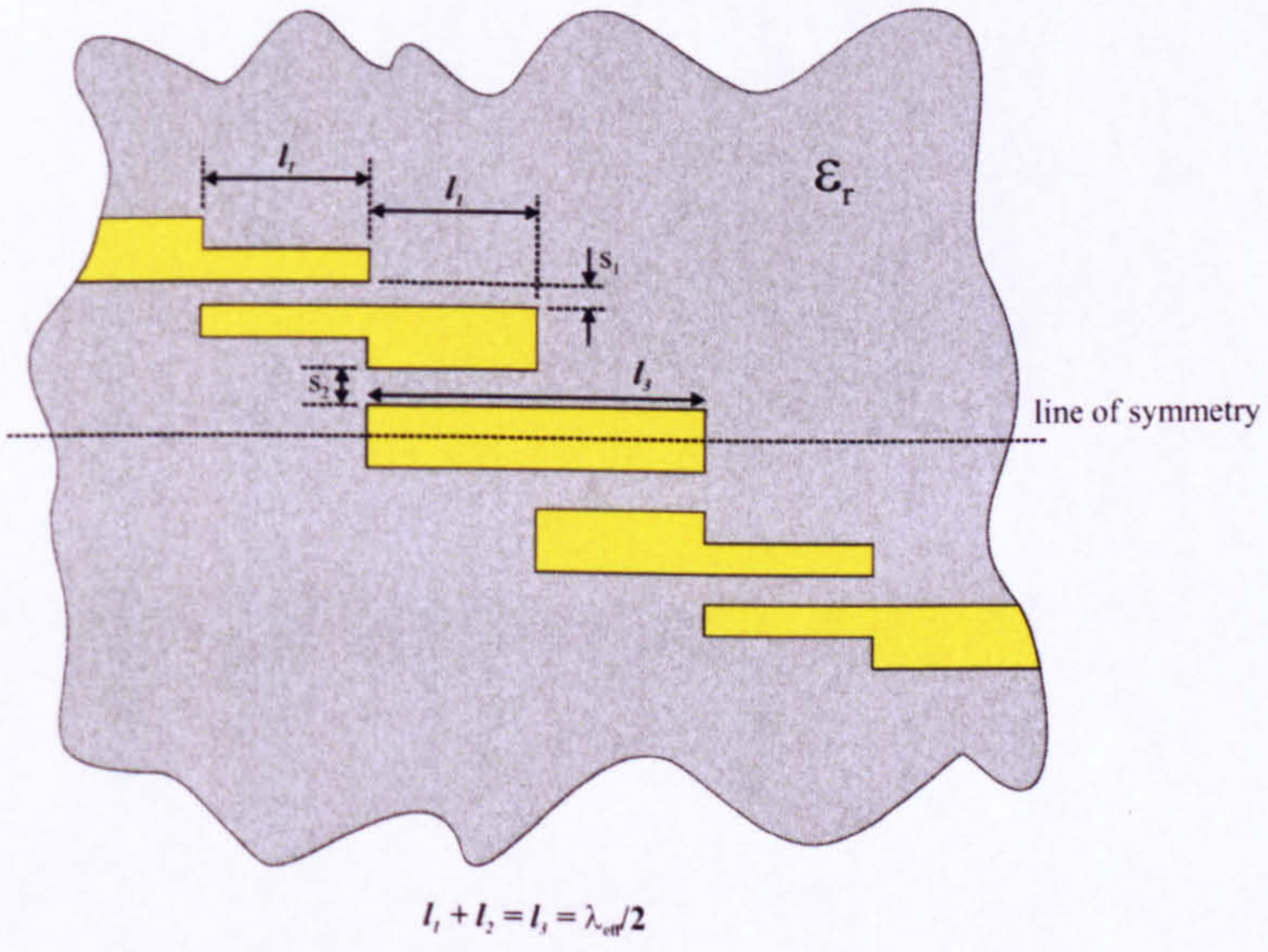

Figure 2.9: Sketch of a edge coupled band pass filter with resonant sections capacitively coupled over gaps s_n, where n is the total number of central resonators, with lengths $l_1 \approx 1_2 \approx \lambda_{eff}/4$ and $1_3 \approx \lambda_{eff}/2$, fabricated on a dielectric of permittivity ϵ_r.

Whilst the edge coupled [85, 58] and ring resonator [59] filters have been used

in previous work for THz sensing, for the purposes of spectroscopy at different frequencies there is an inherent limitation derived from the nature of these filters. Since band-pass filters prevent propagation of all frequencies except the relatively narrow band-pass region, other frequencies are not presented at the device output and are therefore unavailable for spectroscopic measurements. In order to develop such technology for multiple-frequency measurements, band-stop filters now become an interesting prospect, as discussed in Section 2.3.2. A full mathematical treatment of all the band-pass filter designs discussed here is available in [86].

2.3.2 Band-stop Filters

Band-stop filters operate in precisely the opposite fashion to band-pass filters. All frequency components are free to propagate through the system except for a relatively narrow range called the stop-band (Figure 2.10).

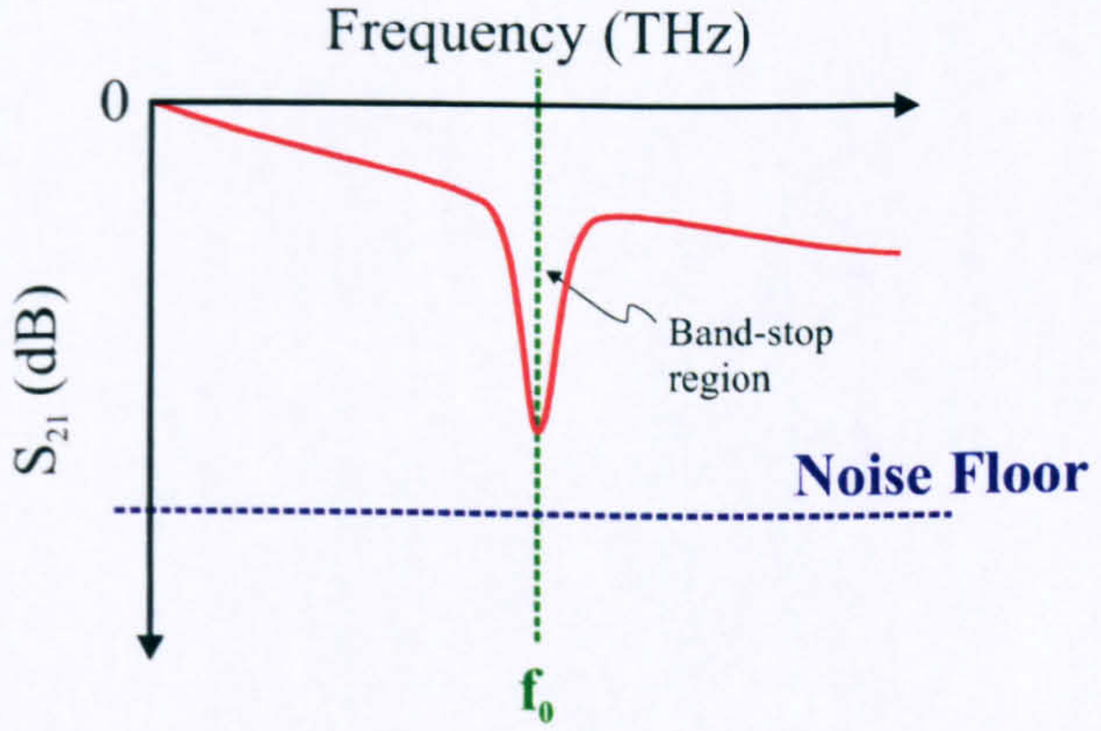

Figure 2.10: Demonstration of the expected transmission response (S_{21}) in decibels of an arbitrary band-stop filter, with f_0 as the chosen resonant frequency.

Whereas band-pass filters couple a particular frequency band across a discontinuity between input and output feedlines, band-stop filters usually *create* a discontinuity by resonating in shunt with the interconnect, and thus removing a selected frequency range. This presents the prospect of arranging, or *cascading*, several filters of varying operational frequency along a single interconnect to allow spectroscopic analysis at many different frequencies. Prior to discussing this in

slightly more detail towards the end of the chapter, several forms of band-stop filters will now be discussed.

Shunt-coupled $\lambda/2$ Filters

The shunt-coupled filter operates in a similar fashion to the series-coupled device discussed previously in Section 2.3.1. Since the stub is open circuited at either end, the section resonates when its length is equal to $\lambda_{eff}/2$ at the chosen frequency of operation. Instead of then being coupled to the output of the system, a standing wave is formed within the resonator which effectively removes this frequency from the output of the device, producing a notch in its transmission (or S_{21}) response. It is the position of this notch which would be monitored when the filter is overlayed with a material on which spectroscopic analyisis will be performed. As seen in Figure 2.11, the stub is coupled capacitively by a gap, s, in a similar fashion to the previous topologies.

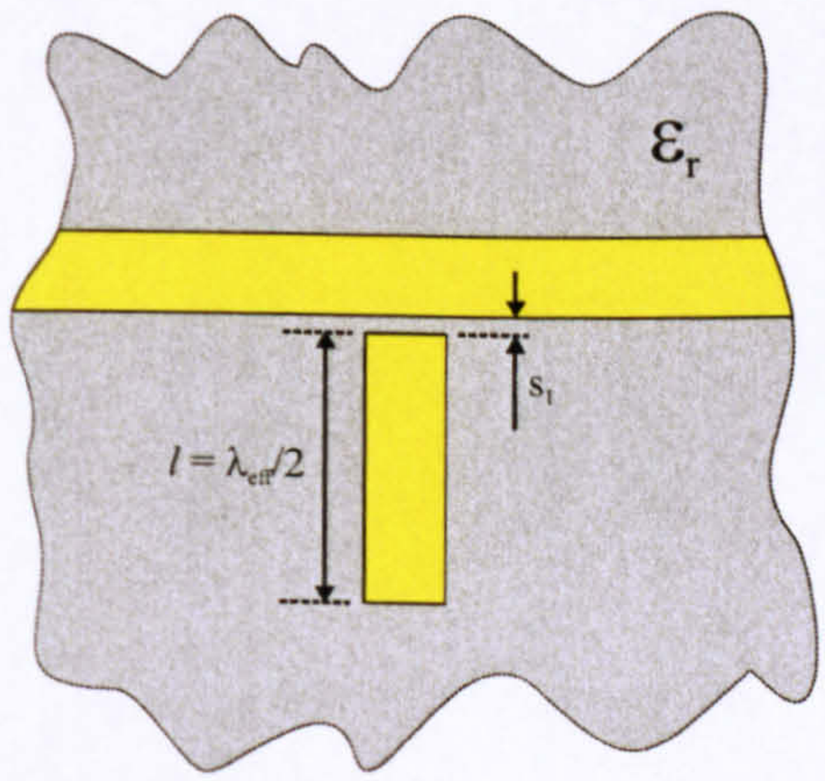

Figure 2.11: Sketch of a $\lambda_{eff}/2$ shunt-coupled stub separated from the main interconnect by a capacitive gap of width s, fabricated on a dielectric of permittivity ϵ_r.

Shunt-coupled L-Resonator

A slight modification to the previous design introduces a right angled bend at a point somwhere along the resonant stub, which is then coupled to the main

transmission line by the side l_1 as in Figure 2.12. Nominally, l_1 and l_2 would be $\lambda_{eff}/4$ in length, though this may change during finalisation of designs due to optimisation.

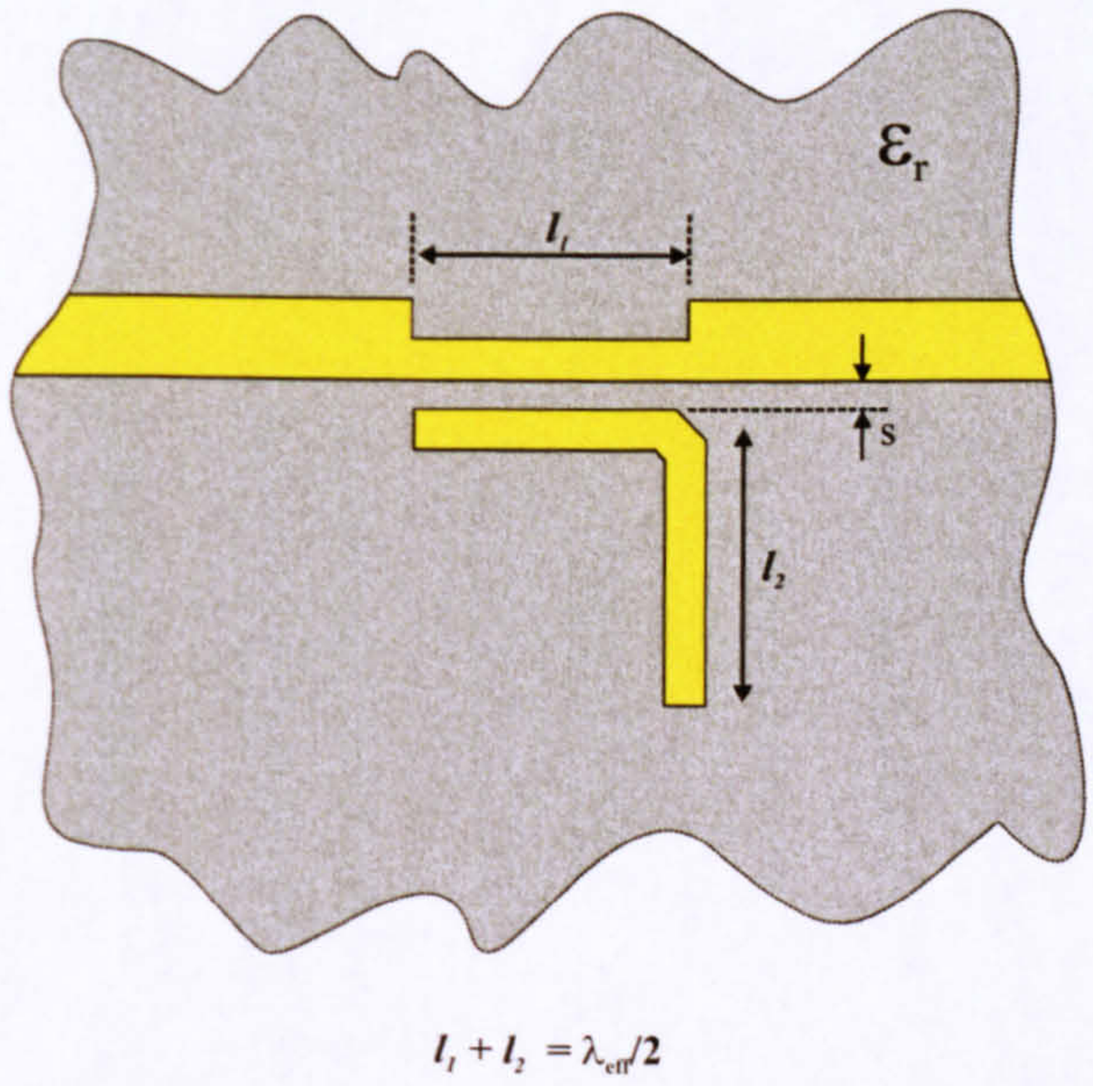

Figure 2.12: Sketch of a $\lambda_{eff}/2$ L-resonator coupled along a side length l_1 across a capcitive gap of width s to the main transmission line, fabricated on a dielectric of permittivity ϵ_r.

The intention behind introducing the L-bend is to increase the length over which the resonator is coupled to the transmission line, similar to the ring resonator discussed in Section 2.3.1. This theoretically allows the gap size to be increased somewhat whilst still maintaining good coupling, an important effect when considering the sub-micron scale gap sizes required for THz operation. As seen for the parallel coupled filter and ring resonator, the line impedance is altered by the presence of the coupled section, and so the line width must be altered to compensate and avoid generation of reflections [87].

Quarter Wavelength Shunt Stubs

So far, all the suggested filter designs have involved a coupled resonator of some variety. Whilst for microwave circuitry this is easily implemented, as we incease

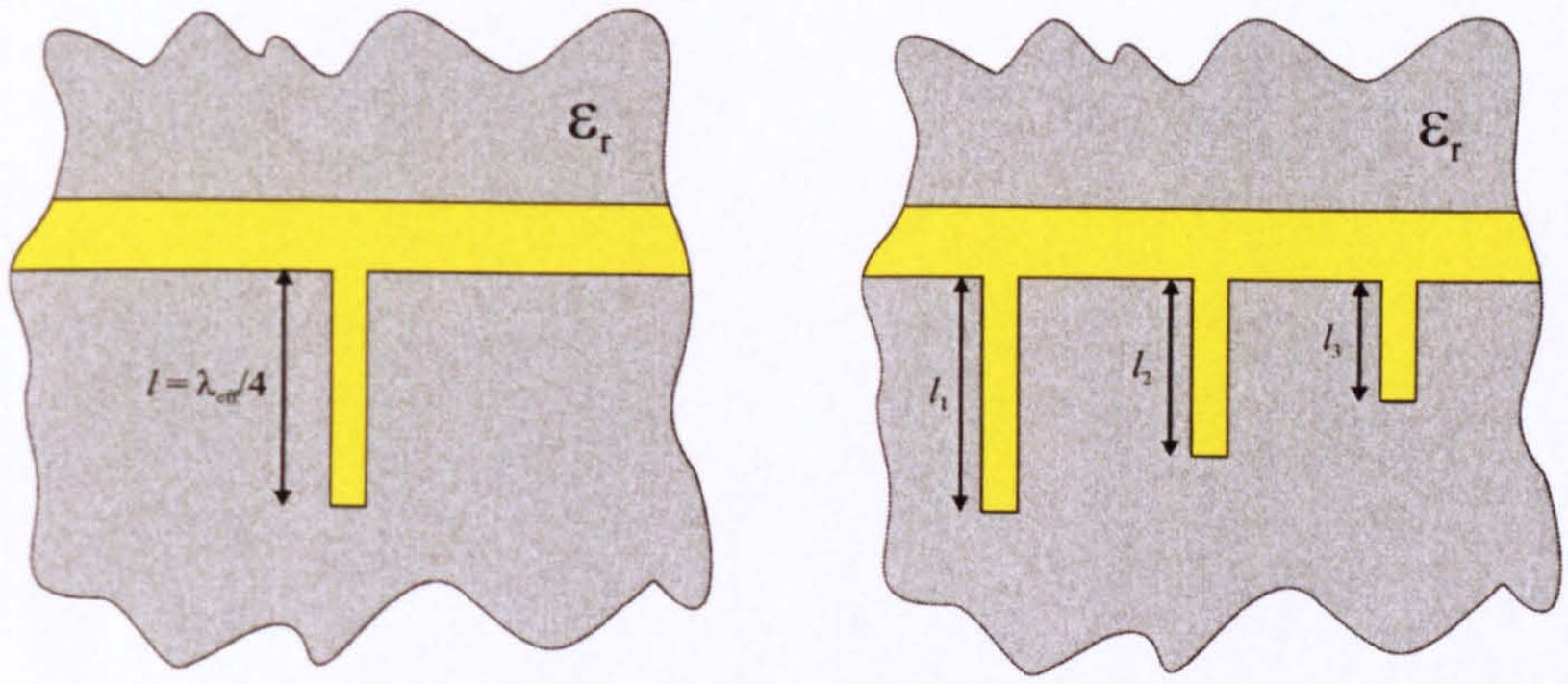

a) b)

Figure 2.13: Sketch of a) a single $\lambda_{eff}/4$ shunt stub and b) multiple shunt stubs of lengths l_1, l_2 and l_3 equal to $\lambda_{eff,1}/4$, $\lambda_{eff,2}/4$ and $\lambda_{eff,3}/4$ respectively, all fabricated on a dielectric of permittivity ϵ_r.

the frequency up to the THz region, the length scales involved *decrease* correspondingly until such gaps may be sub-micron in size. Whilst it is possible to fabricate devices with such dimensions using electron-beam lithography (EBL) or focussed ion beam (FIB) apparatus, if the device is to maintain low cost and be easily implementable using standard photolithographical techniques, these two methods would best be avoided. With this in mind, the following topology was considered the most applicable for use in on-chip spectroscopy. Consisting of a quarter wavelength shunt stub, this device operates as an open circuited $\lambda/4$ termination discussed in Section 2.2.3. At resonance, the stub transforms the open circuited end to a short circuit seen when looking into the stub (i.e. this is what the transmission line 'sees' at resonance), corresponding to the formation of a stop-band occurring at the central resonant frequency. Since no capacitive gaps are present, the design and fabrication of the device seen in Figure 2.13a becomes much more straightforward.

The main advantage of band-stop filters becomes apparent when we appraise Figure 2.13b, which shows a cascade of filters operating at isolated frequencies determined by their respective lengths. The stubs produce a band-stop region in the S_{21} characteristic similar to that in Figure 2.10, but at several distinct frequency

positions, allowing spectroscopic measurements to be performed at multiple frequencies simultaneously. As with all such microstrip filters, each of the stubs will re-resonate at multiples of the fundamental frequency. Unlike the half-wavelength filters, quarter-wave devices re-resonate at odd multiples of the fundamental, i.e. $(2n-1)f_0$ for $n = 1, 2, 3, ...$ This provides an additional advantage over the $\lambda/2$ filters, since fewer higher frequency resonances are present to complicate the S_{21} curve. Whilst designing such a cascade, it is necessary to avoid overlap of harmonic resonances from lower frequency filters with the fundamental resonances produced by higher frequency devices. The final designs for the on-chip systems used in this thesis are presented in Chapter 3.

Chapter 3

Device Design and Fabrication

3.1 THz System Design

The on-chip, THz microstrip designs presented in this Chapter will follow chronologically the order in which new topologies were developed, from first generation to third generation devices, with retrospective insight into the features necessary for a successful on-chip spectroscopic system. Reasons for the evolution of earlier designs will be briefly addressed, though full appreciation of the requirements for the second and third generation devices may only become apparent in future chapters.

3.1.1 THz Interconnects

Although design of THz microstrip transmission lines themselves is relatively straightforward, it is useful to discuss the dimensions chosen in order to understand system characteristics, such as transmission loss. Gold (Au) was chosen as the material for device fabrication due to it's high conductivity ($\sigma = 4.098 \times 10^7$ Sm^{-1}) and propensity for thermal evaporation. Due to the often poor adhesion of Au to arbitrary substrates a thin, usually 10 - 25 nm, adhesion layer of titanium (Ti) is also used between the Au and the dielectric. The interconnect thickness is governed by the skin depth of a propagating signal (Chapter 2, Section 2.2.4),

and should be no less than three times this value. Since skin depth is inversely proportional to frequency, it may seem reasonable to calculate the required metallisation thickness at low frequencies, where the skin depth is greatest. However, to maintain a reasonably constant current density for all frequencies, choosing the thickness as three times the skins depth at the *highest* frequency is more appropriate. This presents a slight problem when considering a broadband system of unknown upper frequency limit. Whilst (2.31) generates a cut-off frequency of 3 THz for TEM transmission in a 50 Ω line on 6 μm BCB, radiative, conductive and dielectric losses will deteriorate the signal long before this point. Assuming a maximum operating frequency of 1 THz allows calculation of the skin depth in a gold transmission line as 78.6 nm, which suggests a transmission line thickness of 250 nm would be appropriate.

The width of the interconnect, along with substrate height, determines its characteristic impedance (2.27). By choosing the thinnest possible BCB layer (6 μm), we obtain greatest planarity of dielectric and also maximise capacitive coupling between transmission line and ground plane. In microwave circuit design, commonly used substrates of known ϵ_r are often fabricated with specific thicknesses and, due to the standardised 50 Ω impedance of microwave measurement networks, transmission lines are often matched to this impedance, generating specific widths of line for different substrates. In our THz on-chip system however, the constraint of impedance matching to external circuitry is not present since THz signals are sampled optically, allowing much greater flexibility in the width used. The upper limit for microstrip width is set by the transverse resonance effect discussed in Chapter 2, Section 2.2.5, which for a 1 THz bandwidth system is 67 μm. The lower limit is determined by the resolution of optical lithography. Whilst it is possible to achieve features of 2 or 3 μm using optical lithographical techniques, one must consider the effect of edge roughness on the properties of a transmission line. Variations in line width caused by edge roughness will alter the local characteristic impedance of the line, which could lead to generation of reflections or spurious modes. In order to minimise these effects, the ratio of line

width to edge roughness should be kept as large as possible. For a 16.2 μm, 50 Ω line, a not unreasonable edge roughness of 0.5 μm would generate errors on the width and impedance of $\pm$ 3 % and $\pm$ 2 % respectively, and therefore this line may be too narrow. Figure 3.1 shows electromagnetic simulations performed for several transmission line widths between the upper and lower limits set for this design.

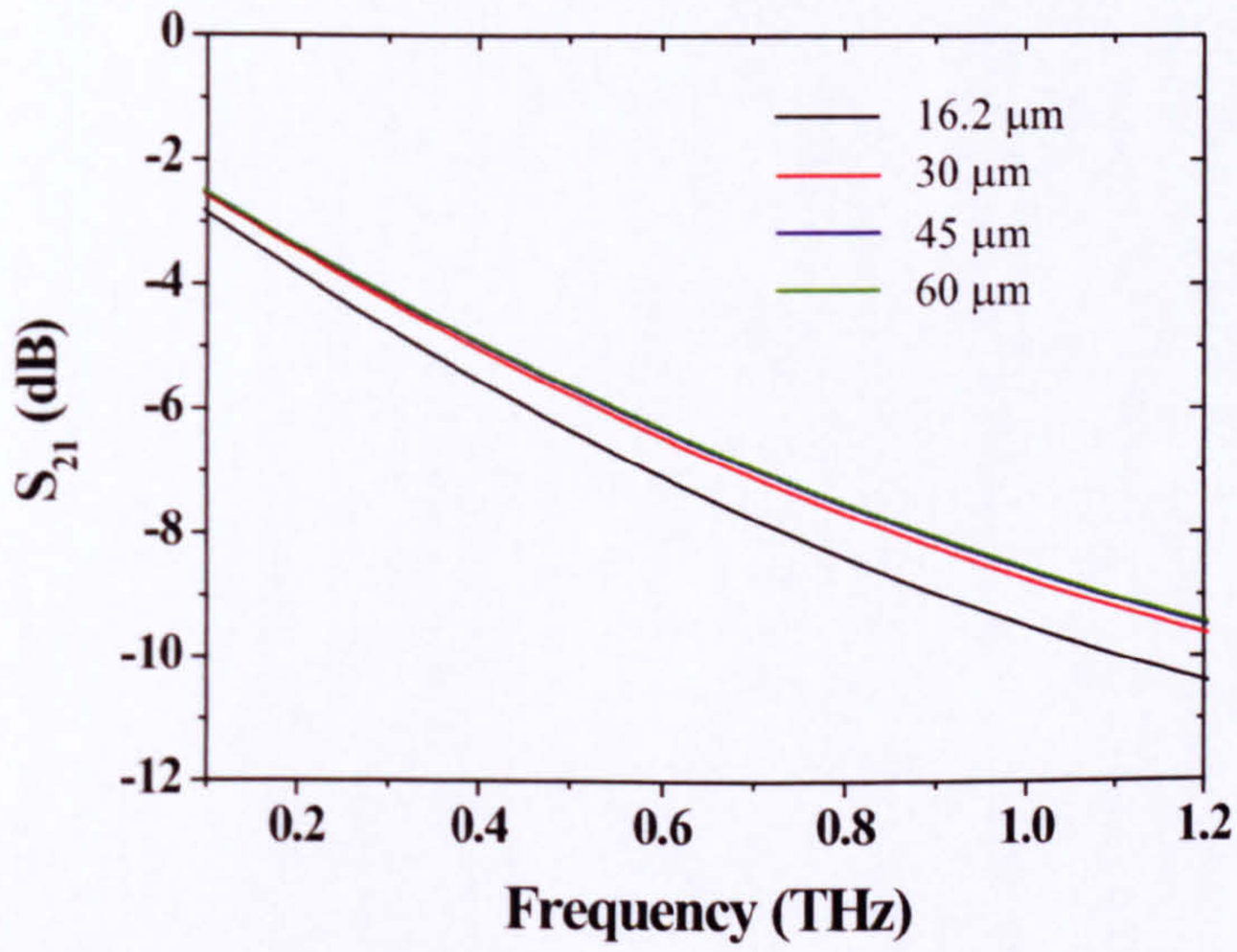

Figure 3.1: Electromagnetic simulations of the transmission characteristics for varying transmission line widths on 6 μm BCB dielectric, performed in Sonnet [88].

The software used to simulate S_{21} parameters in this work was called Sonnet [88], a high frequency electromagnetic simulator using a method of moments technique to solve Maxwell's equations. Verification of the simulation accuracy was confirmed by comparison with two other simulation packages: HFSS, which uses a finite element method to solve Maxwell's equations, and Momentum, a 2D electromagnetic solver. The finite element method used in HFSS, whilst very accurate, becomes prohibitively slow when considering the topologies used in this study. Conversely, whilst Momentum is much faster, it is not designed for use at THz frequencies and also cannot simulate three dimensional structures. Therefore, Sonnet was chosen for use as it maintains the accuracy of HFSS whilst significantly reducing simulation times for the devices used here. The method

used to characterise the loss was to simulate a simple transmission line structure with no filter elements present, mounted on the surface of a BCB dielectric. Simulations were performed at differing line widths, including that corresponding to 50 Ω impedance (16.2 μm) up to 60 μm (just below the upper limit of 67 μm). In order to be able to draw comparisons with existing data from the literature, a line width of 30 μm was included in simulations (as used in [59]) and line thickness was maintained at 250 nm. The differences in loss shown in Figure 3.1 display an increase in attenuation with characteristic impedance as expected. The 30 μm, 45 μm and 60 μm lines all generate similar losses, suggesting that the choice of any of these widths is not critical. A width of 30 μm was therefore chosen, to allow comparison of transmission characteristics with existing publications [59].

3.1.2 THz Filter Designs

As discussed previously, the electrical resonance produced by a quarter wavelength stub is controlled by the stub dimensions. Whilst the length of the stub controls the central frequency of resonance as discussed in Chapter 2, the stub width has an effect on the full-width-half-maximum (FWHM) of the rejection region. Since a change in frequency position of the band stop region provides spectroscopic information on an overlaid dielectric material, it would be advantageous to produce a sharp leading edge (i.e. a narrow filter response) for precise measurements. Reducing the width of the filter stub correspondingly reduces the width of the band stop region, but also increases conductor losses in the device which reduces the filters rejection depth. Figure 3.2 shows Sonnet simulations of quarter wavelength stubs resonant at 600 GHz, varying from the chosen transmission line width (30 μm) down to 5 μm. Below this width, optical lift-off would become more difficult and the ratio of edge roughness to filter width would be significant. The simulated data in Figure 3.2 shows the bandwidth decreasing with stub width as predicted. A width of 5 μm was chosen for two main reasons: firstly, as discussed earlier, this width provides the sharpest resonant feature whilst remaining optically de-

finable and maintaining a reasonable edge roughness to width ratio; secondly, the reduction in active area (i.e. the surface area of the stub) correspondingly reduces the sample volume required for spectroscopic measurements, one of the main advantages of using an on-chip approach.

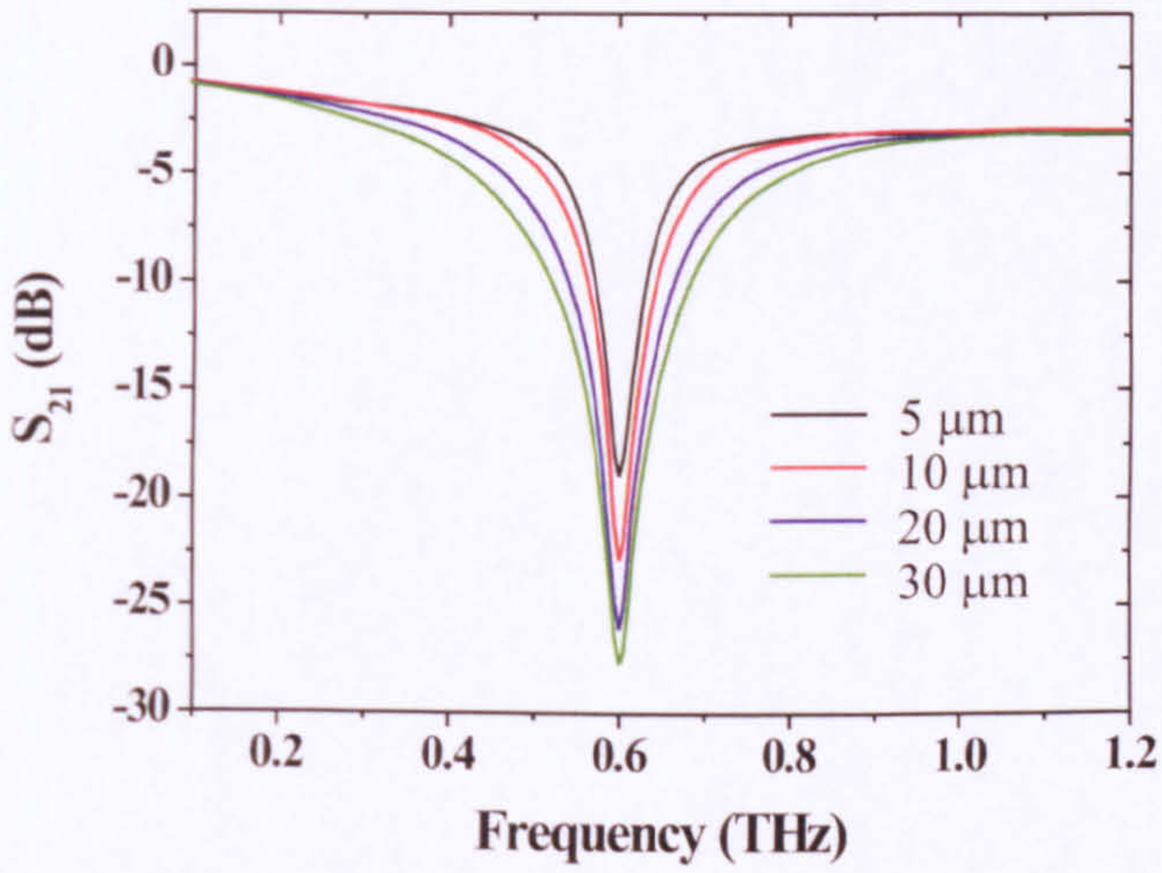

Figure 3.2: Simulations of the transmission characteristics for quarter wave stub filters of varying widths.

A major advantage of this filter topology over those used in existing devices, is the ability to incorporate more than one stub on the same transmission line. Rather than having these stubs resonate at the same frequency (which would further narrow the bandwidth and increase the rejection depth), it was decided to use stubs of differing length and therefore different resonant frequencies. Two main reasons supported this decision; firstly, having several resonators of the same size would, whilst improving the overall filter characteristics, mean that spectroscopic samples would need to be applied to all stubs to produce equivalent resonant shifts in each, thus increasing the sample volume required. Secondly, using different filter sizes would allow us to assess interaction of overlaid materials at several different frequencies simultaneously.

Three main considerations determined the chosen stub lengths (and therefore

resonant frequencies) for each filter. Firstly, the filter resonances must lie within the operational bandwidth of the system, estimated to be ≈ 1.4 THz (see Chapter 4). Secondly, isolation of each filter response within the frequency domain is critical when performing individual measurements on separate filters. Finally, the predicted presence of third harmonics for each filter (Chapter 2, Section 2.2.3) mean that lower frequency devices should be designed such that their harmonics do not spatially interfere with resonances of higher frequency filters. Preliminary stub lengths of 82 μm (600 GHz), 138 μm (350 GHz) and 194 μm (260 GHz) were chosen, with the closest third harmonic (of the 260 GHz resonator) lying at 780 GHz. The simulated response for a transmission line containing all stubs is shown in Figure 3.3. These simulations were performed for a line length of 1 mm to reduce computation time, and are compared to a transmission line structure of the same length, containing no resonant structures.

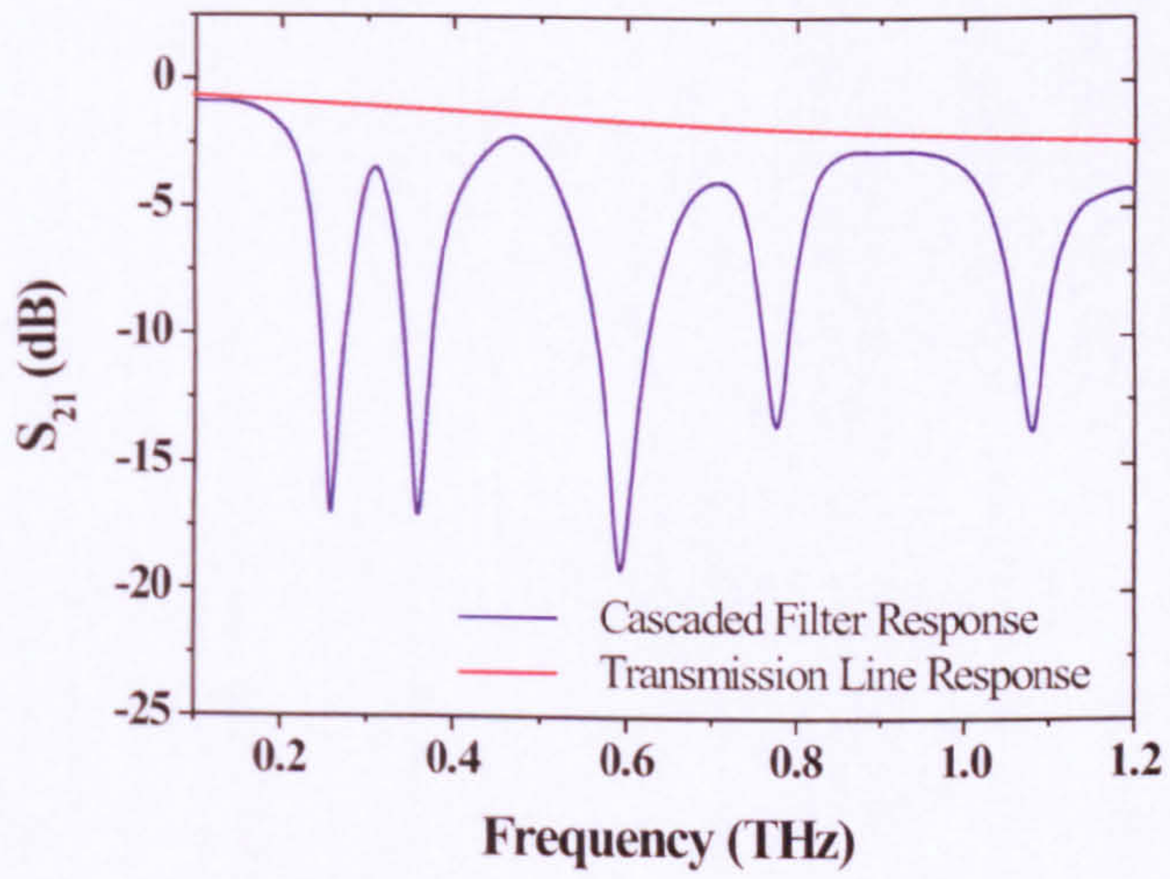

Figure 3.3: Transmission characteristics for a 1 mm transmission line with resonating bandstop stub filters at 260, 350 and 600 GHz, showing third harmonics for the first two stubs at 780 GHz and 1.05 THz respectively.

The simulation shows the resonant features occurring correctly at the desired frequency positions, and also identify the predicted third harmonic of the lowest frequency stub, lying at 780 GHz. Ideally, the signal would return to the loss ex-

hibited by the transmission line in Figure 3.3 after each band rejection area. The simulations however, infer that subsequent resonances begin before the previous is fully complete, but overlap is not sufficient to obscure either the leading edges or the resonance minima of each response. We also notice a slight disparity in the loss exhibited between the non-resonant parts of the filter cascade, and that of the interconnect. This arises from the insertion loss of the filters, which is defined as the ratio of the signal voltage transferred from source to load without filters present, to that transferred with filters inserted between.

3.2 First Generation Device Designs

With the central THz interconnect fully parametrised and individual filters designed, the final step was to provide contact points for connections between the device and external circuitry. The basic design for each device assumes the parallel probe layout suggested in Figure 1.13, Chapter 1. The design was modified so that the contact pads for the probe arms and transmission lines were aligned for ease of electrical access (Figure 3.4). A 4 mm separation between switches was chosen to allow integration of multiple filter devices with sufficient separation to avoid cross coupling.

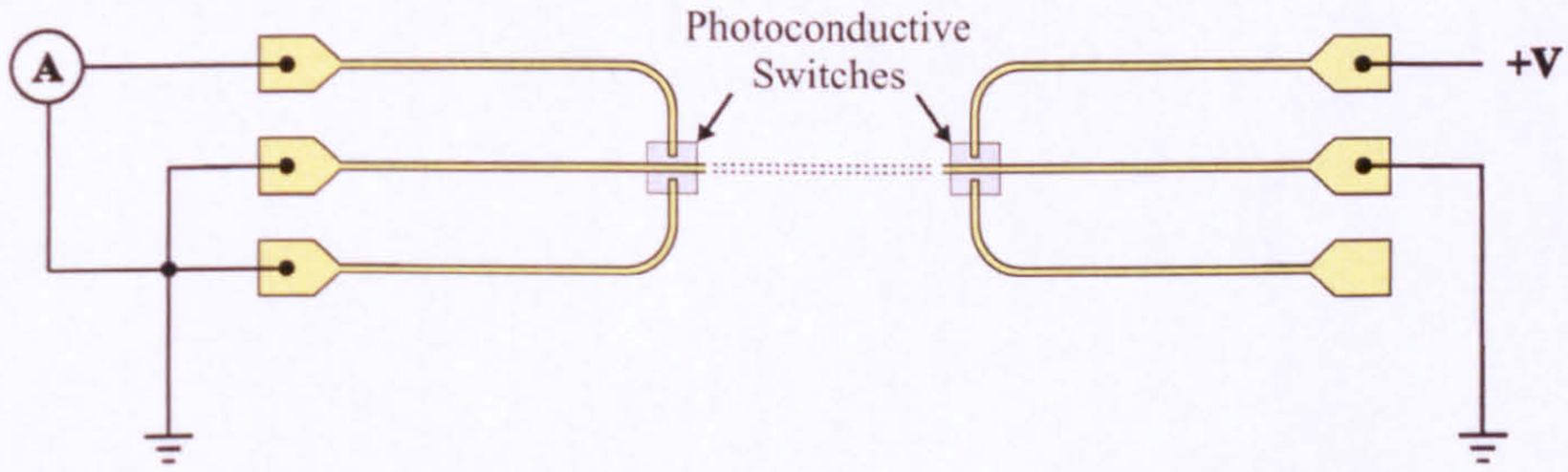

Figure 3.4: Schematic of the transmission line topology used, containing a central transmission line and four converging probe arms, separated by a switch gap.

A total of four probe arms were integrated into the design, two on either switch, to allow input and output measurements to be made, and for redundancy in the event of defects formed in the probe arms during fabrication. The bias connec-

tions in Figure 3.4 show the arrangement necessary for performing output pulse measurements (discussed in Chapter 4).

Typically, photoconductive switches are operated close to their breakdown voltage to maximise output power, where the breakdown field is usually $\geq 5 \times 10^5$ V cm^{-1} [89]. The breakdown voltage of the BCB dielectric has been measured to be 5.3 $\pm$ 0.2 $\times$ 10^6 V cm^{-1} [84] which, for a 6 μm thick layer restricts the maximum operating bias to $\approx$ 3 kV. It was decided that the switch gap, s, in Figure 3.5 could be no less than 5 μm to prevent difficulties in fabrication using optical lithography, which limited the maximum potential across the switch gap, prior to LT-GaAs breakdown, to 250 V.

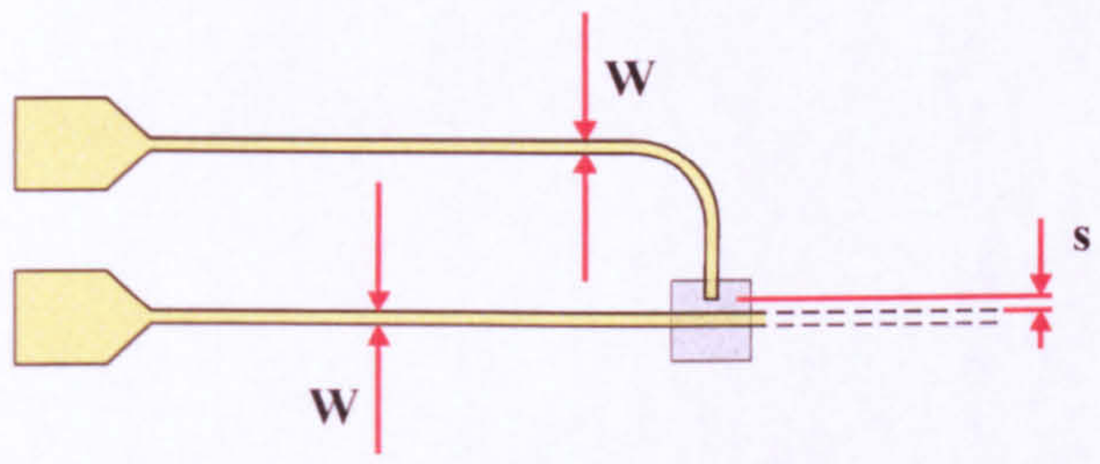

Figure 3.5: Enhanced view of the switch region showing the switch gap, s = 5 μm, and the transmission line and probe arms widths, both W = 30 μm.

The preliminary mask set for the first generation designs contained a selection of straight interconnects between photoconductive switches, individual filters and combinations of two or three filters cascaded on a single interconnect (Figure 3.6).

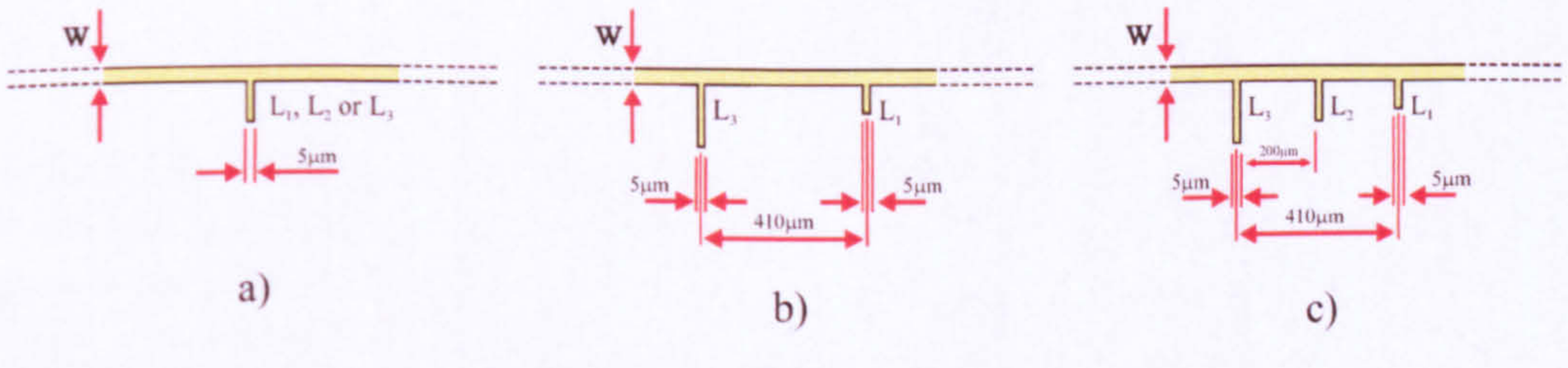

Figure 3.6: Schematic showing a) an individual filter, b) the two outside filters and c) all three elements cascaded on the interconnect. Each resonant element is spatially separated from its neighbour by 200 μm to avoid cross coupling, and lengths L_1, L_2 and L_3 represent the 600 GHz, 350 GHz and 250 GHz filter elements respectively.

This allowed characterisation of each filter, and independent measurement of

the transmission line at THz frequencies. The photoconductive switch geometry is shown in Figure 3.7, and consists of 50 μm square LT-GaAs regions. The probe arm and transmission line overlap of the LT-GaAs region was kept to a minimum to avoid large areas of high permittivity wave guide, which would deteriorate signal propagation. A probe arm overlap of 5 μm left sufficient leeway for alignment in the event of imperfect switch formation. The 'active region' of the transmission line is regarded as the 4 mm length between the two switches. The line was further extended beyond this region by a length of $l_p = 2.4$ mm to square bond pads of side 200 μm.

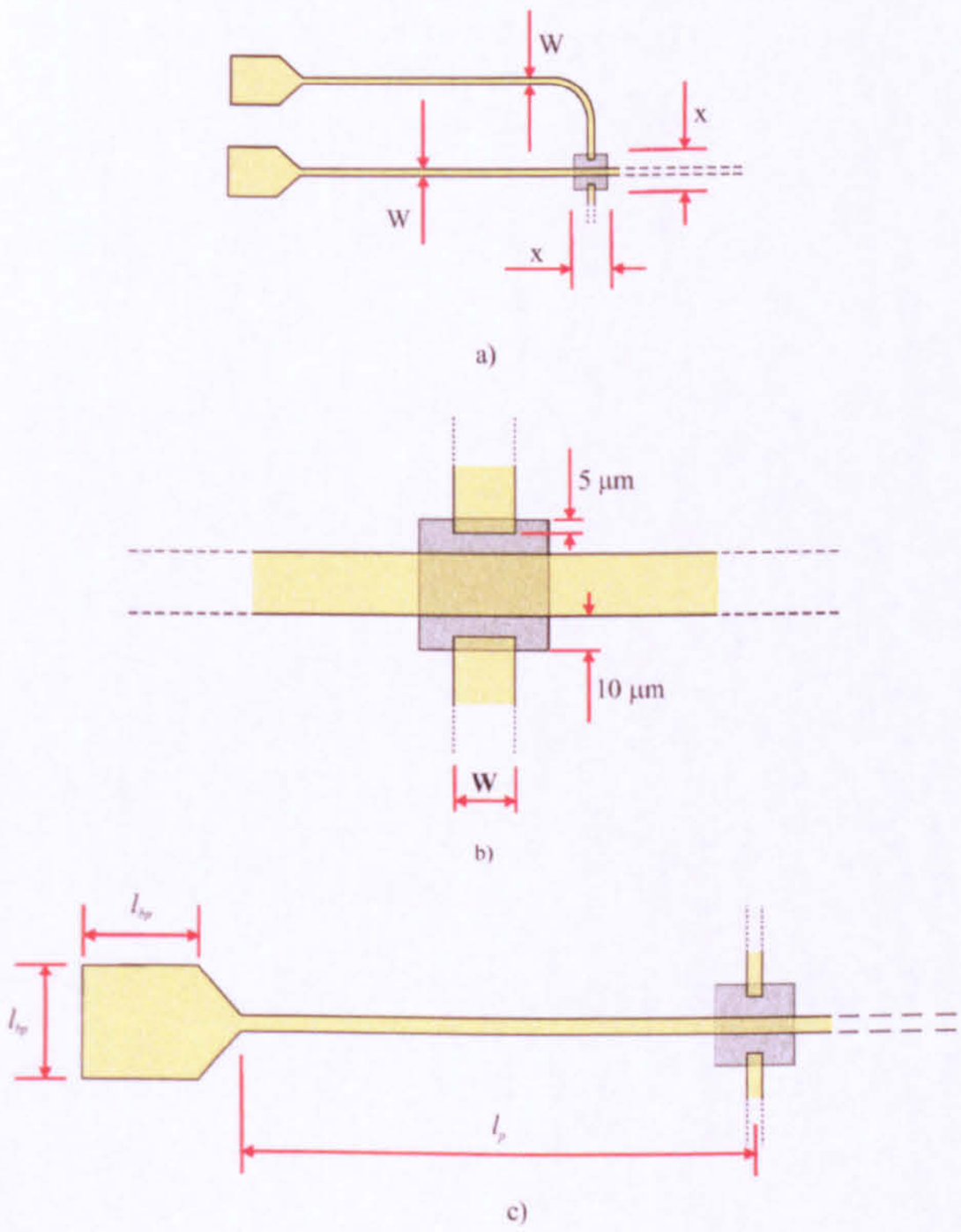

Figure 3.7: Profiles of a) a square LT-GaAs switch of side x = 50 μm with 30 μm probes and interconnect, b) an enlarged image of the switch showing a 5 μm overlap between the probe arms and switch, with a 5 μm separation from the interconnect, and c) The 'non-active' region of the transmission line, where $l_p = 2.4$ mm is the distance from switch to bond pad, and bond pads of side $l_{bp} = 0.2$ mm.

During measurements performed on several transmission lines and filters described by the above designs, the presence of several undesired features in the time domain signal were noted. These appeared after a short delay with respect

to the main THz pulse (see Chapter 4). The origin of these features were attributed to signal reflections, calculated to arise from the bond pads at the ends of the transmission lines. In order to investigate and confirm this experimentally, the first generation designs were slightly modified by increasing the length of the non-active transmission line region from 2.4 to 4.8 mm, with the anticipated result that the first reflection would experience twice the delay seen in prior devices. To fully utilise the new mask set and take advantage of the measured 1.2 THz bandwidth, filter designs of 60 μm, 47 μm and 38 μm were introduced, corresponding to resonances of 800 GHz, 1.0 THz and 1.2 THz respectively. All filters were maintained with a 5 μm stub width.

3.3 Second Generation Device Designs

Second generation devices were designed to remove problematic signal reflections discovered in the first generation, which arose from the short circuit terminations at the end of the transmission line and probe arms. When performing fast Fourier transforms (FFTs) of the time domain data, the presence of reflections leads to regular oscillations in the frequency domain, which can obscure important features. The arrival of the first reflection at a certain delay after the THz signal therefore marks the maximum sampling window available for measurements, and this has direct consequences for the resolution of the FFT. For the previous designs, this resolution was too low to be able to resolve small shifts produced by low permittivity dielectric loads, such as DNA. Figure 3.8 shows the simulated response of a 0.6 THz filter under application of dielectric loads corresponding to the permittivities, ϵ_r, of hybridised and denatured DNA samples, measured at 1.4 and 1.1 respectively [90].

There are several potential methods which may be used to remove these reflections, such as radiation of the unwanted signal via a broadband antenna, attenuation of the signal using a highly absorbing load, or lengthening of the non-active regions to delay the arrival of the reflection sufficiently to produce high resolution

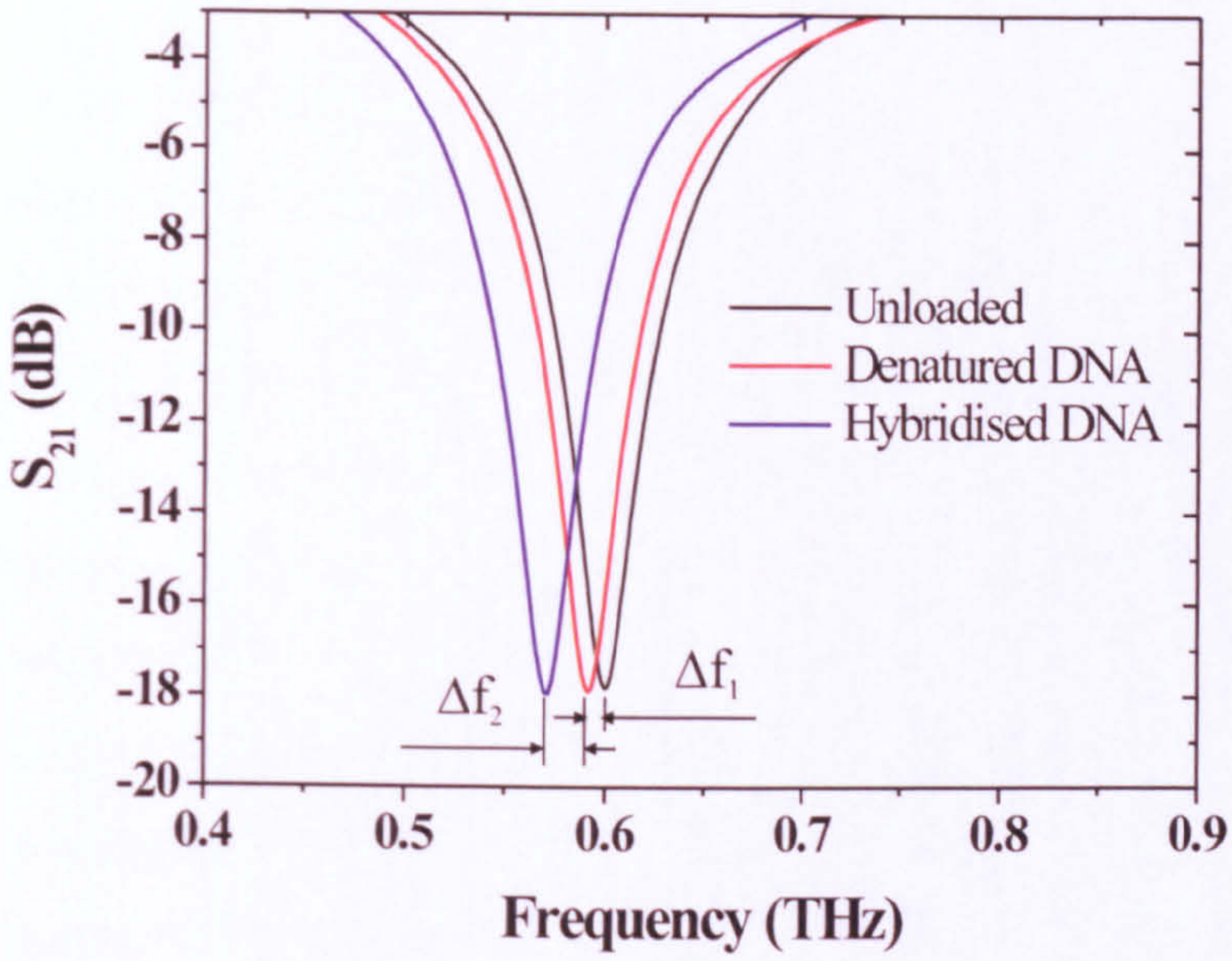

Figure 3.8: Simulated resonant frequency shifts of a 600 GHz filter under application of 10 μm thick dielectric loads of permittivity 1.1 and 1.4, representing denatured and hybridised DNA respectively, with frequency shifts Δf_1 and Δf_2 of 8 GHz and 20 GHz respectively.

FFTs. Of these three solutions, only the latter was considered immediately feasible. A broadband antenna would likely require patterning of the ground plane beneath the dielectric material. Since the BCB layer is formed by spin coating, a profiled ground plane would lead to ripples within the BCB which would alter the thickness of the dielectric layer between the subsequently evaporated microstrip structure and the ground plane. This would change the local dielectric environment around these ripples and produce unwanted reflections, whilst also potentially affecting the quality of lift-off achieved. Application of an absorbing medium to the non-active regions may also be problematic, since few materials exhibiting sufficient absorption across a broad frequency range (0.1 - 1.2 THz) have been characterised or would be suitable. Due to high attenuation of THz radiation in polar liquids, a material such as water would perform the function, but use of a liquid phase absorber is not practical for electrical measurements.

Lengthening of the non-active regions was therefore deemed the most appropriate approach to delay the unwanted signal reflections.

We can see from Figure 3.8 that the required resolution to allow distinction between the two overlaid materials of a thickness which saturates the filter response ($> 4\ \mu m$) is of the order of 8 GHz. However, to produce frequency-shift curves for thicknesses below saturation, a resolution of 2 GHz was deemed more appropriate. The maximum frequency, f_{max} generated by the FFT algorithm used is given in (3.1) and depends on the time step, Δt, between successive data points and the total number of data points used. If there are N input data points, the frequency domain will also have N points spread between $-f_{max}/2$ and $+f_{max}/2$. Therefore, a sampling window of 20 ps in which 2048 data points separated by 10 fs are measured, will produce a frequency spread between -50 and +50 THz with a resolution of 50 GHz.

$$f_{max} = \frac{1}{\Delta t}\left(1 - \frac{1}{N}\right) \tag{3.1}$$

For the majority of FFT algorithms to function correctly without the software applying automatic zero padding or data truncation, the total number of samples taken must be a power of 2, and must be equispaced in the time domain. FFT algorithms which do not have this requirement are much more computationally intensive and not suitable for real time spectroscopic analysis. If we reduce the number of measured points in the 20 ps time window to 1024, increasing the sampling time to 20 fs, the frequency spread narrows to between -25 and +25 THz, which may at first be considered an improvement. However, we now only have half the data points to distribute in this frequency range and therefore the resolution remains at 50 GHz. It can be seen therefore, that simply varying the number of points taken in the same time window does not alter the FFT resolution. To achieve a 2 GHz resolution, (3.1) allows us to calculate a required time window of $\approx$ 500 ps. The length of transmission line required for this delay is calculated using this time and the phase velocity given in (2.13), yielding a

distance of ≈ 90 mm. However, since the signal must propagate along the line, reflect, and propagate back before detection, each non-active region of the device need only be half of this value.

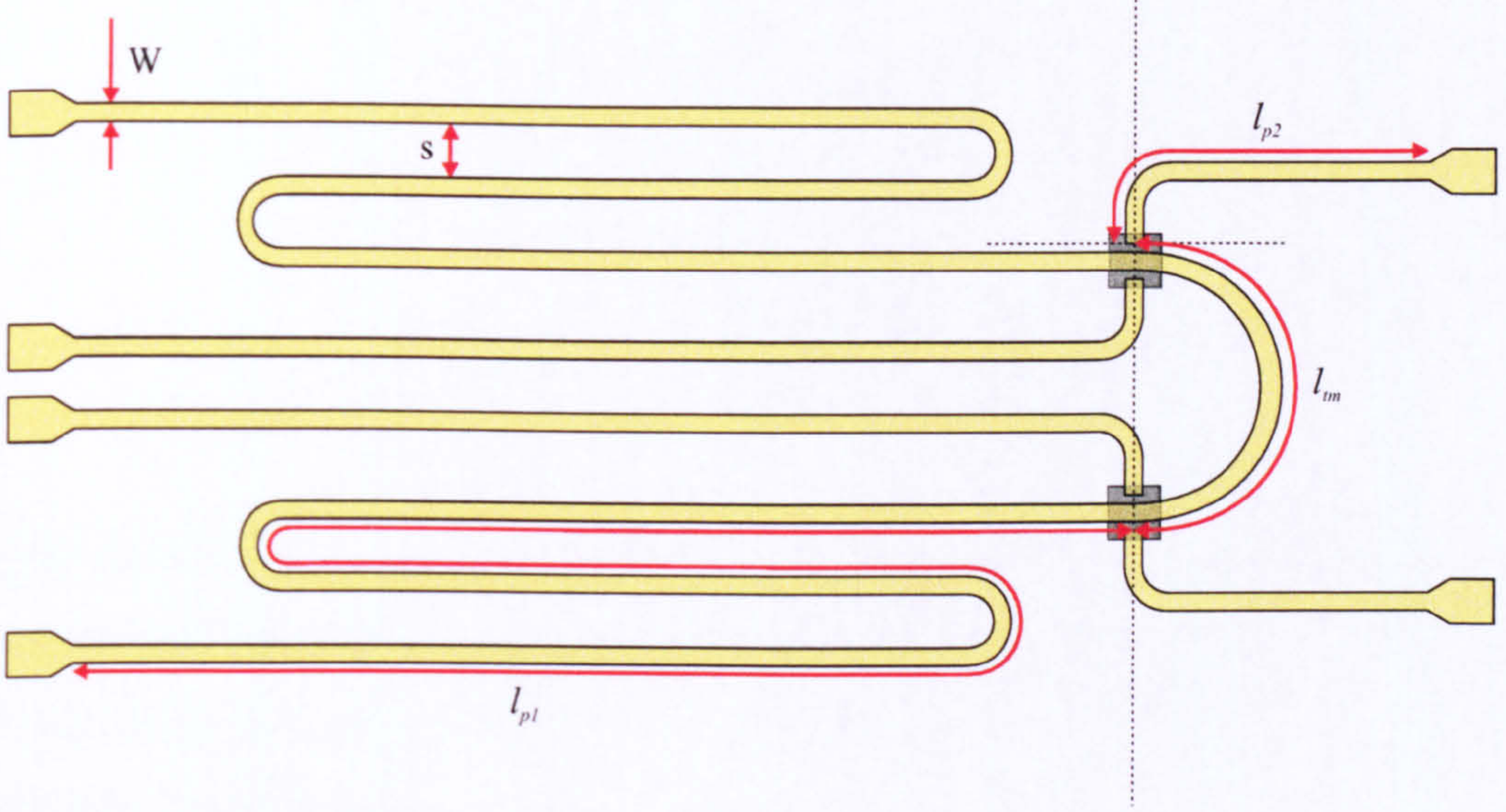

Figure 3.9: Diagram of the second generation curved transmission line and coiled probe arms of width W = 30 μm, with coil separation $s = 700$ μm. Probe arms have length $l_{p1} = 50$ mm and $l_{p2} = 6$ mm, with an active transmission line region of length $l_{tm} = 4$ mm

To improve packing density, the active region of the device was modified into a curved transmission line, as shown in Figure 3.9. The long, non-active regions followed a meandering path to the bond pad terminations, each section separated by 700 μm to provide ≥ 60 dB coupling loss, which means that no cross coupling will occur between the coils.

A second limitation of the first generation devices was revealed under application of dielectric loads onto a dual filter device containing 260 GHz and 600 GHz resonators (see Chapter 5). When loaded individually, the third harmonic of the 260 GHz filter was found to spatially interfere with the resonance of the unloaded 600 GHz, obscuring its response. To solve this problem, a new design for the lower frequency filters was devised using ABCD matrices. An ABCD matrix is a convenient way of describing a two port network, such as the devices used here.

The definitions for the ABCD parameters for a transmission line structure are given in (3.2). A full definition of these parameters is given in Appendix A.

$$\begin{aligned} A &= \cos\theta \\ B &= jZ_0 \sin\theta \\ C &= \frac{j\sin\theta}{Z_0} \\ D &= \cos\theta, \end{aligned} \tag{3.2}$$

where Z_0 is the characteristic defined in Chapter 2, and $\theta = \beta l$, the phase constant and the length of transmission line being considered respectively. The useful result of this is that the input impedance seen looking into a length of transmission line may now be written as

$$Z_{in} = \frac{AZ_l + B}{CZ_l + D}. \tag{3.3}$$

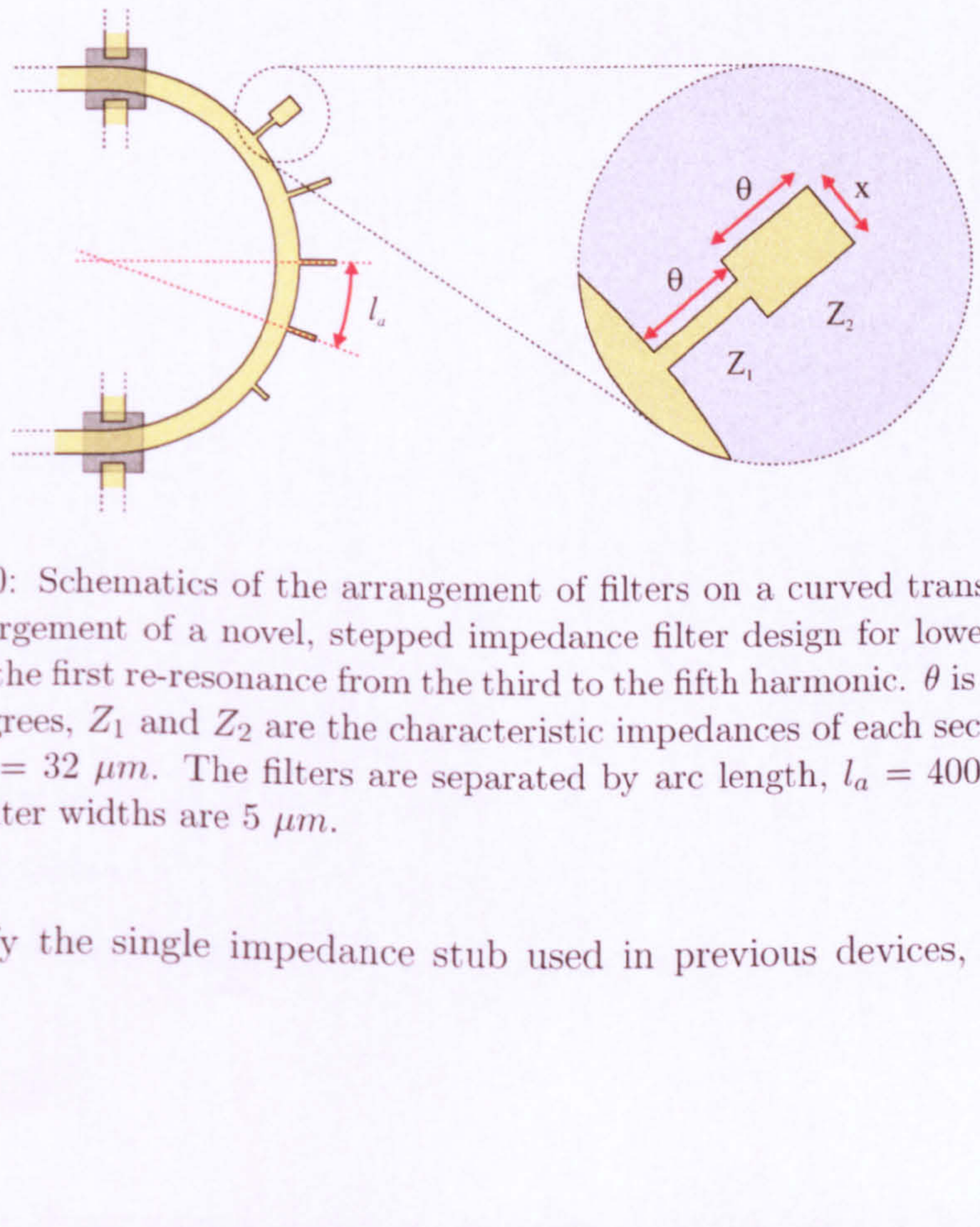

Figure 3.10: Schematics of the arrangement of filters on a curved transmission line, with an enlargement of a novel, stepped impedance filter design for lower frequencies which shifts the first re-resonance from the third to the fifth harmonic. θ is the electrical length in degrees, Z_1 and Z_2 are the characteristic impedances of each section, and the the width x = 32 μm. The filters are separated by arc length, $l_a = 400$ μm, and all unlabelled filter widths are 5 μm.

If we modify the single impedance stub used in previous devices, to the dual

impedance stub shown in the blow-up of Figure 3.10, it can be shown that an impedance ratio Z_1:Z_2 of 3:1, with an angle $\theta = 30°$ ($\equiv 59\ \mu m$) pushes the harmonic from three times to five times the fundamental frequency, which in the case of the 260 GHz filter is from 780 GHz to 1.3 THz. This design was therefore used for all low frequency filters in future devices. The second generation devices contained five cascaded filters operating at 260 GHz, 600 GHz, 800 GHz, 1 THz and 1.2 THz, arranged on the curved transmission line as shown in Figure 3.10.

3.4 Third Generation Device Designs

Fabrication and testing of the second generation devices revealed a significant (50 %) decrease in the system bandwidth, reduced from $\sim$ 1.2 THz to $\sim$ 600 GHz. Whilst simulations suggested that the transmission loss of the curved transmission line was only negligibly greater than its straight counterpart, the increased loss was initially attributed to the presence of the curved interconnect. The length of the active region in this case was calculated for the central path around the arc. If instead we calculate the inner and outer arc diameters of this region, we generate values of 3.953 mm and 4.047 mm respectively. This corresponds to a path difference of 94 μm, or 0.5 ps calculated from the phase velocity of the transmission line. This induced broadening, added to the normal line dispersion, was thought to explain the decreased bandwidth. Since the second generation devices achieved the desired FFT resolution, the third generation retained the lengthy non-active regions, but modified the active region to return it to its original linear form. Such a device is shown in Figure 3.11.

Confining the THz pulse to a linear active region should produce similar results to those obtained in the first generation devices, but at the much higher $\leq$ 2 GHz resolution of the second generation devices. The device in Figure 3.11 also shows tapered probe arms which were introduced to improve metal lift-off, which became very difficult for the second and third generation devices due to an aspect ratio of 1:120:400,000 corresponding to metal thickness, transmission line width

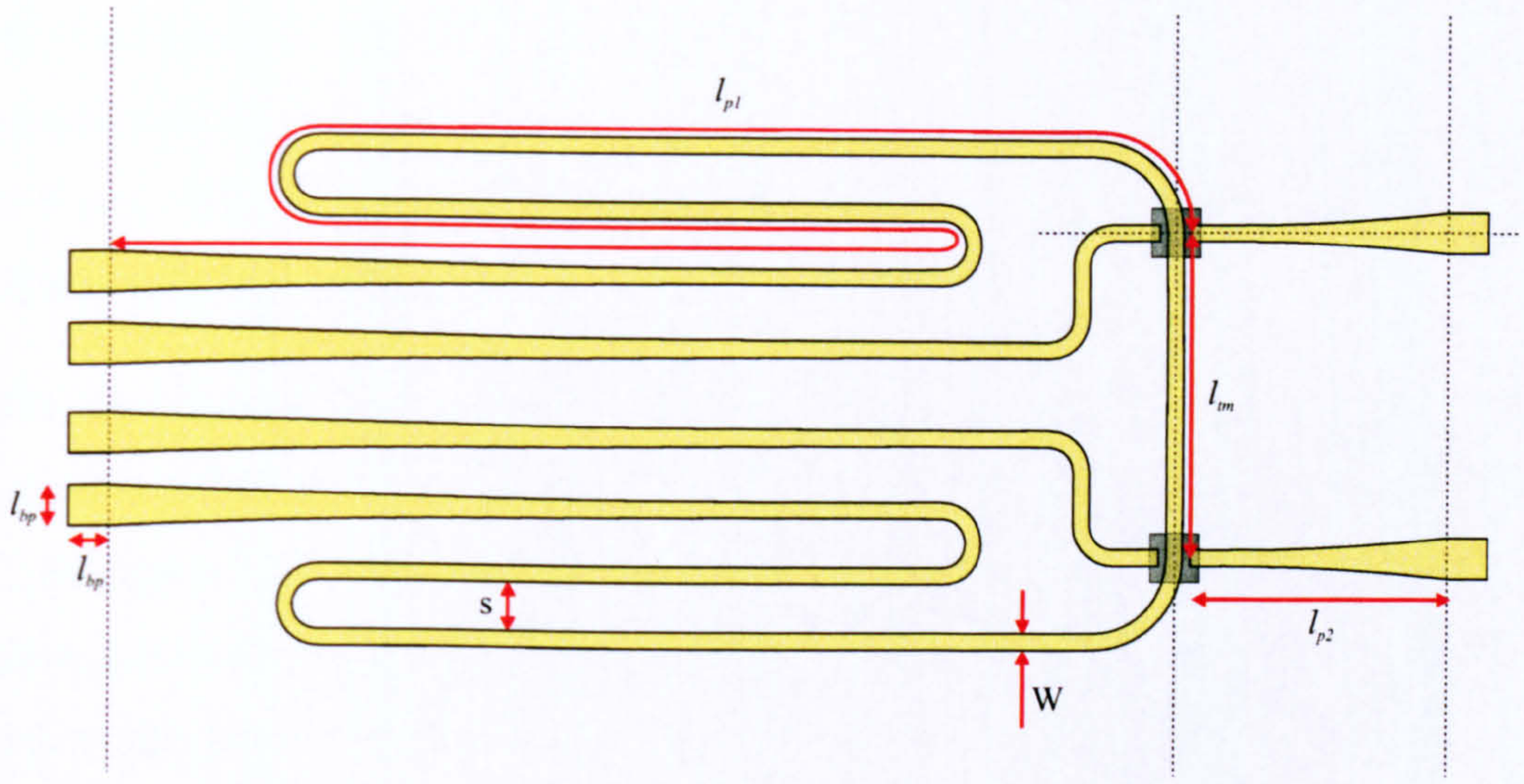

Figure 3.11: Schematic of a third generation filter device of width $W = 30\ \mu m$ flaring out to the bond pad width, $l_{bp} = 200\ \mu m$, separation $s = 700\ \mu m$. Probe arms are of lengths l_{pl} and l_{ps} of 50 mm and 6 mm respectively, and with a linear active region of length $l_{tm} = 4$mm.

and the main THz interconnect length.

3.5 Device Fabrication

Each generation of devices was fabricated using the same cross section of materials. Initially, a 25 nm layer of Ti, followed by a 500 nm Au ground plane were thermally evaporated onto a 4 inch silicon (Si) wafer. The wafer provides a rigid support for the devices without being electrically coupled to the microstrip structure. The BCB dielectric, obtained from DOW Chemicals under the brand-name Cyclotene^{TM}, is pipetted onto the gold surface and is dynamically spread at 100 rpm for 5 seconds on a spin coater, then ramped to 500 rpm for 10 seconds to ensure even coverage of BCB on the wafer. The speed is then further ramped to 2000 rpm for 30 sec to produce an 8.4 μm layer thickness. The chip is then pre-baked at 80 °C for 90 seconds to drive out residual solvent, before being transferred to a vacuum oven. The oven must be purged to $\leq$ 100 ppm O_2 using an inert gas such as nitrogen, to prevent oxidation of the material during

the cure process. The oven is ramped to a final temperature of 250 °C, which is maintained for ≈ 2 hours for a hard cure and produces a final film thickness of ≈ 6 μm. The dielectric and ground plane are now ready for fabrication of the photoconductive switches.

The photoconductive switches are made from low-temperature grown gallium arsenide (LT-GaAs), formed by molecular beam epitaxy as discussed in Chapter 1, Section 1.4.2. However, the growth substrate was modified by replacing the heterostructure in Figure 1.14 with simply a 100 nm AlAs layer between the epitaxially grown, 250 nm thick LT-GaAs and the GaAs support wafer. After cleaving to an appropriate size, black wax is deposited onto the thin film to provide support (see Figure 3.12) and allow film manipulation once it is removed from the growth structure. Prior to thin-film separation, excess material which is not directly supported by the wax is non-selectively etched in a 1:8:40 solution of H_2SO_4:H_2O_2:H_2O at a rate of 1.2 μm / min for one minute. The AlAs layer is subsequently etched away in a 1:10 solution of HF:H_2O at 0 °C for 24 hours. The slow etch rate is required to minimise the rate of production of the reaction by-product H_2 gas which, if produced at high rates, can cause cracking of the film. Upon completion of the etch, the etch solution is diluted to allow safe removal of the fragile thin film by pouring into a container, where the film is supported on the water meniscus. The film may then be transferred, using a vacuum tool, to the surface of the BCB dielectric, where it is subjected to a pressure of ≈ 20 kPa for 24 hours to aid in removal of trapped air and water via capillary action, and in adhesion to the BCB surface by Van-der-Waals forces between thin film and dielectric [46].

The wax may then be carefully removed from the thin film by immersion into trichloroethylene, followed by drying in an N_2 gas flow. Application of S1813 positive photoresist at 5000 rpm creates a 1.2 μm layer thickness after baking at 115 °C for 60 seconds. The device is then mounted in a mask aligner under the appropriate switch mask, which contains opaque chrome areas corresponding to the photoconductive switches, aligned to the thin film region. Following UV

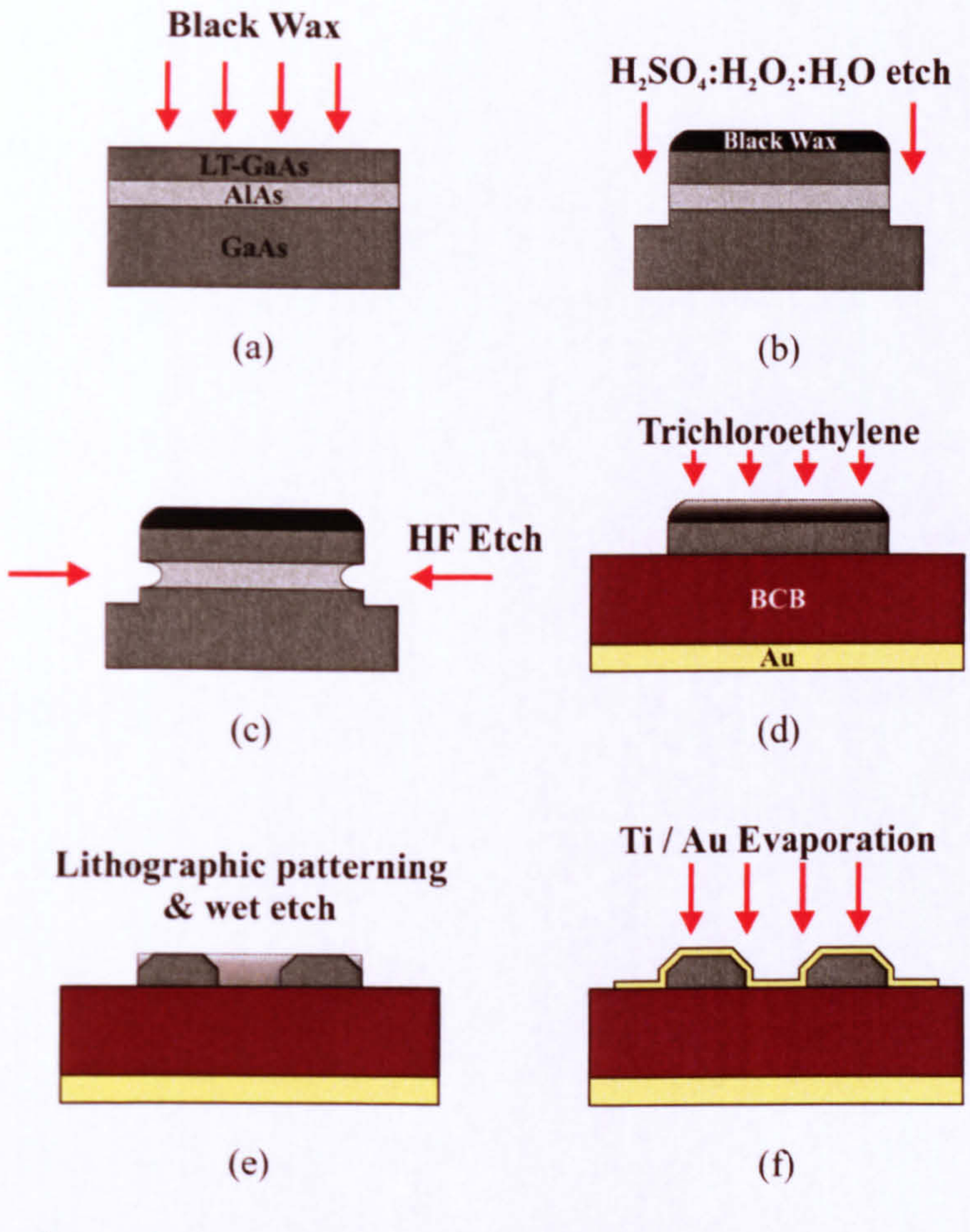

Figure 3.12: A set of schematic diagrams for the fabrication procedure used to construct the LT-GaAs photoconductive switches on BCB dielectric, showing a) black wax deposition onto the growth heterostructure, b) non-selective etching of excess material, c) selective etching of the AlAs release layer, d) removal of the wax in trichloroethylene following transferral to the BCB dielectric, e) patterning of the switches after deposition, exposure and development of photoresist and f) thermal evaporation of the overlaying THz waveguiding structure.

exposure ($\lambda = 450$ nm for 4.5 seconds at 8 mW / cm^2), the resist is developed for $\approx$ 1 minute in MF-319 developer, rinsed in deionised water and dried under N_2 gas flow, leaving protective squares of photoresist over the regions of LT-GaAs which will form the photoconductive switches. The excess material is etched in a 1:8:1000 solution of H_2SO_4:H_2O_2:H_2O at a rate of 40 nm / sec, chosen to produce photoconductive switches with 45° edge profiles to avoid breakage of overlaid metallic layers. This process has been developed specifically for this project and is the first known use of photoconductive thin-film transfer in the UK. The whole

process is described graphically in Figure 3.12.

Once the switch fabrication is complete, the device is ready for deposition of the waveguiding structure, consisting of 25 nm Ti surmounted by 250 nm Au, as discussed in Section 3.1.1. Two methods were used for this stage of the fabrication, the second being introduced due to complications arising from equipment and chemical failure involved with the preliminary technique. Both techniques will be discussed here.

3.5.1 Chlorobenzene Lift-off Process

The positive photoresist, S1813, was used again for this stage of fabrication. The same resist deposition parameters are used as for the switch fabrication step, followed by careful alignment of the mask containing the transmission line structures with the switches on the BCB dielectric. The exposure parameters also remain the same, but upon completion of exposure the device is immersed into chlorobenzene for $\sim$ 2 minutes. The chlorobenzene chemically hardens the surface of the resist making it less susceptible to the MF-319 developer.

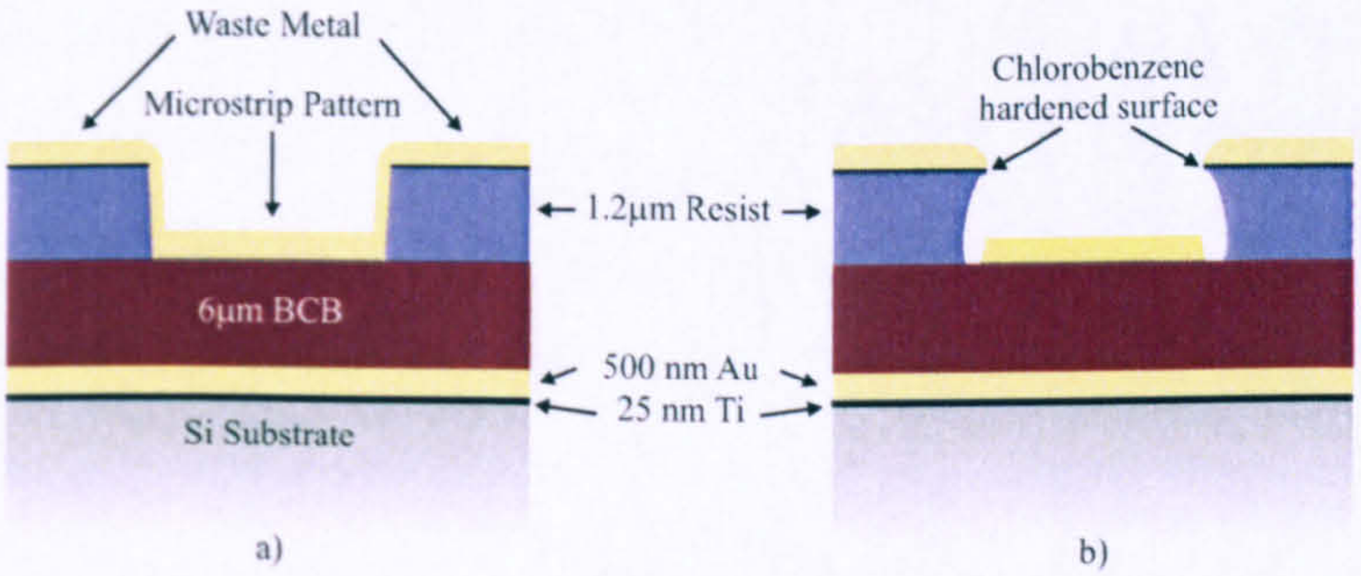

Figure 3.13: Representation of the difference between a) direct lift-off with no undercut causing metal linkage and b) lift-off subsequent to a chlorobenzene induced undercut to prevent metal linkage.

Once dried, the sample is transferred into the developer where, due to the hardened resist surface, it forms an undercut profile in the UV exposed regions. The undercut helps prevent metal linkage between the evaporated transmission line

structure and the excess material evaporated onto the surrounding photoresist (Figure 3.13).

3.5.2 Dual Layer Lift-off Process

This technique uses a different lift-off approach, which removes the chlorobenzene step and introduces two new photoresists; PMMA (poly-methyl-methacrylate) and S1805, a less viscous version of S1813 which forms thinner layers. The exact form of PMMA used had a molecular weight of $M_r = 495,000$ at 8 % concentration in Anisole.

In this process, the PMMA is spin coated at $\sim$ 4000 rpm to produce a 500 nm thick layer over the device and immediately transferred to an oven to bake for $\sim$ 2 hours at 170 ° C. The S1805 resist is spun onto the surface of the hardened PMMA at 2000 rpm to produce a 200 nm thick layer, which is baked at 115 °C for 60 secs to remove residual solvent. The S1805 is aligned with and exposed through the transmission line mask in an identical fashion to that used in the chlorobenzene process, and is then developed in MF-319 for $\sim$ 40 seconds (note there is *no* chlorobenzene step here). The device is then placed in a deep-UV source (λ = 250 nm) for 16 minutes, which exposes the PMMA through the S1803 which acts as a mask, and is then over-developed in a mixture of 1:3 MIBK:IPA devlopers for 70 seconds to create a large undercut beneath the S1805 resist. This process is shown diagramatically in Figure 3.14.

Whichever of the described lift-off processes is used, the subsequent metal evaporation is identical. In order to promote adhesion between the Ti layer evaporated onto the BCB dielectric, the surface undergoes a passive argon plasma process under vacuum, which removes a monolayer of organic residue which forms on the BCB surface in atmospheric conditions. This can be performed in a thermal evaporator prior to metal evaporation, avoiding exposure of the device to air between the two steps. Once complete, 25 nm of Ti followed by 250 nm of Au

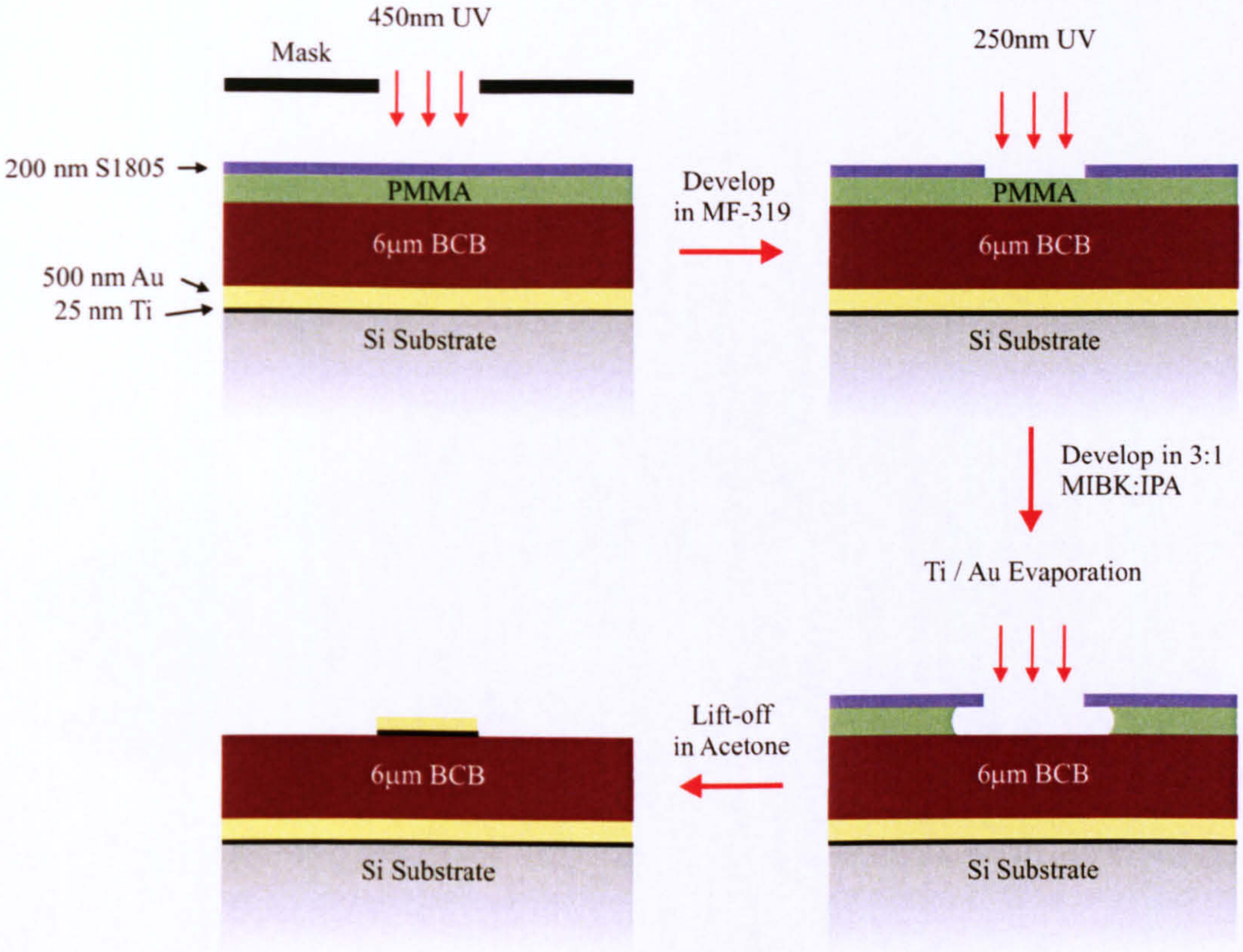

Figure 3.14: Diagram of the dual-layer lift-off process using PMMA and S1805 photoresists.

is evaporated onto the chip. Lift-off is performed in acetone, which removes the photoresist, and hence unwanted metal deposits from the chip surface, revealing the microstrip structure.

3.6 External Connections

Upon completion of fabrication, the device is mounted onto a copper printed circuit distribution board using highly insulating general electrical (GE) varnish.

Electrical contacts are made between the microstrip and the copper track by 17 μm diameter gold bond wire, as seen in Figure 3.15. Since wedge-bonding gold wire to copper track can be extremely difficult, small gold bond pads are first attached to the copper tracks using highly conducting silver epoxy, to which the

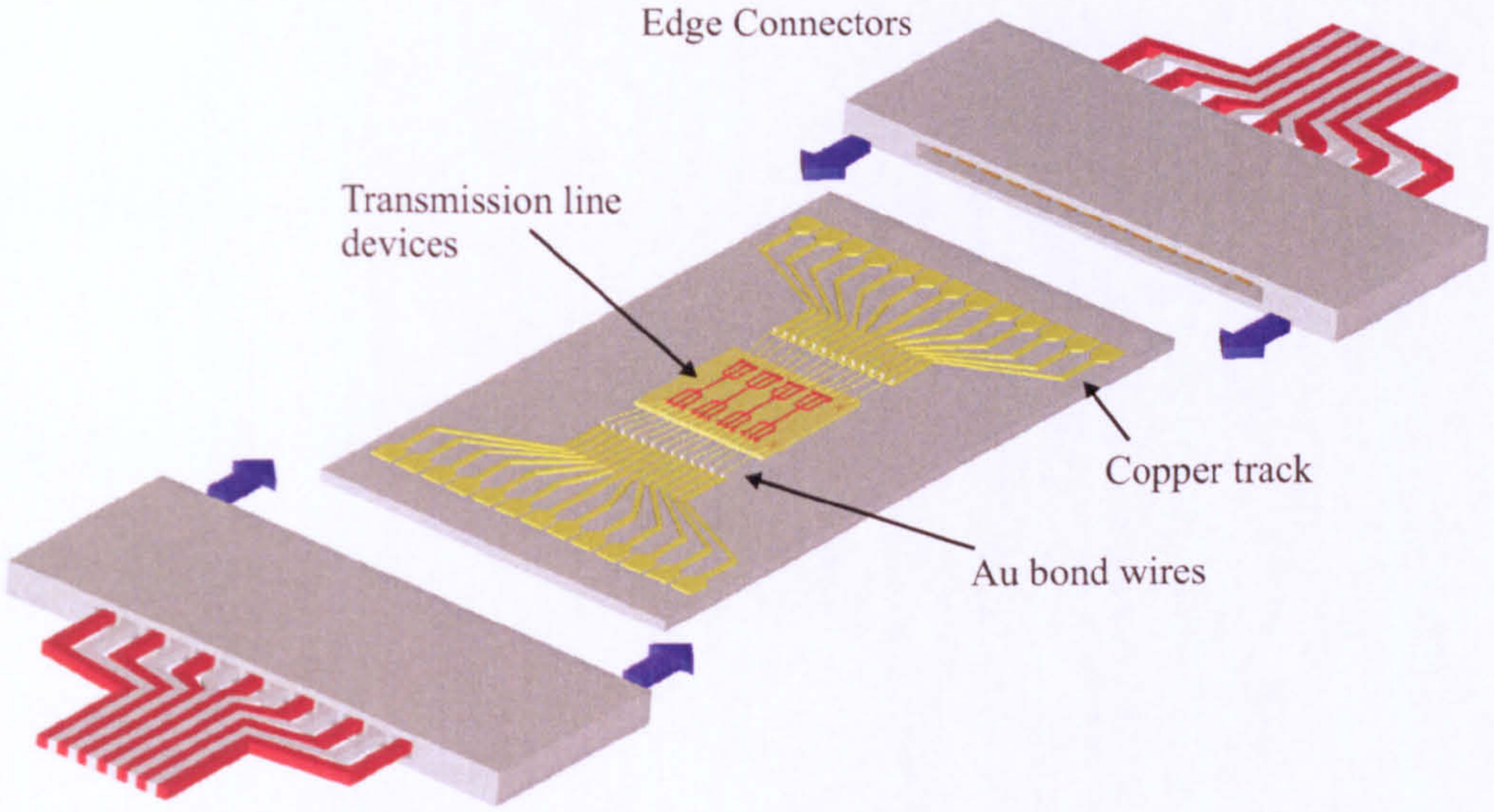

Figure 3.15: 3-d representation of an on-chip, THz microstrip transmission line device mounted on a PCB distributor.

bond wires may then be attached. The whole circuit board is now ready to be mounted in the optical setup described in Chapter 4.

Chapter 4

Photoconductive Switch and THz Interconnect Characterisation

4.1 Introduction

This Chapter will discuss the characterisation of 50 μm square, LT-GaAs photoconductive switches, fabricated using the technique described in Chapter 3 and developed specifically for this project, followed by a detailed study of the operation of first generation THz interconnects at both room and cryogenic temperatures.

4.2 Experimental Setup

The devices were characterised in an optical pump-probe setup using an 800 nm near-infrared (NIR), 80 MHz pulsed Ti:sapphire laser of pulse width $\sim$ 100 fs. The laser beam is split into two separate parts, named the *pump* and *probe*, using a beamsplitter placed at a 45° angle in the beam path. The pump beam passes along paths 6 - 8 in Figure 4.1 and is focussed directly onto a photocondcutive switch which becomes the source of the THz bandwidth transients generated in the on-chip system. The probe beam is passed along a delay line via paths 1 - 5, before illuminating the second switch where the on-chip THz transients are

gated and detected using a lock-in amplifier. The exact switch illuminated by the probe beam depends upon whether an input or output pulse is being measured. By varying the length of the probe beam time-delay, the THz pulse may be gated at sequential points along its curve form, allowing a scan to reveal the pulse shape of the THz signal in the time domain.

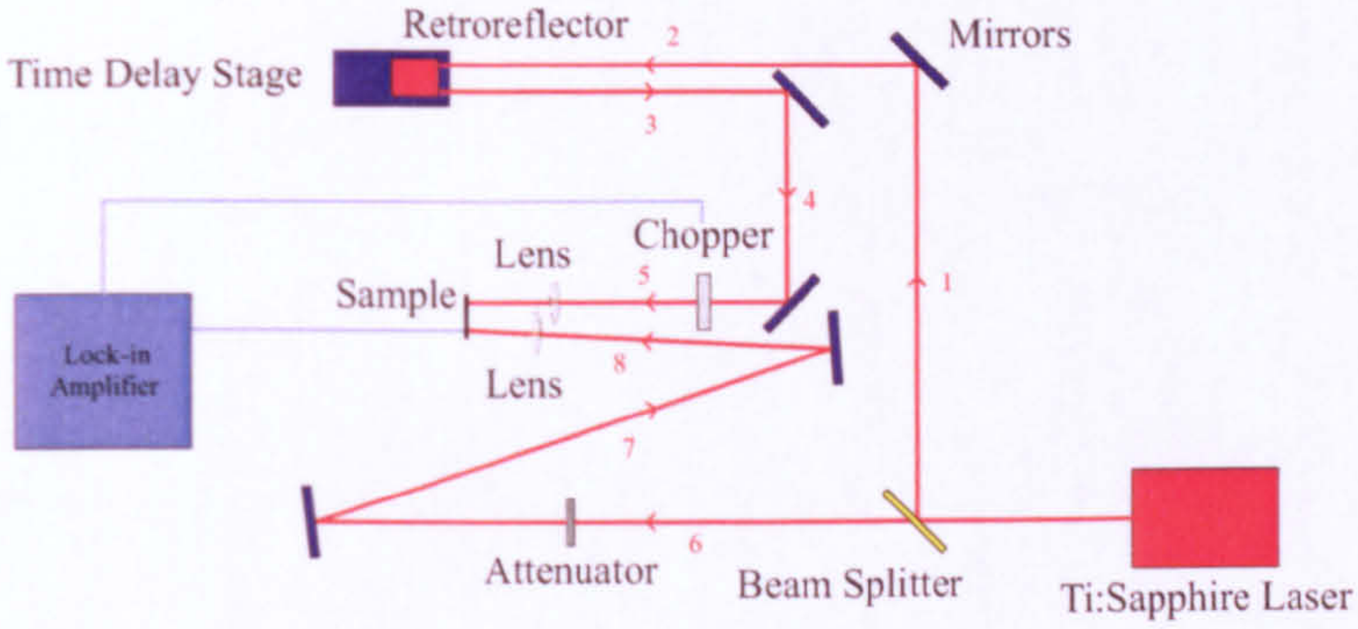

Figure 4.1: A schematic of the optical setup used to generate THz pulses, with the probe beam travelling via paths 1-5, and the pump beam via paths 6-8.

Prior to measurements being performed, it is critical that the overlap of the pump and probe beam paths, i.e. the point at which the path lengths are equal, is found when the retroreflector in Figure 4.1 is positioned towards the front end of the delay stage (i.e. when the probe path length is shortest). This corresponds to the position at which a THz pulse peak will be detected, and allows scans to be performed across the signal for the length of the stage, allowing maximum capture of spectroscopic information. In order to ascertain the exact position of the translation stage when overlap occurs, the 'sample' in Figure 4.1 is replaced with a photodiode sensitive to NIR radiation, and focussed on to by both pump and probe beams. The point at which the two paths are of equal length (overlap) corresponds to a region of constructive interference between the two pulsed beams, which generates a peak in the photocurrent of the diode as measured by a lock-in amplifier, shown in Figure 4.2.

The stage shown in Figure 4.1 provided short, high resolution (4 $\mu m \equiv 13$ fs free space time of flight) scans over a maximum range of 25 mm. However, to aid in pulse location and to provide the option of scanning over larger areas, the

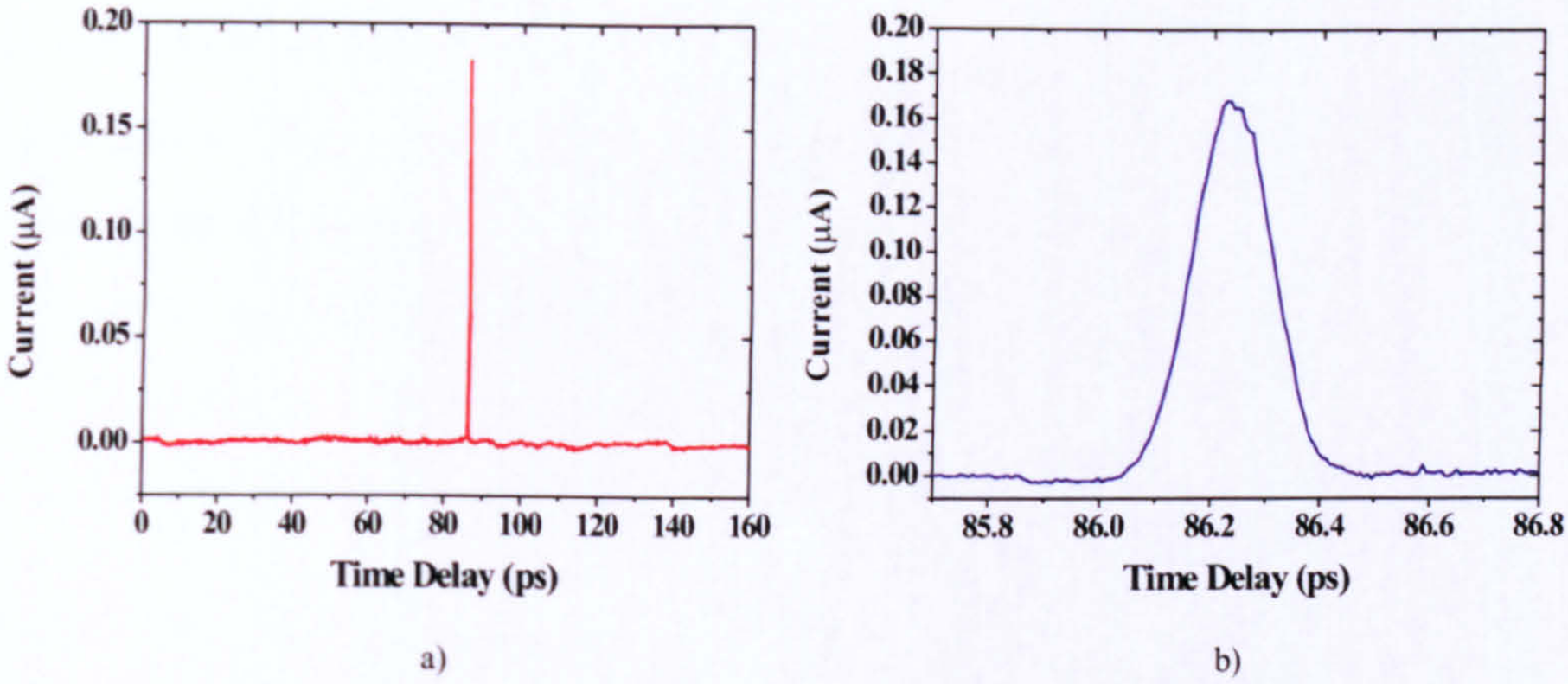

Figure 4.2: Graphs of the laser overlap with a) showing the full stage travel and b) showing a more accurate scan around the peak.

setup shown in Figure 4.1 was altered to introduce a second time delay stage, of maximum scan length 150 mm. The design modifications are shown in Figure 4.3, with alterations also having been made to the pump arm to compensate for the presence of the second stage (and thus increased path length) in the probe arm.

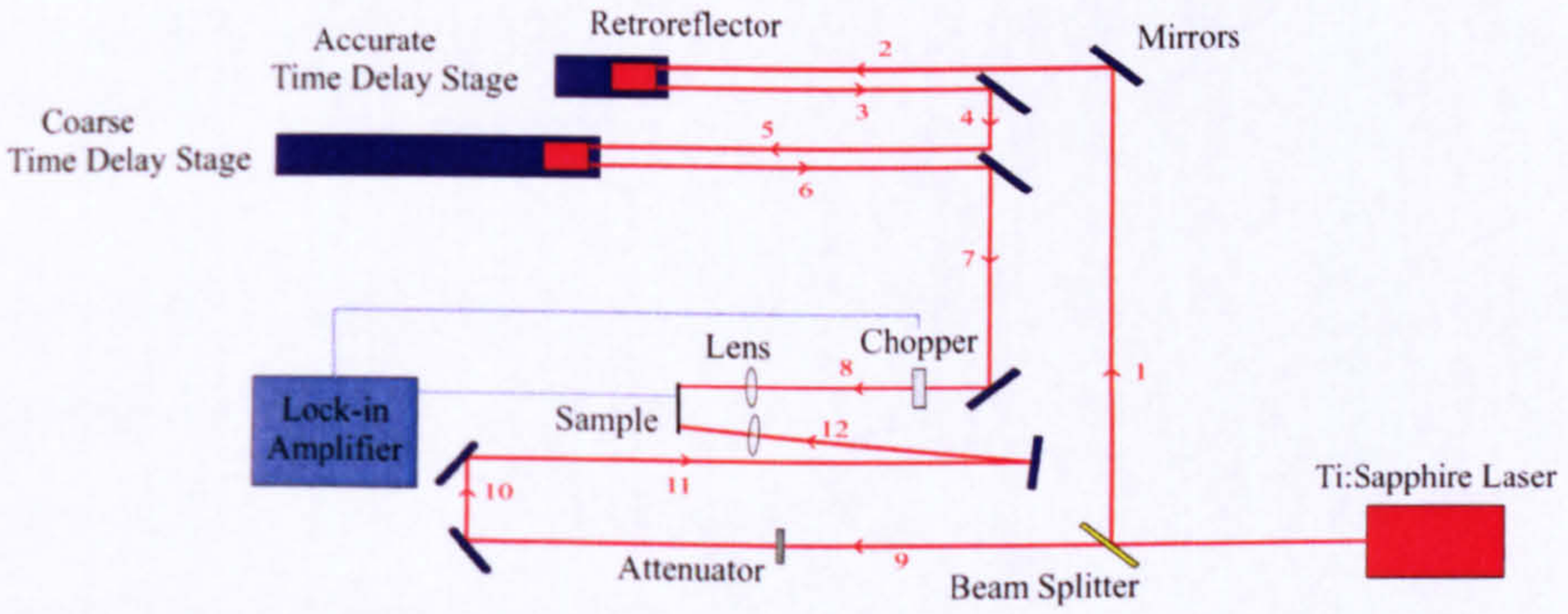

Figure 4.3: Schematic of the modified optical setup incorporating a second time delay stage. The probe and pump beams now travel via paths 1-8, and 9-12 respectively.

Initial tests were performed with an optical power of 8.5 mW as this was well within the safety limits of the microstrip device. Signals were measured at 10V, 5V, 0V, -5V and -10V to observe the effect on the generated THz pulse. The tests discussed in this Chapter involved laser intensities ranging from 8.5 mW

to 35 mW. Subsequent to these tests, it was discovered that a focussed beam of 80 mW was sufficient to destroy the BCB dielectric layer and short circuit the transmission line to the ground plane beneath, thus destroying the device. All future tests maintained sub-50 mW laser power for safety.

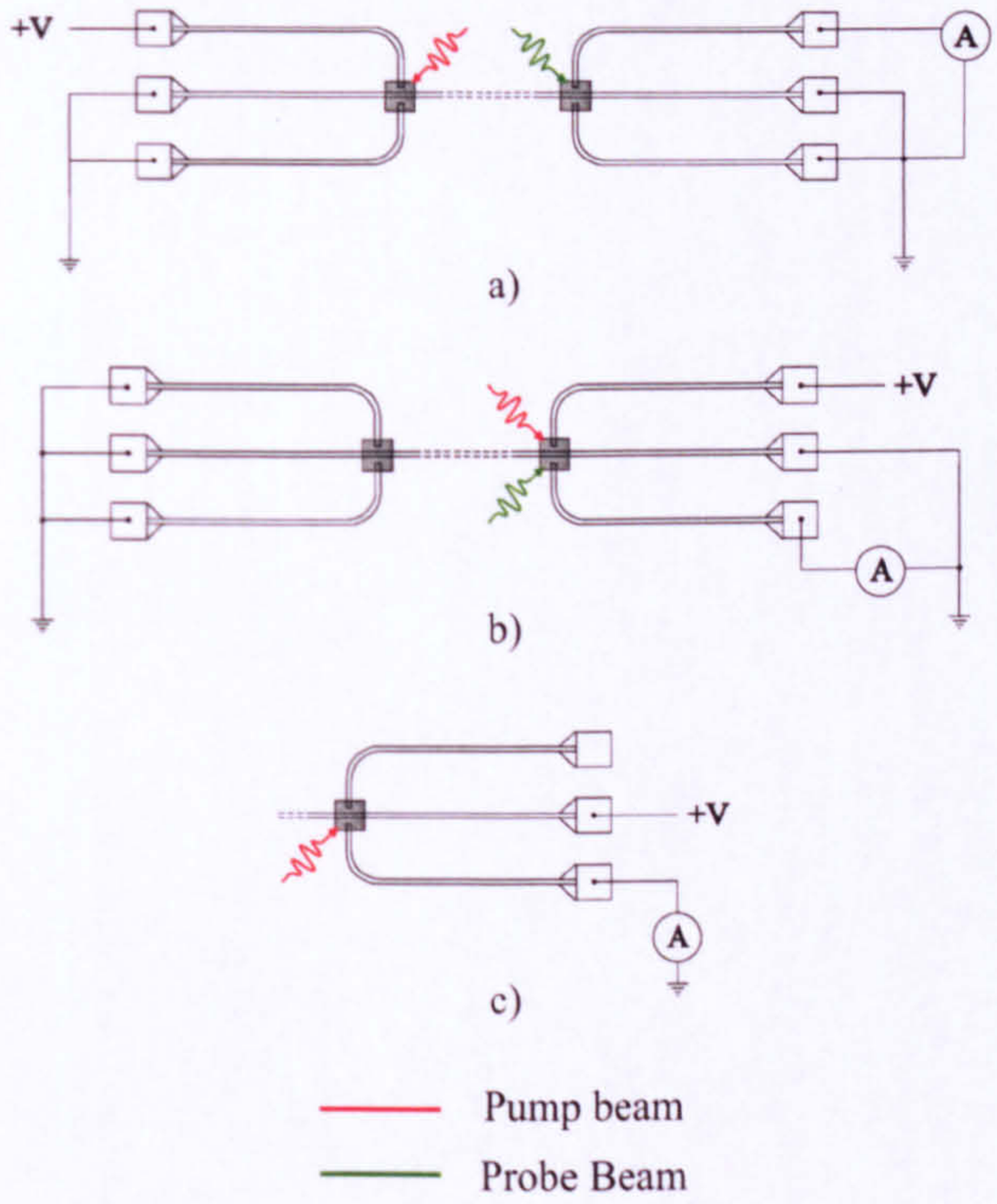

Figure 4.4: A Schematic showing the circuit connections for a) transmitted pulse measurements, b) input pulse measurements and c) switch characterisation.

Figure 4.4a shows the bias connections for measuring a pulse transmitted through the microstrip line. All connections were earthed with the exception of the biased pump arm, and the probe arm which was connected in series to a lock-in amplifier. Figure 4.4b displays the device arrangement for measuring the input pulse prior to propagation along the microstrip structure. This information is useful in calculating the attenuation in the line, and the difference in pulse widths prior to and subsequent to travelling down the line will give an idea of the dispersion. Finally, Figure 4.4c shows the arrangement used for characterising an individual photoconductive switch. Only two connections are made here - one on the pump arm and one on the nearest end of the transmission line, which allows photocurrent under varying bias to be directly measured.

To assess reproducibility between devices of both the photoconductive switch behaviour and transmission line characteristics, two separate devices fabricated to the same specifications, but on separate chips, were assessed at room temperature. A third device was characterised at both cryogenic and room temperatures to assess low temperature effects on THz generation and propagation.

4.3 Room Temperature Characterisation

4.3.1 LT-GaAs Switch Characterisation

Photocurrent characteristics of LT-GaAs switches were measured on two independent devices using the biasing arrangement displayed in Figure 4.4c, prior to performing any THz experiments. Dark current measurements (with no laser pulse incident on the sample) were measured as nanoamps in magnitude implying a dark resistivity of several megaohms.

The DC current passing through the switches was measured at varying bias voltages with the expectation of observing linear, ohmic responses [91], assuming carrier saturation did not occur within the switches. Each current measurement was repeated on the pump and probe switches for varying beam intensity, as shown in Figure 4.5a and 4.5b for device 1, and Figure 4.6a and 4.6b for device 2. The responses were linear as expected, and the variation of beam power at a constant bias of 10 V, shown in the inserts, is also linear.

Both devices present similar photocurrents for equal biasing and illumination conditions, with slight differences explained by variations in switch quality resulting from fabrication. From these tests, one may assume equal carrier generation within each switch, which is an important characteristic for S parameter calculations for each device, as discussed in Section 4.3.3.

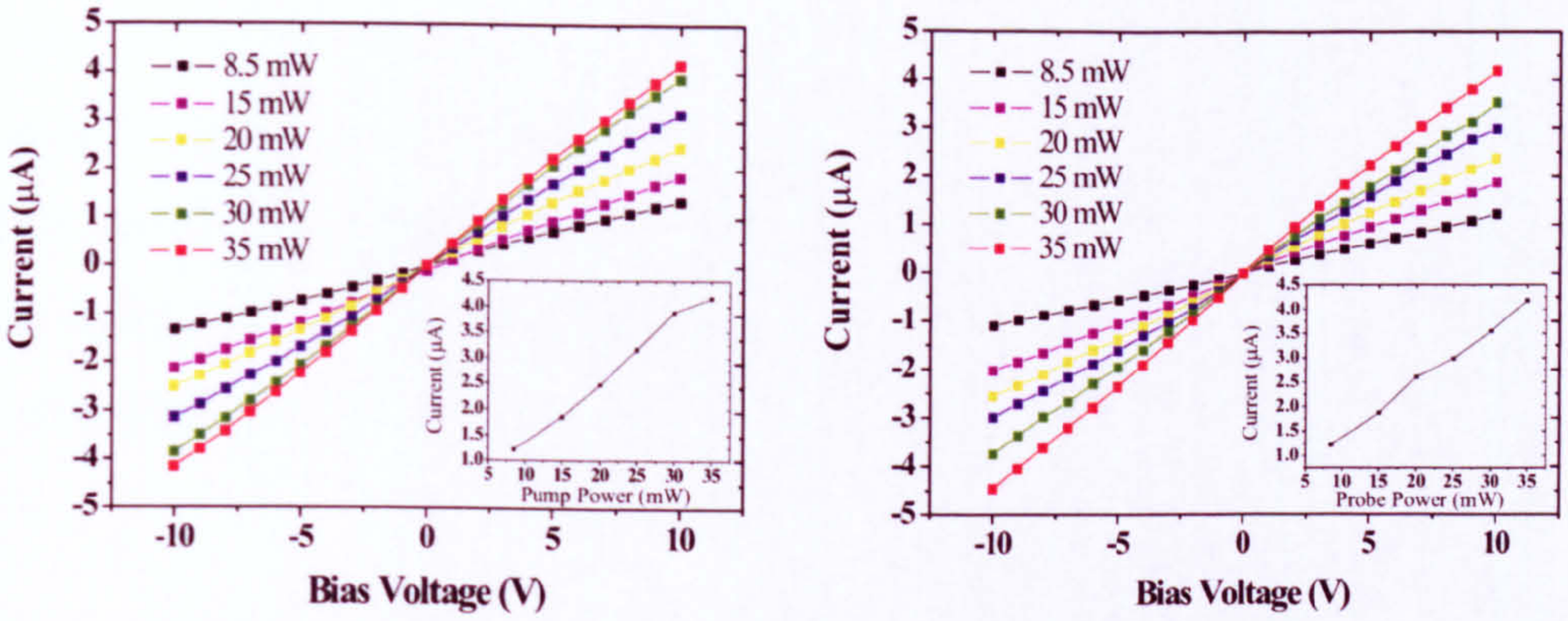

Figure 4.5: Current versus applied voltage for device 1 for a) the pump switch and b) the probe switch at varying laser powers, with insets of the current achieved at 10 V bias for each power. Lines are drawn as guides to the eye.

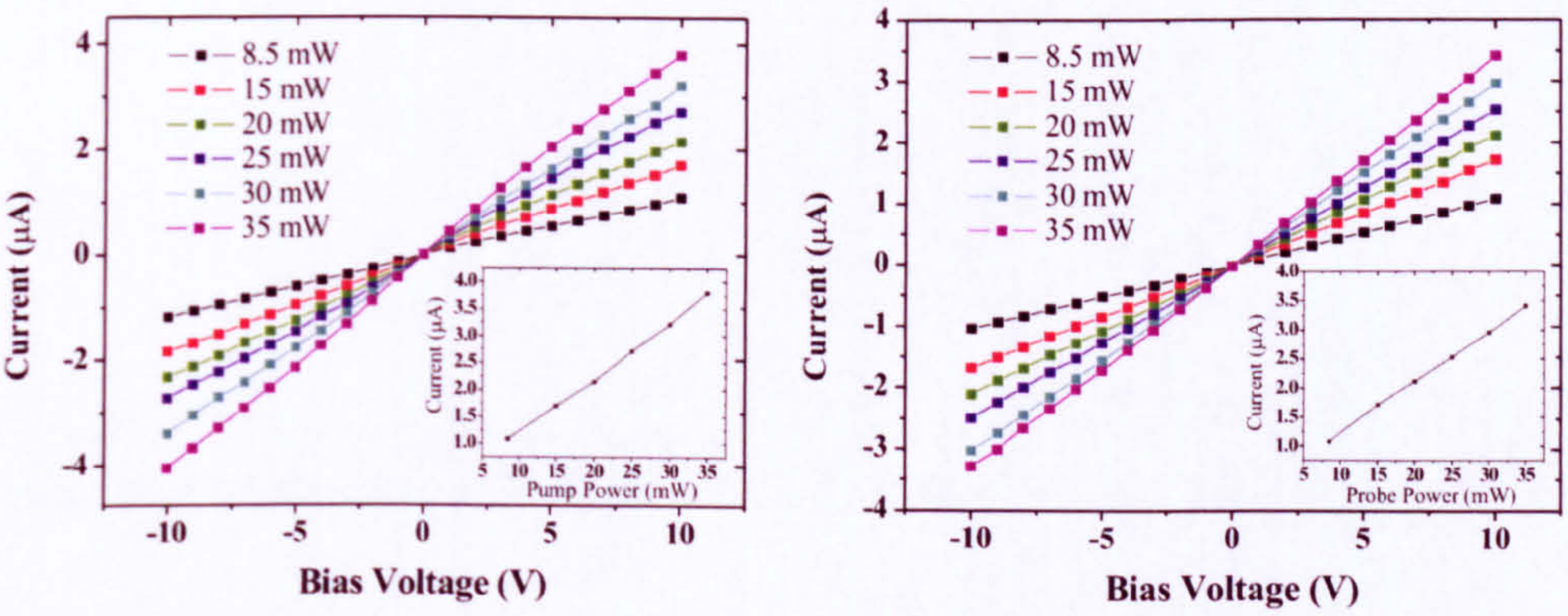

Figure 4.6: Current versus applied voltage for device 2 for a) the pump switch and b) the probe switch at varying laser powers, with insets of the current achieved at 10 V bias for each power. Lines are drawn as guides to the eye.

4.3.2 Output Pulses

Once it was understood how the photoconductive switches would react to varying biases and laser powers, it was appropriate to begin THz pulse measurements using the two devices. The pump and probe beams were set to the same powers in order to achieve equal carrier generation in each switch on the devices. Time

resolved measurements of each THz pulse shape are obtained by scanning the probe beam across the signal. Continuing the scan beyond the THz pulse will reveal further features in the tail of the pulse, including any reflections of the THz signal from discontinuities within the transmission line. Figure 4.7 shows the signal voltage generated on device 1 for several differing bias voltages applied to the pump switch.

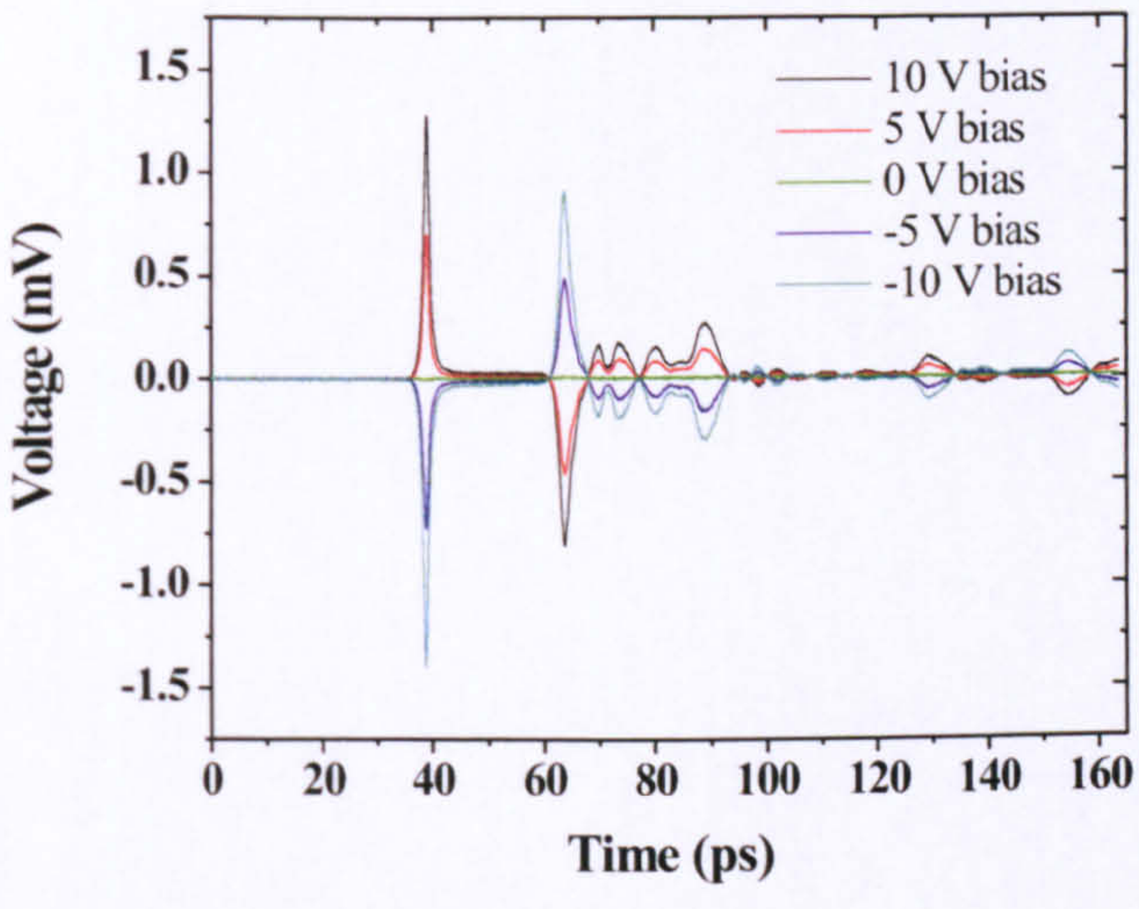

Figure 4.7: Voltage data for device 1 generated from full scans of a 25 mm time delay stage, each step corresponding to a time of flight increase of 80 fs for the probe beam.

The first peak shown in Figure 4.7 is identified as the THz pulse, followed by several other features which may be explained with reference to reflections within the transmission line geometry. Four large features in the signal, identified in Figure 4.8, will be considered as these will be readily identifiable when they occur in the second device.

At first glance it may appear that the bias of each reflected signal varies in sign somewhat randomly across the scan, but the bias direction can be explained with reference to Chapter 2, Section 2.2.3, which discusses terminated transmission lines. It is shown that reflections from a short circuit undergo a 180° phase inversion, i.e. a positively biased travelling wave is reflected as a negatively biased

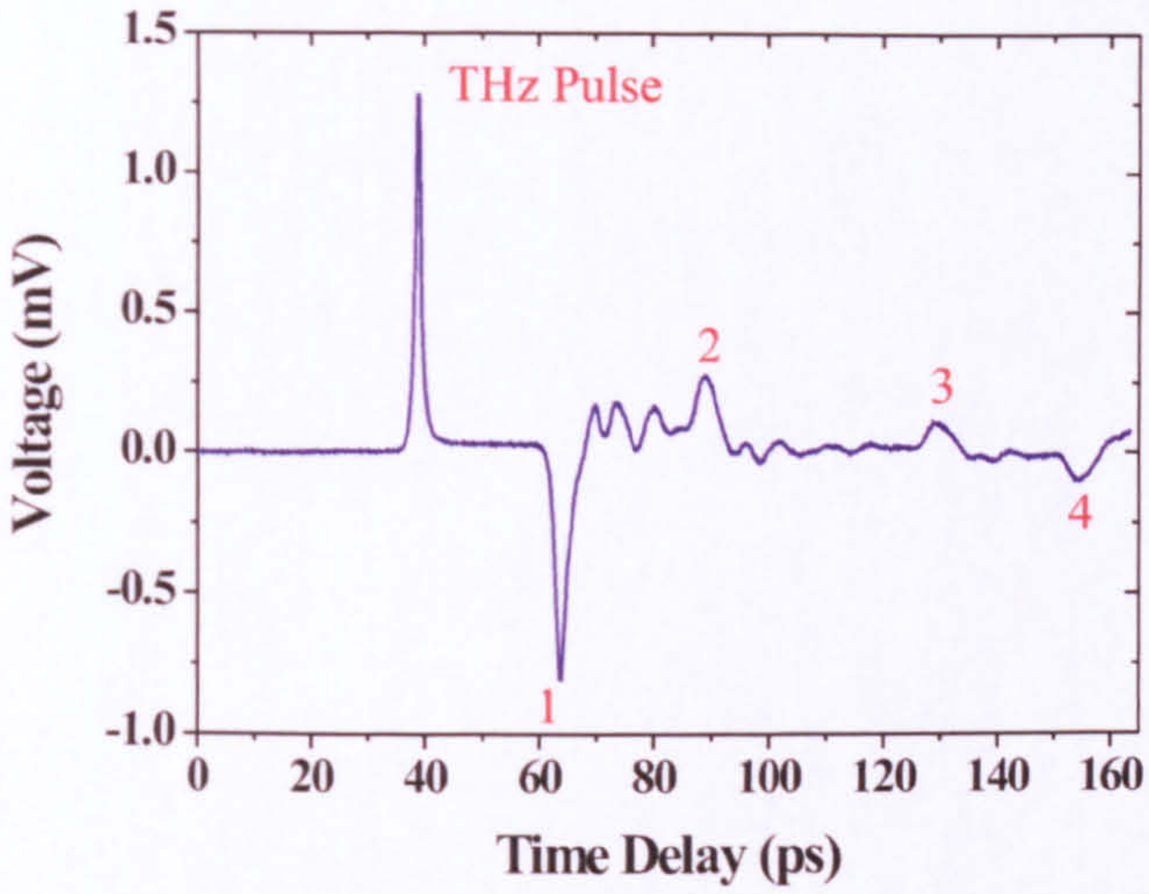

Figure 4.8: A single current scan of device 1 with a 10V Pump bias voltage applied, with major reflections labelled 1 - 4.

signal, whilst reflections from open circuits retain their original bias direction. Figure 4.9 shows how the reflections are generated from discontinuities in the transmission line design, most significantly from where the transmission line terminates at the bond pads. Whether the features are negative or positive can be explained by the number of reflection interfaces that the pulse encounters on its propagation path before it is gated at the detection pulse, and by considering that all line terminations are short circuits.

For a positive THz pulse, the first subsequent time domain feature (labelled 1 in Figures 4.8 and 4.9) should be negative in sign since it undergoes a single reflection from a short circuit interface, clearly demonstrated to be true in Figures 4.7 and 4.8. This reflection is also largest in magnitude for two reasons; it undergoes the shortest propagation path and therefore is attenuated least, and it is also a combination of two separate signals which traverse equal path distances in opposite directions, and interfere constructively on detection. The second major peak seen undergoes two reflections which would imply a 360° phase inversion and is therefore of the same bias as the THz pulse. The subsequent peaks may

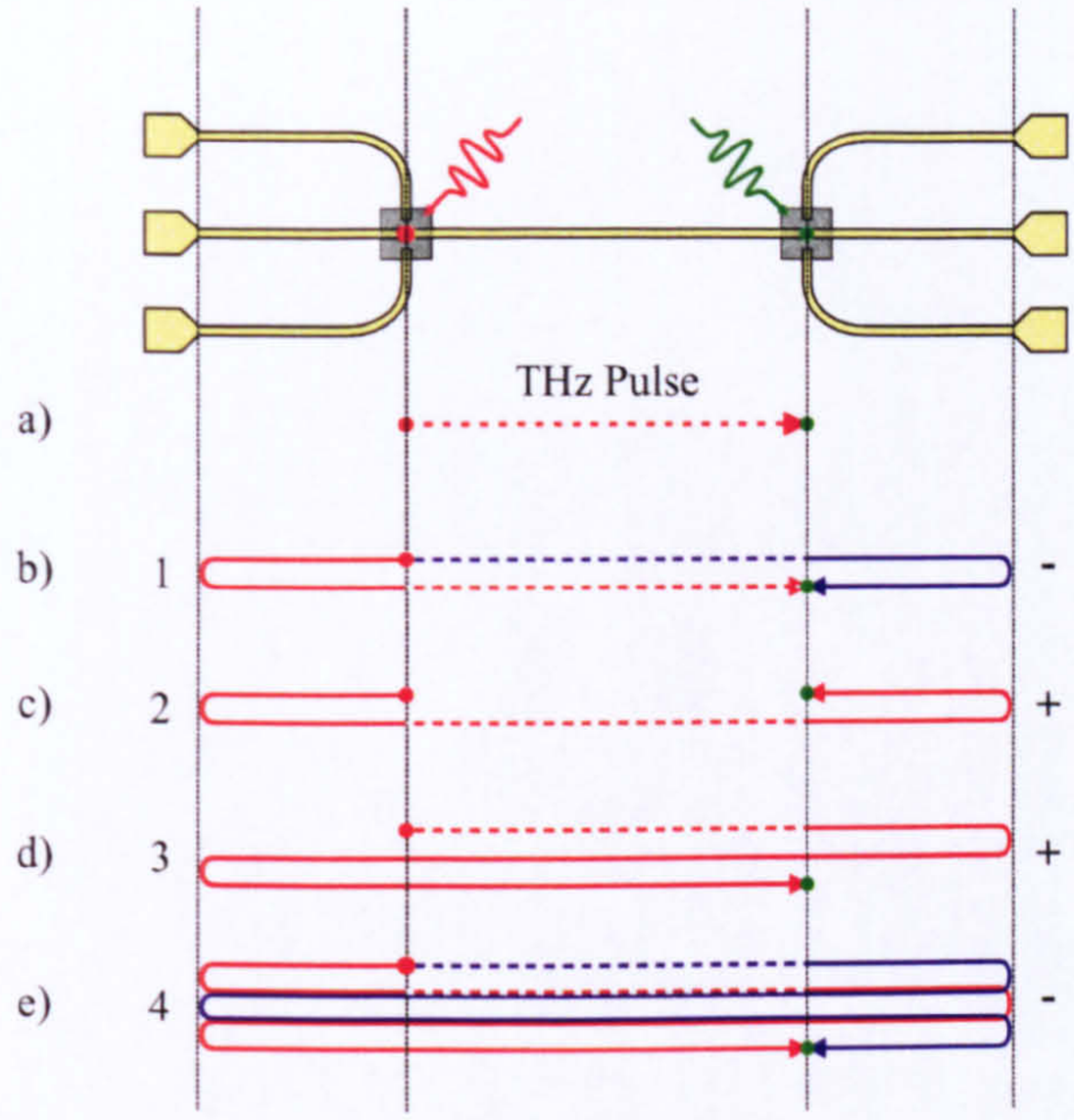

Figure 4.9: Demonstration of the pulse paths required to generate a) the THz pulse, b) reflection 1, c) reflection 2, d) reflection 3 and e) reflection 4. The dashed lines represent the path distance which is shared with the THz pulse, and the solid lines are the subsequent travel of the reflected pulses.

be analysed in a similar fashion by referring to Figure 4.9. Since the second device was identical in design to the first, it was anticipated that the signal would exhibit the same reflections. Figure 4.10 shows data obtained by varying the pump bias between +10 V and -10 V on device 2 and reveals similar features in the tail, generated from reflections at specific points on the transmission line. More importantly perhaps, is the fact that the reflections exhibit the same bias directions with respect to the main THz pulse as for the first device as seen in Figure 4.11, confirming the theoretical explanation for the bias variation of reflected signals within the device.

By considering the time delays, Δt, between the THz pulse and each reflected signal, and the distance, d, travelled by each reflection (measured from the device design), we can calculate the phase velocity, v_p within the line using:

$$v_p = \frac{d}{\Delta t}. \tag{4.1}$$

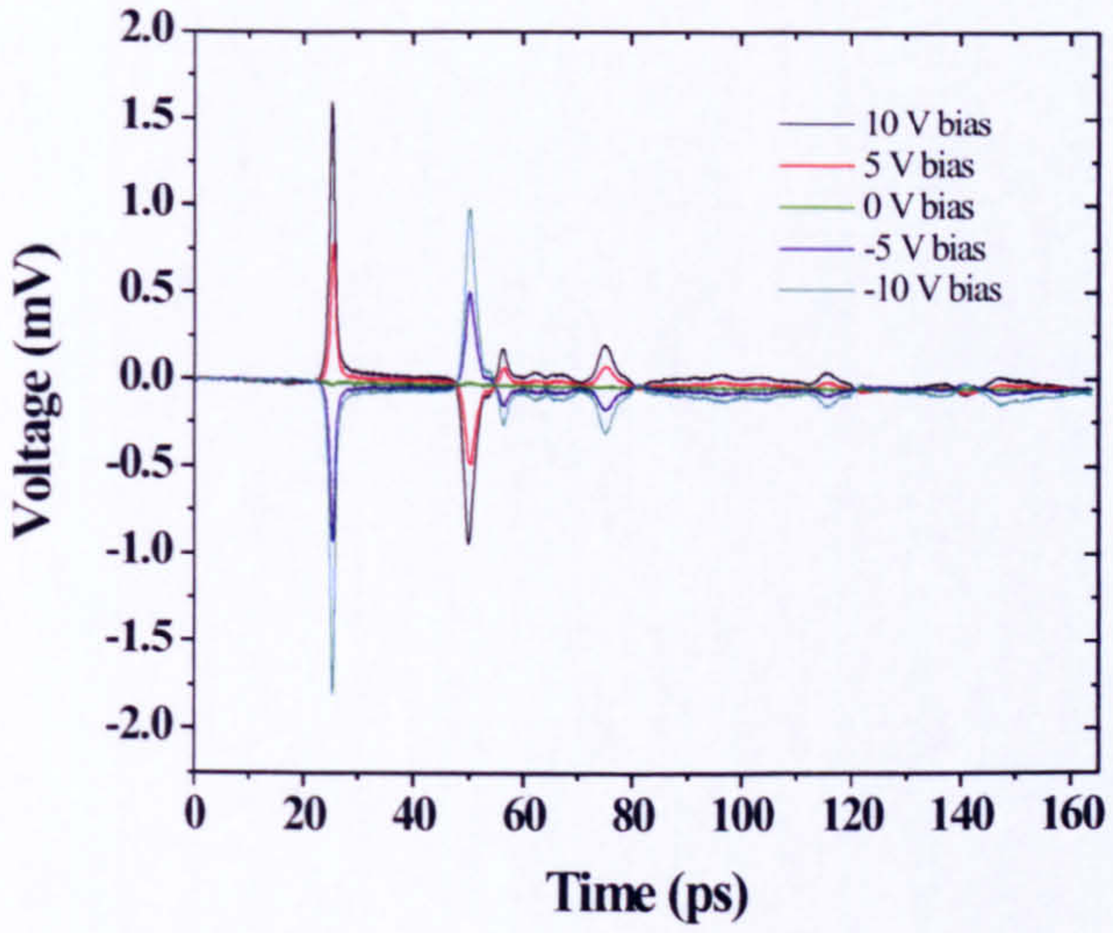

Figure 4.10: The Voltage scans performed on device 2 for pump switch biases 10 V, 5 V, 0 V, -5 V and -10 V.

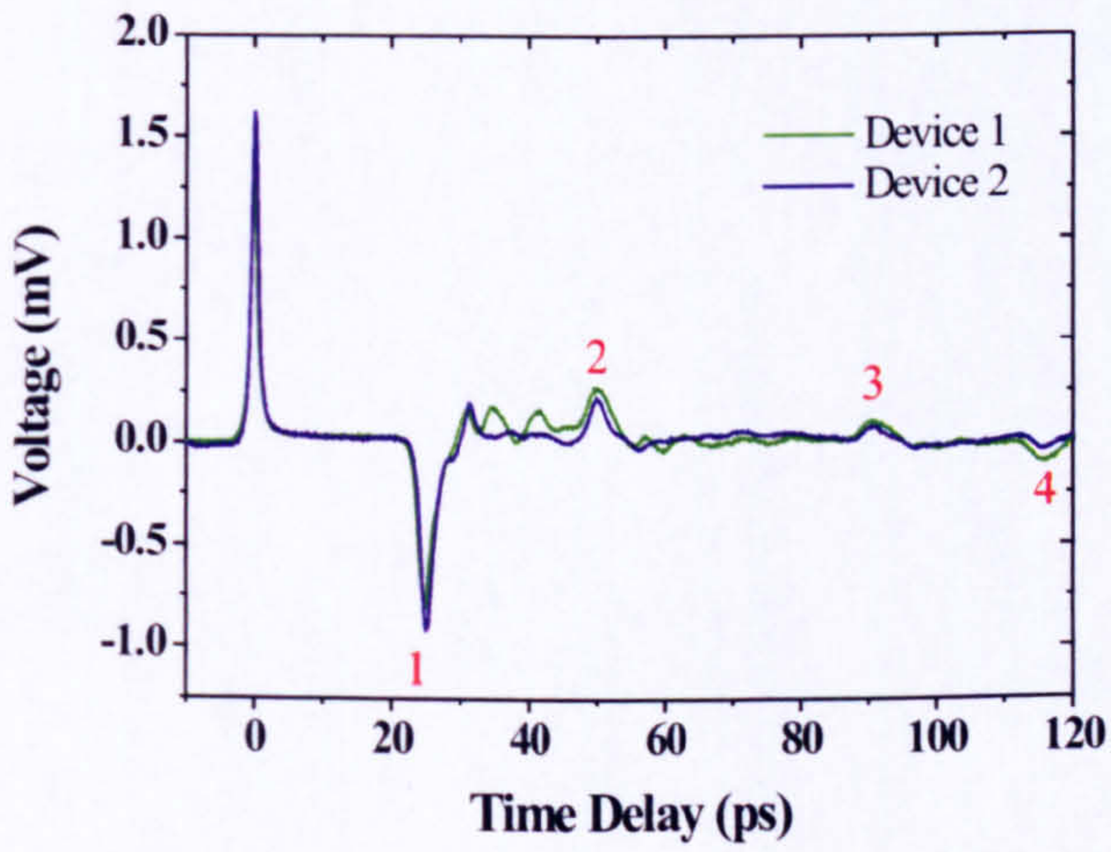

Figure 4.11: Comparison of the Voltage Scans for Device one and two showing the four main reflection peaks.

The velocities may then be used in:

$$\epsilon_{eff} = \left(\frac{c}{v_p}\right)^2, \tag{4.2}$$

to calculate the effective permittivities for the transmission line structure, shown in Tables 4.1 and 4.2 for devices 1 and 2 respectively. By rearranging (2.26) from Chapter 2 in terms of the relative permittivity, we obtain:

$$\epsilon_r = \left(\epsilon_{eff} - \frac{1}{2} + \frac{1}{2x}\right)\left(\frac{1}{\frac{1}{2} + \frac{1}{2x}}\right), \tag{4.3}$$

using the substitution

$$x = \sqrt{\frac{1}{1 + \frac{12d}{W}}}, \tag{4.4}$$

for a transmission line of width, W, atop a dielectric of thickness, d, which allows calculation of the relative permittivity of the BCB dielectric. Average values for the effective permittivity of $\epsilon_{eff} = 2.37 \pm 0.04$ and 2.38 ± 0.04 were found for devices 1 and 2, with corresponding relative permittivities of $\epsilon_r = 2.78 \pm 0.06$ and 2.79 ± 0.05, compared to the previously published experimental value of 2.65 [84]. The slight disparity from the published value is likely to be caused by different preparation conditions during fabrication which can alter the dielectric properties of BCB. The permittivity is, however, constant between the two devices, suggesting good reproducibilty in the fabrication process.

Reflection	Time Delay, Δt (ps)	Distance, d (mm)	ϵ_{eff}	ϵ_r
1	24.75	4.80	2.3896	2.8019
2	49.86	9.80	2.3266	2.7203
3	90.57	17.66	2.3640	2.7687
4	115.82	22.46	2.3963	2.8106

Table 4.1: Table showing positions of reflected signals for device one as timed from the THz pulse, yielding an average relative permittivity of $\epsilon_r = 2.78$ for BCB, compared to the published value of 2.65 [84].

Performing a Fast Fourier Transform (FFT) of the data points around the THz peak converts the time domain signal into the frequency domain, allowing analysis of the frequency components contained within the pulse as well as showing the

Reflection	Time Delay, t (ps)	Distance, d (mm)	ϵ_{eff}	ϵ_r
1	24.86	4.80	2.4141	2.8337
2	49.95	9.80	2.3381	2.7352
3	90.63	17.66	2.3703	2.7769
4	115.89	22.46	2.3962	2.8106

Table 4.2: Table showing positions of reflected signals for device two as timed from the THz pulse, generating an average relative permittivity of $\epsilon_r = 2.79$ for BCB, compared to the published value of 2.65 [84].

signal to noise ratio of the device. Figure 4.12 shows a normalised FFT of a THz signal generated at 10 V bias in device 1 and reveals that there is usable signal up to at least 1.2 THz. The SNR is approximately 800:1 at the lowest frequency, but decreases as system loss increases. This may need to be improved on future devices if possible, for measurements at higher frequencies.

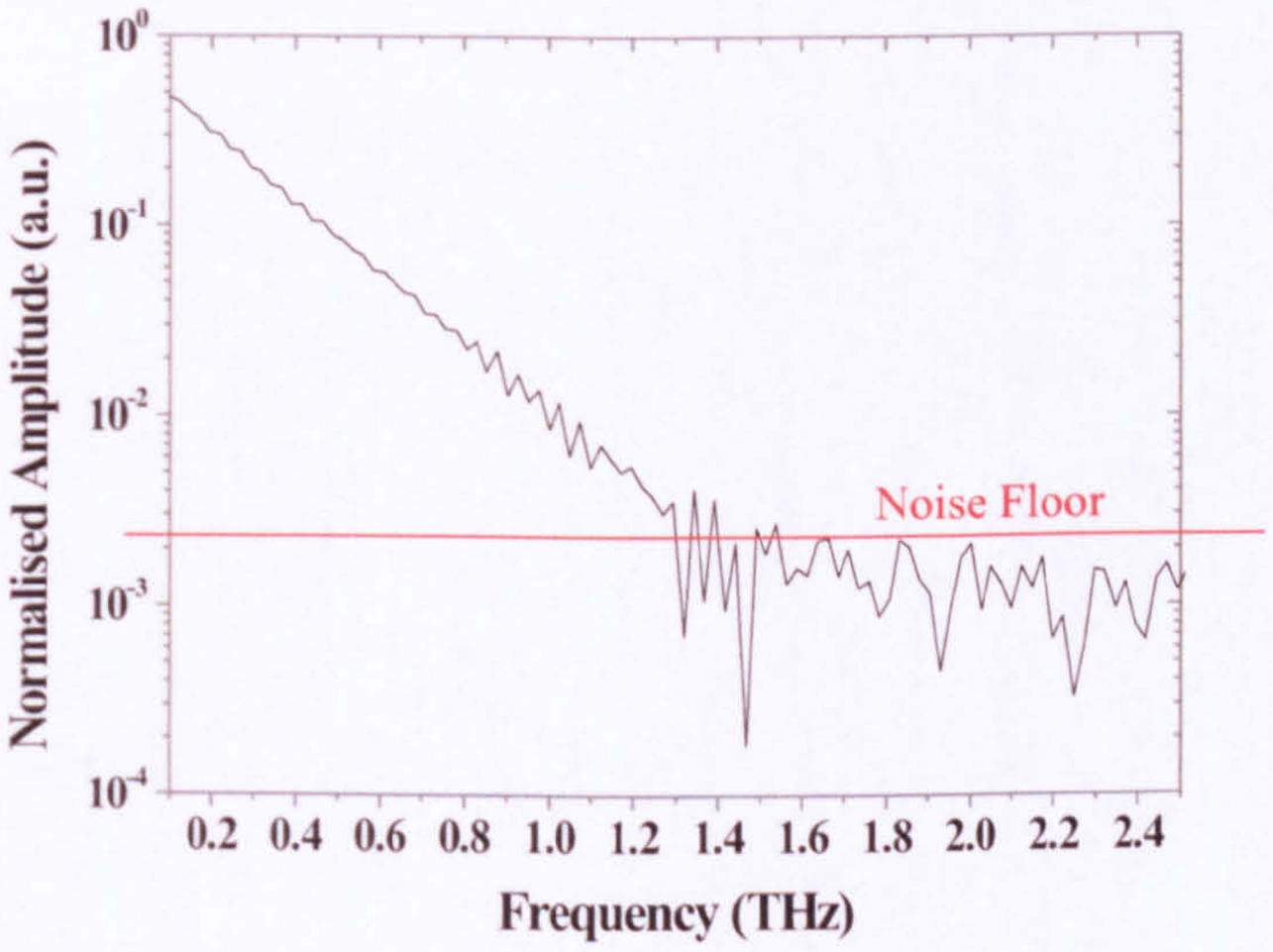

Figure 4.12: Fast Fourier Transform performed of the THz peak seen in Figure 4.8.

4.3.3 Input Pulses

In order to be able to calculate the attenuation in the line, the input pulse (i.e. the pulse before propagation through the microstrip structure) must be measured

using the biasing and illumination conditions shown in Figure 4.4b. Since the test device is symmetrical, reflections were expected to occur at the same time delays and with the same bias with respect to the THz pulse as seen for the output pulse. By performing FFTs of both the input ($\mathcal{F}_{[V_{in}]}$) and output ($\mathcal{F}_{[V_{out}]}$) voltage signals we can use:

$$S_{21} = 20log\left(\frac{\mathcal{F}_{[V_{out}]}}{\mathcal{F}_{[V_{in}]}}\right), \tag{4.5}$$

to calculate the S_{21}, or transmission characteristics, for the transmission line structure. Equation (4.5) is only valid for a transmission line with matched input and load impedances, which in the case of the devices measured here is true if equal photocurrent is generated at each switch. This is achieved by subjecting each switch to the same biasing and illumination conditions.

The shape of the input pulses is shown in Figure 4.13 and reveals that the signal reflections generate features in the expected positions, equivalent to those seen for the transmitted pulse. The noise levels are observed to be somewhat greater than for the output signal measurements, a likely result of the pump and probe beams slightly overlapping across the device, creating an undesirable background photocurrent. Using the FFT data from the input and output signals in (4.5) to generate S_{21} information reveals that the transmission loss measured at different pump switch bias voltages agree well, and provide a value of -10.0 $\pm$ 0.3 dB loss at 600 GHz for a 4 mm propagation distance, compared to a value of -6.5 dB simulated in Sonnet [88].

The difference in values between the simulated and measured loss could be caused by several different factors: increased loss due to edge roughness of fabricated devices, which could introduce higher order propagating modes; differences in focussing conditions between the input and output pulses which would alter the relative ratio between them and affect the measured loss; and differences in the quality of the photoconductive switches, such as the presence of micro-fractures

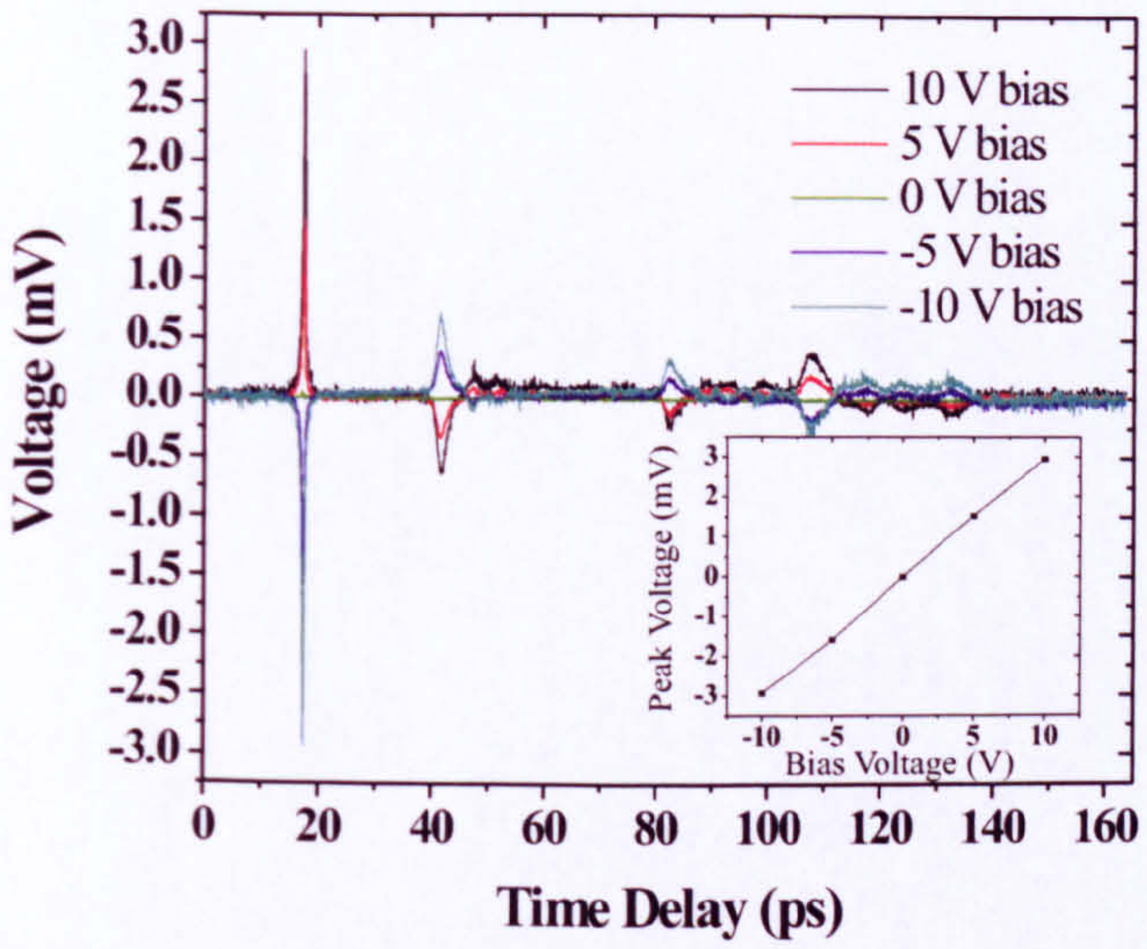

Figure 4.13: Voltage scans of the output signal at varying pump bias for Device 1, with an inset of the peak voltages measured between -10 V and +10 V pump bias.

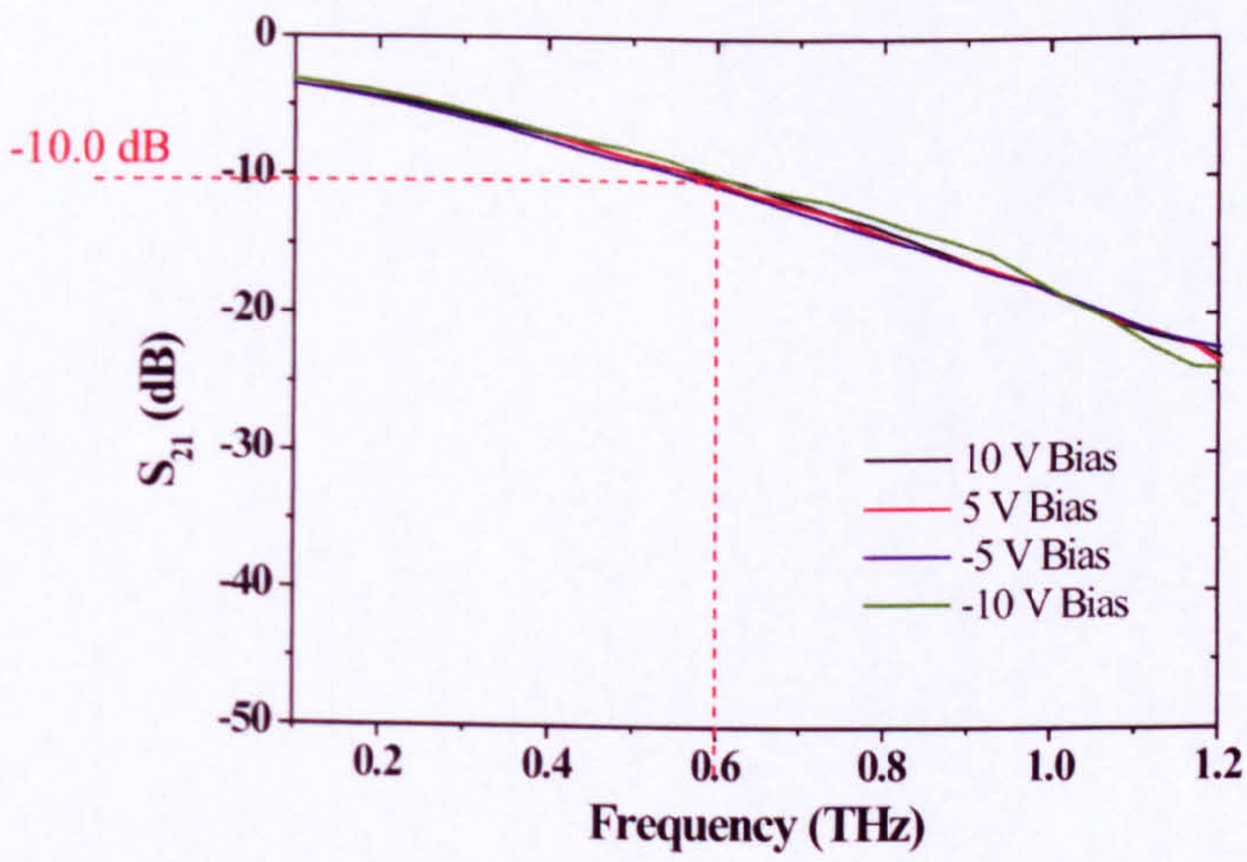

Figure 4.14: S_{21} signal for Device 1 calculated from varying bias voltages.

which may introduce extra dispersion at higher frequencies.

The pulse entering device 2 was measured in the same fashion as for device 1 and the data was used to calculate S_{21} parameters using (4.5) as previously.

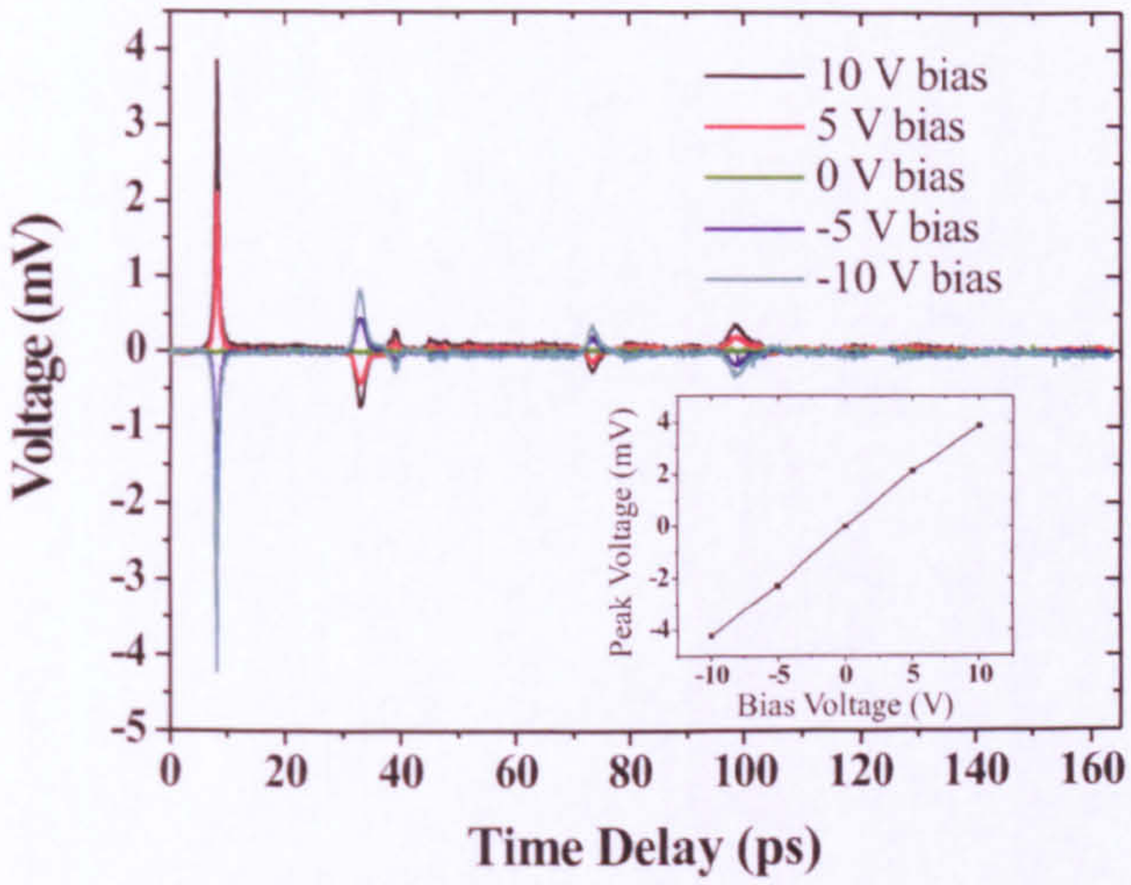

Figure 4.15: Voltage scans of the output signal at varying pump bias for Device 2, with an inset of the peak voltages measured between -10 V and +10 V pump bias.

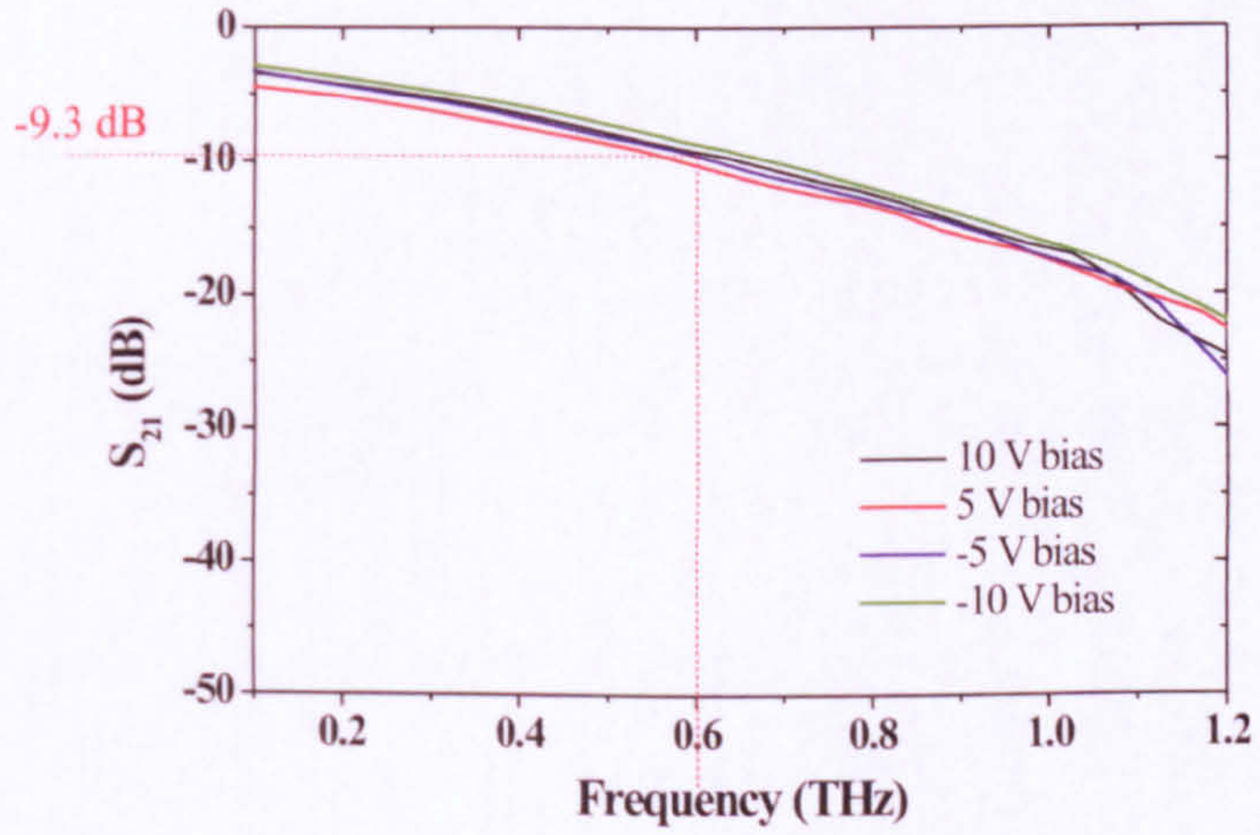

Figure 4.16: S_{21} signal for Device 2 calculated from varying bias voltages.

Again the expected reflections are observed in the input signal due to the symmetrical nature of the device. The linear increase in peak strength with voltage is expected due to the ohmic response of the photoconductive material used, shown in Figure 4.5 and Figure 4.6. Figure 4.16 shows an attenuation of -9.3 $\pm$ 0.8 dB at 600 GHz, which is in good agreement with the loss experienced for Device 1.

4.3.4 Further Analysis

Further tests were performed on this device including variation of the pump and probe powers independently to observe the effects on SNR, FWHM and signal intensity. For continuity, a control power of 8.5 mW was used to allow comparison with previous data. If the devices were being understood correctly, it was expected that increasing the probe power would eventually saturate the gated signal, since the THz pulse strength itself would not be increasing. Conversely, increasing the pump power would *not* cause saturation of the detected pulse magnitude since the signal could theoretically increase indefinitely until carrier saturation occurs in the switch, or the sample is damaged. Figure 4.17 shows the effects of altering

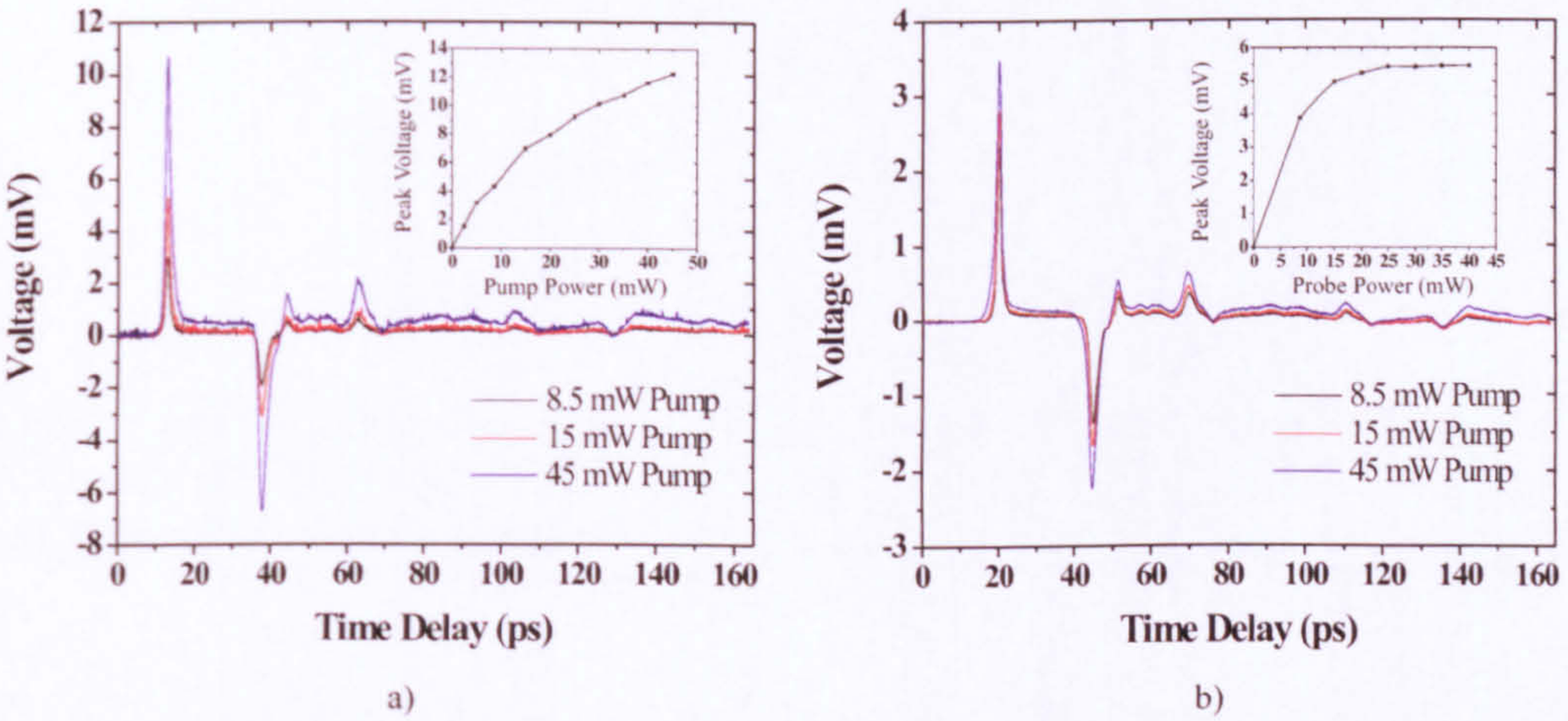

Figure 4.17: Effect on the *transmitted* signal of a) varying the PUMP power whilst maintaining 8.5 mW PROBE power and b) varying the PROBE power whilst maintaining 8.5 mW PUMP power, with inserts of peak voltage v. laser power. Only three scans are shown on each graph for clarity, and lines are drawn as a guide to the eye.

the the pump power at constant probe power and vice versa, on the magnitude of the THz signal measured on the output switch. The insets in Figure 4.17a and 4.17b show the expected linear and saturation curves for the peak voltages when increasing the pump power or probe power respectively.

Increasing the laser powers also affects the FWHM of the generated (and thus also transmitted) THz pulse. Figure 4.18 displays normalised THz peaks for

several different pump beam intensities and demonstrates the FWHM increasing approximately linearly with pump power. The reason for this increase is possibly due to localised heating within the switch region caused by both the increased photocurrent and the increased laser intensity focussed onto the switch. This effect is discussed more fully in Section 4.4.

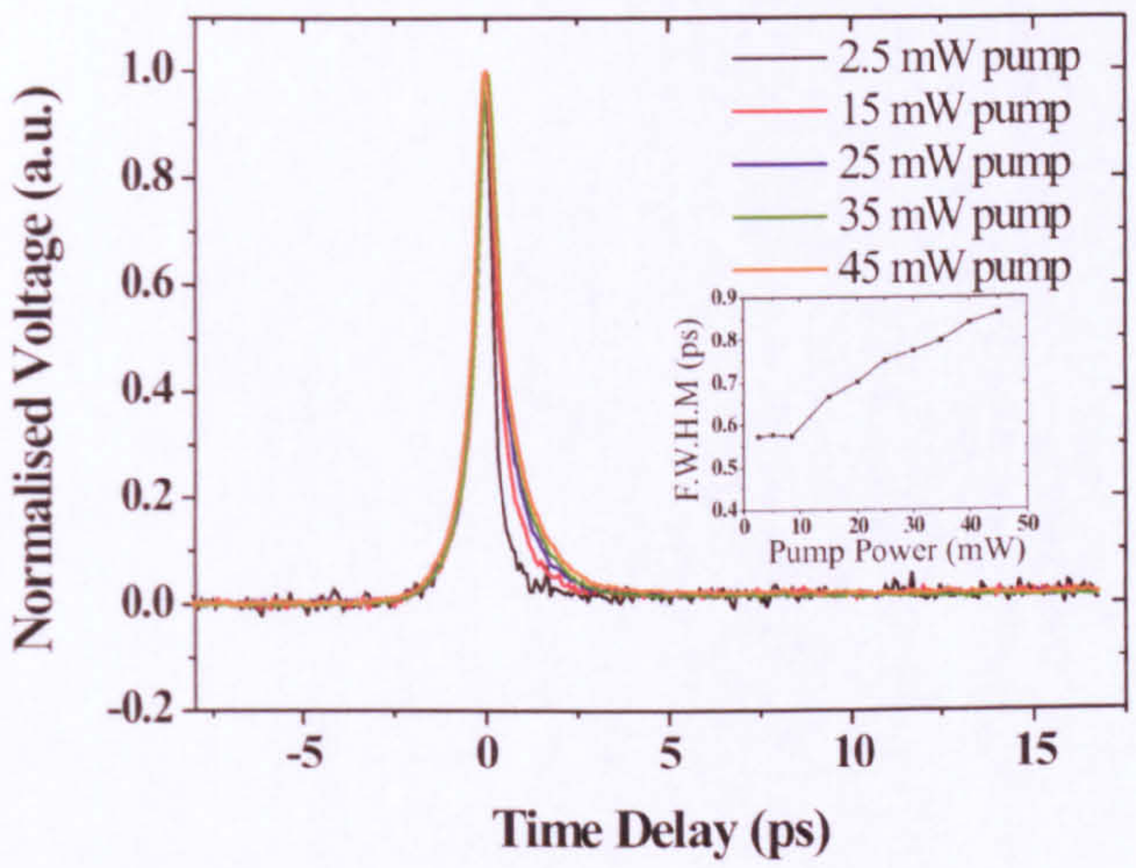

Figure 4.18: Normalised voltage scans of the input pulse for Device Two with insert showing the FWHM plotted against Pump Power. Only five plots are shown in the main Figure for clarity. Lines on the inset are as a guide to the eye.

The inset in Figure 4.18 shows that the FWHM of the THz signal decrease linearly with pump power down to a lower limit of ≈ 0.55 ps. Overall, the characterisation of these devices has shown the generation of ultrashort, sub-picosecond (≈ 0.5 - 0.8 ps) transient voltage pulses containing THz radiation up to 1.2 THz, which enter and propagate along an on-chip microstrip system.

4.4 Cryogenic Temperature Characterisation

On-chip, guided-wave THz techniques are also of interest in the study of semiconductor based systems, such as two-dimensional electron gases, since the microstrip

geometry allows rigid control over the interaction length between the probing signal and the system being measured, potentially leading to highly sensitive device characterisation. Until now, LT-GaAs was unproven as a suitable emitter or detector of THz frequency transients at cryogenic temperatures, nor had the BCB dielectric been demonstrated as a useful propagation medium for microstrip geometries at such temperatures.

The device used for characterisation at cryogenic temperatures was identical in geometry to those tested in Section 4.3, with modifications made to the distribution circuit to enable mounting on the cold finger of a continuous flow cryostat. Good thermal contact was provided by a via through the distribution board, between the silicon substrate of the device and the cold finger, which was filled with thermal paste. An identical pump - probe setup was used as for room temperature measurements, with the cryostat placed in the sample position in Figure 4.3. Optical access was provided to the sample within the cryostat via transparent quartz windows, as seen in Figure 4.19.

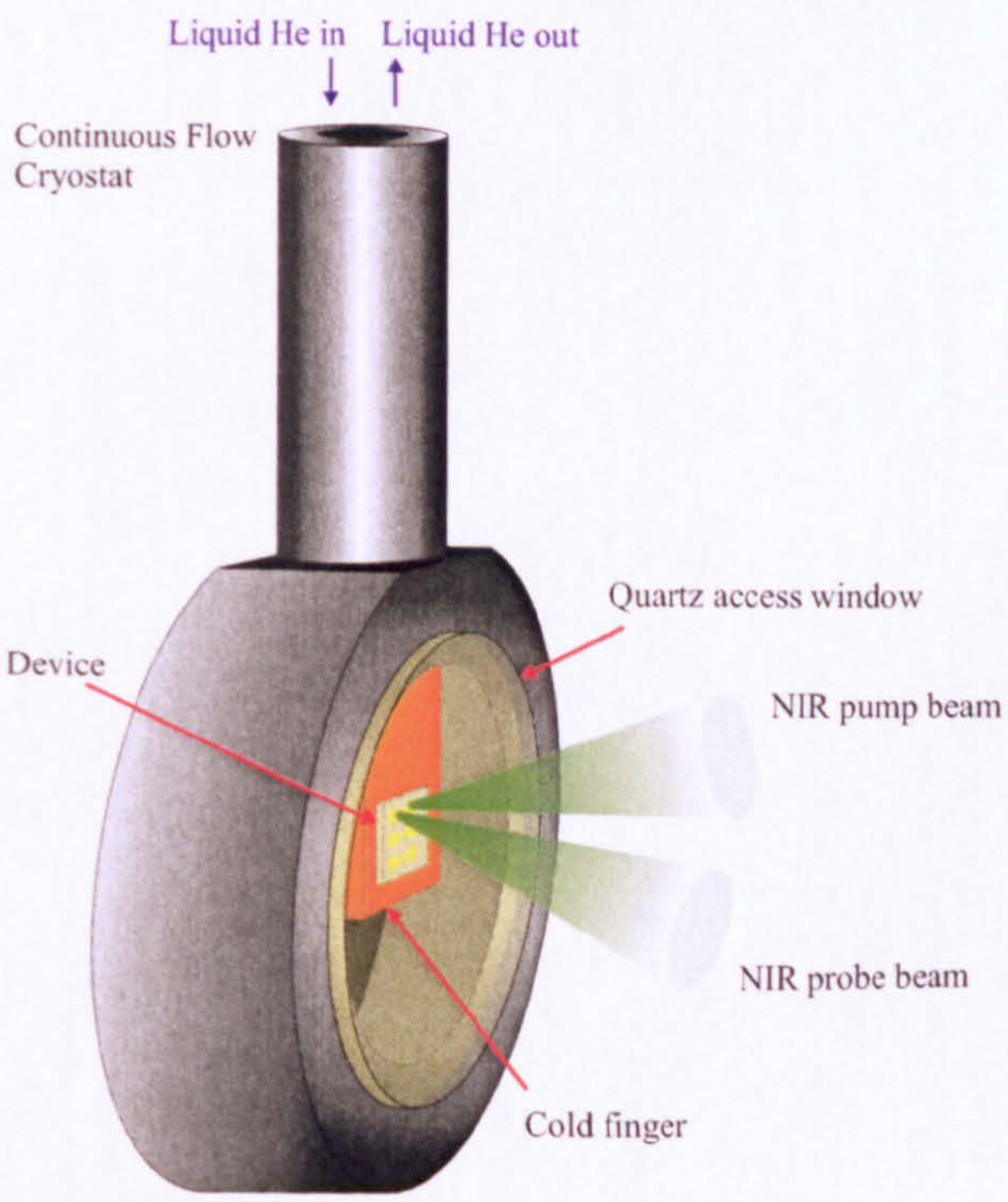

Figure 4.19: Schematic diagram of a transmission line mounted within a continuous flow cryostat, with optical access provided by transparent quartz windows.

Measurements at both room and cryogenic temperatures were performed with the sample mounted in the cryostat behind the quartz windows to allow direct comparisons between both conditions. The laser beams are focussed through the windows onto the photoconductive switches, avoiding the pulse dispersion of optical fibre-coupled methods, encountered by Shaner *et al.* [62] for example. Measurements of room temperature photocurrent in each switch, both with and without the quartz window in place, revealed an approximately 70 % reduction in photocurrent for the former, attributed to multiple reflections of the laser at the window interface and a small increase in the beam focus. THz pulses were generated at a pump switch bias of 50 V for laser powers from 1 to 60 mW, and time resolved measurements of the pulses were taken by variation of the probe beam time delay as described previously. The cryostat was cooled from 296 K to 4 K by a continuous flow of liquid helium, over a period of $\approx$ 10 minutes. This slow cooling rate was sufficient to avoid cracking of the BCB surface (experienced in initial experiments), taken to be caused by differential thermal contraction of the dielectric and supporting substrate. Furthermore, there was no evidence of reduced adhesion between the LT-GaAs thin film switches and the BCB dielectric on subsequent investigation by optical microscopy.

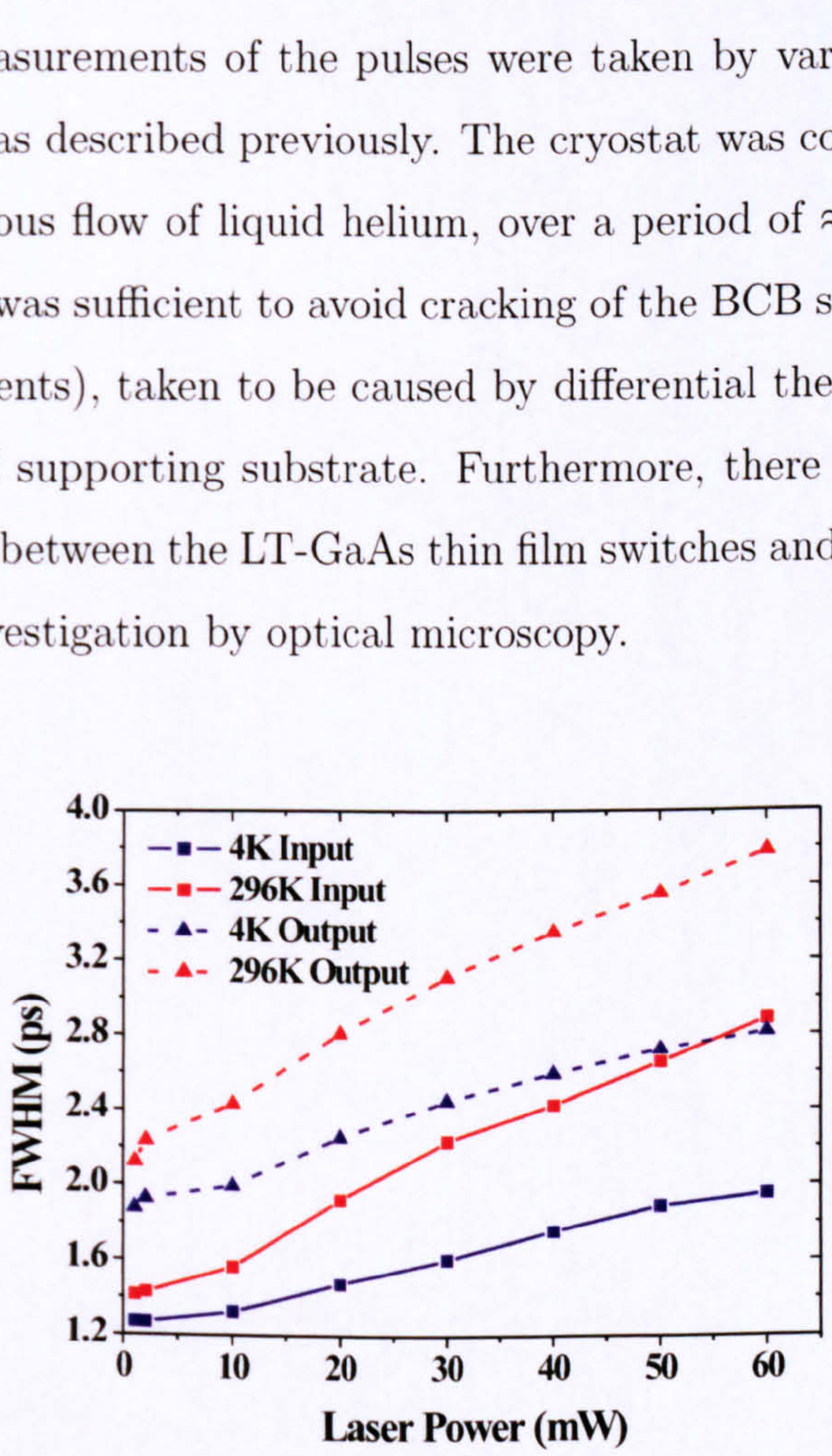

Figure 4.20: Comparison of the FWHM between input and output pulses at 296 K and 4 K operation for a 4 mm THz interconnect. Lines are drawn as a guide to the eye.

At room temperature, the minimum measured pulse width measured for this device was equal to 1.3 ps for the input pulse, and 2.1 ps for the output pulse. The corresponding FWHM at 4 K were found to be reduced by $\approx$ 10 % as shown in Figure 4.20. The room temperature pulsewidths were broader for this device than for previous devices due to a change in the LT-GaAs growth suppliers and hence a difference in carrier lifetimes (increased from 250 fs for Cambridge wafers, to 450 fs for Manchester wafers used in this device).

Three-dimensional carrier simulations performed by Castro-Camus *et al.* [24], discussed in Chapter 1, suggest that contributions to the generated THz pulse width in LT-GaAs switches arise from three main sources. The first contribution comes from the pulse width of the NIR excitation and detection laser signals, measured in this system using two photon autocorrelation as $\sim$ 80 fs. The second arises from the finite spot size of the focussed laser beams which is in the region of 20 μm. This causes a pulse broadening, Δt, calculated using $\Delta t = d/v_{ph}$, where d is the diameter of the focussed beam spot, of $\sim$ 100 fs per switch. The final contribution arises from the carrier lifetime within the photoconductive material, measured for the LT-GaAs used in this sample as 420 fs using pulsed terahertz photoreflectivity. The latter mechanism is the only likely property to alter as a function of device temperature, whilst the first two should remain constant. It is proposed therefore, that the carrier lifetime in LT-GaAs thin films reduces with film temperature. Supported evidence is provided when we consider the FWHM at higher excitation powers in Figure 4.20. Higher beam powers will generate localised heating within the thin film which will act to counter the cooling action of the continuous flow cryostat and cause broadening of the THz pulse. Broadening is also seen at room temperature for both this device and the devices in Section 4.3. The room temperature pulse widths in Figure 4.20 increase at a slightly higher rate as a function of laser power than the cryogenic measurements, since no cooling is provided to moderate the localised heating caused by the incident laser beam.

Figure 4.21a and Figure 4.21b show normalised time domain measurements at 4 K

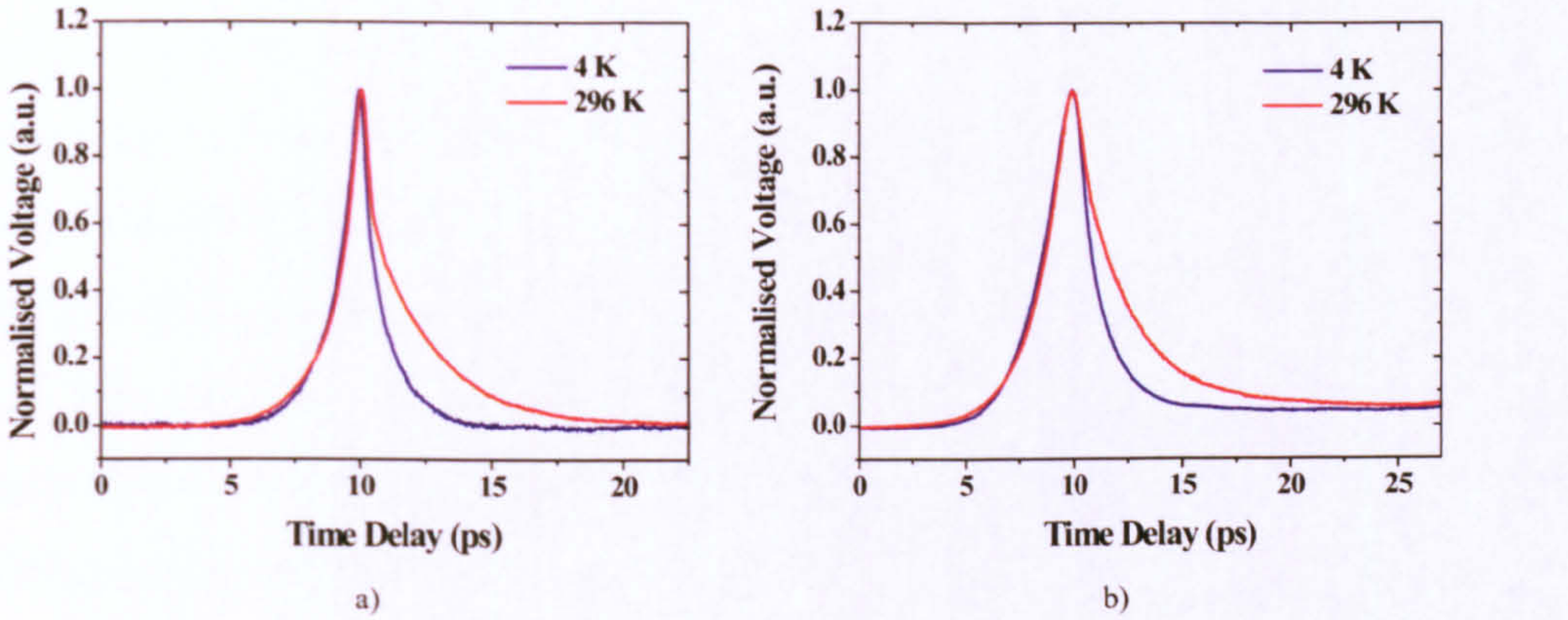

Figure 4.21: Time domain measurements of a) the input and b) the output pulses of a 4 mm THz interconnect at 296 K and 4 K.

and 296 K of the input and output pulses respectively, generated at 60 mW optical power, clearly demonstrating the difference in pulse widths. We also observe that the pulse broadening along the microstrip line at both temperatures is in the region of 0.9 ps, which suggests that the transmission properties of the BCB dielectric have not altered in the transition from room to cryogenic temperatures. However, if we consider the peak THz voltages as a function of power at the two temperatures in Figure 4.22a and Figure 4.22b, we see a decrease in the *difference* between the input and output voltage maximums as we move to 4 K from 296 K.

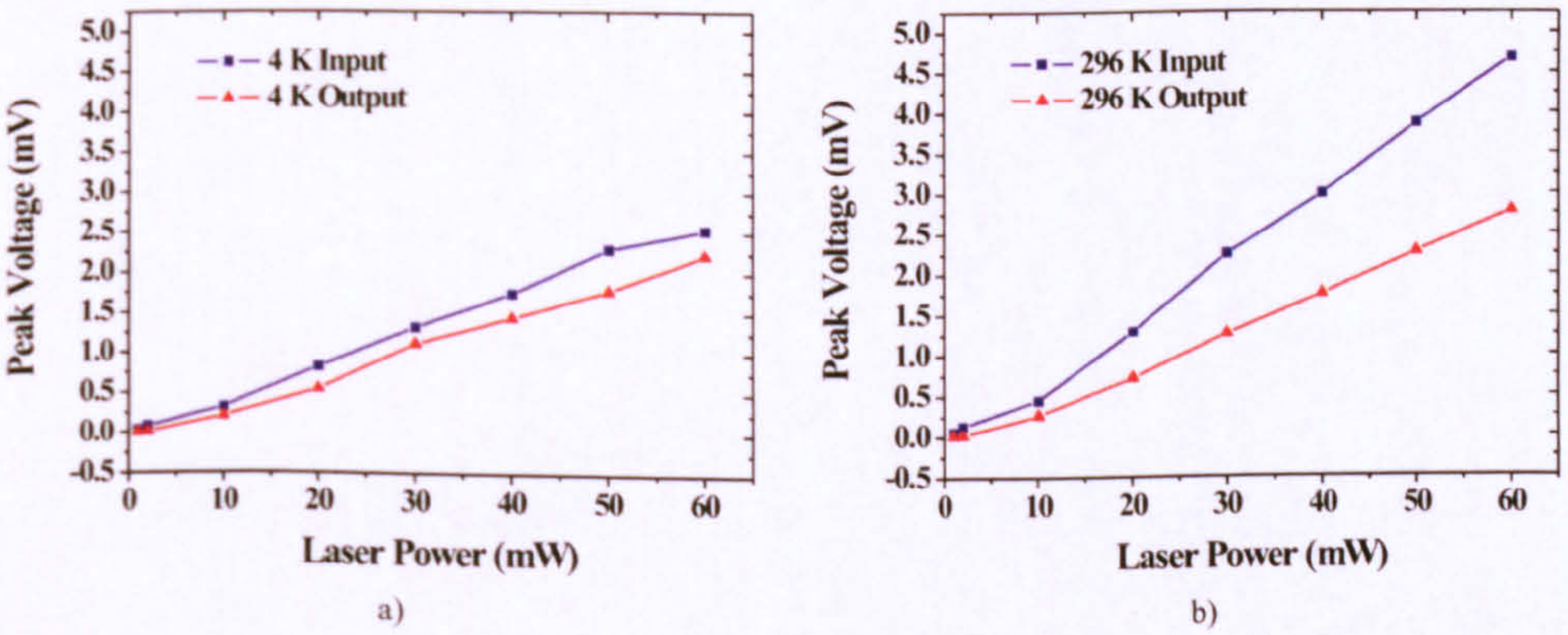

Figure 4.22: Measurements of the peak input and output voltages of a THz signal at a) 4 K and b) 296 K.

This is suggestive of a reduction in attenuation of the THz signal when propa-

gating along the microstrip structure at cryogenic temperatures, most likely attributable to a reduction in conductor resistance, and therefore loss, at the lower temperature. This process has demonstrated that gold microstrip on BCB is a suitable propagation medium for THz radiation for a broad temperature range of between 4 K and 296 K, and also that LT-GaAs is a suitable emitter and detector of THz radiation within this temperature range [92, 93]. The device design presented here is therefore suitable for picosecond measurements of semicoductor based systems, as discussed in Chapter 1.

Chapter 5

First Generation Terahertz Filters

5.1 Introduction

Having in the previous chapter demonstrated the generation and detection of picosecond time scale voltage transients using LT-GaAs photoconductive switches integrated into on-chip microstrip interconnects, the introduction of microstrip band-stop filters at positions along the interconnect, as discussed in Chapters 2 and 3, is now appropriate. Filter structures create a high concentration of electric field lines on resonance, in comparison to transmission line structures, and so provide a sensitive probe of overlaid materials affecting the dielectric environment of the field and altering the filter's resonant frequency. This chapter will consider measurements performed on First Generation devices based on the dimensions discussed in Chapter 3, including single, dual and triple cascaded filter structures. Comparisons between measured and simulated data are provided.

5.2 Single Frequency Filters

In order to demonstrate proof of principle of operation for the band stop filter designs presented in Chapter 3, Section 3.2, it was appropriate to first fabricate a device containing a single resonator, as opposed to a cascaded device. The frequency of operation was chosen as 600 GHz which, as shown in Chapter 4, should

lie in approximately the centre of the device bandwidth, with corresponding stub dimensions of $5 \times 82\ \mu m$. A graphical representation of the device is given in Figure 5.1. Measurements on this device were performed using the optical pump-probe experiment described in the previous chapter, again utilising a 100 fs pulse width, 80 MHz repetition rate Ti:Sapphire laser source.

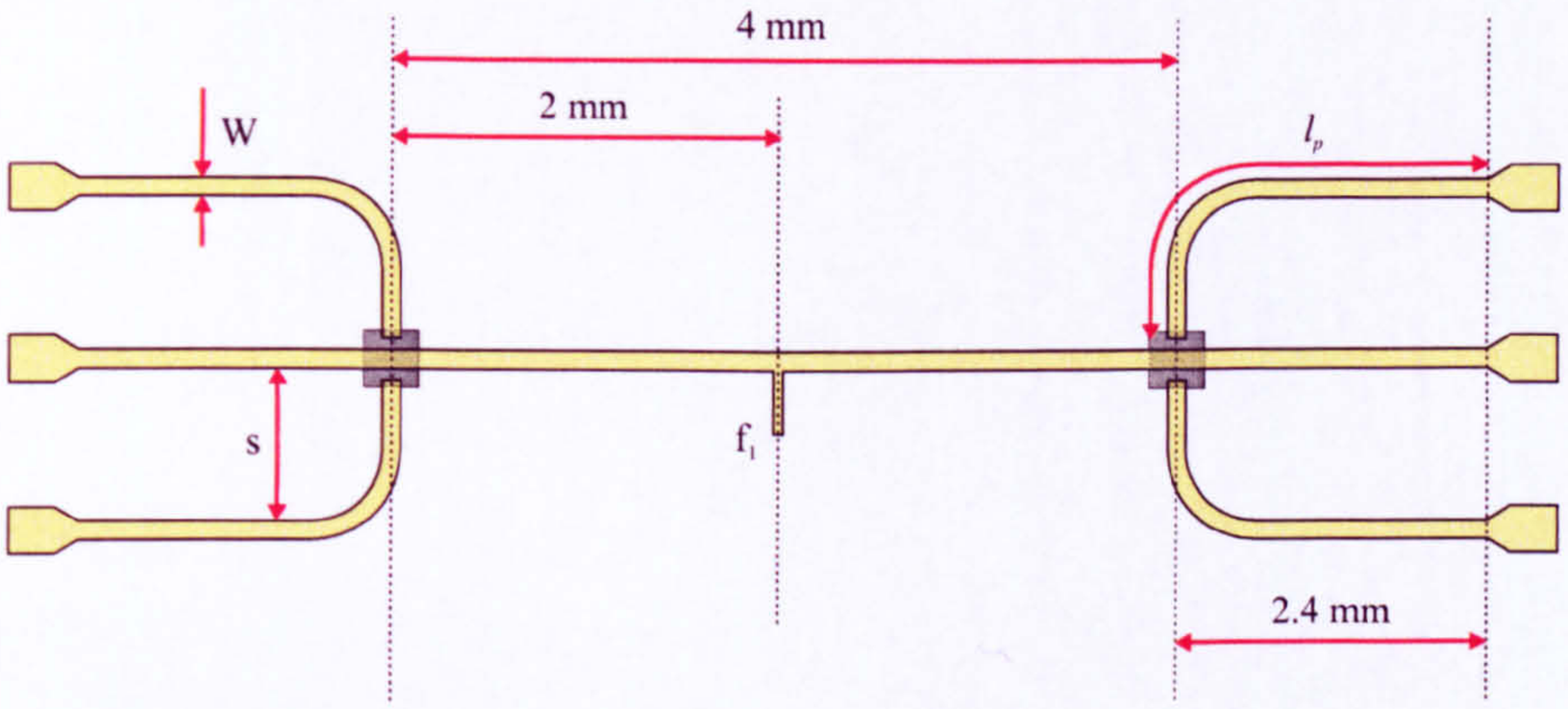

Figure 5.1: Graphical representation of a transmission line of width W = 30 μm, with active region of length 4 mm between two photoconductive switches, and non-active regions of length 2.4 mm. The device contains a filter, f_1, of dimension $5 \times 82\ \mu m$ operational at 600 GHz, situated 2 mm from either switch. Probe arms are of length $l_p = 3.0$ mm, separated from the central transmission line by s = 700 μm

The origins of the reflections discussed in Chapter 4 are well understood and, since the reflected peaks are not used in Fourier transforms, future scans were performed in the time window between start of the THz pulse and the first reflection. Figure 5.2 shows a comparison between the input and output pulses of a THz interconnect containing a 600 GHz filter, demonstrating a generated pulsewidth of 0.69 ps, which is comparable to those measured for the simple interconnects in Chapter 4. Immediately one can recognise a change in pulse shape between the input pulse and the output after transmission through the filter, caused by the removal of a frequency band from the broadband output signal. The frequency removal leads to time domain oscillations, some of which form a superposition with the main peak, as evidenced by the 'shoulder' labelled in Figure 5.2. Such oscillations can be replicated numerically by performing an FFT of the input pulse from Figure 5.2 and artificially introducing a brick-wall filter, by setting the real and imaginary

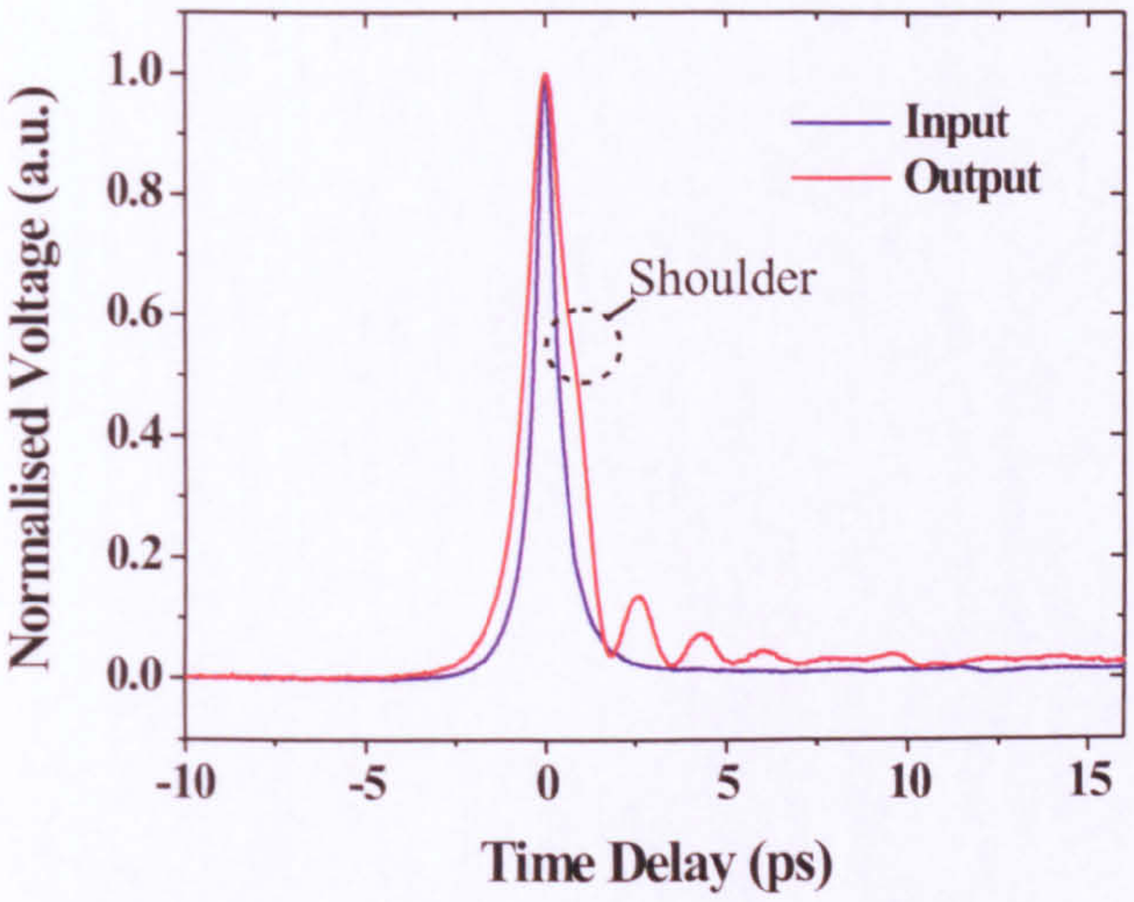

Figure 5.2: Comparison of the input and output signals of a transmission line containing a 600 GHz quarter wave resonator, showing a shoulder formed on the output by a superposition of time domain oscillations with the main THz signal.

FFT components to zero for a range of frequencies equal to the band stop region of the 600 GHz filter. An inverse FFT can then be performed on the resulting data. The results of this are shown in Figure 5.3 which demonstrates similar oscillations in the time domain to those seen in a real filter device, including the 'shoulder' seen in Figure 5.2.

The slight pulse broadening observed between the input and output pulses in Figure 5.2 is caused by signal dispersion within the line due to mismatched phase velocities of the broad band of frequencies contained within the THz pulse, as discussed in Chapter 2. We note that the brick-wall filter is applied to the *input* pulse from figure 5.2, and so pulse broadening is not observed in Figure 5.3 since no dispersion has occurred.

The time window available for measurements on the real device was $\approx$ 26 ps and yet, as may be inferred from Figure 5.2, the oscillations in the tail of the pulse caused by the filter may well extend beyond this range. Since this data is hidden in signal reflections it is unusable and is therefore not included in our FFT

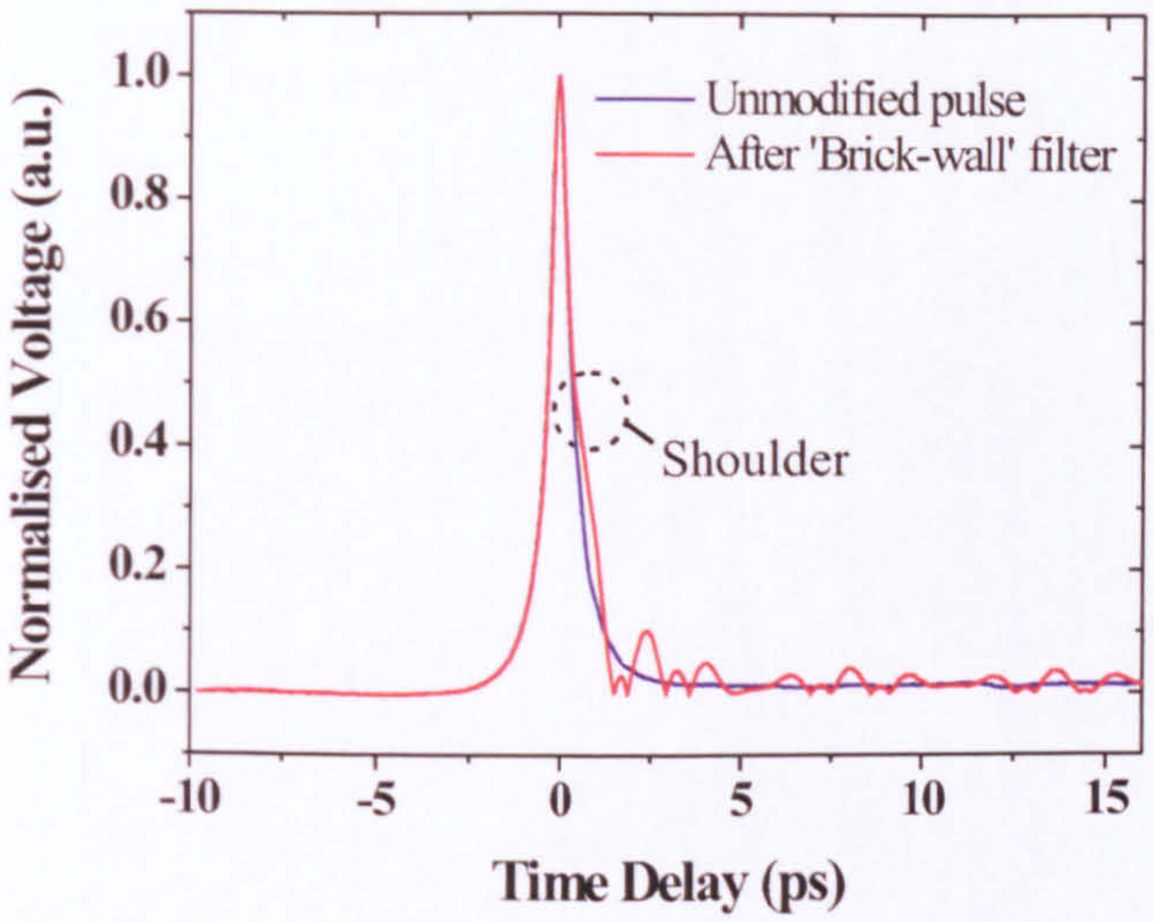

Figure 5.3: Graph of an unfiltered THz input pulse compared to the same pulse which has been modified by introducing an artificial brick-wall filter at 600 GHz.

calculations. However, due to the decreasing amplitude of the tail features, the effect of data beyond the 26 ps window is unlikely to have a significant effect on an FFT of the pulse shape. Figure 5.4 shows S_{21} characteristics for this filter and, as expected, the loss of data beyond the sampling window has not caused deviation in the measured signal from the expected response. Also contained in Figure 5.4 is a plot of the simulated transmission for an identical device, performed in Sonnet. The measured frequency position of the device resonance agrees very well with the simulated value. The slight difference in peak position is likely a result of fabrication tolerances such as edge roughness. The device also exhibits up to 1.2 THz bandwidth as for the interconnects analysed in the previous chapter. It may also be seen that at higher frequencies, the loss in the measured system deviates from the simulated response, increasing to higher values. This is due to limitations in the simulation such as the inability to simulate the effects of edge roughness whilst maintaining reasonable simulation times. However, the important features of the device operation, i.e. the resonance position, bandwidth and signal to noise ratio still allow useful measurements to be performed.

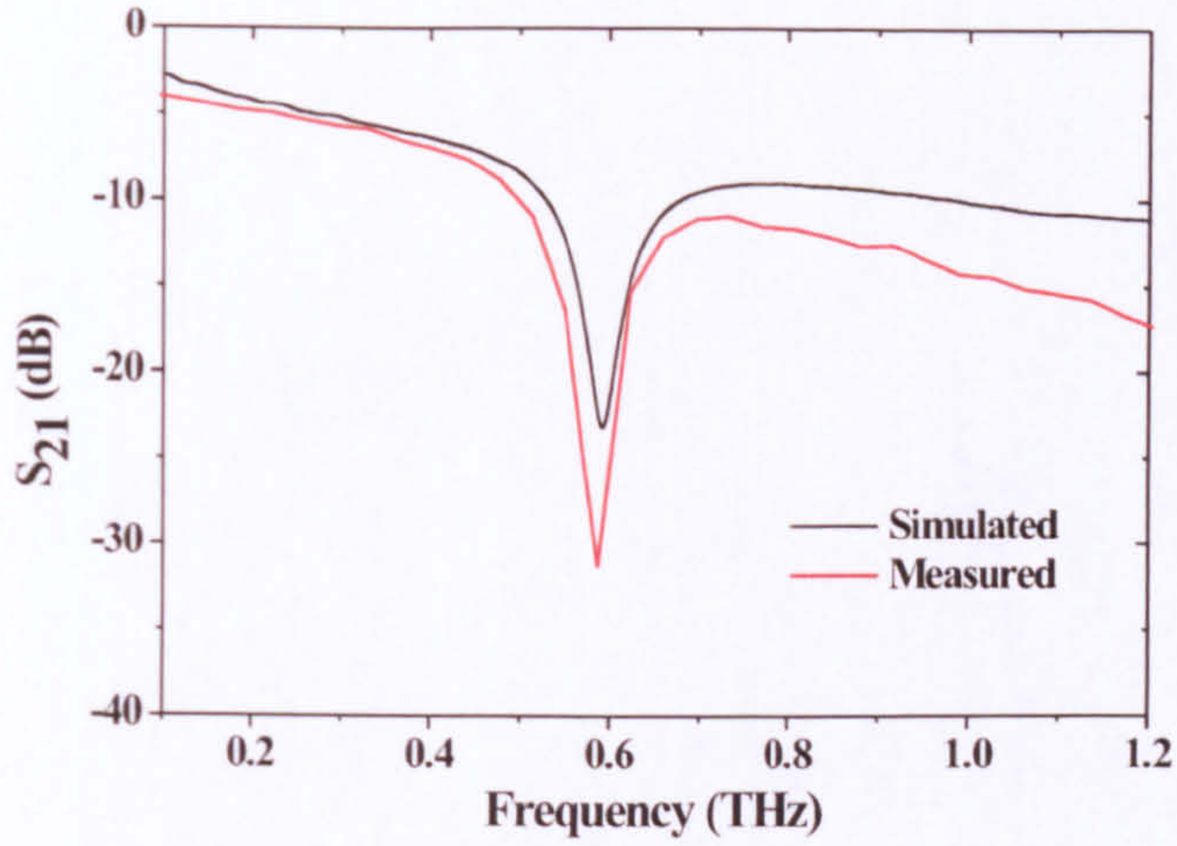

Figure 5.4: Graph of the measured and simulated S_{21} characteristics for a THz microstrip interconnect containing a 600 GHz filter element.

One of the main limitations to this design arises from the restricted sampling window available for measurements, which in turn limits the frequency resolution to, in this case, $\approx$ 37 GHz. The origin of the reflections which constrain the sampling time are described theoretically in Chapter 4, but in order to assess them empirically a slight modification was made to the first generation filters which involved increasing the non-active transmission line region from 2.4 mm to 4.8 mm (Chapter 3, Section 3.2). The time of travel for the *first* reflection should increase proportionally by a factor of two, doubling the sampling window and therefore doubling the frequency resolution of the Fourier transforms. The increase in delay to subsequent reflections must be calculated with reference to Figure 4.9, Chapter 4. The reflection delays are given in Table 5.1, alongside calculations for the effective and relative permittivities. The device with lengthened probe arms was also designed to incorporate a 1 THz filter, instead of 600 GHz, to test the ability of the devices to resolve a resonance close to the apparent upper limit of 1.2 THz. Figure 5.5 shows a comparison between long scans performed on the 600 GHz filter discussed above, and the new 1 THz filter with the extended non-active regions.

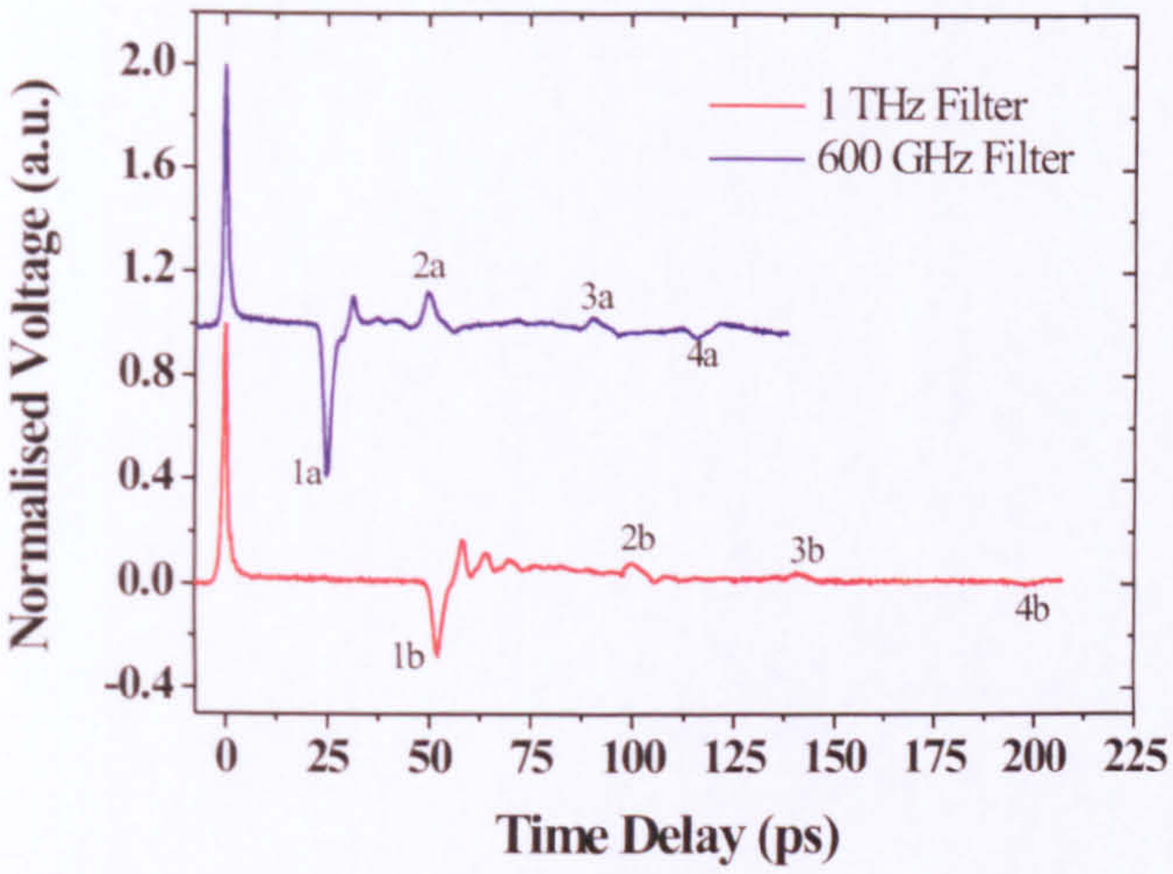

Figure 5.5: Comparison of long time domain scans of a 600 GHz device and a 1 THz device with 2.4 mm and 4.8 mm non-active regions respectively. The four reflections identified in Chapter 4 are labelled on each trace, with suffix a or b for the 600 GHz and 1 THz traces respectively.

Ref.	Time Delay, t (ps)	Distance, d (mm)	ϵ_{eff}	ϵ_r
1b	50.19	9.60	2.4600	2.8932
2b	100.06	19.20	2.4443	2.8729
3b	140.51	27.20	2.4017	2.8176
4b	199.17	38.80	2.3715	2.7785

Table 5.1: Table showing positions of reflected signals a 1 THz filter device (with extended non-active regions) as timed from the THz pulse, generating an average relative permittivity of $\epsilon_r = 2.84$, compared to the published value of 2.65 [84].

All the reflections identified in Figure 5.5 occur at the expected positions and provide relative and effective permittivities of 2.84 $\pm$ 0.06 and 2.42 $\pm$ 0.05 respectively, in excellent agreement with the devices measured in Chapter 4.

A comparison between the output signals for the 1 THz and 600 GHz filters is shown in Figure 5.6. Again, the effect of the filter element on the output pulse shape is readily evident, though the change in shape when compared to the output from the 600 GHz device is different due to a different frequency range being removed from the broad band signal.

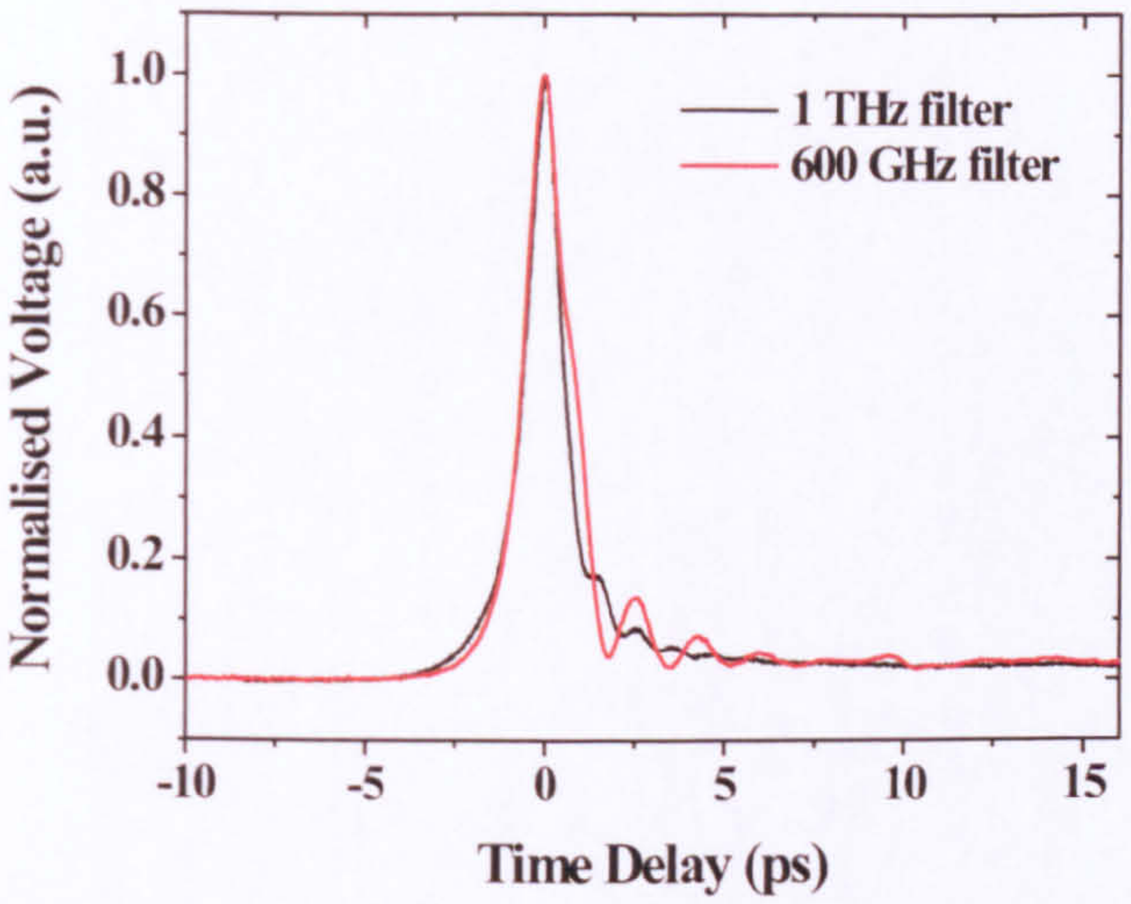

Figure 5.6: Comparisons between the output signals of a 1 THz filter and a 600 GHz filter.

Analysis of the S_{21} characteristics for the 1 THz filter in Figure 5.7 demonstrates the increase in frequency resolution gained by the lengthened sample window (i.e. a longer data scan) demonstrated in Figure 5.5, enabled by extending the non-active transmission line regions. As predicted, the frequency resolution has doubled from 37 GHz for the 600 GHz filter, to $\approx$ 18 GHz for the 1 THz filter. We also see similar device characteristics in terms of a 1.2 THz device bandwidth and a maximum 800:1 SNR.

The simulated bandstop position is again slightly mismatched with the measured device. This is again attributed to edge roughness and fabrication tolerances of the filter which, at higher frequencies (and therefore shorter stubs) has an increased effect on resonance position. It may also be an effect of the (still relatively low) frequency resolution which masks the true minimum of the band stop response. This device is the highest known recorded microstrip band stop filter to date, whilst the previous 600 GHz device is the highest frequency published microstrip band stop device [94].

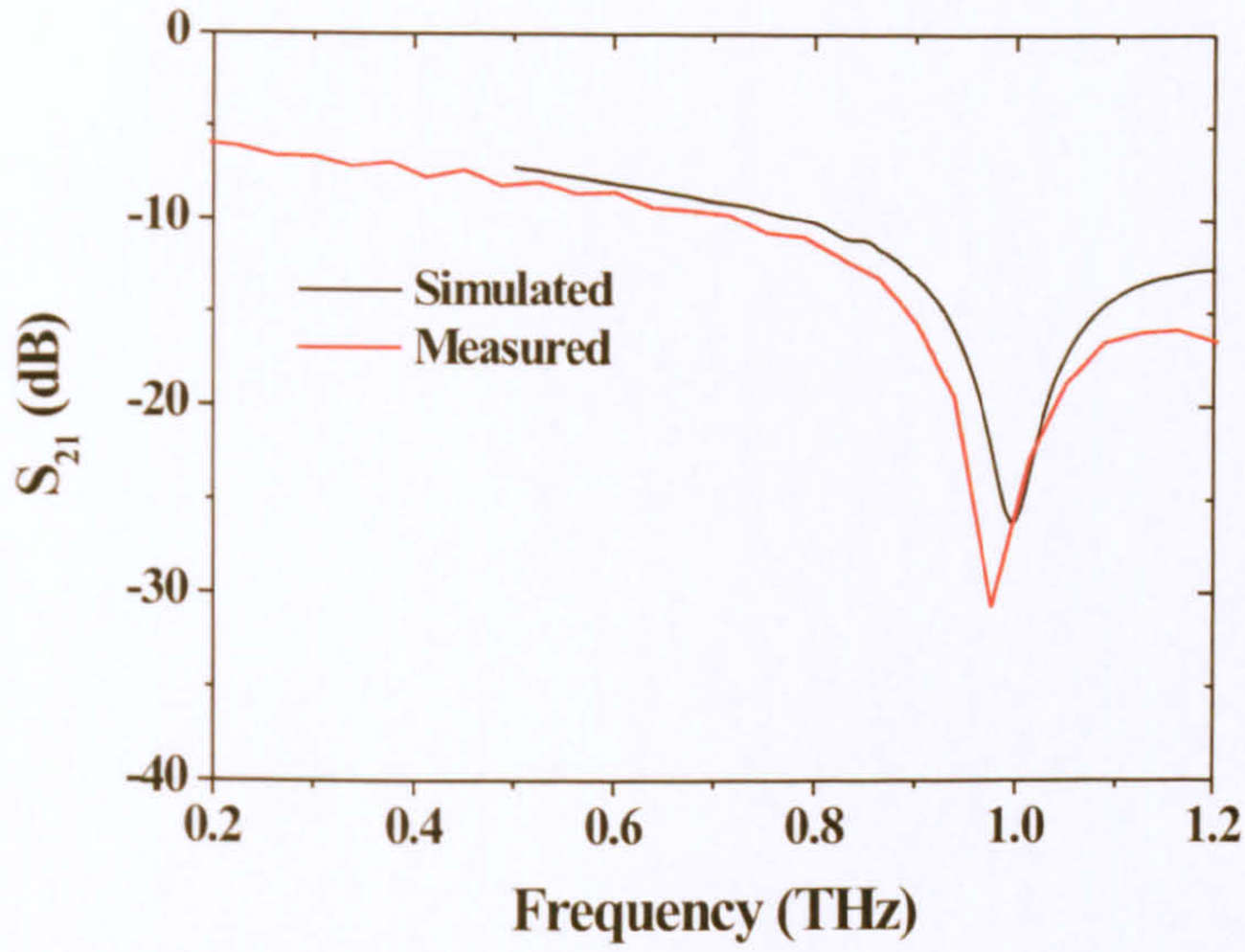

Figure 5.7: S_{21} characteristics for a microstrip interconnect containing a 1 THz band stop filter, compared to simulated parameters for a device of equivalent geometry.

5.3 Multiple Frequency resonators

Having demonstrated proof-of-principle of operation for the band stop filters designed for this work, the next logical step was to analyse a cascaded device, i.e. one which contains separate resonators, connected by a THz interconnect and operating at different frequencies within the system bandwidth. The first such device to be fabricated and measured consisted of a 260 GHz filter in parallel with a 600 GHz filter. Since two frequency bands are being removed from the spectrum of the generated THz signal (instead of a single band as for the previous devices), the time domain oscillations created a much more complex tail to the THz pulse, seen in Figure 5.8.

The input and output pulses were somewhat larger in magnitude for this device than the single frequency devices examined previously, with an input pulse width of 1.33 ps compared to < 1 ps for all previous devices, with the exception of the device measured in Chapter 4, Section 4.4 at 4 K. This may be be attributed to the LT-GaAs used for this and subsequent devices being fabricated using a Manchester MBE facility, and having carrier lifetime of $\approx$ 450 fs as measured

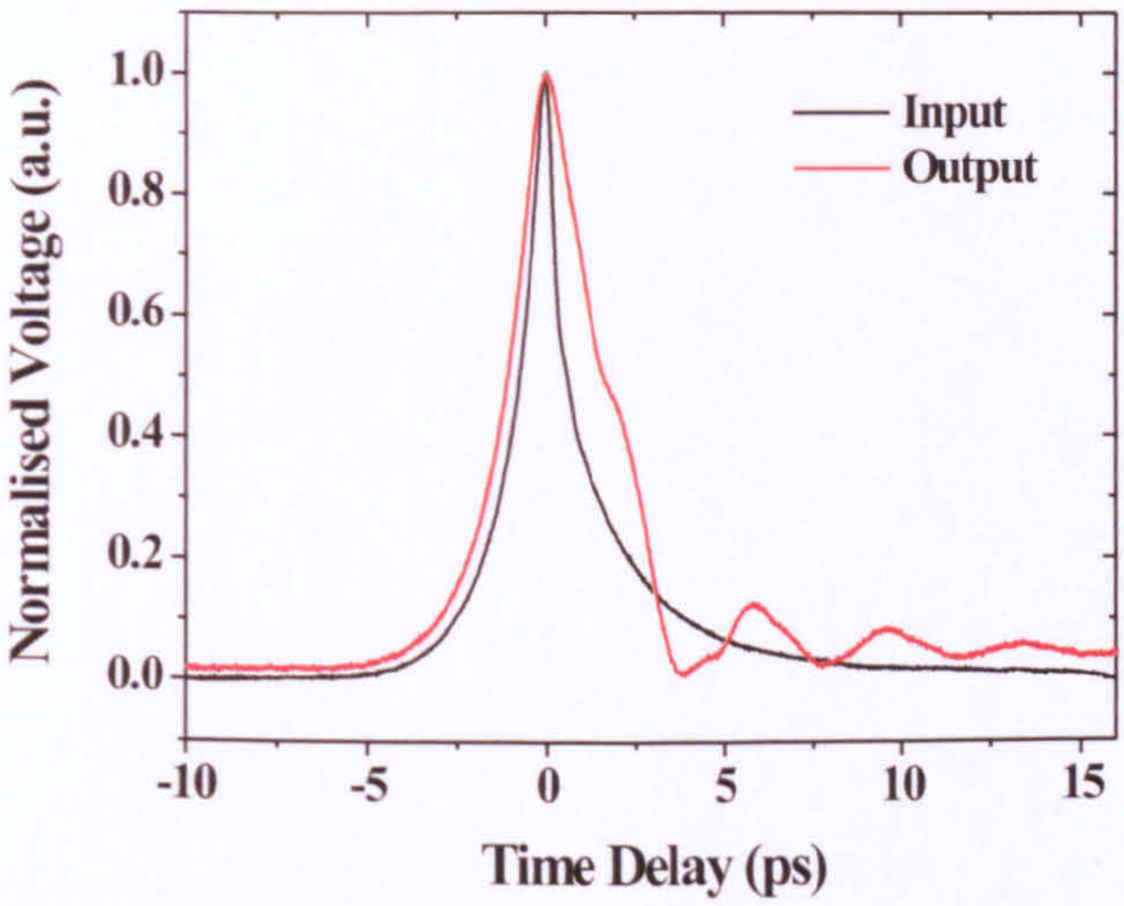

Figure 5.8: Comparison of the input and output pulses for a 4 mm microstrip interconnect containing filters operating at two independent fundamental frequencies of 260 GHz and 600 GHz.

using broadband THz reflectivity (c.f. a measured value of 250 fs for the previous thin film, grown at Cambridge facilities). However, referring to Figure 5.9 it may be seen that the total system bandwidth appears unaffected by this change.

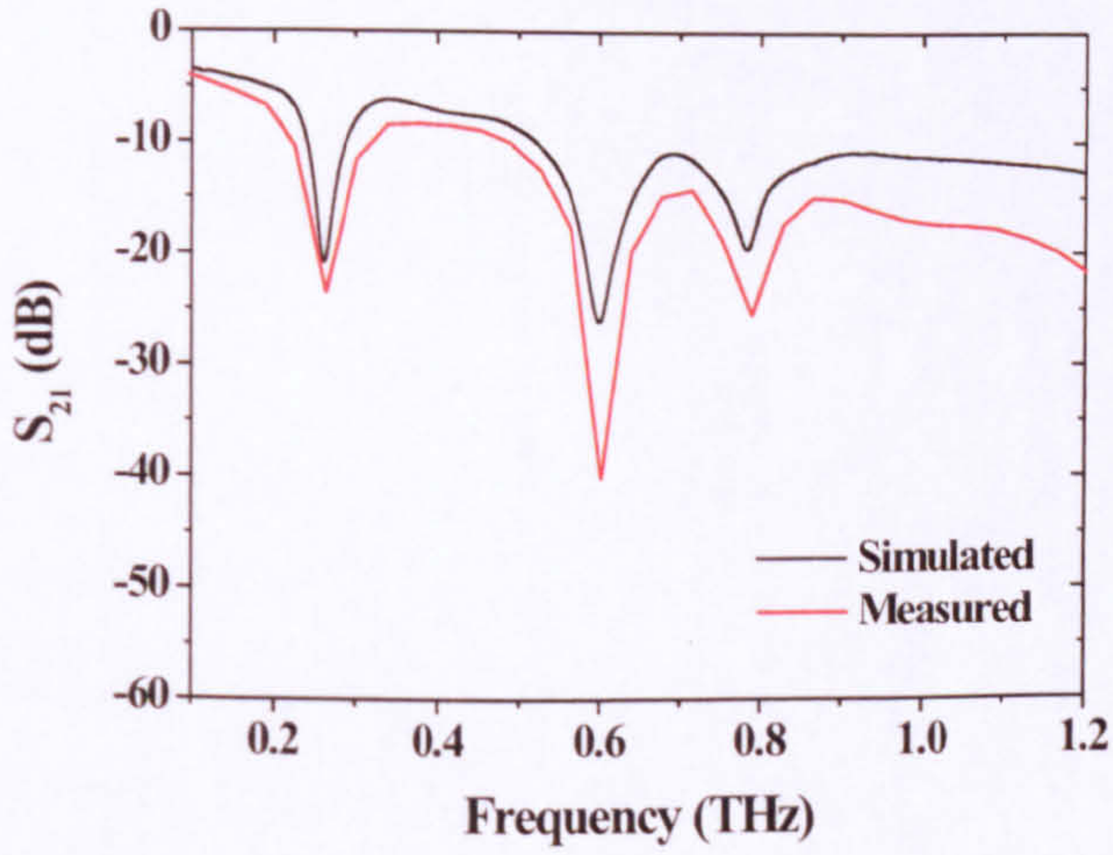

Figure 5.9: Measured S_{21} characteristics for a dual frequency device compared to simulated values, with resonators operating at 260 GHz and 600 GHz, with a third resonant feature identified as the third harmonic of the 260 GHz resonator.

Figure 5.9 shows a similar difference in the high frequency losses between simulated and measured data as to that seen in previous devices. The measured device exhibits the expected resonances at 260 GHz and 600 GHz, and also provides empirical proof of the filter harmonics in the form of the feature at 780 GHz, which corresponds to the third harmonic of the 260 GHz stub. An important criteria of cascaded designs for multiple frequency sensing of overlaid material, is clear spatial isolation of resonances in the frequency domain to avoid overlap of the responses when individual filters are loaded. Figure 5.9 shows this condition to be satisfied for the two frequency cascade device.

In order to test the electrical isolation of the filters, each was individually loaded with a dielectric test material. A commercial photoresist, Shipley 1813 (S1813), was chosen as a test material due to prior knowledge of processing parameters. The resist had previously unknown refractive index at THz frequencies, so a free-space THz spectroscopy study was performed through a 180 μm layer of resist, deposited on a 1 mm thick, spectroscopy grade high resistivity silicon wafer, which is transparent to THz radiation in the frequency band analysed, for comparison with the on-chip analysis to be performed. Figure 5.10 shows a reasonably constant refractive index and relative permittivity for the S1813 of n = 1.65 and $\epsilon_r = 2.72$ respectively, up to a frequency of 2 THz.

To ensure that the filters were loaded to saturation, a large quantity of S1813 was deposited onto each one individually using micropipetting techniques using a Narishige microinjector and micromanipulator. The thickness of deposited material was measured using a surface profiler, and found to be 16 μm and 14 μm over the 260 GHz and 600 GHz stubs. From simulations, the expected shift for the 260 GHz and 600 GHz filters loaded to saturation is 35 GHz and 80 GHz respectively. Figure 5.11a and b show the shifts in resonance position for individual loading of the 260 GHz and 600 GHz filter, measured at 37 GHz and 77 GHz, agreeing well with the simulated predictions within the limitations of device resolution. Also seen in Figure 5.11a, is that loading of the 260 GHz device to saturation, whilst leaving the 600 GHz resonator unloaded, causes the third harmonic of the 260

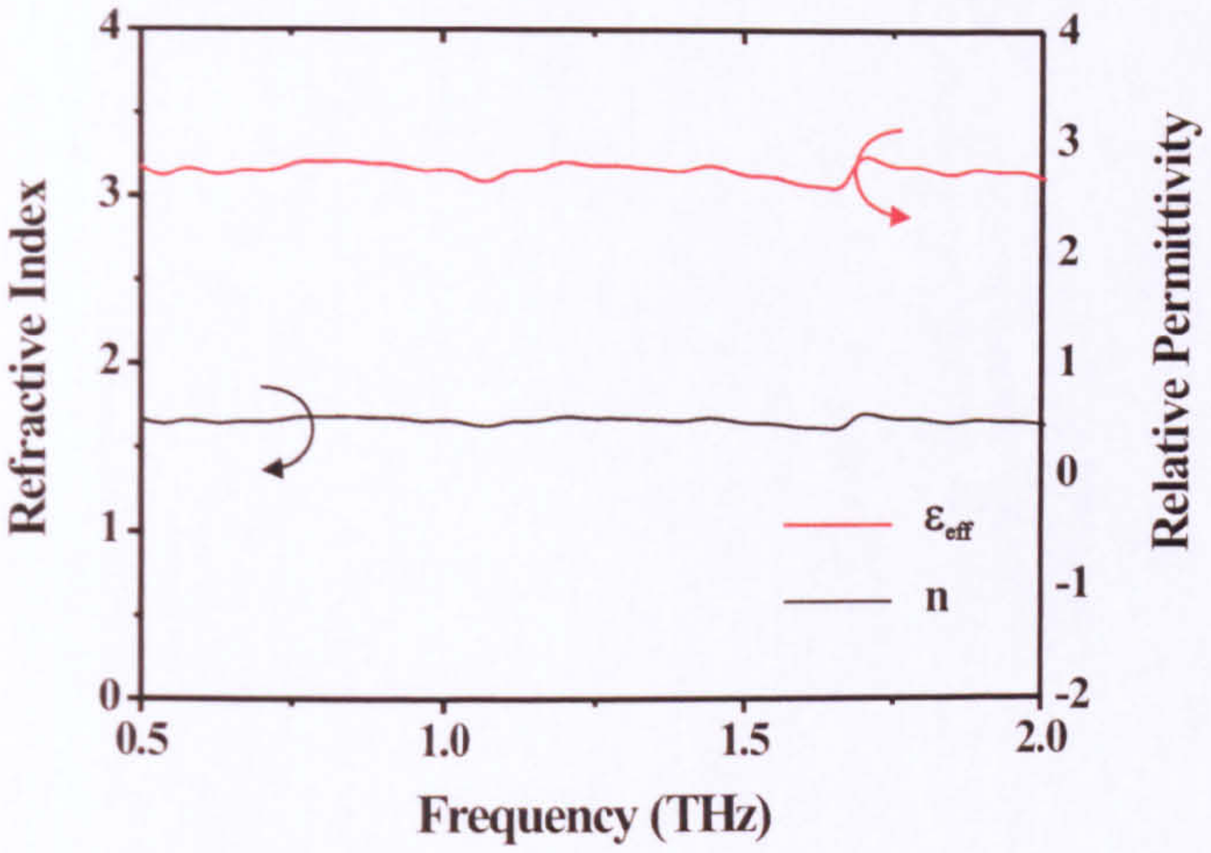

Figure 5.10: Results from a broadband THz free space measurement of the refractive index and relative permittivity of commercial photoresist S1813, performed through a 180 μm layer deposited on a spectroscopy grade high resistivity silicon wafer.

GHz filter to spatially overlap the second resonator's frequency response. The resulting pulse superposition may interfere with measurements of the resonant shift produced by the 600 GHz device under dielectric loading, should the 600 GHz shift not be great enough to maintain spatial separation from the harmonic feature. It was this limitation that spurred the development of a new stub design for lower frequency resonators, discussed in Chapter 3, Section 3.3, which was incorporated into second and third generation devices.

The data presented in Figure 5.11 demonstrates good *electrical* isolation between the two filters, i.e. individual loading of one filter does not cause a frequency shift in the response of the second, a necessary property for individual sensing at each stub frequency. The concept of cascaded filters was further demonstrated by introducing three stubs to the active region of a new device, operating at frequencies of 800 GHz, 1 THz and 1.2 THz. The high frequencies would utilise the upper extreme of the device bandwidth, whilst lower frequency filters were omitted to remove harmonic features which would overcrowd the frequency spectrum. The S_{21} data displayed in Figure 5.12a shows successful operation of the three

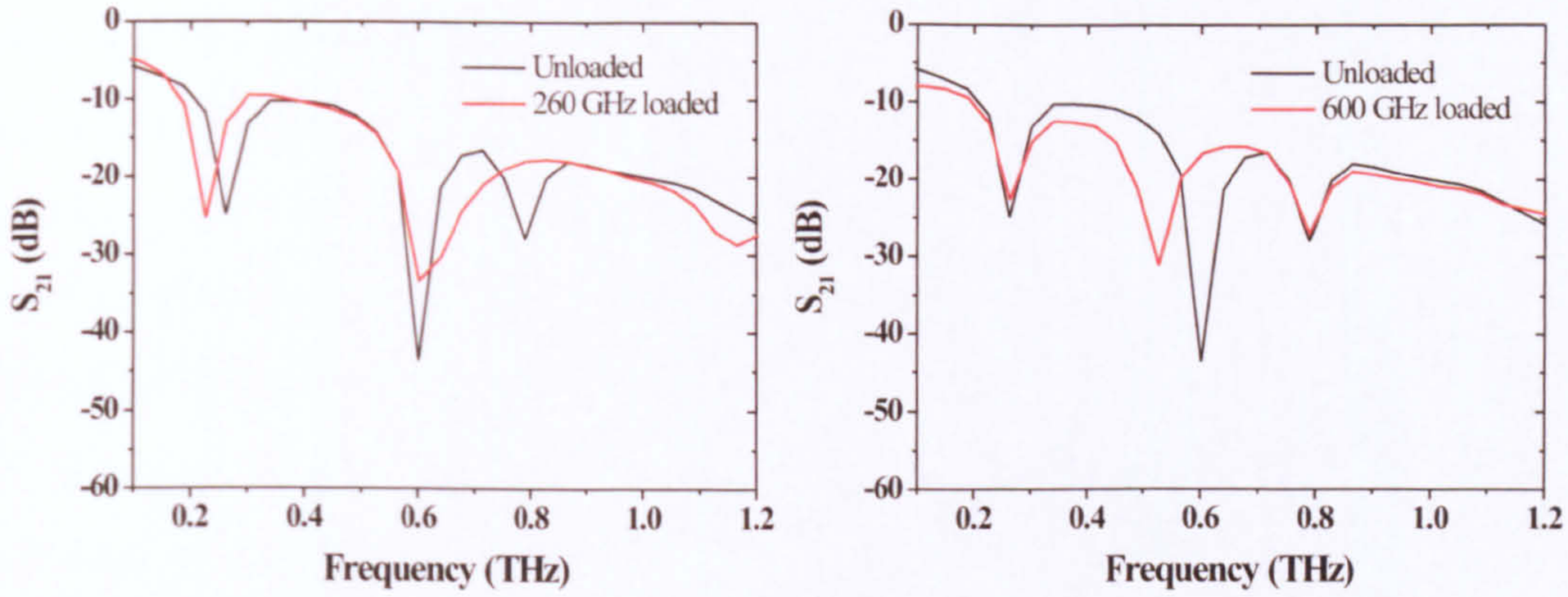

Figure 5.11: Individual frequency shifts of a) 260 GHz and b) 600 GHz resonators under application of dielectric load of thickness $\approx 16\ \mu m$ and $14\ \mu m$ respectively.

frequency device, as well as a comparison between the unloaded response and the saturation response of the three filters under application of the same photoresist material.

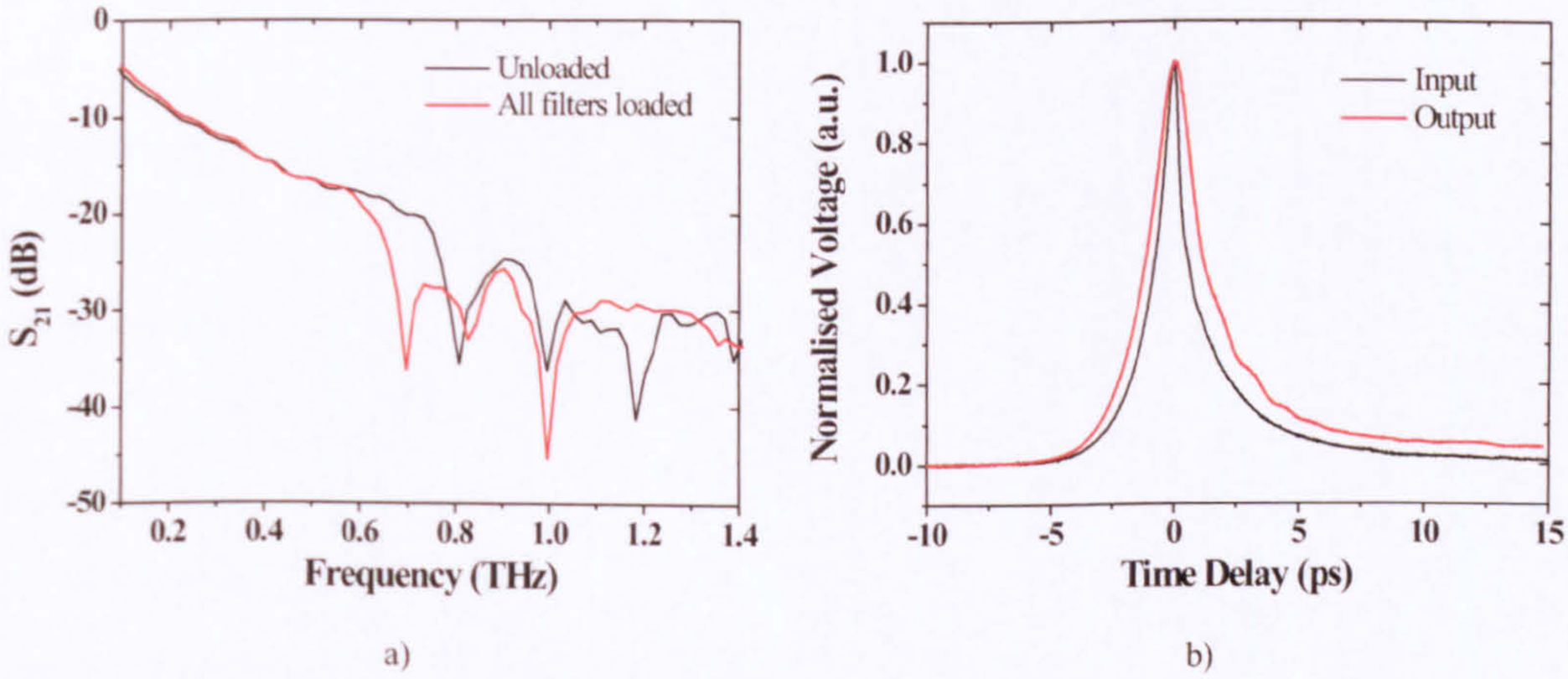

Figure 5.12: Showing a) S_{21} characteristics for a triple cascade device operating at 800 GHz, 1 THz and 1.2 THz, showing the unloaded and saturated responses, and b) a comparison of the input and output pulses.

Figure 5.12b shows a comparison of the input and output pulses for the three frequency device, and again we see an increase in FWHM from the earlier, single frequency devices, from ≈ 0.7 ps previously, to ≈ 1.33 ps on the input pulse for

this device. Although the expected three filter responses are present in Figure 5.12a, the time taken in producing a clean enough signal to generate the displayed response suggests that the increased pulsewidths generated in the new LT-GaAs material, experienced for both cascade filters discussed so far, may be limiting the upper bandwidth of the device. This made the 1.2 THz filter response extremely difficult to resolve and it was evident that the peak of the rejection region was buried in the noise floor. However, application of overlaid S1813 photoresist to each filter to saturation produced shifts of 112 GHz, 137 GHz and 201 GHz for the 800 GHz, 1.0 THz and 1.2 THz filters, agreeing well with simulated saturation shifts of 108 GHz, 134 GHz and 196 GHz respectively. Although the resonances in this device were in the expected frequency positions, the limitation in system bandwidth which affects the higher frequency filters suggested that further spectroscopic analysis of overlaid materials would be more appropriate using the dual frequency device discussed previously.

5.4 Characterisation of Overlaid Dielectric Material

Although the dual cascade device measured in Section 5.3 is limited by the close proximity of the 780 GHz harmonic resonance to the 600 GHz filter response, loading each stub simultaneously with the same material avoids overlap of the two features and allows measurements to be performed on both filters. A systematic characterisation of the photoresist dielectric properties was performed on each stub by depositing a range of material thicknesses and producing a saturation curve of thickness versus frequency shift.

Initially, attempts were made to perform all deposition using micropipetting techniques involved heat-drawn glass capillaries, with inner tip diameters of $\approx 1.3\,\mu m$. However, there were two main hindrances encountered when depositing S1813 from a glass pipette. Firstly, under initial tests the photoresist was found to be strongly hydrophyllic, meaning weak polar bonds would form between the S1813 molecules and the glass surface creating a very low contact angle between the two.

In practical terms, this meant that upon attempted deposition of the material, photoresist would run up the sides of the capillary instead of forming an easily depositable bead on the end.

A solution to this problem was found by silinating the surface of the glass capillary to make it nonpolar, or hydrophobic (Figure 5.13). This has the effect of repelling hydrophyllic molecules such as S1813, causing it to bead on the end of the pipette with a high contact angle to the glass. The first silination process tested was vapour deposition of dimethyldichlorosilane, but polymerisation of the chemical often caused capillary blockage. The process was adapted by replacing the polymeric material with trimethylchlorosilane which, due to the presence of only a *single* chlorine per molecule, does not polymerise on a glass surface. This solution will be equally applicable when depositing biomolecular substances, such as DNA, which are often stored in hydrophyllic aqueous or saline based buffers.

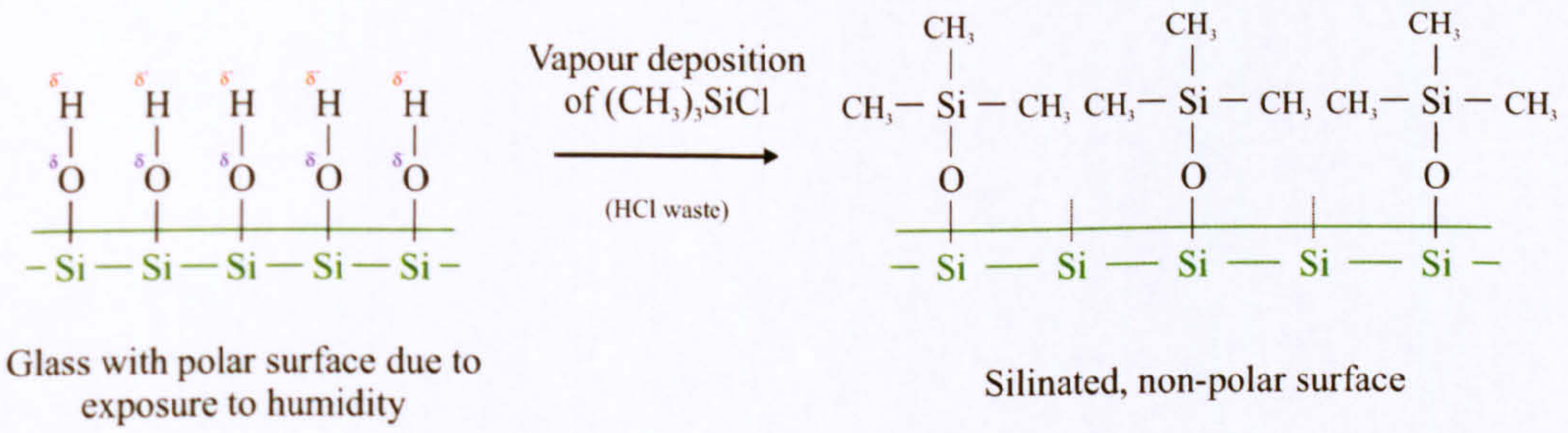

Figure 5.13: Demonstration of the silination process for a glass surface using trimethylchlorosilane.

A second difficulty was encountered when attempting deposition of layers thinner than 4 μm. Due to the viscosity of S1813 and the rapid evaporation of solvent from within the resist, deposition of such thin layers was impossible using a micrcappillary. Therefore, spin coating techniques were used to provide thicknesses of overlaid material in the range 0.5 μm to 4 μm, and thicknesses from 4 μm to 14 μm were provided by silinated capillary deposition.

After each deposition of S1813, the sample underwent a bake period at 115 °C to remove solvent from within the resist layer. The deposited substance was then

carefully measured using surface profilometry to ascertain the layer thickness. The sample was then remounted in the optical pump-probe arrangement described in Chapter 4 for measurements of the input and output pulse, followed by removal of the S1813 layer in acetone. This was repeated ten times for each device and pulse measurements were made after each cleaning cycle to test for device degradation or damage. Figure 5.14a and 5.14b show enhanced views of the resonance peaks measured after application of each dielectric load for the 260 GHz and 600 GHz filters.

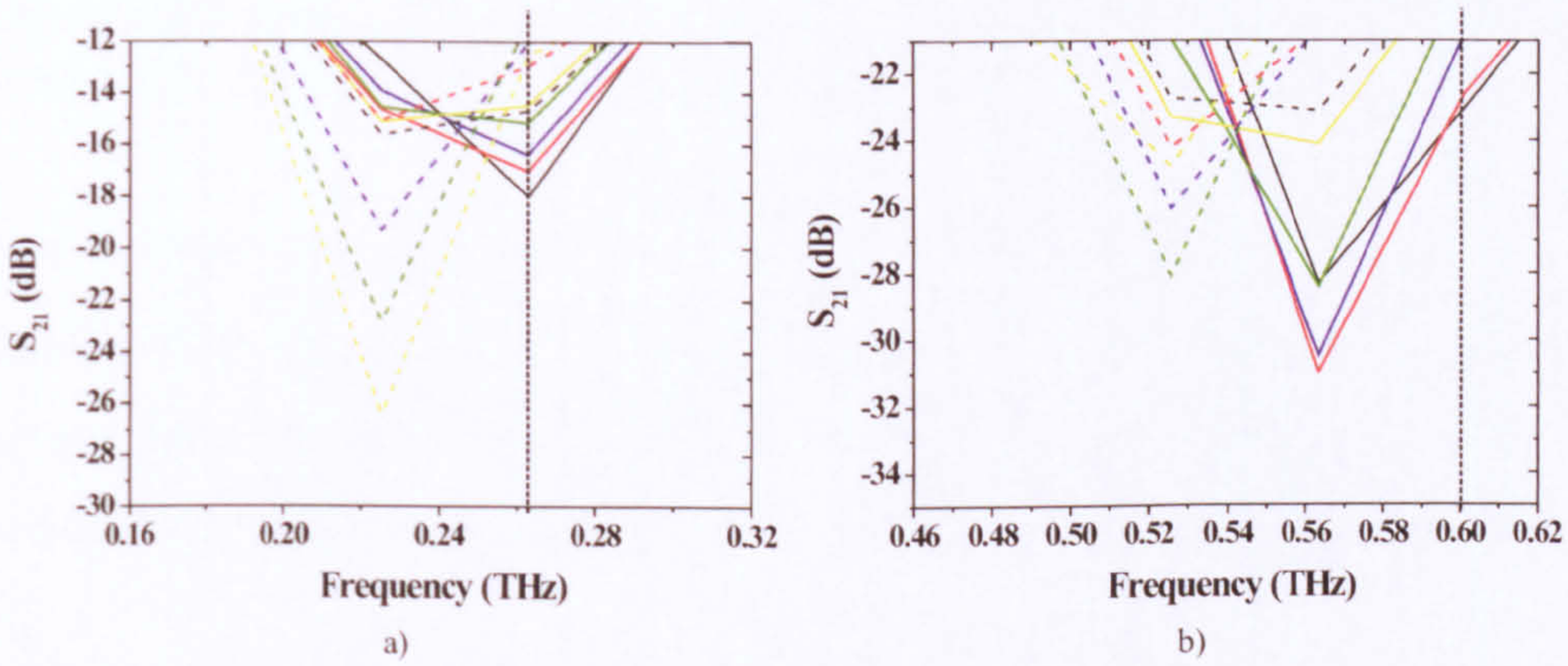

Figure 5.14: Resonance peaks measured for a) 260 GHz and b) 600 GHz filters respectively under application of S1813 loads of varying thickness. The dashed vertical line represents the unloaded peak position.

Evident in Figure 5.14 is that the low frequency resolution is restricting measurement of the exact shift experienced for a particular load thickness. However, the exact position of the resonance minimum, whilst not being directly measurable, will affect positions of the adjacent data points. This fact may be utilised to provide a more accurate sense of the frequency shift using curve fitting techniques. For this, a cubic spline fit was used which passes around the original data points whilst calculating the likely curve between points to produce an accurate shape. The curve fits are shown for each filter in Figure 5.15a and 5.15b, each shift labelled with a number from 1 to 10 moving from the thinnest to thickest deposited material.

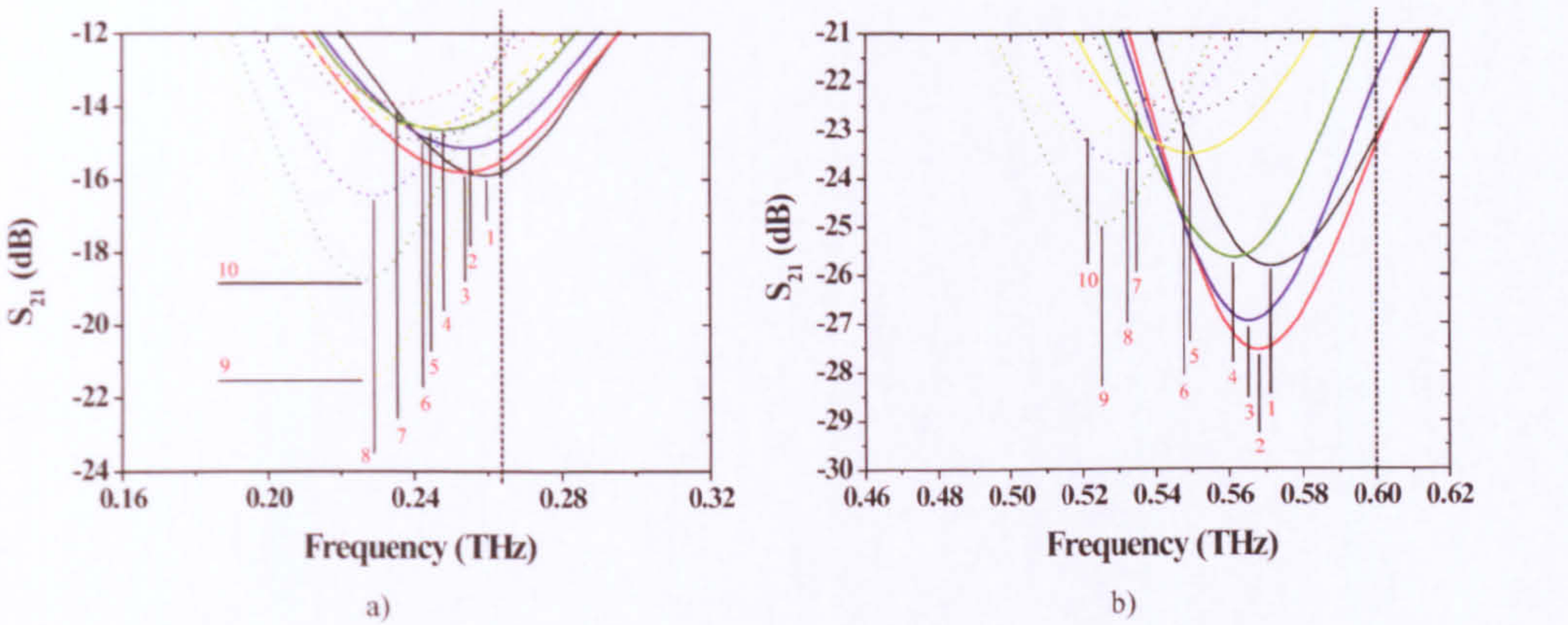

Figure 5.15: Cubic spline fitting applied to resonance peaks measured for a) 260 GHz and b) 600 GHz filters respectively under application of S1813 loads of varying thickness labelled 1 - 10. The dashed vertical line represents the unloaded peak position.

One now begins to appreciate the differences between each frequency shift for increasing thickness of dielectric load, allowing construction of saturation curves involving frequency shift versus thickness for each of the resonators. This data is shown in Figures 5.16a) and 5.16b) for the 260 GHz and 600 GHz filters respectively.

The data in Figures 5.16a and 5.16b are both compared to simulated curve forms representing overlaid dielectrics of permittivity $\epsilon_r = 2.00$, 2.72 and 3.50. The central simulated value was chosen as the permittivity measured for S1813 in a free space THz transmission measurement discussed in Section 5.3, whilst the remaining simulations were performed for permittivities approximately equidistant from the central value. It can be clearly seen from Figure 5.16 that the measured curve forms agree extremely well with the simulated permittivity of 2.72 and therefore also with the free space measurement. It may also be see that the curves for each filter begin to saturate at the same sample thickness of $\approx 4\ \mu m$. The deviation in the position of some measured data points from the simulated values is likely a result of the curve fitting, which itself arises again from the device's low resolution. The implication for first generation devices is that more accurate spectroscopy is performed by using sample thicknesses which saturate

the filter response ($> 4\ \mu m$).

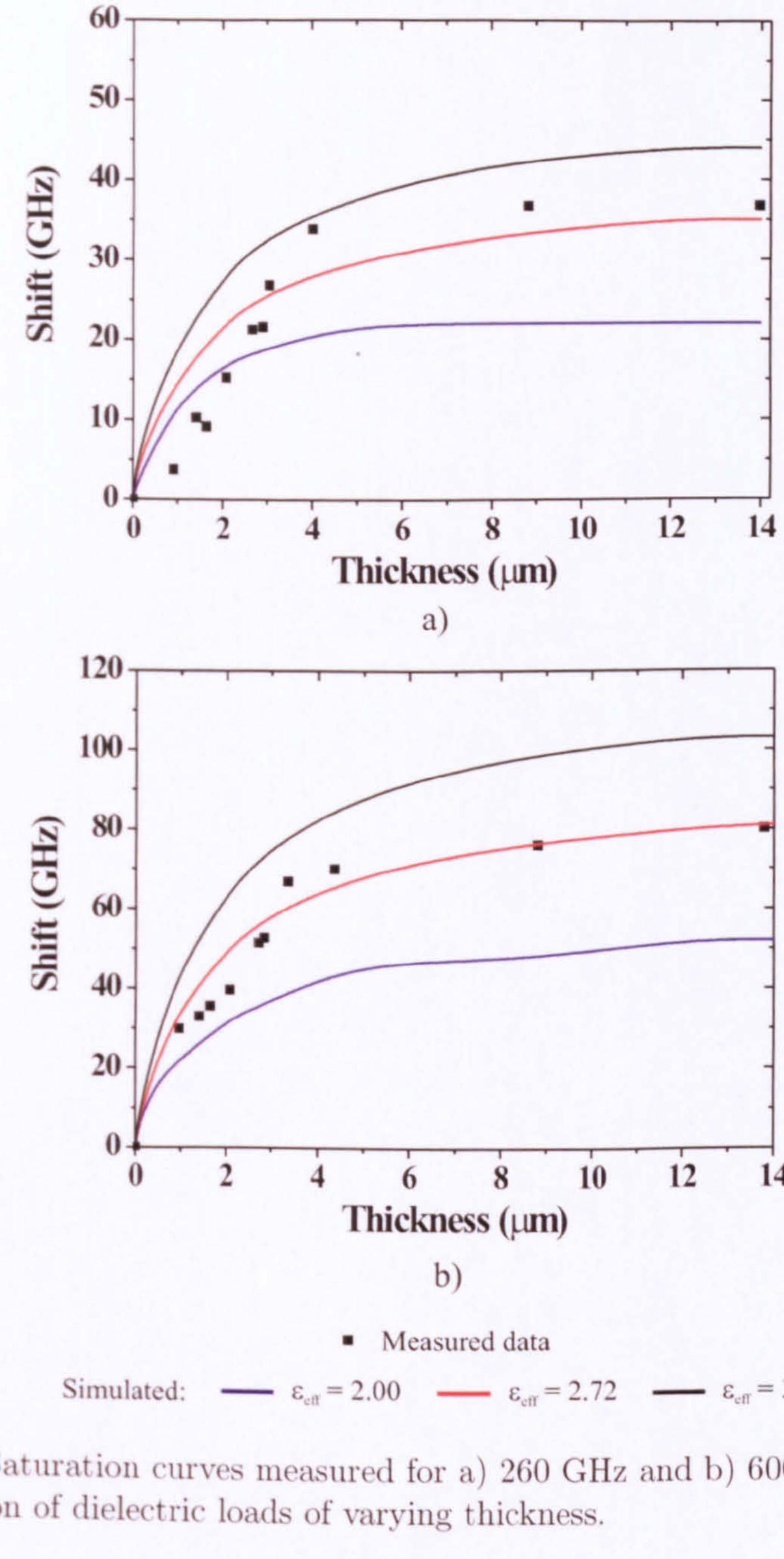

Figure 5.16: Saturation curves measured for a) 260 GHz and b) 600 GHz resonators under application of dielectric loads of varying thickness.

If we now consider the sample volumes required for the free space and on-chip measurement, we begin to appreciate one of the major advantages provided by an on-chip approach. Assuming ideal circumstances, the free space study requires a sample of even thickness over the focal point of the THz signal. The system

used had a focal diameter of 1 mm, and the thickness of material measured was 180 μm. Such thicknesses are required to produce an appreciable absorption in the THz signal. The volume of such a sample is $\approx 1.4 \times 10^{-10}$ m^3. If we now consider the on-chip alternative, measured at 600 GHz, the active stub region is 5 $\mu m \times 82$ μm, and requires a thickness of only 4 μm to achieve saturation. This represents a total volume of 1.6×10^{-15} m^3, corresponding to a reduction of five orders of magnitude. In reality, the sample volume for the free space approach was approximately two orders of magnitude larger than the ideal case in order to provide a large enough defect-free, uniform thickness surface area for measurements. Although the on-chip sample volumes were also slightly larger than the ideal case, it was only by a factor of four or five meaning a total sample volume reduction of six orders of magnitude. Such reductions in sample requirement represents a large step forward in the practical implementation of on-chip THz techniques for the characterisation of thin films across a range of applications.

Chapter 6

Second and Third Generation Filters for Biomolecular Sensing

6.1 Introduction

The previous chapter demonstrated the operation of novel single and cascaded band stop filters at THz frequencies, and their direct applicability for use in sensing of overlaid material at isolated THz frequencies. Some limitations of first generation devices were also revealed, predominantly caused by low frequency resolution as a result of reflections at interfaces within the microstrip device. This chapter describes second and third generation devices, designed to alleviate this problem and to create on-chip geometries suitable for detection of low permittivity overlaid films, such as biomolecules. S_{21} characteristics for the new devices are presented, followed by preliminary investigations into spectroscopic sensing of overlaid DNA films.

6.2 Second Generation Devices

The frequency resolution of first generation devices limited their application for sensing overlaid materials of low dielectric constant. The material measured in Chapter 5, Section 5.4 has a measured permittivity of 2.72, and yet still required

curve fitting of the S_{21} parameters to produce saturation curves of overlaid material thickness versus frequency shift. Therefore sensing materials of lower permittivity, including biomolecules such as single stranded ($\epsilon_r = 1.1$) and double stranded ($\epsilon_r = 1.4$) DNA [90], would not be possible using this generation of devices. Modifications to the non-active transmission line region, described in Chapter 3, Section 3.3, delay arrival of the first signal reflection for a sufficient period to allow FFT resolutions to be increased to ≤ 1 GHz which, according to the simulation presented in Figure 3.8, Chapter 3, should be more than sufficient to resolve the difference between overlaid samples of similar, low permittivities such as the two forms of DNA. The high resolution offered by the new devices also presents a platform more able to cope with an increased number of resonators operating at different frequencies within the device bandwidth, since resolution of individual resonances will be more accurate. In total, five resonators operating at 260 GHz, 600 GHz, 800 GHz, 1.0 THz and 1.2 THz were included in the design for second generation devices, with the 260 GHz filter adopting the novel topology presented in Chapter 3 and fully described in Appendix A, designed to remove re-resonance from three times to five times the fundamental operating frequency.

Fabrication of the new generation devices was found to be significantly more difficult that for previous generations, mainly due to the greatly increased aspect ratio between the transmission line dimensions of 1:120:400,000 (height:width:length). However, several devices were successfully fabricated, one of which is shown in the micrograph presented in Figure 6.1. The micrograph shows all five filter devices cascaded along a curved transmission line, increasing in operational frequency from 260 GHz on the far right, to 1.2 THz on the far left, and separated by angles of 20° measured from the centre point of the transmission line curve. The filters were situated on the outside arc path so that they are radially divergent from adjacent resonators and maintain greater than or equal to 400 μm separation to prevent cross coupling. The two switch regions labelled in Figure 6.1 were spatially separated by $(8/\pi)$ mm to give a total active region length of four millimetres as for all previous devices discussed in this work.

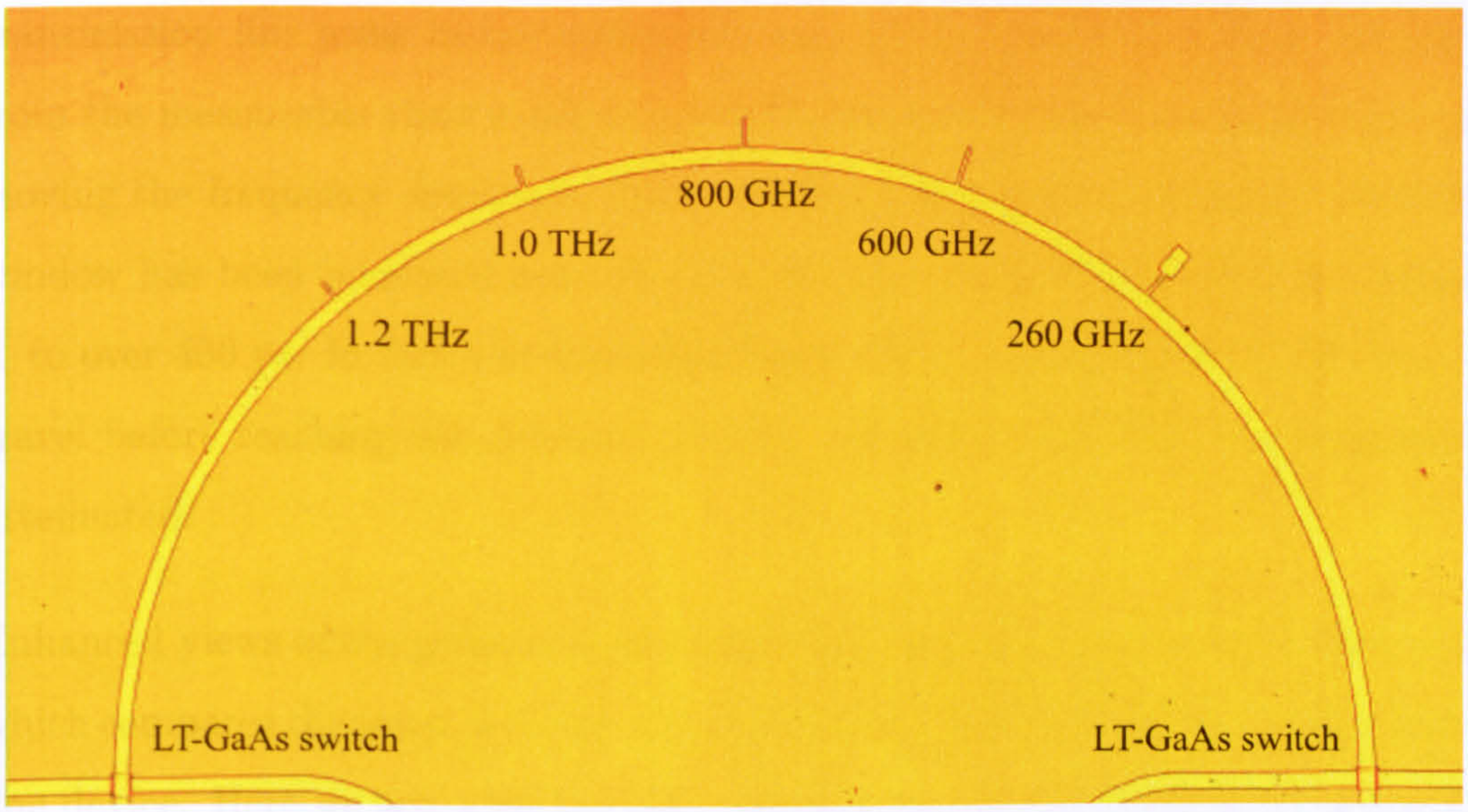

Figure 6.1: Micrograph of the active region of a second generation transmission line device, containing five filter elements.

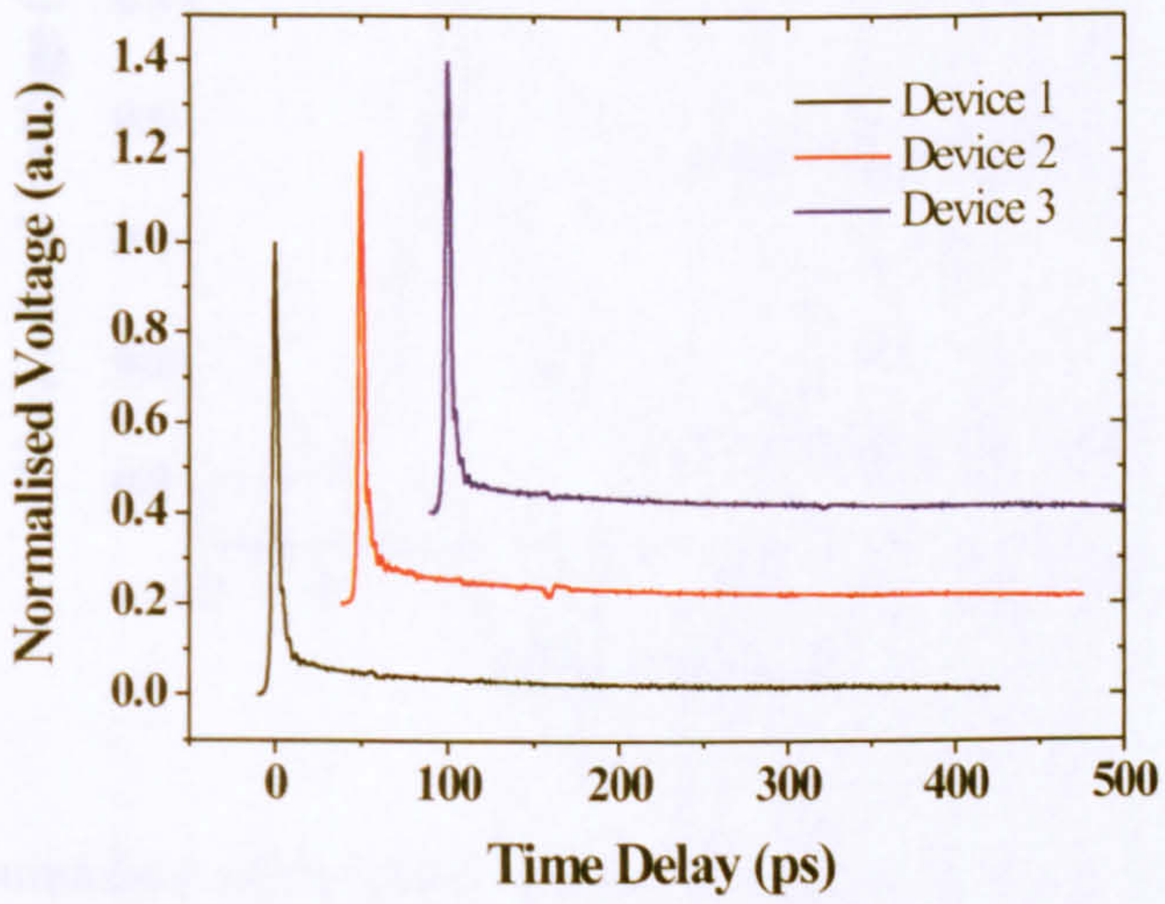

Figure 6.2: Comparison of output pulses for three separate second generation devices, demonstrating the lack of reflections present in the measured signal due to increasing the non-active transmission line lengths. Each pulse is vertically and horizontally offset from adjacent traces by 0.2 and 50 ps respectively, for clarity.

Figure 6.2, which shows output pulse measurements for three separate devices of the design shown in Figure 6.1, demonstrates that the introduction of long

transmission line arms in the non-active region has removed the first reflection from the measurable time window of the second generation device, therefore removing the frequency resolution constraints seen for previous designs. The time window has been increased from 26 ps in the first devices measured in Chapter 4, to over 400 ps. In fact, the reflections have such a significant path distance to travel before reaching the detection switch (100 mm), that they are completely attenuated.

Enhanced views of the pulse measurements in Figure 6.2 are shown in Figure 6.3 which compares the input and output pulses for the five filter, curved transmission line device. Here we see a further pulse broadening on the input signal from 1.3 ps for the cascaded filter in Chapter 5 to 2.4 ps here.

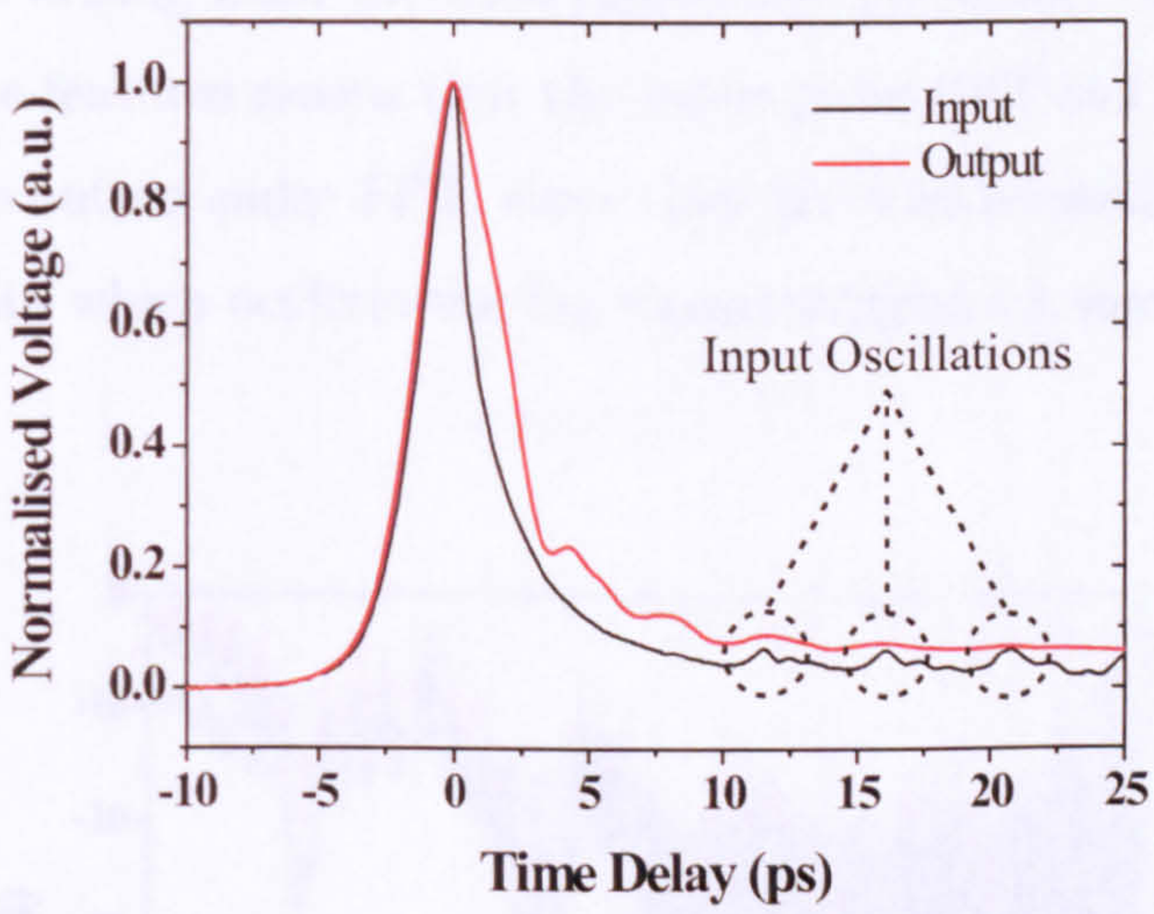

Figure 6.3: Comparison of the input and output pulses of a second generation device having a curved active region containing filters operating at 260 GHz, 600 GHz, 800 GHz, 1.0 THz and 1.2 THz.

Similarly, the output pulse of the device here is measured at 3.7 ps, compared to 2.3 ps for the first generation cascaded device. Clearly, the pulse broadening observed between this device and those tested previously is likely to have a significant effect on the frequency components contained within the generated signal,

but the exact origins of the pulse width increase are unclear.

A second interesting feature revealed in Figure 6.3 is the presence of oscillations on the *input* pulse. Whereas output pulse oscillations are expected due to the removal of frequency components, the input pulse should normally have no such features. However, the oscillations occur regularly at separations of 4.5 ps after the first occurance, which itself is delayed by 11.5 ps from the main THz pulse. Using an average effective permittivity of $\epsilon_{eff} = 2.4$, calculated from the devices in Chapters 4 and 5, the velocity of signals within the line, calculated using (4.2), may be used in conjunction with the time delay to each oscillation to estimate the corresponding path distance travelled within the microstrip. The results show that the reflections arise from the filter stubs themselves, rather than other microstrip interfaces. This leads to five such oscillations (one from each filter) with the largest arising from the dual impedance resonator. Unfortunately, the presence of these features means that the input pulse FFT can no longer be used to normalise the output pulse FFT, since they give rise to oscillations within the frequency domain which occlude the S_{21} characteristics, as seen in Figure 6.4.

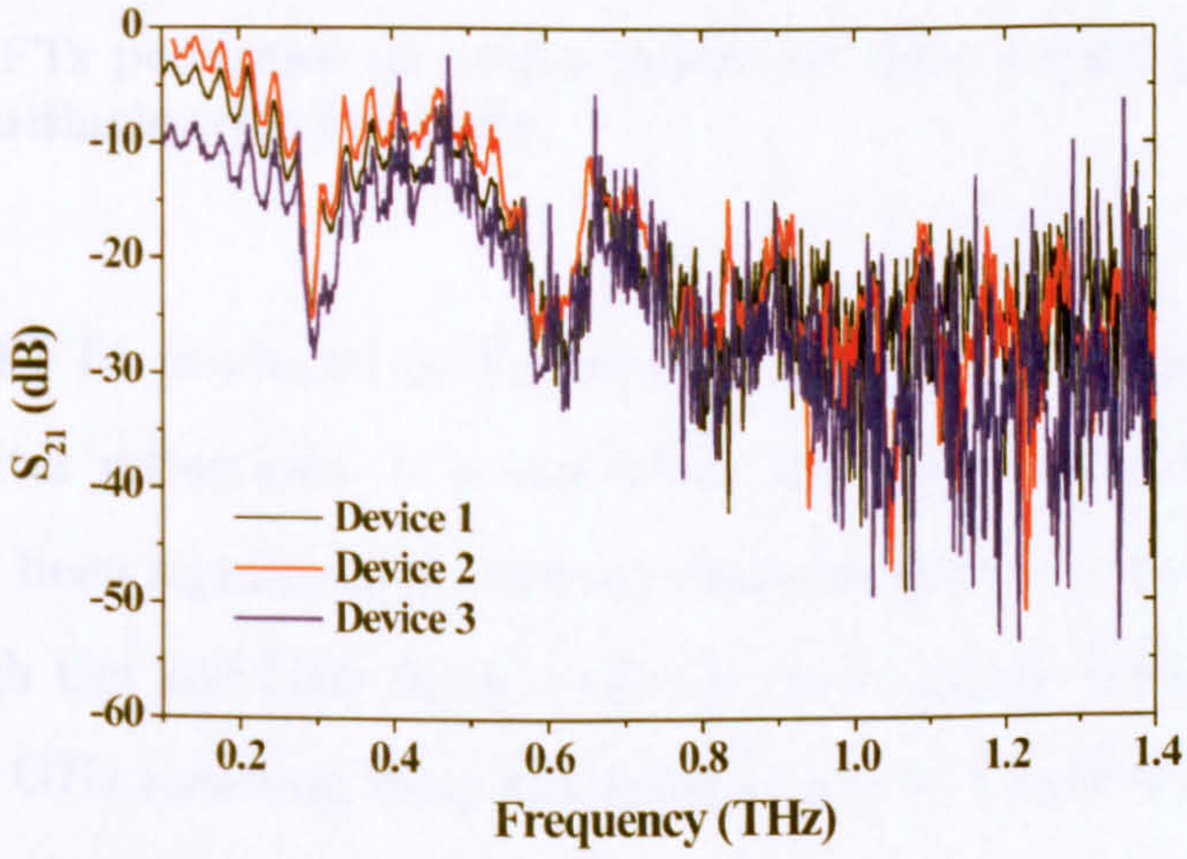

Figure 6.4: Frequency domain oscillations in the S_{21} parameters generated from regular features occurring in input pulse measurements, due to reflections from filter interfaces.

Although several filter responses are evident in Figure 6.4, the frequency oscillations obscure the true peak positions. However, using only output pulse FFTs still produces the required frequency response for each resonator, albeit in arbitrary units rather than decibels, and will therefore still allow tracking of the band stop region under application of a dielectric load. Output pulse FFTs for the three devices are shown in Figure 6.5.

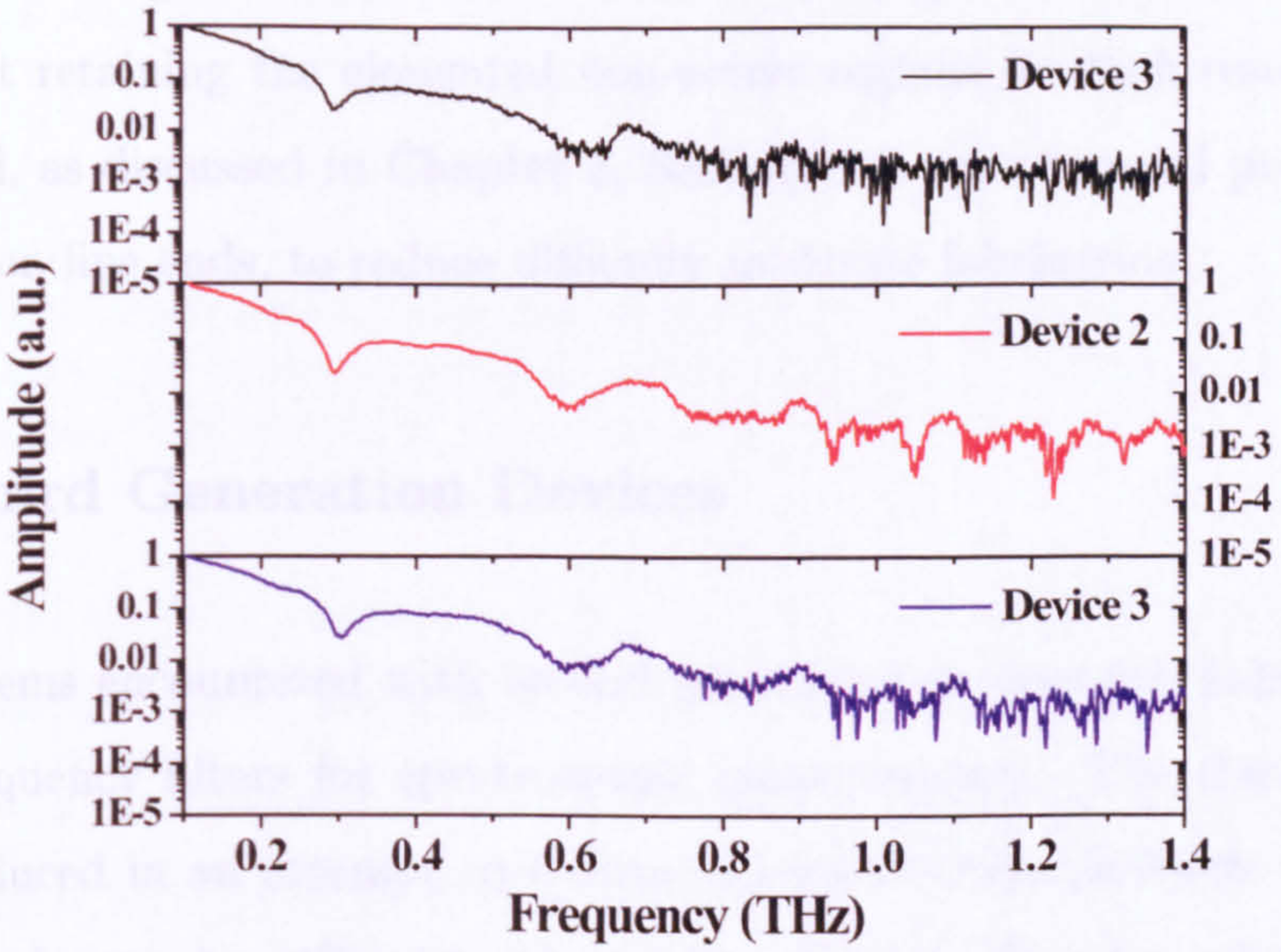

Figure 6.5: FFTs performed on output pulses for three second generation devices, shown on a logarithmic scale for clarity.

Although the FFTs produced in Figure 6.5 remove the oscillatory problem introduced by filter reflections, it is now clear that the bandwidth of this device has apparently been significantly reduced when compared to previous generation chips. Although the 260 GHz filter is clearly resolved, the SNR decreases below 20:1 above 525 GHz meaning filter responses at higher frequencies are lost in system noise. The minimum of the 600 GHz response is buried in the noise floor, so spectroscopic measurements using this filter would have to be performed by monitoring the leading edge of the band stop response, for example. This reduction in bandwidth was attributed to the large output pulse width, previously mea-

sured at 3.7 ps. It was speculated that the path distance experienced by a pulse propagating around the transmission line on the outside bend, would be greater than that for a pulse on the inside bend, introducing a structural dispersion to augment normal frequency dispersion. By calculating the inner and outer arc radius of the transmission line structure and using the phase velocity of a signal within the line, a time difference of 0.5 ps would be experienced between currents flowing along either path. To remove this path difference, third generation devices were designed which returned the active region to a linear transmission line, whilst retaining the elongated non-active regions for high resolution. Also introduced, as discussed in Chapter 3, Section 3.4, were tapered probe arm and transmission line ends, to reduce difficulty in device fabrication.

6.3 Third Generation Devices

The problems encountered with second generation devices precluded the use of higher frequency filters for spectroscopic measurements. The third generation was introduced in an attempt to reduce or remove these problems to allow the on-chip devices to be utilised to their full potential. By reintroducing a linear active region, it was hoped that the output THz pulses would be reduced in width by approximately 0.5 ps. From examination of Figure 6.6, it is shown that the pulse width has only decreased by $\approx$ 0.2 ps. Whilst this is less than expected, if we also consider that the input pulse itself has increased from 2.4 ps for the second generation device characterised in Section 6.2, to 2.8 ps for this device, the *relative* pulse dispersion for the third generation device is 0.6 ps *less* than for the previous device. This implies that removal of the curved transmission line has indeed reduced dispersion, but does not explain the seemingly continuous increase in *input* pulse width between devices. Although unlikely, it is possible that material degradation of the epitaxially grown LT-GaAs was causing an increase in carrier lifetime which would subsequently lead to pulse broadening.

Present in the input pulse shown in Figure 6.6 are similar oscillations within

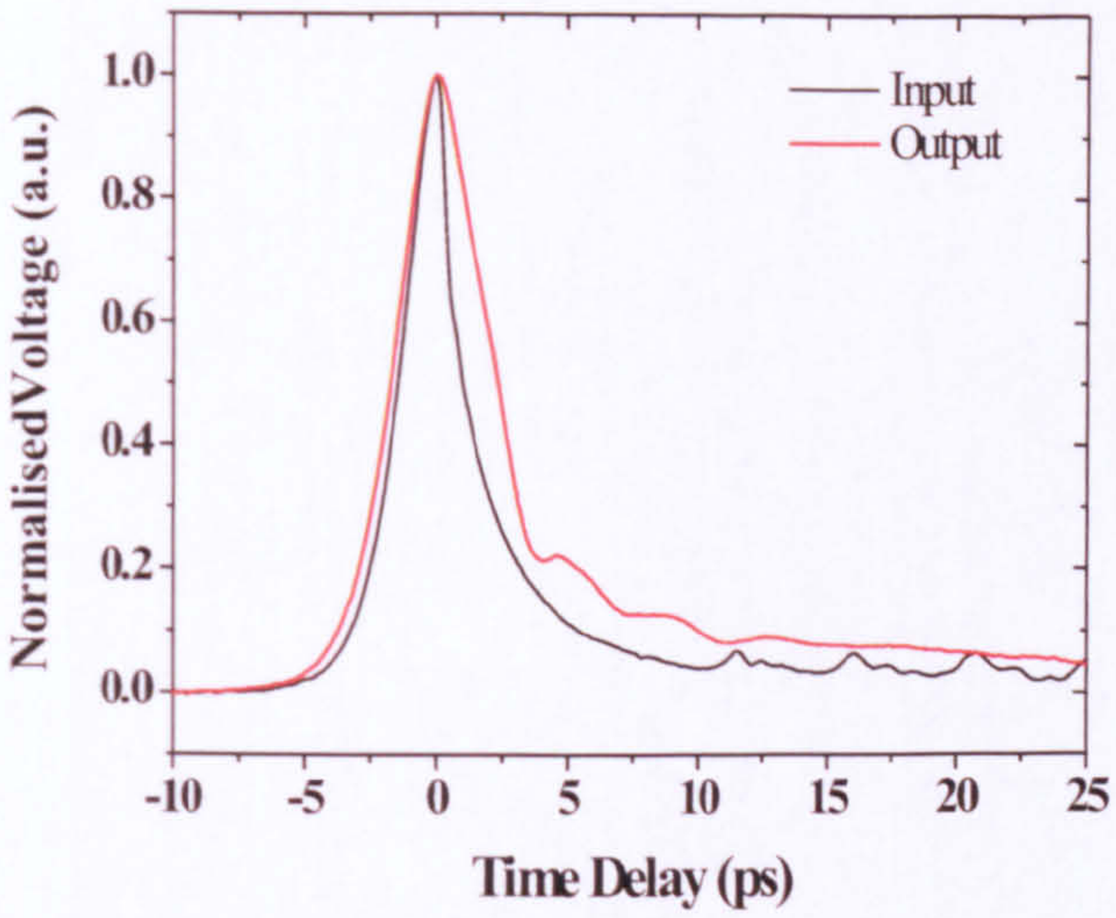

Figure 6.6: Comparison between the input and output pulses for a third generation device containing five filter elements on a 4 mm THz microstrip interconnect, operating at 260 GHz, 600 GHz, 800 GHz, 1.0 THz and 1.2 THz.

the pulse tail to those encountered in Section 6.2, attributed to reflections from filter interfaces. Again, this means calculation of S parameters for the device is impractical and spectroscopic measurements must therefore be performed using FFTs of the output pulse only.

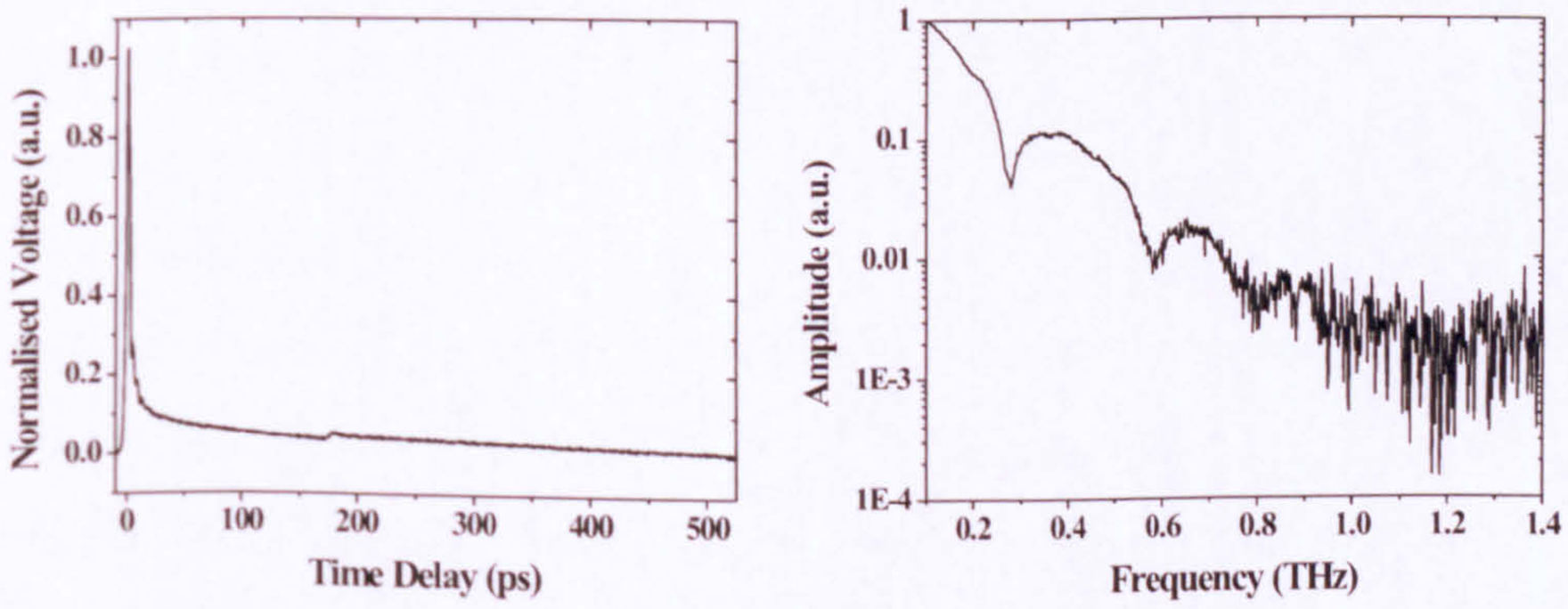

Figure 6.7: Showing a) and output pulse from a third generation, five filter cascade with b) its corresponding FFT.

A full scan of the output pulse is shown in Figure 6.7a alongside a Fourier trans-

form of the pulse in 6.7b. Immediately one may recognise a slight sharpening of the filter responses at both 260 GHz and 600 GHz, and a response lying at 800 GHz is also becoming more resolved, but overall the bandwidth is only slightly improved from the previous generation of devices. Whilst the output pulse and device dispersion have been somewhat reduced in the transition from generation two to generation three, the increased input pulse width is limiting generation of high frequency transients which enter the transmission line.

Further examination of several third generation devices, including that which produced the response shown in Figure 6.7, revealed unusual metal deposits seemingly composed of the titanium adhesion layer, forming a cladding around the edges of the device. Micrographs of the deposits are given in Figure 6.8, and clearly show a darker material forming a barrier around device features. On several devices, the material formed short circuits across LT-GaAs regions (Figure 6.8b) rendering the switches unusable. In cases where links were not formed across the switch (Figure 6.8d) there were still barrier regions on either side of the switch gap. Re-examination of several second generation devices revealed similar formations. The presence of this extra, undesired material was attributed to contamination of chemicals used rather than processing error, due to the large number of independent devices on which it occurred, and also due to the high uniformity of the layer, most evident in Figure 6.8c. It is possible that the presence of these titanium barriers was introducing coupling losses which could cause attenuation of high frequency components as they are coupled into the transmission line structure. The presence of the layer around the filter structures in Figure 6.8a and 6.8e could also be adversely affecting filter response. To investigate these effects, an alternative fabrication technique was adapted for these devices which used completely different chemicals, discussed in Chapter 3, Section 3.5.2. The process involves a dual layer lift-off technique which avoids use of chlorobenzene, and also produces extremely accurate lift-off due to large undercutting of the subsurface PMMA resist layer.

The results of the new technique were very encouraging, as there was no evidence

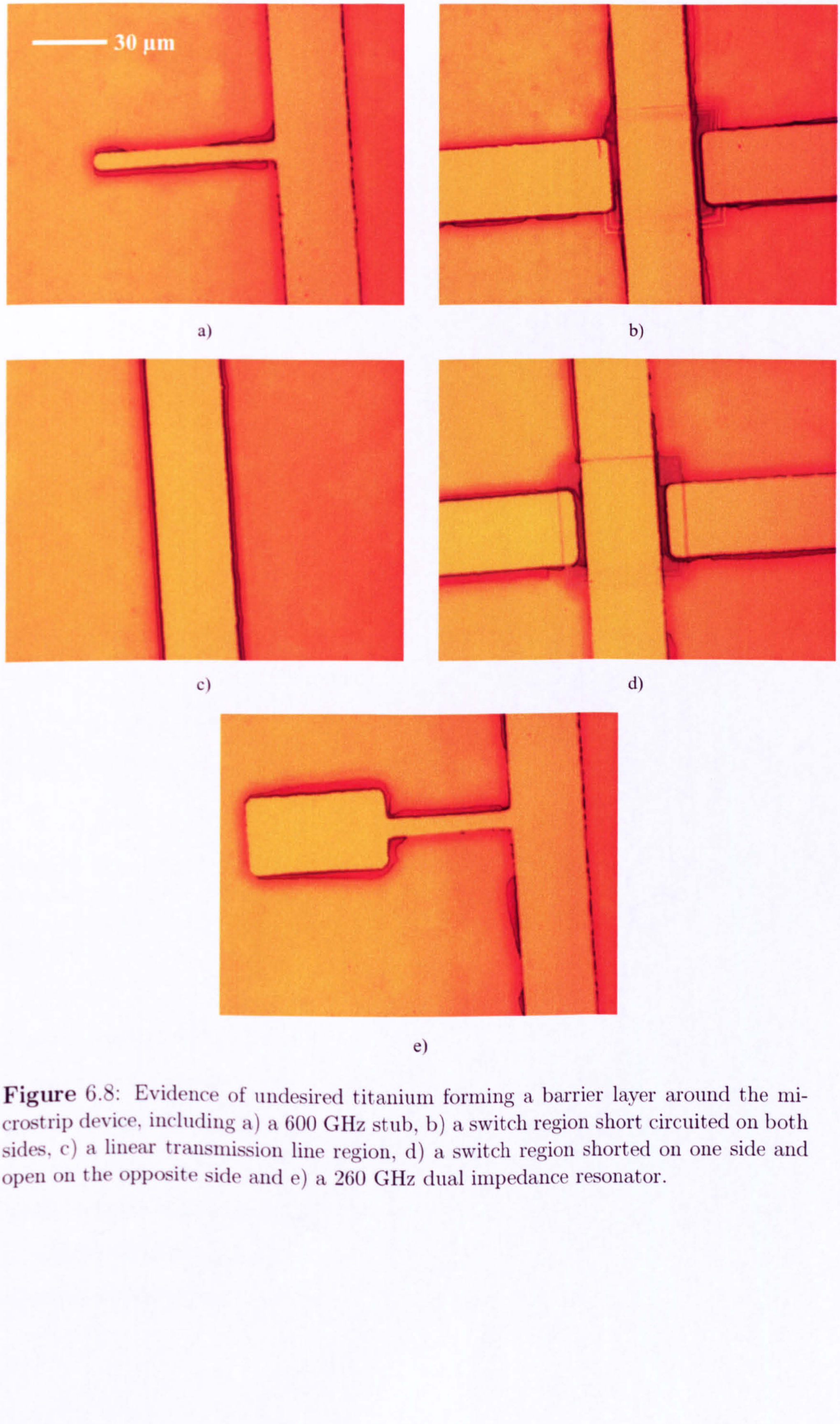

Figure 6.8: Evidence of undesired titanium forming a barrier layer around the microstrip device, including a) a 600 GHz stub, b) a switch region short circuited on both sides, c) a linear transmission line region, d) a switch region shorted on one side and open on the opposite side and e) a 260 GHz dual impedance resonator.

of Ti around the device edges. The edge roughness of devices fabricated using this new technique was also moderately reduced, as may be seen in Figure 6.9.

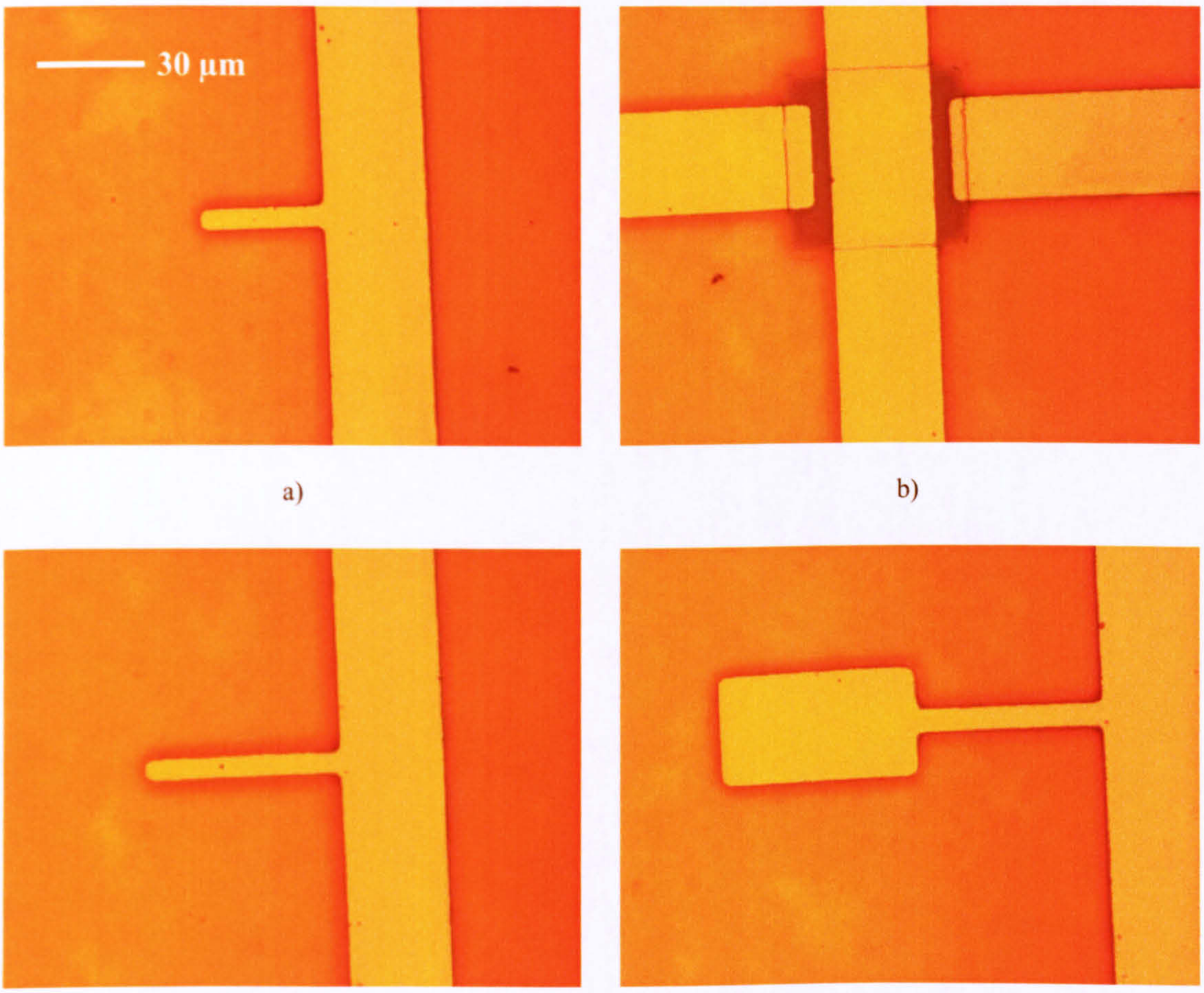

Figure 6.9: Micrographs of new devices fabricated using a bilayer lift-off process designed to remove the titanium layer observed in Figure 6.8, showing a) a 1 THz filter, b) an LT-GaAs switch region, c) an 800 GHz filter and d) a dual impedance 260 GHz filter.

Having changed the fabrication technique to avoid excess titanium at the device edges, output pulse measurements were performed on the new devices and compared to that for the previous device, to assess the impact upon pulse width. As may be ascertained from Figure 6.10, there is little or no difference in pulse width between the devices with and without the titanium layer, suggesting that no dispersive effects are caused by its presence, and also that the bandwidth of the bilayer devices has not improved upon previous achievements.

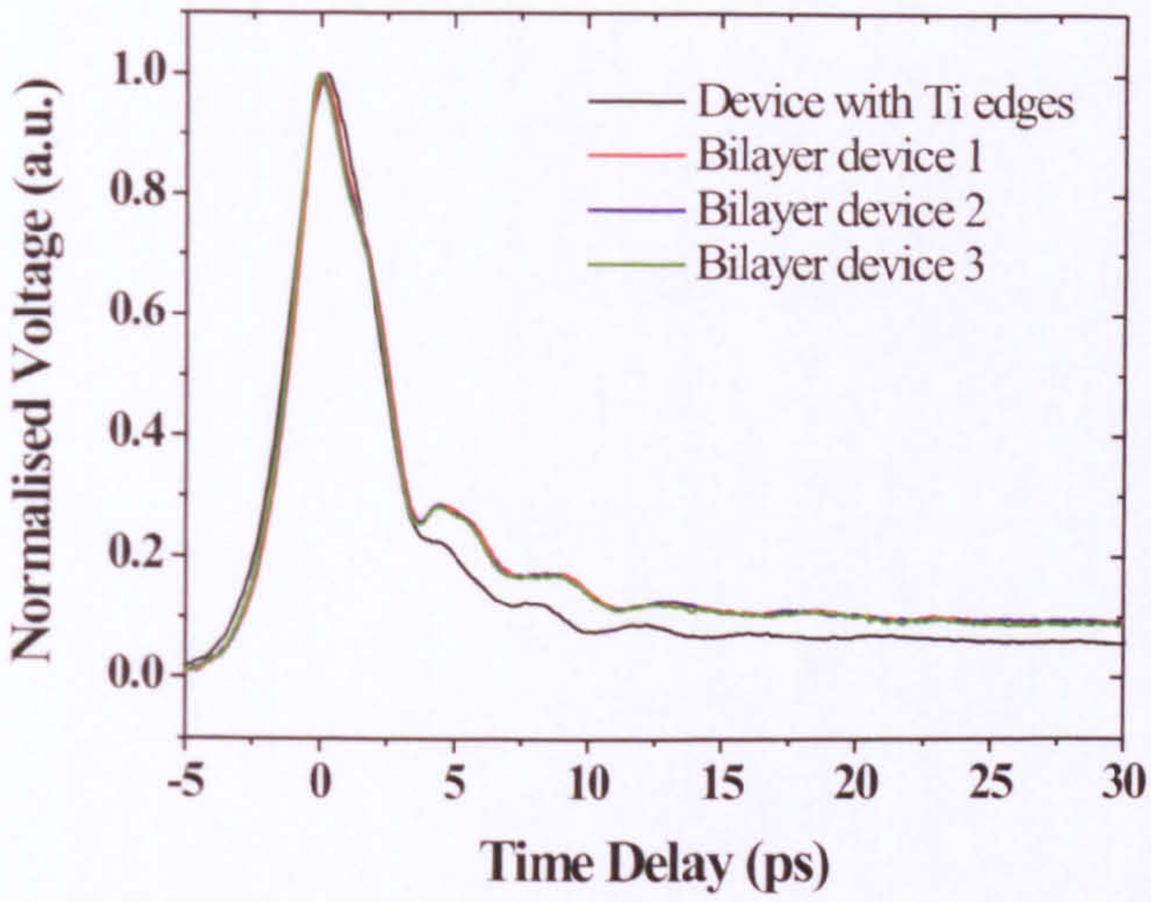

Figure 6.10: Comparison of the output pulses for a device containing a titanium layer around microstrip features, with three new devices fabricated using a bilayer process to remove the titanium edge.

Also evident in Figure 6.10 however, is the presence of more accentuated features in the pulse tail caused by the better defined filter edges, which therefore should produce stronger resonances. Comparison of FFTs between output pulses from a Ti edged device and a bilayer device shows this to be the case, where the new devices produce a much sharper and deeper rejection region for both the 260 GHz and 600 GHz filters, as shown in Figure 6.11. The filter responses of the bilayer device have also shifted slightly higher in frequency, since removal of the titanium edge reduces the effective length of the filters and therefore moderately increases their frequency of resonance. The noise present in the FFT performed on the bilayer device's output pulse is slightly greater than previously due to a small reflection in the time domain sample which arose from a defect in the transmission line close to the active region.

Although the new fabrication process has improved individual filter responses, there still remains the problem of increased pulse widths which have been observed since the transition between LT-GaAs growth suppliers. In order to assess whether this is truly the cause of the wider pulses, a new device was fabricated

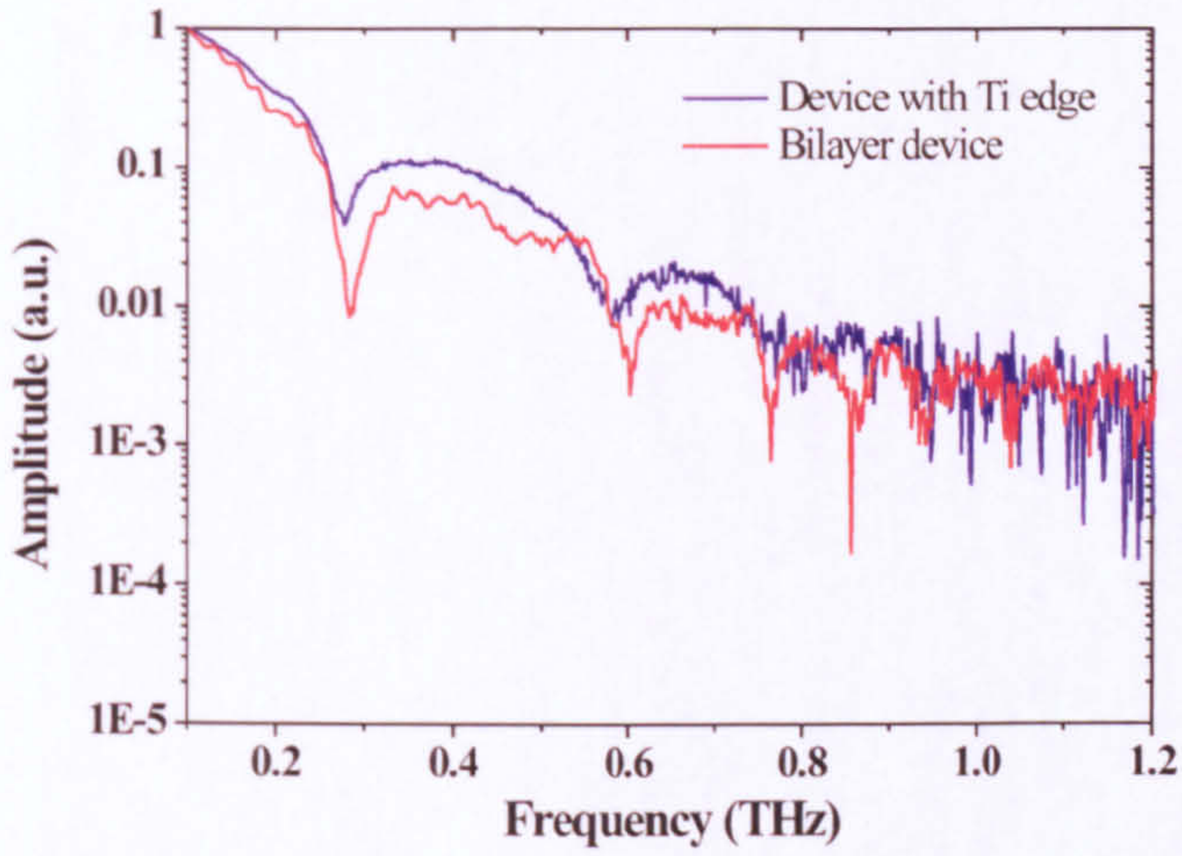

Figure 6.11: Comparisons of the output pulse Fourier transform for a device containing titanium edge profiles with one derived from a bilayer device.

from remains of the original LT-GaAs wafer, grown in Cambridge (henceforth referred to as wafer-C), which was used for the transmission line devices and single frequency filters presented in Chapters 4 and 5. The device was fabricated using the bilayer process, and made to exactly the same specifications as the third generation bilayer device measured in Figure 6.11 which used the newer LT-GaAs material, grown in Manchester (wafer-M), to allow direct comparison. Assuming perfect fabrication, the only variable between the two devices would be the LT-GaAs photoconductive material of which the switches were fabricated. A comparison of input and output pulses for the two devices is provided in Figure 6.12a and 6.12b respectively, demonstrating a significant reduction in the generated pulse width for the device containing wafer-C (i.e. the original material) photoconductive switches.

The input pulse width of the device using wafer-C LT-GaAs was measured as 0.8 ps, which is directly comparable to the pulse widths measured for room temperature transmission line devices in Chapter 4, also of 0.8 ps, and to the single frequency filters characterised in Chapter 5. This reduction in pulse width has significanty changed the appearance of the output pulse, shown in Figure 6.12b.

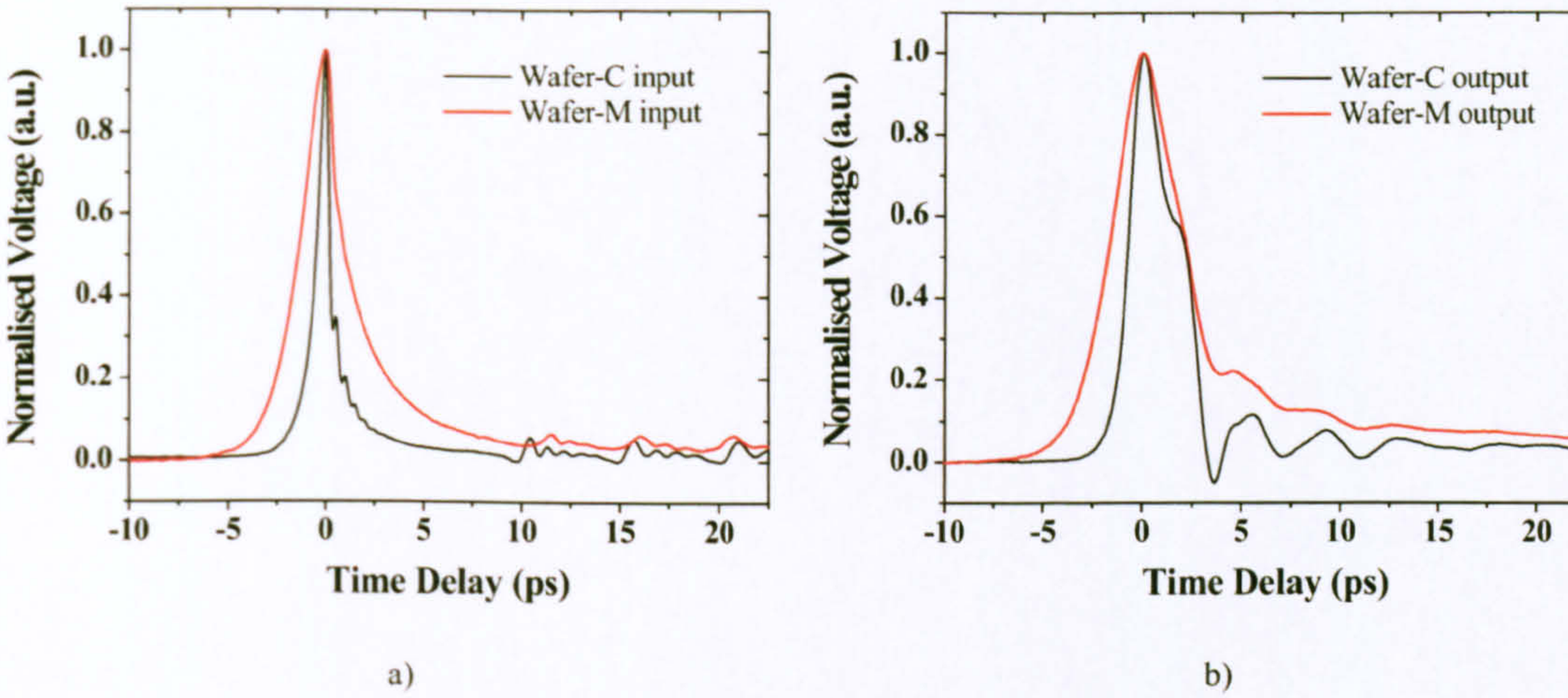

Figure 6.12: Comparisons of a) input and b) output pulses for 5-frequency filter devices fabricated using photoconductive material from wafer-C and wafer-M.

It can be seen that, due to the reduced output pulse width, the tail features are more prominent and there is less superposition of these features with the main THz pulse, evident in the more pronounced shoulder seen on the wafer-C signal.

Having discovered the cause of increased input pulse width to be the choice of LT-GaAs wafer material, the device fabricated using wafer-C material was used for further measurements of overlaid molecular systems. Analysis of the frequency content of the new device should reveal a higher system bandwidth due to the pulse width reduction. Figure 6.13 shows a comparison between FFT's of the output pulses in Figure 6.12b, and clearly demonstrates not only reduction in noise and a return of the system bandwidth to $\approx$ 1 THz, but also a reduced attenuation as a function of frequency due to greater content of higher frequency components. The 260 GHz response was measured at 278 GHz, due to the new filter design introduced in Chapter 3, Section 3.3. The 278 GHz, 600 GHz and 800 GHz filter responses are clearly demonstrated at the expected locations and exhibit a dramatic improvement in definition over previous devices. The response of the 1.0 THz and 1.2 THz filters, whilst being present within the FFT, clearly dip into the system noise floor which occludes their true shape and precludes their use for measurements of overlaid systems.

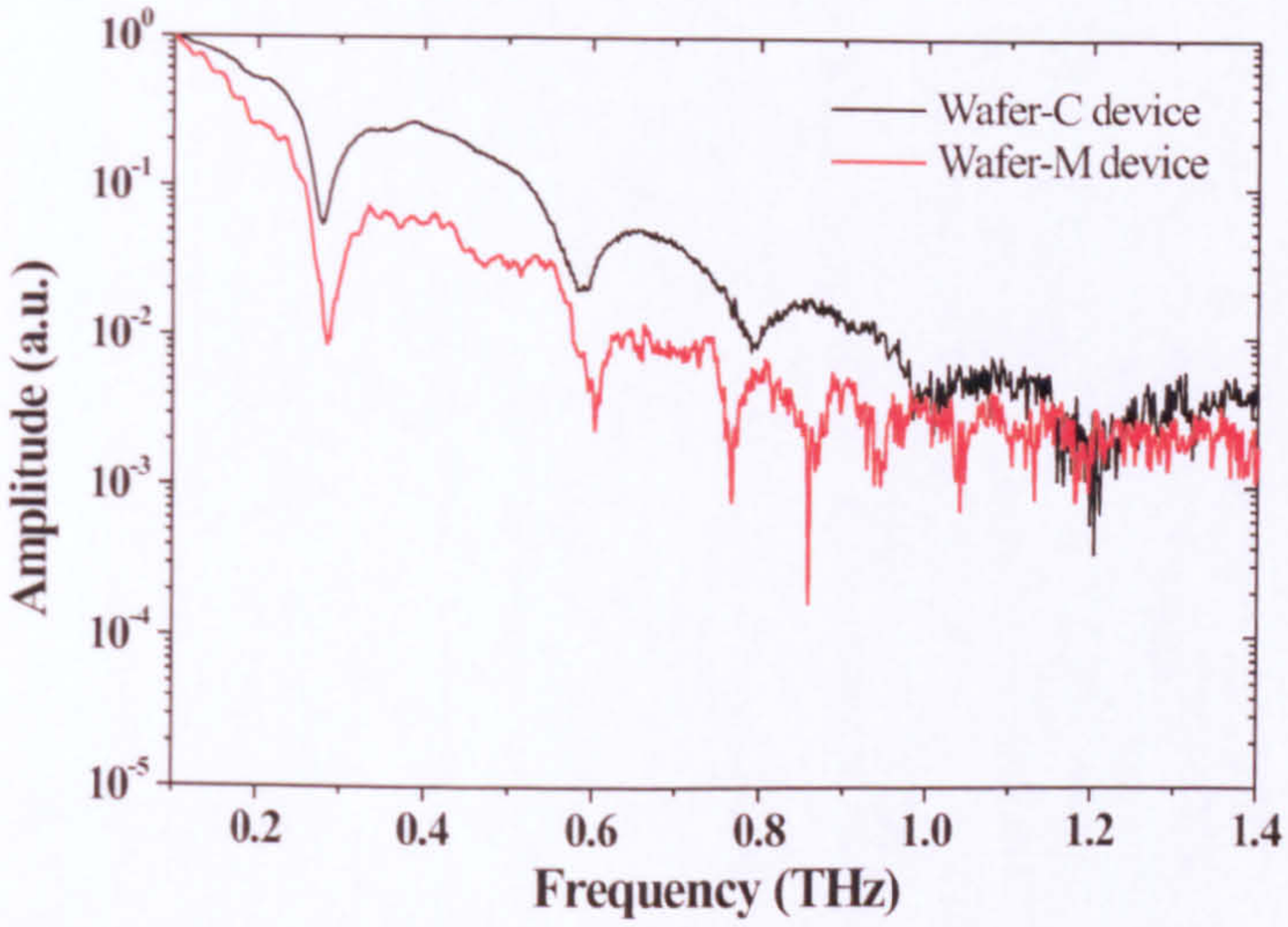

Figure 6.13: Comparison of FFT's performed on output pulses produced by third generation devices using LT-GaAs photoconductive switches fabricated using wafer-C and wafer-M, provided from different growth sources.

The new device was clearly suitable for high resolution measurements of the properties of overlaid biomolecular systems at three independent frequencies. Detailed measurements of loading the 278 GHz filter with DNA will be discussed in the following section.

6.4 Analysis of Overlaid DNA Thin Films

The DNA chosen for analysis was a short plasmid, modified from [95], of length 3307 base pairs (3.307 kbp). Longer DNA strands were not used since they cause blockage of the microcapillaries during deposition due to agglomeration. The DNA was prepared using the method outlined in Appendix B to produce solutions of 1 μg / μl in a water buffer. Water was used to avoid salt deposits forming on the filters from normal DNA buffer solutions, which themselves would alter the dielectric response. To prolong the lifetime of the DNA it was frozen until used. The DNA was split equally into two parts, one of which was left untouched and therefore remained in its double stranded (DS) form. The second part was denatured into single strands (SS) by heating to 100 °C and flash cooling in a

water - ice mixture to prevent rehybridisation. Each DNA sample was measured individually by deposition of $\approx 120\ \mu m$ diameter drops to ensure full stub coverage. The drop was allowed to evaporate under ambient conditions, and then the filter response was measured several times over a period of 1 hour to ensure that the maximum water content had been removed. After these measurements, subsequent deposition and measurement steps were performed to increase thickness and therefore produce a greater frequency shift. After several measurements, the filter was cleaned using deionised water and measured again to ensure the response had returned to the unloaded state. The device was then cleaned several more times to ensure complete removal of the double stranded DNA. The process was repeated for single stranded material following exactly the same procedure.

Unfortunately, the exact thickness of DNA material deposited on the stubs could not be directly measured using available equipment. The layers were too thin for a standard surface profiler to discern, whilst surface roughness of the Ti/Au - BCB - Ti/Au layered device, measured at ~ 9 nm using atomic force microscopy, was larger than the thickness of DNA (~ 2 nm), which means very thin layers are undetectable using and atomic force microscope (AFM). As the layers increase in thickness, the AFM tip dips into the highly amorphous, soft material and cannot resolve its thickness above the filter. However, the molar quantity of DNA deposited on the stub can be estimated using the diameter of the deposited drop, which was recorded for this purpose, alongside knowledge of the drop shape on the device surface. This was measured using a goniometer which records the drop profile during and after deposition onto a surface, as shown in Figure 6.14.

The photograph in Figure 6.14c shows that the contact angle between drop and surface is $\sim 90\ °$, which allows us to consider the drop as hemispherical in shape. The slight deviation from a perfect hemispherical profile is due to gravity compressing the drop, but as the drop size decreases the surface tension will dominate the drop shape and increase its hemispherical nature. The volume, V, of the drop can therefore given by:

a) b) c)

Figure 6.14: Goniometer images of a drop of 3.307 kbp plasmid in aqueous solution at 1 μg / μl concentration, onto a microstrip device surface, fabricated on BCB dielectric showing a) drop formation, b) drop contact and c) drop release. The circle shows approximate hemispherical shape of the deposited drop.

$$V = \frac{\pi d^3}{12}, \tag{6.1}$$

using the drop diameter, d. Using the DNA concentration in combination with the volume of deposited solution, allows us to calculate the mass, m, of DNA within the drop. The number of moles, n, of DNA may then be ascertained using the mass of a single plasmid, $M_r = 3.564 \times 10^{-18}$ g, in:

$$n = \frac{m}{\mathring{A} \times M_r}, \tag{6.2}$$

where $\mathring{A}= 6.022 \times 10^{23}$ is Avogadro's number, defined as the number of atoms in 12 g of carbon ^{12}C.

The volume of each drop was calculated to be 4.52×10^{-13} m^3 ($\equiv 4.52 \times 10^{-4}$ μl), which equates to a mass of m $= 4.52 \times 10^{-10}$ g of DNA. The number of moles is then calculated to be M $= 0.211$ femtomoles, and represents the total number of moles present in a drop of diameter 120 μm. However, the active region of the stub has a total surface area of ~ 2183 μm^2 (calculated from the dual impedance stub dimensions of (5×59) $\mu m^2 + (32 \times 59)$ μm^2, discussed in Chapter 3 and Appendix A), compared to the total drop contact area of ~ 11309 μm^2, a ratio of

5.2:1. Therefore the amount of DNA directly interacting with the stub is less than the total DNA within the droplet. Since the exact value cannot be calculated due to possible uneven DNA distribution subsequent to evaporation of the drop, it was assumed that all of the DNA present was affecting the frequency response. The effect of loading on the absolute frequency position of the 278 GHz filter for both DS and SS DNA loads is shown in Figure 6.15, which shows distinct changes in the resonant frequency position for each case. The curves in Figure 6.15 have been moderately smoothed to clarify the results.

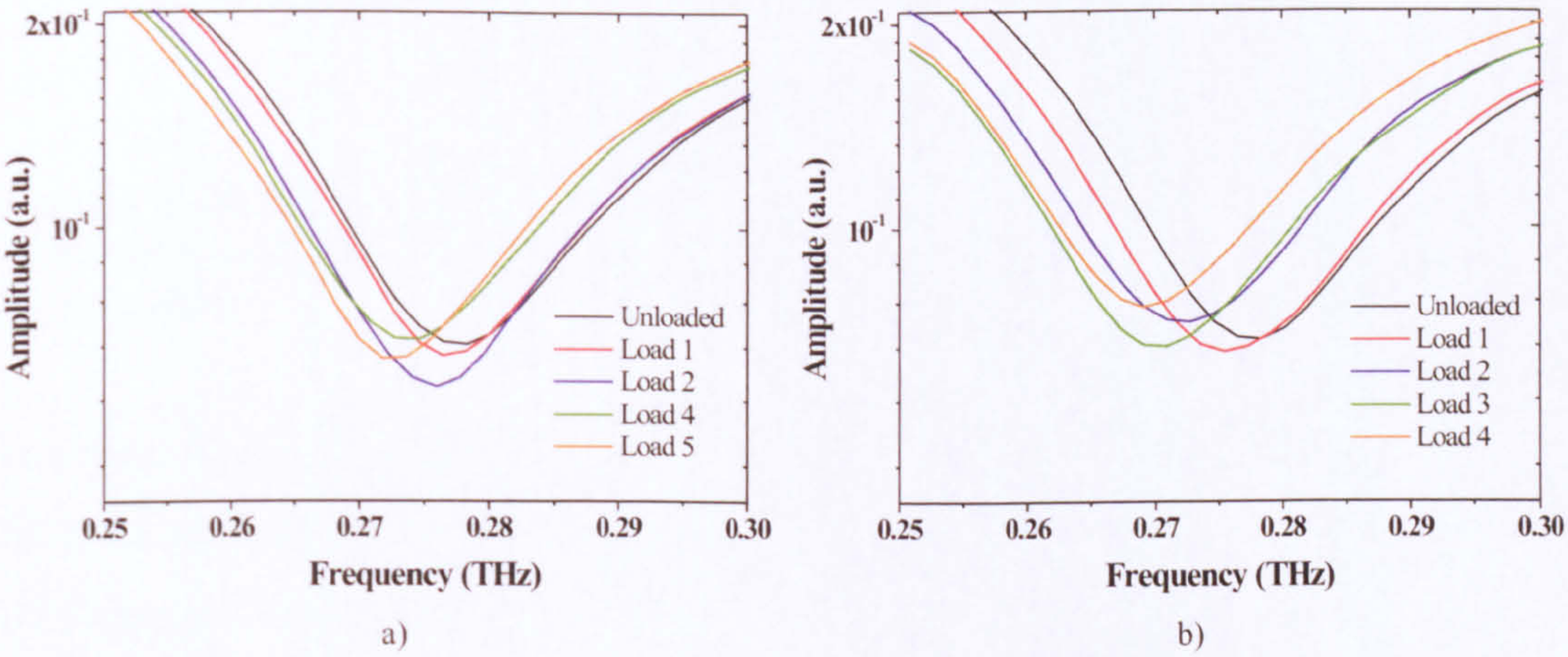

Figure 6.15: The effect on the resonance position of a 278 GHz filter under application of DNA films in a) single stranded (SS) and b) double stranded (DS) conformations.

The measurements performed using SS DNA loads were slightly different since for load 3, two deposits were made with only one subsequent measurement. As a result the data points in Figure 6.15 jump from load 2 to load 4, and an extra deposition was made (load 5) to maintain equal numbers of data points for each DNA conformation. The frequency shifts are more easily understood when they are plotted as a function of deposited DNA molar quantity on the stub surface. This data is given in Figure 6.16 for both DS and SS DNA conformations.

The line fits for the frequency shifts as a function of DNA molar quantity in Figure 6.16, suggest that the devices are working in the more linear region of the expected curve, not having yet reached saturation, and that therefore the film thickness is

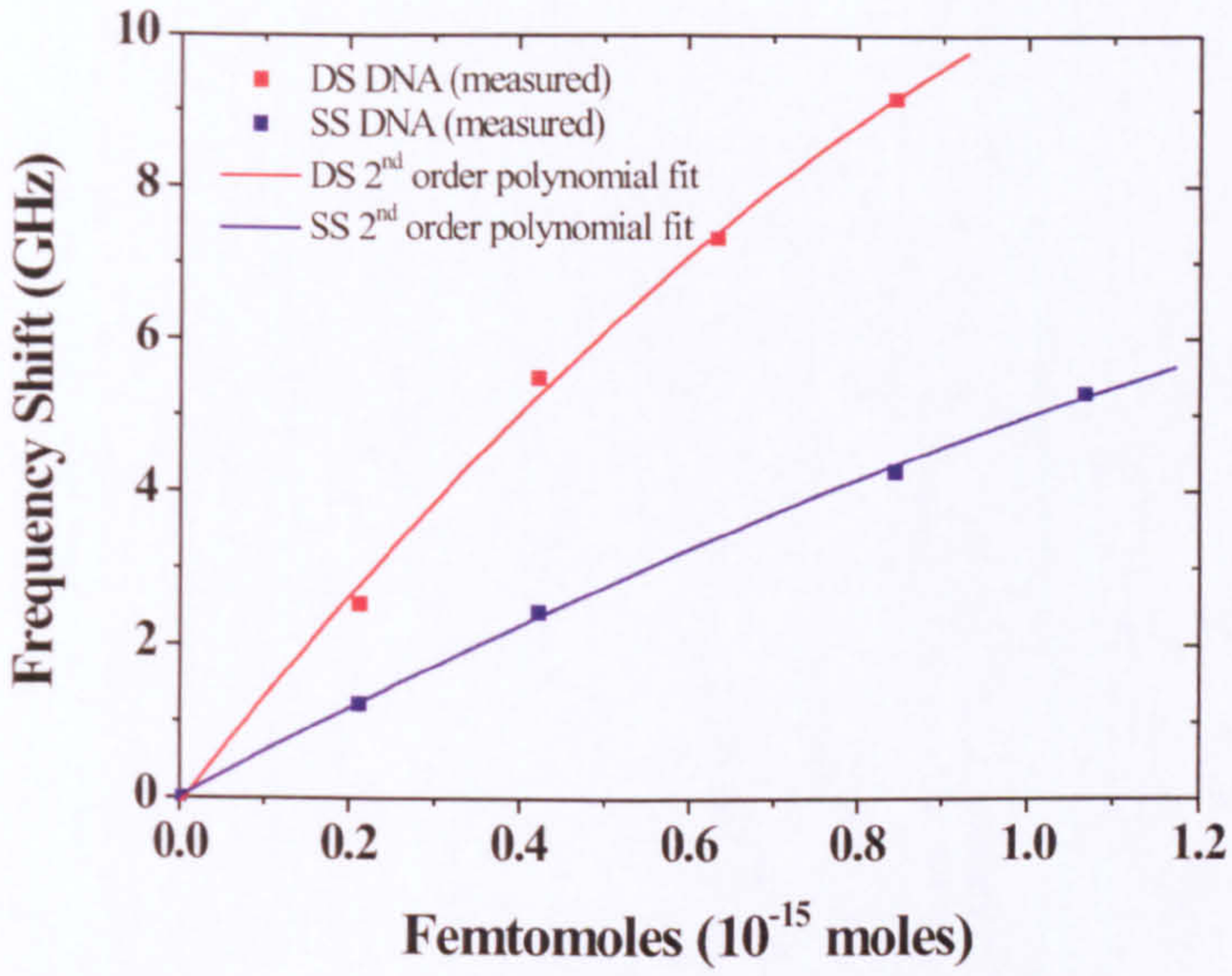

Figure 6.16: Frequency shift as a function of molar quantity of overlaid DNA in femtomoles on a 278 GHz resonator, in both single (SS) and double (DS) stranded conformation.

less than 4 μm. There is a distinct difference in the frequency shifts for DS and SS DNA conformations, demonstrating the ability of the high resolution device to distinguish between single and double stranded DNA molecules for concentrations down to below 0.21 f mol. The most sensitive microstrip device in the literature offers a sensitivity of 40 f mol [59], although this is for loaded DNA of length 20 bp (c.f 3.307 kbp here). However, one may use the relative resonant shift per base pair, $r_{shift/bp}$, to more accurately compare this device with the literature, calculated using:

$$r_{shift/bp} = \left[1 - \frac{f_{ref}}{f_{shift}}\right] / n_{bp}, \tag{6.3}$$

where f_{shift} is the absolute frequency of the shifted response, f_{ref} is the unloaded frequency, and n_{bp} is the number of base pairs derived from the number of moles, n, calculated from (6.2), multiplied by Avagadro's number and the number of base pairs per DNA strand. For the device here, an average value of $r_{shift/bp}$ for DS DNA is calculated as 2.14×10^{-14} with a maximum value of $r_{shift/bp} = 2.35$

$\times 10^{-14}$, a slight improvement in sensitivity and distribution when compared to equivalent values of 1.3×10^{-14} and 2.8×10^{-14} quoted from Nagel *et al.* [59]. However, the active area of the devices in [59] is quoted as 0.27 mm^2, or 270,000 μm^2, which is $\sim$ 123 times larger than the device measured here. This result implies an increase in sensitivity by two orders of magnitude, in terms of frequency shift per unit active area, for the device presented here when compared to existing technologies. This result agrees very well with comparisons of simulated frequency shift per unit active area for several device topologies in [96].

However, the estimate of the surface coverage, or packing density, of the functionalised DNA surface given by Nagel *et al.* in Ref. [59] is somewhat vague. A value of 4×10^{10} DNA strands per mm^2 for *single stranded* DNA is quoted from Ref. [97], which was then assumed by the authors to be an upper limit for the *double stranded* DNA used, on the basis that DS DNA is twice as large and therefore fewer molecules will fit into the same space. However, there is evidence that the packing density of DS DNA is actually much *greater* than for SS DNA, due to a reduction in the degrees of freedom of the DS molecule [98]. Referring to Figure 6.17a, we see that the flexible SS DNA strand creates an exclusion zone around it where it sterically hinders the surface binding of other SS DNA molecules [99]. However, the more rigid DS DNA in Figure 6.17b has a much narrower exclusion zone due to a much greater persistence length ($\sim$ 50 nm compared to $\sim$ 1 nm for SS DNA, dependent on base configuration and ionic conditions [100]), and packs densely onto the gold surface at an approximate 45° angle [101]. After *in situ* denaturing of the tethered DNA, the possible increase in packing density would then interfere with subsequent re-hybridisation due to electrochemical repulsion between adjacent probe SS DNA molecules [102].

However, if one takes the assumption by Nagel *et al.* to be accurate, there is still the issue of the SS DNA non-specifically adsorbing to the gold surface [103] and the polypropylene dielectric surface [104, 105] at points along its backbone, via non-covalent amine bonds, meaning non-thiol-tethered DNA molecules are present on the surface (Figure 6.17a). A standard method of preventing non-

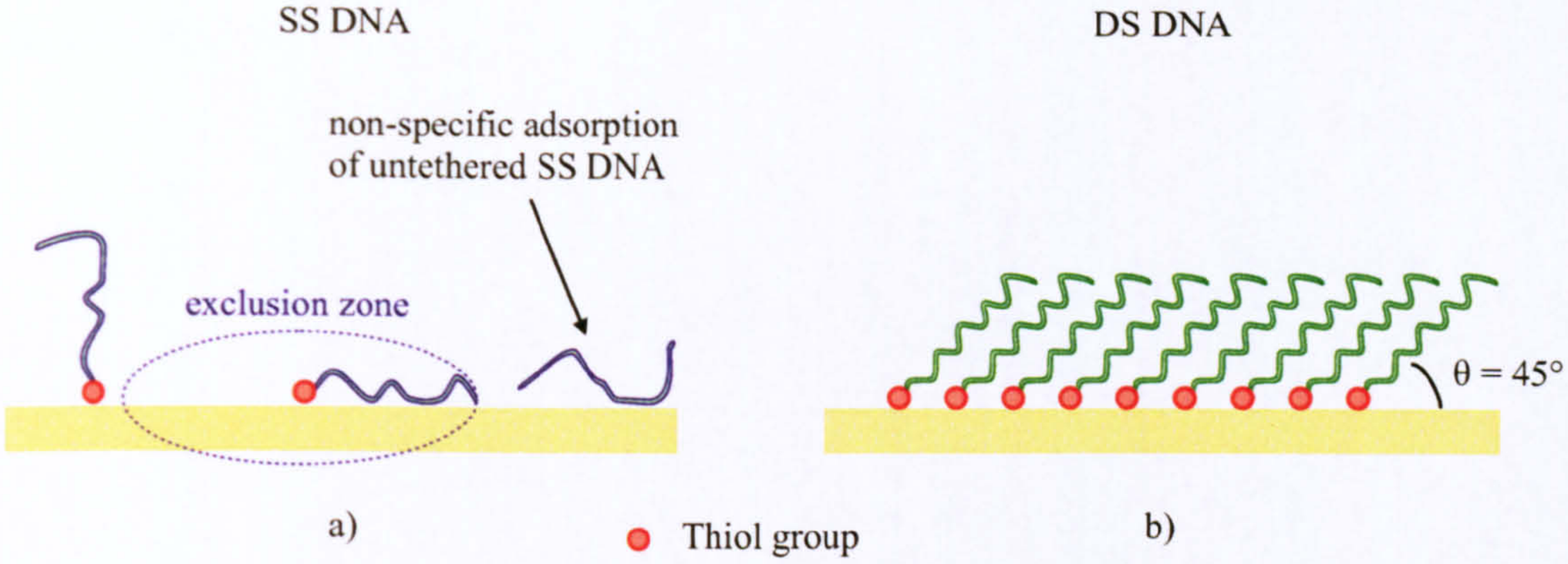

Figure 6.17: Representations of thiol-modified surface coverage of a) SS DNA and d) DS DNA on a gold surface.

specific binding is by coating the surface with a spacer molecule, mercaptohexanol (MCH) [106, 60]. This molecule also has the effect of forcing the tethered DNA strands into a more upright conformation which increases the probability of hybridisation when exposed to complementary strands. In Ref. [59], the SS DNA modified chip was immersed in a mixture of complementary strands and MCH molecules, to prevent complementary molecules adsorbing onto the gold resonator surface. However, it is unlikely that the MCH would displace SS DNA adsorbed to the *polypropylene* surface, i.e. in the coupling gap between resonators where there is a high electric field concentration. It is therefore possible that a proportion of the shift observed in Ref. [59] is attributable to an increased concentration of SS DNA molecules, rather than a hybridisation event, which complicates the results.

The technique used for the work presented in this thesis avoids complications of non-specific adsorption by excess molecules, since no *in-situ* hybridisation is performed and all deposited molecules, being of the same hybridisation state, are contributing to the observed frequency shift in the same fashion, and are accounted for in calculations of the relative shift per base pair, $r_{shift/bp}$. In conclusion, the band stop filter device presented here offers at least two orders of magnitude improvement in sensitivity per unit active area over existing technologies, with the added advantage of offering independent, multiple frequency THz

measurements.

Chapter 7

Conclusions and Future Work

The work presented in this thesis developed a novel on-chip, guided wave terahertz system sensitive enough to measure differences in the binding state of overlaid biomolecular systems, such as DNA. In the course of the work, several novel device designs and fabrication techniques were developed to achieve this target. In order to generate THz radiation in-plane with the microstrip device, a novel technique for fabrication of isolated photoconductive switch regions, formed from thin film layers of LT-GaAs material was successfully developed, allowing lithographical definition of arbitrary switch patterns. The biased switches, under illumination by a pulsed femtosecond laser source, generated sub-ps (down to $\sim$ 0.55 ps) time domain voltage signals, containing frequency components up to 1.2 THz, which could enter and propagate along a microstrip waveguide fabricated over the switch surface. The characteristics of the waveguiding dielectric were measured at room temperature, signifying the potential for use of this system for analysis of overlaid biomolecular films. System losses of $\sim$ 2.5 dBmm^{-1} at 600 GHz were observed (c.f. $\sim$ 3 dBmm^{-1} in the literature [48]) and a maximum signal to noise ratio of 800:1 at 100 GHz was achieved. Measurements of devices operating at cryogenic temperature were also performed, which presents prospects for THz characterisation of semiconductor based quantum systems down to liquid He temperatures. Proof that LT-GaAs is a suitable emitter and detector of THz signals, and that BCB is a suitable dielectric waveguiding material at cryogenic

temperatures was given.

By introducing resonant, passive band stop filter elements into the active region of the transmission line (i.e. between two consecutive photoconductive switches), resonant features were formed within the S_{21} device parameter whose frequency positions altered as a function of the thickness and permittivity of an overlaid dielectric load. Whilst other devices in the literature offered multiple frequency measurements [59], these were in the form of harmonics of the fundamental device resonance, which restricts characterisation to one material at a time. Owing to the novel design and the nature of the filters designed for this work, it was possible to cascade several devices of various frequencies on a single interconnect allowing measurements to be performed at different, isolated frequencies within the device bandwidth. This allows measurement of several different materials simultaneously, or a single material across multiple frequencies. Full characterisation of a dual resonator device under application of a commercial photoresist showed excellent agreement with the frequency responses obtained from 3-d electromagnetic simulations, using a dielectric permittivity obtained in subsequent free space measurements. The on-chip measurements were performed using a sample volume approximately six orders of magnitude less than the corresponding free space measurement. This emphasises one of the main advantages of on-chip measurements over free space studies, and represents the first complete characterisation of a THz frequency filter under application of varying thickness of overlaid dielectric film. Cascaded devices containing two, three and five resonant structures were demonstrated, with a maximum frequency of operation at 1.2 THz.

Further developments to the device design enhanced the frequency resolution from ~ 37 GHz in first generation topologies, to < 2 GHz in second and third generation devices. This ultrahigh resolution allowed the subsequent characterisation of 3.307 kbp DNA plasmids in single and double stranded form, overlaid in varying molar quantities onto a 278 GHz filter. The device demonstrated the ability to distinguish between the two forms of DNA in quantities down to less than 0.211 femtomoles. The average resonant shift per base pair was found to be

2.14×10^{-14}; almost twice that of other published data [59], and is likely to be higher since conservative estimates of the DNA quantities were used. The device's surface area was $\sim$ 123 times smaller than previous ring-resonator topologies from Ref [59] and therefore represents an increase in sensitivity per unit area of two orders of magnitude.

7.1 Future Work

The work presented in this thesis represents a step forward in the development of on-chip, guided wave THz systems. The uses for this type of device are broad ranging, from measurement of the dielectric permittivity of overlaid material, through monitoring of biomolecular interactions, to analysis of two dimensional electron gas systems at cryogenic temperatures. However, there is still much room for subsequent development of this technology which would further increase the scope of applications suited to such devices. Measurement of overlaid DNA films onto higher frequency filters is necessary to assess to the differences in frequency shift, and hence sensitivity of the different resonators. For comparison with simulated data, it would be useful to obtain information on the exact thickness of the overlaid DNA layer, using interference microscopy or radio labelling for example. It would also prove interesting to be able to topographically map the orientation of the DNA on the surface to assess the effects of clustering and uniformity of dispersion. A logical additional step would be to functionalise the gold surface of the microstrip filters, as performed by Nagel *at al.*, including the MCH spacer layer, to assess the difference in shift observed between the more ordered deposition achieved using this technique and the random orientations achieved from the deposition techniques used here.

The devices are not limited to measurement of DNA binding events, and measurements could be extended to other biomolecular systems exhibiting binding events, such as antigen - antibody or other protein systems. Due to the possibility of functionalising the gold surface, there is also the potential for binding

carbon nanotubes onto the filters. Nanotubes have been shown to act as traps for gas molecules [107], and therefore a nanotube functionalised filter could realistically act as a gas sensor, since trapped gas molecules would change the dielectric environment of the filter stub in a similar fashion to that observed between SS and DS DNA.

One of the main limitations with the on-chip devices developed for this work lies with the system bandwidth at the device output. This is controlled by two main parameters: the bandwidth of the input pulse generated in the pump LT-GaAs photoconductive switch, and the dispersion and loss within the microstrip waveguide. The former quantity is itself controlled by two factors: the growth conditions (and hence resultant carrier lifetime) of the LT-GaAs material itself, as evidenced by the tests performed in Chapter 6 between the Manchester- and Cambridge- grown wafers, and the time domain pulse width of the illuminating laser source. It would be interesting to assess the effect on the pulse width generated in the devices presented here under illumination by, for example, a 10 fs laser source, which has been demonstrated to generate $>$ 35 THz bandwidth in free space arrangements [22]. However, higher frequency components are likely to be greatly attenuated within the microstrip line as the signal propagates due to excitation of higher order modes and due to the cutoff frequency of the microstrip, as discussed in Chapter 3. To alleviate this somewhat, shorter line lengths between optical switches could be used which would reduce system attenuation and potentially allow higher frequency components to be used. Use of a lower permittivity dielectric would have a similar effect, although to date only one such material, polyprolpylene, has been characterised at THz frequencies and has its own inherent limitations such as increased thickness and surface roughness compared to the BCB used here.

Further developments to the system may involve more complex or more sensitive filter topologies, which would require more in-depth knowledge of microstrip filter theory, but would potentially further reduce the amount of material required for testing. The on-chip technique could also be extended to coplanar waveguide,

which would help alleviate the limitations of dielectric material since the majority of the electric field is confined between the in-plane centre conductor and ground planes instead of within the dielectric.

Appendix A

ABCD Matrices for Transmission Lines

A.1 Derivation of ABCD parameters

In order to derive the ABCD matrix for a two-conductor transmission line, one may begin by considering the lumped-element line in Figure A.1, where Z is the series impedance of a section, length Δx, and Y is the shunt admittance of the same section.

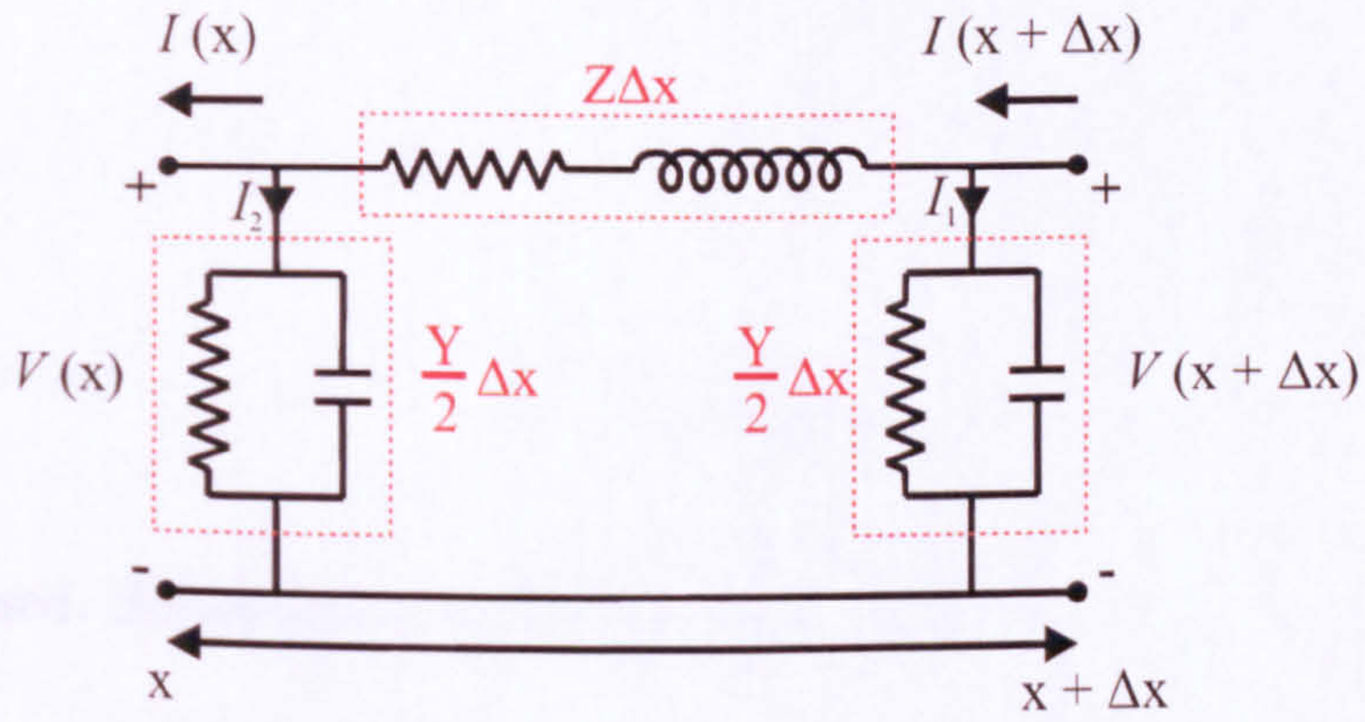

Figure A.1: Lumped element representation of a two conductor transmission line of length Δx, with series impedance Z and shunt admittance Y.

Application of Kirchoff's voltage a current laws to the circuit in Figure A.1 yield:

$$I(x+\Delta x) = I(x) + I_1 + I_2,$$
$$= I(x) + V(x+\Delta x)\frac{Y}{2}\Delta x + V(x)\frac{Y}{2}\Delta x,$$
$$\therefore \frac{I(x+\Delta x) - I(x)}{\Delta x} = [V(x+\Delta x) + V(x)]\frac{Y}{2}, \tag{A.1}$$

and

$$V(x+\Delta x) = V(x) + (I(x+\Delta x) - I_1)Z\Delta x,$$
$$= V(x) + (I(x) + I_2)Z\Delta x,$$
$$= V(x) + I(x)Z\Delta x + V(x)\frac{Y}{2}\Delta x Z\Delta x, \tag{A.2}$$
$$\therefore \frac{V(x+\Delta x) - V(x)}{\Delta x} = I(x)Z + V(x)\frac{Y}{2}Z\Delta x, \tag{A.3}$$

where the substitutions

$$I_1 = V(x+\Delta x)\frac{Y}{2}\Delta x \tag{A.4}$$

and

$$I_2 = V(x)\frac{Y}{2}\Delta x \tag{A.5}$$

have been used. Substituting (A.2) into (A.1) yields:

$$\frac{I(x+\Delta x) - I(x)}{\Delta x} = V(x)\frac{Y}{2} + I(x)\frac{Y}{2}Z\Delta x + V(x)\frac{Y^2}{4}\Delta x Z\Delta x + V(x)\frac{Y}{2}. \tag{A.6}$$

Taking the limits as $\Delta x \rightarrow 0$ for (A.3) and (A.6) yields:

$$\frac{dV(x)}{dx} = I(x)Z, \tag{A.7}$$

and

$$\frac{dI(x)}{dx} = V(x)Y. \tag{A.8}$$

To solve these equations we take the second derivative of (A.7) to give:

$$\frac{d^2V(x)}{dx^2} = Z\frac{dI(x)}{dx} = YZV(x) \tag{A.9}$$

where we can now define $\gamma = \sqrt{ZY}$ as the propagation constant, and $Z_0 = \sqrt{\frac{Z}{Y}}$ as the characteristic impedance of the transmission line. The general solution to the homogeneous equation presented in (A.9) has the form:

$$V(x) = K_1 e^{\gamma x} + K_2 e^{-\gamma x}, \tag{A.10}$$

where K_1 and K_2 are arbitrary constants. The current is therefore given from (A.7) as:

$$\begin{aligned} I(x) &= \frac{\frac{dV(x)}{dx}}{Z}, \\ &= \frac{1}{Z}\left[K_1\gamma e^{\gamma x} - K_2\gamma e^{-\gamma x}\right], \\ &= \frac{1}{Z_0}[K_1 e^{\gamma x} - K_2 e^{-\gamma x}], \end{aligned} \tag{A.11}$$

using the substitutions for γ and Z_0 as discussed above. To determine K_1 and K_2, boundary conditions are applied at $x = 0$ to (A.10) and (A.11), yielding:

$$V(x) = V(0) = V_R = K_1 + K_2,$$

and

$$I(x) = I(0) = I_R = \frac{1}{Z_0}(K_1 - K_2),$$

which, solving for K_1 and K_2 gives:

$$K_1 = \frac{V_R + Z_0 I_R}{2}, \tag{A.12}$$

and

$$K_2 = \frac{V_R - Z_0 I_R}{2} \tag{A.13}$$

which, when substituted back into (A.10) generates:

$$\begin{aligned} V(x) &= \left(\frac{V_R + Z_0 I_R}{2}\right) e^{\gamma x} + \left(\frac{V_R - Z_0 I_R}{2}\right) e^{-\gamma x} \\ &= V_R \left[\frac{e^{\gamma x} + e^{-\gamma x}}{2}\right] + Z_0 I_R \left[\frac{e^{\gamma x} - e^{-\gamma x}}{2}\right] \\ &= V_R \cosh(\gamma x) + Z_0 I_R \sinh(\gamma x). \end{aligned} \tag{A.14}$$

Similarly, we may solve for the current in (A.11) to obtain:

$$I(x) = \frac{V_R}{Z_0} \sinh(\gamma x) + I_R \cosh(\gamma x) \tag{A.15}$$

Equations (A.14) and (A.15) may be expressed in matrix form as:

$$\begin{bmatrix} V(x) \\ I(x) \end{bmatrix} = \begin{bmatrix} \cosh(\gamma x) & Z_0 \sinh(\gamma x) \\ \frac{\sinh(\gamma x)}{Z_0} & \cosh(\gamma x) \end{bmatrix} \begin{bmatrix} V_R \\ I_R \end{bmatrix} \tag{A.16}$$

which characterises the voltage and current along a transmission line at an arbitrary position, x. If we consider the lossless case, where the propagation constant $\gamma = \alpha + j\beta$ becomes $\gamma = j\beta$, we can now rewrite (A.16) as:

$$\begin{bmatrix} V(x) \\ I(x) \end{bmatrix} = \begin{bmatrix} \cos(\beta x) & jZ_0 \sin(\beta x) \\ \frac{j \sin(\beta x)}{Z_0} & \cos(\beta x) \end{bmatrix} \begin{bmatrix} V_R \\ I_R \end{bmatrix} \tag{A.17}$$

The ABCD matrix for a transmission line is therefore defined as:

$$\begin{bmatrix} A & B \\ C & D \end{bmatrix} = \begin{bmatrix} \cos(\beta x) & jZ_0 \sin(\beta x) \\ \frac{j \sin(\beta x)}{Z_0} & \cos(\beta x) \end{bmatrix} \tag{A.18}$$

A.2 Dual Impedance Stub

In order to design a dual impedance stub, (3.3) from Chapter 3, repeated here for convenience, must be used:

$$Z_{in} = \frac{AZ_l + B}{CZ_l + D} \tag{A.19}$$

which describes the input impedance, Z_{in} seen looking into a section of transmission line, terminated in a load impedance, Z_l. The stub is broken down into two impedances Z_1 and Z_2 as seen in Figure A.2, with assosciated input impedances of $Z_{in,1}$ and $Z_{in,2}$, and load impedances $Z_{l,1}$ and $Z_{l,2}$.

If we first consider the stub section of impedance Z_2, the load impedance $Z_{l,2} = \infty$ since it terminates in an open circuit. Using this value in (A.19) and replacing A, B, C and D with their matrix values from (A.18) gives:

$$Z_{in,2} = \frac{Z_{l,2} \cos\theta + jZ_2 \sin\theta}{\frac{jZ_{l,2} \sin\theta}{Z_2} + \cos\theta},$$

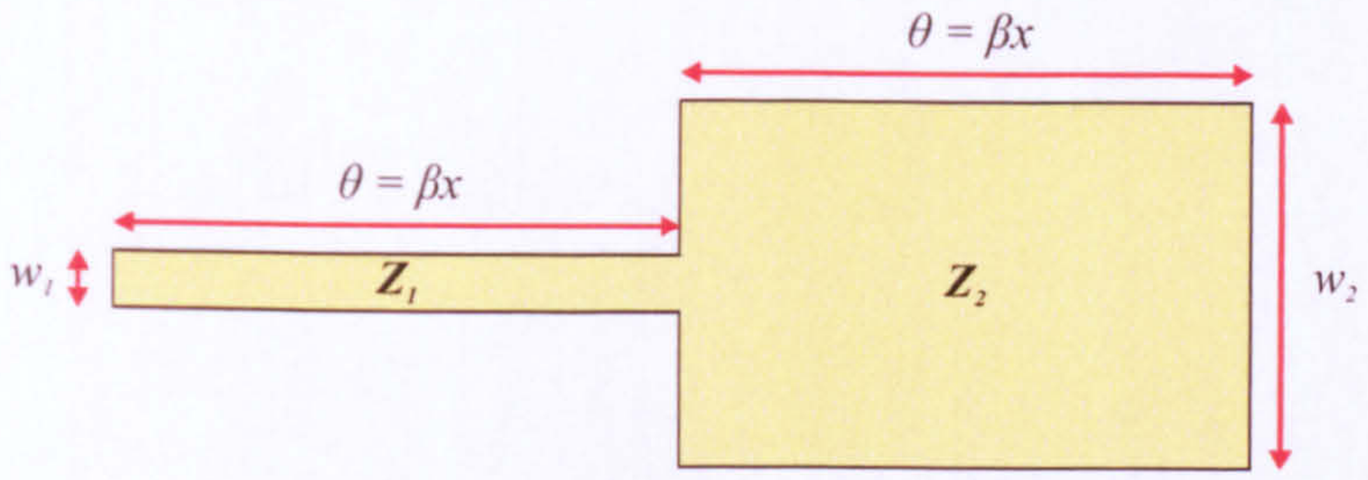

Figure A.2: Schematic of a dual impedance resonator with characteristic impedances of Z_1 and Z_2 and corresponding widths w_1 and w_2. Both regions have equal electrical length, $\theta = \beta x$.

where $\theta = \beta x$ which, dividing through by $Z_{l,1}$ gives:

$$\begin{aligned} Z_{in,2} &= \frac{\cos\theta + \frac{jZ_2 \sin\theta}{Z_{l,2}}}{j\,\sin\theta + \frac{\cos\theta}{Z_{l,2}}}, \\ &= Z_2 \frac{\cos\theta}{j\sin\theta}, \\ &= \frac{Z_2}{j\tan\theta}. \end{aligned} \tag{A.20}$$

Now considering the second stub region of impedance Z_1, we can see that the load impedance for this stub, $Z_{l,1}$, is equal to the input impedance for the previous stub section, given by (A.20). Therefore $Z_{in,1}$ is given by:

$$Z_{in,1} = \frac{Z_{l,1}\cos\theta + jZ_1\sin\theta}{\frac{jZ_{l,1}\,\sin\theta}{Z_1} + \cos\theta},$$

$$Z_{in,1} = \frac{\frac{Z_2}{j\tan\theta}\cos\theta + jZ_1\sin\theta}{\frac{j\frac{Z_2}{j\tan\theta}\,\sin\theta}{Z_1} + \cos\theta}.$$

At resonance, $Z_{in,1}$ becomes equal to zero, since the stub acts as a short circuit, therefore:

$$\frac{Z_2}{j\tan\theta}\cos\theta = -jZ_1\sin\theta,$$

$$\therefore Z_2\cos^2\theta = Z_1\sin^2\theta,$$

$$\therefore \frac{Z_2}{Z_1} = \tan^2\theta. \tag{A.21}$$

We can now choose an impedance ratio Z_2:Z_1 which will generate an electrical length, θ, which will be equal for each stub. For continuity, the higher impedance (and therefore narrow stub section) was maintained at 34 Ω (5 μm). If we then choose Z_2 to be one third of this value (corresponding to a width of 32 μm), the ratio 1:3 gives an electrical length of 30°, equivalent to 59 μm.

Appendix B

DNA Plasmid Preparation

A bacterial E. coli strain (JM109) containing a 3307 base pair (3.307 kbp) pGEM plasmid from [95] was grown at 37 °C overnight in 50 ml of Luria Broth (LB). The LB is supplemented with 100 μg / μl of the antibiotic ampicillin, to maintain the plasmid construct which contains an ampicillin resistance gene. The plasmid floats freely in the cytoplasm within the cell, as seen in Figure B.1, whilst the cell genomic DNA is attached to the phospholipid cell wall. Since the E. coli is a procaryotic organism, it contains no organelles (such as a cell nucleus) and it is therefore reasonably straightforward to separate the plasmid from the rest of the cell structure.

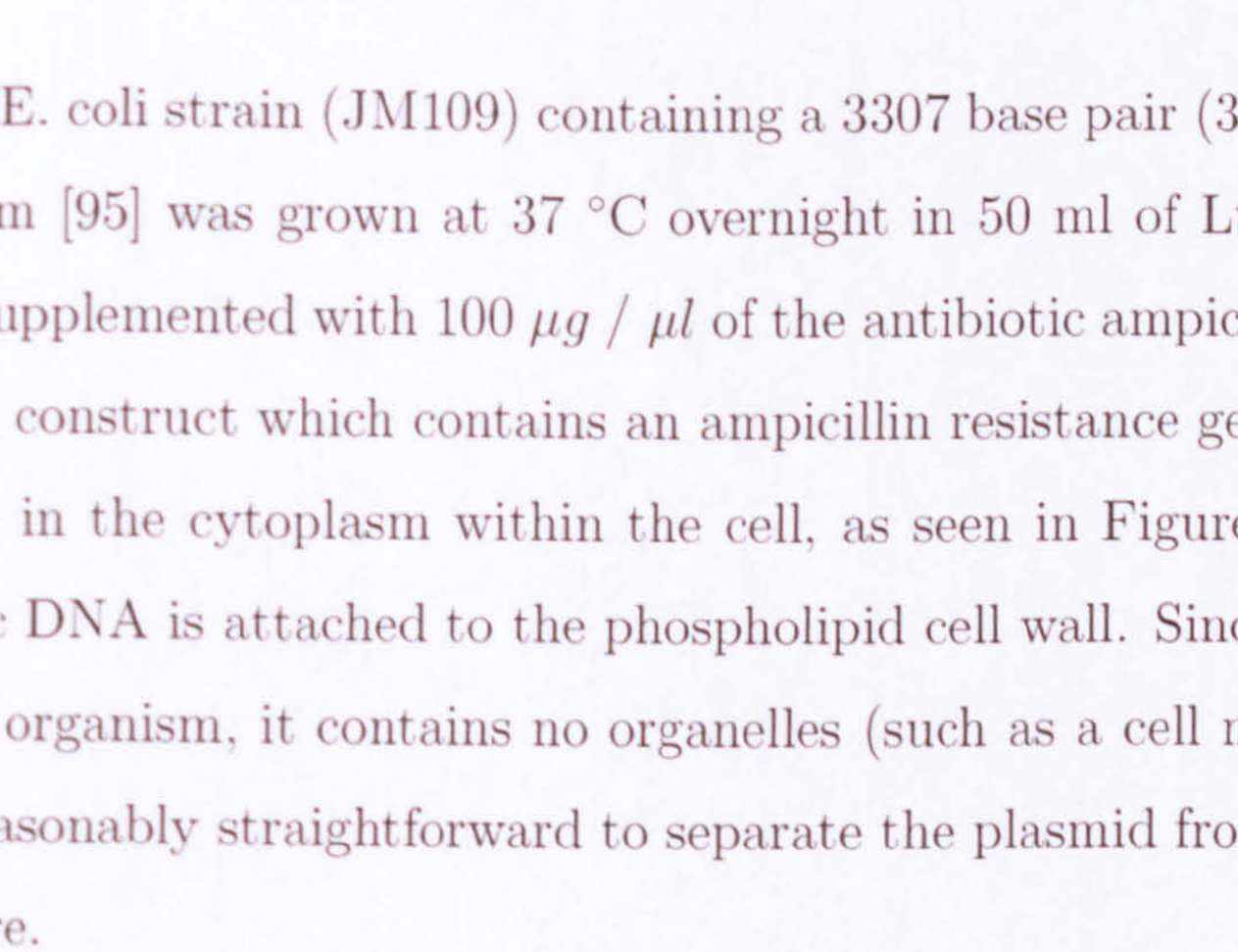

Figure B.1: Simplified diagram of a bacterial cell containing a non-native plasmid DNA which contains a resistance gene to the antibiotic, ampicillin.

Plasmids were purified using a QIAGEN Plasmid Midi Kit (Qiagen catalogue

number 12143) as per the manufacturers instructions. Briefly, the bacterial cells were resuspended in a buffer solution and then lysed using a NaOH solution. Proteins were then precipitated using acetic acid, and since the genomic DNA and cell wall are attached, the resulting protein flocculate may be centrifuged to remove the precipitated protein and the attached genomic DNA from the mix whilst the plasmid remains in solution.

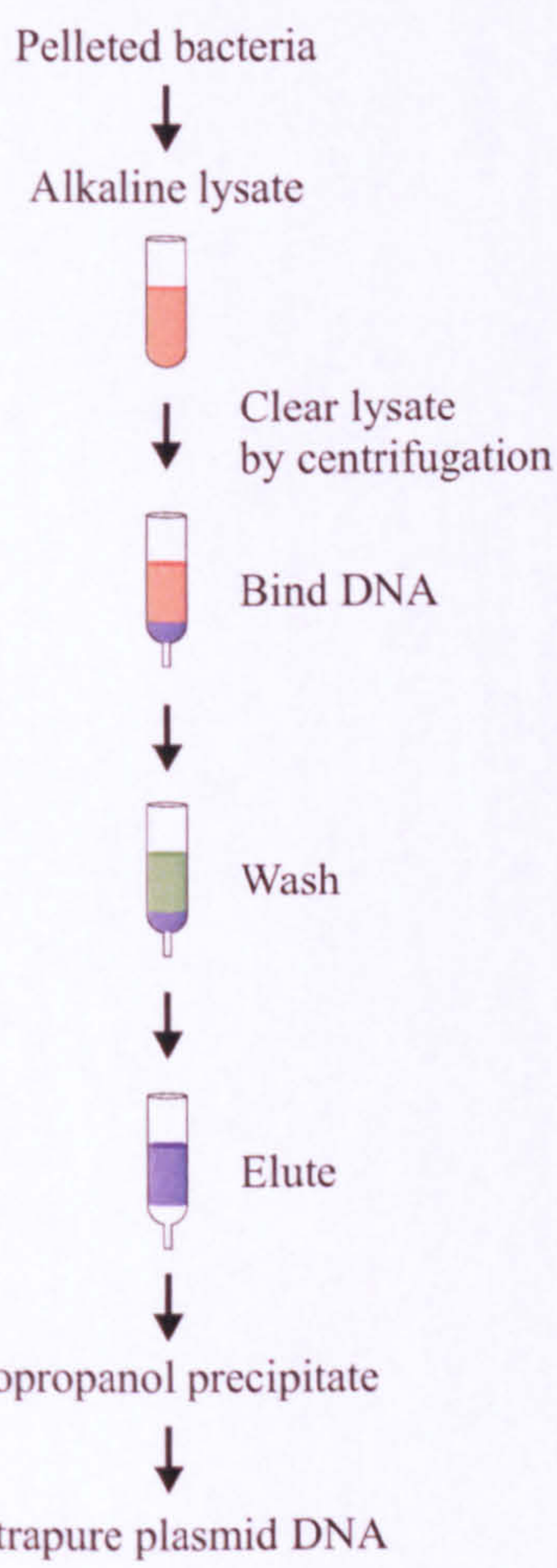

Figure B.2: Flow diagram of the plasmid purification procedure, adapted from [108].

The remaining plasmid solute is then purified on a Qiagen column via gravity flow (Figure B.2). After purification, the plasmid is eluted from the column using 5 ml of Tris buffer (pH 8.0) and precipitated to concentrate using 0.7 volumes of isopropanol and centrifugation. The DNA pellet was washed twice in 80 % ethanol and dried. The dried pellet was then resuspended in 50 μl of deionised

H_2O. The plasmid concentration was determined by measuring its absorbance at 280 nm using a BioPhotometer (Eppendorf), and could subsequently be diluted to achieve the 1 μg / μl concentration used for measurements in Chapter 6.

Appendix C

Conferences and Publications

'Terahertz frequency range band-stop filters', Appl. Phys. Lett 86, 213503 (2005), J. Cunningham, **C. Wood**, A. G. Davies, I. C. Hunter, E. H. Linfield, H. E. Beere

'Multiple-frequency terahertz pulsed sensing of dielectric films', Appl. Phys. Lett 88, 071112 (2006), J. Cunningham, **C. Wood**, A. G. Davies, C. K. Tiang, P. Tosch, D. Evans. E. H. Linfield, I. C. Hunter, M. Missous

'On-chip photoconductive excitation and detection of pulsed teraherz radiation at cryogenic temperatures', Appl. Phys. Lett. 88, 142103 (2006), **C. Wood**, J. Cunningham, P. C. Upadhya, E. H. Linfield, I. C. Hunter, A. G. Davies, M Missous

'Guided-wave terahertz devices for sensing the properties of overlaid dielectric films', **Invited paper**, Proc SPIE vol. 6120, 61200P (Mar 2006), **C. Wood**, J. E. Cunningham, A. G. Davies, I. C. Hunter, P. Tosch, E. H. Linfield

'On-chip pulsed terahertz systems and their applications', **Invited paper**, Int. J. Infrared. Milli. vol 27, No. 4 (2006), **C. Wood**, J. Cunningham, I. C. Hunter,

P. Tosch, E. H. Linfield, A. G. Davies

'Pulsed terahertz sensing of dielectric thin films using cascaded filter arrays', Conference Digest of the Joint 30^{th} International Conference on Infrared and Millimeter Waves and 13^{th} International Conference of Terahertz Electronics, Fort Williamsburg, p. 586 (2005), **C. Wood**, J. Cunningham, A. G. Davies, I. C. Hunter, P. Tosch, E. H. Linfield, M. Missous

'Electromagnetic simulation of terahertz frequency-range filters for genetic sensing', submitted J. Appl. Phys. (2005), C. K. Tiang, J. Cunningham, **C. Wood**, I. C. Hunter, A. G. Davies

'Measurement and simulation of the sensitivity of terahertz frequency range passive filter elements to overlaid dielectrics', Conference Digest of the Joint 31^{st} International Conference on Infrared and Millimeter Waves and 14^{th} International Conference of Terahertz Electronics, Shanghai (2006), **C. Wood**, J. Cunningham, C. K. Tiang, M. Byrne, I. C. Hunter, E. H. Linfield, A. G. Davies

'Cryogenic excitation and detection of terahertz radiation in microstrip circuits', Conference Digest of the Joint 31^{st} International Conference on Infrared and Millimeter Waves and 14^{th} International Conference of Terahertz Electronics, Shanghai (2006), J. Cunningham, **C. Wood**, P. C. Uphadya, E. H. Linfield, A. G. Davies

Band Stop Filter, International Patent WO 2006/064192, **C. D. Wood**, J. E. Cunningham, A. G. Davies, I. C. Hunter (2006)

Band Stop Filter, UK Patent Application GB0427322.3, Cunningham, J., **Wood C.**, Davies A. G., Hunter I. C. (2005)

References

[1] P. F. Taday, "Applications of terahertz spectroscopy to pharmaceutical sciences", *Phil. Trans. R. Soc. Lond. A*, vol. 362, pp. 351–364, 2004.

[2] K. Humphreys, J.P. Loughran, M. Gradziel, W. Lanigan, T. Ward, J. A. Murphy, and C. O'Sullivan, "Medical applications of terahertz imaging: a review of current technology and potential applications in biomedical engineering", in *Engineering in Medicine and Biology Society, 2004. EMBC 2004. Conference Proceedings. 26th Annual International Conference of the*, 2004, vol. 1, pp. 1302–1305.

[3] V. P. Wallace, A. J. Fitzgerald, S. Shankar, N. Flanagan, R. Pye, J. Cluff, and D. D. Arnone, "Terahertz pulsed imaging of bassal cell carcinoma *ex vivo* and *in vivo*", *Brit. J. Derm.*, vol. 151, pp. 424–432, 2004.

[4] S. P. Mickan, A. Menikh, H. Liu, C. A. Mannella, R. MacColl, D. Abbott, J. Munch, and X-C. Zhang, "Label-free bioaffinity detection using terahertz technology", *Phys. Med. Biol.*, vol. 47, no. 21, pp. 3789–3795, 2002.

[5] T. H. Maiman, "Stimulated optical radiation in ruby", *Nature*, vol. 187, pp. 493–494, 1960.

[6] F. L. Pedrotti, *Introduction to Optics*, Prentice-Hall, Englewood Cliffs, N.J., 2 edition, 1993.

[7] P. A. Franken, A. E. Hill, C. W. Peters, and G. Weinrich, "Generation of optical harmonics", *Phys. Rev. Lett.*, vol. 7, no. 4, pp. 118–120, 1961.

[8] M. Houe and P. D. Townsend, "An introduction to methods of periodic poling for second harmonic generation", *J. Phys. D: Appl. Phys.*, vol. 28, pp. 1747–1763, 1995.

[9] Y. Liu, S. Kurimuri, M Nakamura, S. Takekawa, and K Kitamura, "Effective aperture in periodically poled Mg-doped stoichiometric $LiTaO_3$ for quasi-phase-matched optical parametric oscillation", *Jap. J. Appl. Phys.*, vol. 45, no. 5A, pp. 4064–4067, 2006.

[10] M. Yamada, N. Nada, M. Saitoh, and K. Watanabe, "First-order quasi-phase matched $LiNbO_3$ waveguide periodically poled by applying an external field for efficient blue second-harmonic generation", *Appl. Phys. Lett.*, vol. 62, no. 5, pp. 435–436, 1993.

[11] T. J. Edwards, D. Walsh, M. B. Spurr, C. F. Rae, and M. H. Dunn, "Compact source of continuously and widely-tunable terahertz radiation", *Opts. Expr.*, vol. 14, no. 4, pp. 1582–1589, 2006.

[12] T. Tanabe, K. Suto, J. I. Nishizawa, and T. Sasaki, "Characteristics of terahertz-wave generation from gase crystals", *J. Phys. D: Appl. Phys.*, vol. 37, no. 2, pp. 155–158, 2004.

[13] M. Rochat, L. Ajili, H. Willenburg, and J. Faist, "Low-threshold terahertz quantum-cascade lasers", *App. Phys. Lett.*, vol. 81, no. 8, pp. 1381–1383, 2002.

[14] Q. Hu, H. Callebaut, E. Duerr, S. Kohen, K. Konistis, S. Kumar, J. Montoya, B. Williams, J. Montoya, and E.K. Duerr, "Terahertz quantum cascade lasers and electronics", *Materials Research at MIT*, 2003.

[15] J. Ouellette, "Quantum cascade lasers turn commercial", *American Institute of Physics*, 2001.

[16] D. C. Larrabee, G. A. Khodaparast, F. K. Tittel, J. Kono, M. Rochat, L. Ajili, J. Faist, H. Beere, E. Linfield, Y. Nakajima, M. Nakai, S. Sasa,

M. Inoue, and S. J. Chung, "Application of teraherz quantum cascade lasers to semiconductor cyclotron resonance", *Opt. lett.*, vol. 29, no. 1, pp. 1–3, 2004.

[17] T. Chakraborty and V. Apalkov, "Quantum casade transitions in nanostructures", *Adv. in Phys.*, vol. 52, no. 5, pp. 455–521, 2003.

[18] M. Razeghi and S. Slivken, "High power quantum cascade lasers grown by gas MBE", *Opto-Elec. Rev.*, vol. 11, no. 2, pp. 85–91, 2003.

[19] S. Jayaraman and C. H. Lee, "Observation of two-photon conductivity in GaAs with nanosecond and picosecond light pulses", *Appl. Phys. Lett.*, vol. 20, no. 10, pp. 392–395, 1972.

[20] M. Born and E. Wolf, *Principles of Optics: Electromagnetic theory of propagation, interference and diffraction of light*, Cambridge University Press, 7^{th} edition, 1999.

[21] P. H. Siegel, "Terahertz technology", *IEEE Trans. Mic. Theo. Tech.*, vol. 50, no. 3, pp. 910–928, 2002.

[22] Y. C. Shen, P. C. Upadhya, E. H. Linfield, H. E. Beere, and A. G. Davies, "Ultrabroadband terahertz radiation from low-temperature-grown GaAs photoconductive emitters", *Appl. Phys. Lett.*, vol. 83, no. 15, pp. 3117–3119, 2003.

[23] M. B. Johnston, D. M. Whittaker, A. Corchia, A. G. Davies, and E. H. Linfield, "Simulation of terahertz generation at semiconductor interfaces", *Phys. Rev. B.*, vol. 65, pp. 165301, 2002.

[24] E. Castro-Camus, J. Lloyd-Hughes, and M. B. Johnston, "Three-dimensional carrier-dynamics simulation of terahertz emission from photoconductive switches", *Phys. Rev. B.*, vol. 71, pp. 195301, 2005.

[25] A. Luukanen, R. H. Hadfield, A. J. Miller, and E. N. Grossman, "A superconducting antenna coupled microbolometer for THz applications", in

Proc. SPIE. THz for military and security applications, 2004, vol. 5411, pp. 121–126.

[26] Christoph Ludwig and Jurgen Kuhl, "Studies of the temporal and spectral shape of terahertz pulses generated from photoconducting switches", *Appl. Phys. Lett.*, vol. 69, no. 9, pp. 1194–1196, 1996.

[27] R. P. Prasankumar, A. Scopatz, D. J. Hilton, A. J. Taylor, R. D. Averitt, J. M. Zide, and A. C. Gossard, "Carrier dynamics in self-assembled ErAs nanoislands measured by optical-pump THz-probe spectroscopy", *Quant. Elec. and Las. Sci. Conference*, vol. QELS 05, no. 1, pp. 446 – 448, 2005.

[28] Q. Wu and X.-C. Zhang, "Free-space electro-optics sampling of mid-infrared pulses", *Appl. Phys. Lett.*, vol. 71, no. 10, pp. 1285–1286, 1997.

[29] N. C. J. van der Valk, T. Wenckebach, and P. C. M. Planken, "Full mathematical description of electro-optic detection in optically isotropic crystals", *J. Opt. Soc. Am. B*, vol. 21, no. 3, pp. 622–631, 2004.

[30] C. Kubler, R. Huber, S. Tubel, and A. Leitenstorfer, "Ultrabroadband detection of multi-terahertz field transients with gase electro-optic sensors: Approaching the near infrared", *Appl. Phys. Lett.*, vol. 85, no. 16, pp. 3360–3362, 2004.

[31] M. King and J. Wiltse, "Surface-wave propagation on coated or uncoated metal wires at millimeter wavelengths", *IEEE Trans. Ant. Prop.*, vol. 10, no. 3, pp. 246–254, 1962.

[32] J.C. Wiltse, "Surface-wave propagation on metal wires at millimeter-wave and terahertz frequencies", in *The Joint 30th International Conference on Infrared and Millimeter Waves and 13th International Conference on Terahertz Electronics*, 2005, vol. 2, pp. 557–558.

[33] K. Wang and D. M. Mittleman, "Metal wires for terahertz wave guiding", *Nature*, vol. 432, pp. 376–379, 2004.

[34] J. Wang, "From DNA biosensors to gene chips", *Nuc. Acid. Res.*, vol. 28, no. 16, pp. 3011–3016, 2000.

[35] R. F. Cregan, B. J. Mangan, J. C. Knight, T. A. Birks, P. St. J. Russell, P. J. Roberts, and D. C. Allan, "Single-mode photonic band gap guidance of light in air", *Science*, vol. 285, no. 5433, pp. 1537–1539, 1999.

[36] H. Han, H. Park, M. Cho, J. Kim, I. Park, and H. Lim, "Terahertz pulse propagation in plastic photonic crystal fibers", in *IEEE MTT-S International Microwave Symposium Digest*, 2002, vol. 2, pp. 1075–1078.

[37] S. Q. Lou, T. Y. Guo, H. Fang, H. L. Li, and S. S. Jian, "A new type of terahertz waveguides", *Chin. Phys. Lett.*, vol. 23, no. 1, pp. 235–238, 2006.

[38] D. H. Auston, "Picosecond optoelectronic switching and gating in silicon", *App. Phys. Lett.*, vol. 26, no. 3, pp. 101–103, 1974.

[39] U. D. Keil and D. R. Dykaar, "Ultrafast pulse generation in photoconductive switches", *J. Quant. Elec*, vol. 32, no. 9, pp. 1664–1671, 1996.

[40] D. H. Auston, "Impulse response of photoconductors in transmission lines", *IEEE J. Quant. Elec.*, vol. 19, no. 4, pp. 639–648, 1983.

[41] D. H. Auston, A. M. Johnson, P. R. Smith, and J. C. Bean, "Picosecond optoelectronic detection, sampling and correlation measurements in amorphous semiconductors", *Appl. Phys. Lett.*, vol. 37, no. 4, pp. 371–373, 1980.

[42] H. Němec, F. Kadlec, P. Kužel, M. Khazan, S. Schnüll, and I. Wilke, "Carrier dynamics in low-temperature grown gaas studied by THz emission spectroscopy", *IRMMW - Thz. Gen. App.*, vol. 3, pp. 61–64, 2001.

[43] C-D. Lee, H. J. Lee, S. K. Noh, C. Park, C. G. Park, S-J. Park, and K-S. Lee, "Fabrication of self-assembled quantum dots in lattice-matched GaAs/AlGaAs system", *J. Kor. Phys. Soc*, vol. 33, no. 1, pp. S262–S265, 1998.

[44] M. Konagai, M. Sugimoto, and K. Takahashi, "High efficiency GaAs thin film solar cells by peeled film technology", *J. Crys. Grow.*, vol. 45, pp. 277–280, 1978.

[45] E. Yablonovitch, T. Gmitter, J. P. Harbison, and R. Bhat, "Extreme selectivity in the lift-off of epitaxial GaAs films", *Appl. Phys. Lett.*, vol. 51, no. 26, pp. 2222–2224, 1987.

[46] E. Yablonovitch, D. M. Hwang, T. J. Gmitter, L. T. Florez, and J. P. Harbison, "Van der Waals bonding of GaAs epitaxial lift-off films onto arbitrary substrates", *Appl. Phys. Lett.*, vol. 56, no. 24, pp. 2419–2421, 1990.

[47] A. Yi-Yan, W. K. Chan, T. J. Gmitter, L. T. Florez, J. L. Jackel, E. Yablonovitch, R. Bhat, and J. P. Harbison, "Grafted GaAs detectors on lithium niobate and glass optical waveguides", *IEEE Phot. Tech. Lett.*, vol. 1, no. 11, pp. 379–380, 1989.

[48] M. Nagel, T. Dekorsy, M. Brucherseifer, P. H. Bolivar, and H. Kurz, "Characterisation of polypropylene thin-film microstrip lines at millimetre and submillimetre wavelengths", *Mic. Opt. Tech. Lett.*, vol. 29, no. 2, pp. 97–100, 2001.

[49] C. Wood, J. Cunningham, A. G. Davies, I. C. Hunter, P. Tosch, D. A. Evans, E. H. Linfield, and M. Missous, "Pulsed THz sensing of dielectric thin films using cascaded filter arrays", in *The Joint 30th International Conference on Infrared and Millimeter Waves and 13th International Conference on Terahertz Electronics*, Virginia, 2005, IRMMW.

[50] J. D. Watson and F. H. C. Crick, "Genetical implications of the structure of deoxyribonucleic acid", *Nature*, vol. 171, pp. 964–967, 1953.

[51] J. D. Watson and F. H. C. Crick, "Molecular structure of nucleic acids", *Nature*, vol. 171, pp. 737–738, 1953.

[52] C. van Ingen, "Biology's century: just the beginning for microarrays", *Nature Genetics*, vol. 32, no. 4, pp. 463, 2002.

[53] D. E. M. Feldker, E. R. de Kloet, M. R. Kruk, and N. A. Datson, "Large-scale gene expression profiling of discrete brain regions: Potential, limitations, and application in genetics of aggressive behavior", *Behav. Gen.*, vol. 33, no. 5, pp. 537 – 548, 2003.

[54] M. Bykhovskaia, B. Gelmont, T. Globus, D. L. Woolard, A. C. Samuels, T. H. Duong, and K. Zakrzewska, "Prediction of DNA far-IR absoprtion spectra based on normal mode analysis", *Theor. Chem. Acc.*, vol. 106, pp. 22–27, 2001.

[55] H. Urabe, Y. Sugawara, M. Tsukakoshi, and T. Kasuya, "Low-frequency raman spectra of guanosine and nucleotides in ordered states: Origin of the lowest-frequency mode", *J. Chem. Phys.*, vol. 95, no. 8, pp. 5519–5523, 1991.

[56] B. M. Fischer, M. Walther, and P. U. Jepsen, "Far-infrared vibrational modes of DNA components studied by terahertz time-domain spectroscopy", *Phys. Med. Biol.*, vol. 47, pp. 3807–3814, 2002.

[57] M. Brucherseifer, M. Nagel, P. Haring Bolivar, H. Kurz, A. Bosserhoff, and R. Bttner, "Label-free probing of the binding state of DNA by time-domain terahertz sensing", *Appl. Phys. Lett.*, vol. 77, no. 24, pp. 4049–4051, 2000.

[58] M. Nagel, P. H. Bolivar, M. Brucherseifer, H. Kurz, A. Bosserhoff, and R. Bttner, "Integrated THz technology for label-free genetic diagnostics", *Appl. Phys. Lett.*, vol. 80, no. 1, pp. 154–156, 2002.

[59] M. Nagel, F. Richter, P. H. Bolivar, and H. Kurz, "A functionalized THz sensor for marker-free DNA analysis", *Phys. Med. Biol.*, vol. 48, pp. 3625–3636, 2003.

[60] T. M. Herne and M. J. Tarlov, "Characterization of DNA probes immobilized on gold surfaces", *J. Am. Chem. Soc.*, vol. 119, pp. 8916–8920, 1997.

[61] T. N. Theis, J. P. Kotthaus, and P. J. Stiles, "Two-dimensional magnetoplasmon in the silicon inversion layer", *Solid State Commun.*, vol. 24, no. 4, pp. 273–277, 1977.

[62] E. A. Shaner and S. A. Lyon, "Picosecond time-resolved two-dimensional ballistic electron transport", *Phys. Rev. Lett.*, vol. 93, no. 3, pp. 037402–4, 2004.

[63] M. C. Nuss, P. M. Mankiewich, R. E. Howard, B. L. Straughn, T. E. Harvey, C. D. Brandle, G. W. Berkstresser, K. W. Goossen, and P. R. Smith, "Propagation of terahertz bandwidth electrical pulses on $YBa_2Cu_3O_{7\delta}$ transmission lines on lanthanum aluminate", *Appl. Phys. Lett.*, vol. 54, no. 22, pp. 2265–2267, 1989.

[64] E. A. Shaner and S. A. Lyon, "Time-resolved impulse response of the magnetoplasmon resonance in a two-dimensional electron gas", *Phys. Rev. B.*, vol. 66, no. 4, pp. 041402, 2002.

[65] I. C. Hunter, *Theory and Design of Microwave Filters*, vol. 48, IEE electromagnetic wave series, 2001.

[66] D. M. Pozar, *Microwave Engineering*, Wiley, Crawfordsville, 2nd edition, 1998.

[67] S. Ramo, J. R. Whinnery, and T. van Duzer, *Fields and Waves in Communication Electronics*, John Wiley & Sons, New York, 3^{rd} edition, 1994.

[68] M. Kobayashi, "Longitudinal and transverse current distributions on microstriplines and their closed-form expression", *IEEE Trans. Mic. Theo. Tech.*, vol. MTT-33, no. 9, pp. 784–788, 1985.

[69] K. C. Gupta, R. Garg, and I. J. Bahl, *Microstrip Lines and Slotlines*, Artech House, Boston, 2^{nd} edition, 1979.

[70] H. Sun, *Transmission Loss and Dispersion in Conductor-Backed Coplanar Waveguide*, PhD thesis, University of Alberta, 2003.

[71] S. B. Cohn, "Slot line on a dielectric substrate", *IEEE Trans. Mic. Theo. Tech.*, vol. 17, no. 10, pp. 768–778, 1969.

[72] C. P. Wen, "Coplanar waveguide, a surface strip transmission line suitable for nonreciprocal gyromagnetic device applications", in *Microwave Symposium Digest, G-MTT International*, 1969, vol. 69, pp. 110–115.

[73] J. Browne, "Broad-band amps sport coplanar wave-guide", *Microwaves & RF*, vol. 26, no. 2, pp. 131–134, 1987.

[74] N. Zamdmer, Q. Hu, S. Verghese, and A. Forster, "Mode-discriminating photoconductor and coplanar waveguide circuit for picosecond sampling", *Applied Physics Letters*, vol. 74, no. 7, pp. 1039–1041, 1999.

[75] J. Zehentner and J. Macháč, "Properties of CPW in the sub-mm wave range and its potential to radiate", in *Microwave Symposium Digest., 2000 IEEE MTT-S International*, 2000, vol. 2, pp. 1061–1064.

[76] G. A. Kousaev, M. J. Deen, and N. K. Nikolova, "A parallel-plate waveguide model of lossy microstrip lines", *IEEE Micro. Wire. Comp. Lett.*, vol. 15, no. 1, pp. 27–29, 2005.

[77] R. Horton, B. Easter, and A. Gopinath, "Variation of microstrip losses with thickness of strip", *Electron. Lett.*, vol. 7, no. 17, pp. 490–491, 1971.

[78] W. Heinrich, "Full-wave analysis of conductor losses on MMIC transmission lines", *IEEE Transactions on Microwave Theory and Techniques*, vol. 38, no. 10, pp. 1468–1472, 1990.

[79] M. Konno, "Conductor loss in thin-film transmission lines", *Electron. Commun. Jpn. Pt. II-Electron.*, vol. 82, no. 10, pp. 83–91, 1999.

[80] J. C. Rautio and V. Demir, "Microstrip conductor loss models for electromagnetic analysis", *IEEE Trans. Mic. Theo. Tech.*, vol. 51, no. 3, pp. 915–921, 2003.

[81] M. Nagel, C. Meyer, H. M. Heiliger, T. Dekorsy, H. Kurz, R. Hey, and K. Ploog, "Optical second-harmonic probe for ultra-high frequency on-chip interconnects with benzocyclobutene", *App. Phys. Lett.*, vol. 72, no. 9, pp. 1018–1020, 1998.

[82] E. H. Fooks and R. A. Zakarevicius, *Microwave Engineering Using Microstrip Circuits*, Prentice Hall, 1st edition, 1990.

[83] R. K. Hoffman, *Handbook of Microwave Integrated Circuits*, Artech House, Norwood, 1987.

[84] Dow Chemicals, "Cyclotene 4000 series advanced electronic resins (photo BCB)", *Data Sheet.*

[85] M. Nagel, P. H. Bolivar, M. Brucherseifer, H. Kurz, A. Bosserhoff, and R. Buttner, "Integrated planar THz resonators for femtomolar sensitivity label-free detection of DNA hybridization", *App. Opt.*, vol. 41, no. 10, pp. 2074–2078, 2002.

[86] G. Matthaei, L. Young, and E. M. T. Jones, *Microwave Filters, Impedance-matching Networks, and Coupling Structures*, Artech House, North Bergen, 1980 Reprint.

[87] H. C. Bell, "L-resonator bandstop filters", *IEEE Trans. Mic. Theo. Tech.*, vol. 44, no. 12, pp. 2669 – 2672, 1996.

[88] Sonnet Software Inc., "Sonnet".

[89] S. Verghese, K. A. Mcintosh, and E. R. Brown, "Optical and terahertz power limits in the low-temerpature-grown GaAs photomixers", *Appl. Phys. Lett.*, vol. 71, no. 19, pp. 2743–2745, 1997.

[90] P. H. Bolivar, M. Brucherseifer, M. Nagel, H. Kurz, A. Bosserhoff, and R. Bttner, "Label-free probing of genes by time-domain terahertz sensing", *Phys. Med. Biol.*, vol. 47, pp. 3815–3821, 2002.

[91] X. Zheng, Y. Xu, R. Sobolewski, R. Adam, M. Mikulics, M. Siegel, and P. Kordoe, "Femtosecond response of free-standing LT-GaAs photoconductive switch", *Appl. Opt.*, vol. 42, no. 9, pp. 1726–1731, 2003.

[92] C. Wood, J. Cunningham, P. C. Upadhya, E. H. Linfield, I. C. Hunter, and A. G. Davies, "On-chip photoconductive excitation and detection of pulsed terahertz radiation at cryogenic temperatures", *Appl. Phys. Lett.*, vol. 88, pp. 142103, 2006.

[93] C. Wood, J.E. Cunningham, A. G. Davies, I.C. Hunter, P. Tosch, and E.H. Linfield, "Guided-wave terahertz devices for sensing the properties of overlaid dielectric films", *Proc. of SPIE*, vol. 6120, pp. 61200P1–3, 2005.

[94] J. Cunningham, C. Wood, A. G. Davies, I. Hunter, and E. H. Linfield, "Terahertz frequency range band-stop filters", *Appl. Phys. Lett.*, vol. 86, no. 21, pp. 213503.1–213503.3, 2005.

[95] P. Tosch, C. Walti, A.P.J. Middelberg, and A.G. Davies, "Generic technique to generate large branched DNA complexes", *Biomacromolecules*, vol. 7, no. 3, pp. 677–681, 2006.

[96] C. K. Tiang, J. E. Cunningham, C. Wood, I. C. Hunter, and A. G. Davies, "Electromagnetic simulation of terahertz frequency-range filters for genetic sensing", *J. Appl. Phys.*, accepted for publication 2006.

[97] K.A. Peterlinz, R.M. Georgiadis, T.M. Herne, and M.J. Tarlov, "Observation of hybridization and dehybridization of thiol-tethered DNA using

two-color surface plasmon resonance spectroscopy", *J. Am. Chem. Soc.*, vol. 119, no. 14, pp. 3401–3402, 1997.

[98] S. O. Kelley, N. M. Jackson, M. G. Hill, and J. K. Barton, "Long-range electron transfer through DNA films", *Angew. Chem. Int. Ed.*, vol. 38, no. 7, pp. 941–945, 1999.

[99] R. Levicky, T.M. Herne, M.J. Tarlov, and S.K. Satija, "Using self-assembly to control the structure of DNA monolayers on gold: A neutron reflectivity study", *J. Am. Chem. Soc.*, vol. 120, no. 38, pp. 9787–9792, 1998.

[100] J. J. Gooding and G. C. King, "Nucleic acid biosensors based upon surface assembled monolayers: exploiting and enhancing materials properties", *J. Mater. Chem*, vol. 15, pp. 4876–4880, 2005.

[101] S. O. Kelley, J. K. Barton, N. M. Jackson, L. D. McPherson, A. B. Potter, E. M. Spain, M. J. Allen, and M. G. Hill, "Orienting DNA helices on gold using applied electric fields", *Langmuir*, vol. 14, no. 24, pp. 6781–6784, 1998.

[102] Y. Ishige, M. Shimoda, and M. Kamahori, "Immobilization of DNA probes onto gold surface and its application to fully electric detection of DNA hybridization using field-effect transistor sensor", *Jap. J. Appl. Phys.*, vol. 45, no. 4B, pp. 3776–3783, 2006.

[103] C. Walti, R. Wirtz, W. A. Germishuizen, D. M. D. Bailey, M. Pepper, A. P. J. Middelberg, and A. G. Davies, "Direct selective functionalization of nanometer-separated gold electrodes with DNA oligonucleotides", *Langmuir*, vol. 19, pp. 981–984, 2003.

[104] C. Gaillard and F. Strauss, "Avoiding DNA loss and denaturation upon storage in plastic microtubes", *Axygen Scientific Application Notes*, 2000.

[105] C. Gaillard and F. Strauss, "Avoiding adsorption of DNA to polypropy-

lene tubes and denaturation of short DNA fragments", *Axygen Scientific Application Notes*, 1998.

[106] Y. K. Cho, S. Kim, G. Lim, and S. Granick, "A surface forces study of DNA hybridization", *Langmuir*, vol. 17, pp. 7732–7734, 2001.

[107] J. Suehiro, G. Zhou, and M. Hara, "Fabrication of a carbon nanotube-based gas sensor using dielectrophoresis and its application for ammonia detection by impedance spectroscopy", *J. Phys. D: Appl. Phys.*, vol. 36, pp. L109–L114, 2003.

[108] Qiagen, *Qiagen Plasmid Purification Handbook*, 3rd edition, 2005.